Computer Simulations for Thorium doped Tungsten Crystals

Dissertation

Institut für Physik
Mathematisch-Naturwissenschaftliche Fakultät
Universität Augsburg

eingereicht von
Bernd Eberhard

Augsburg, Dezember 2008

Erster Gutachter:	Prof. Dr. Ferdinand Haider
Zweiter Gutachter:	Priv.-Doz. Dr. Karl-Heinz Höck
Dritter Gutachter:	Prof. Dr. Georges Martin

Tag der mündlichen Prüfung: 17.07.09

Contents

List of Figures

List of Tables

Chapter 1

Introduction

Since the beginning of the 20th century tungsten illuminates the world. To understand why tungsten is that important in lighting industry up to now, one may take a look at the basic principles of artificial illumination. The human eye has two different kinds of receptor systems interleaved: the *rod* retina and the *cone* retina, responsible for low illumination, i.e. for twilight and night-time use, and for daytime, i.e. color seeing, respectively. Measurements of the spectral sensitivity of the light receptors, see Fig. 1.1, show, that the overall sensitivity of the cones peaks in the yellow-green, i.e. at wavelengths of about $\lambda \approx 555$nm, whereas the rods are most sensitive in the green ($\lambda \approx 507$nm). There are three different kind of cones in the retina of the human eye, each of which differ in their colored light absorptions, loosely called red, green and blue cones, responsible for color seeing. The sensation of the whole spectrum of colors is provided by exciting the three cone types differently.

For artificial lighting, most often *temperature radiation* is used. A *black body* at a given temperature T radiates electromagnetic waves according to the famous *Planck law* [Pla01]:

$$I(\lambda, T) = \frac{2hc^2}{\lambda^5} \frac{1}{e^{\frac{hc}{\lambda k_B T}} - 1}$$

where $I(\lambda, T)$ denotes the *spectral radiance*, i.e. the energy per unit time per unit surface area per unit solid angle per unit wavelength. h is Planck's constant, k_B Boltzmann's constant, c the speed of light and λ the wavelength of the emitted electromagnetic wave. The black body radiation versus λ for different temperatures is shown in Fig. 1.2.

Real matter, however, usually is not adequately described as an idealized black body, i.e. it's radiance differs from Planck's law considerably. The ability to radiate energy is maximal for a black body, a fact, that is responsible

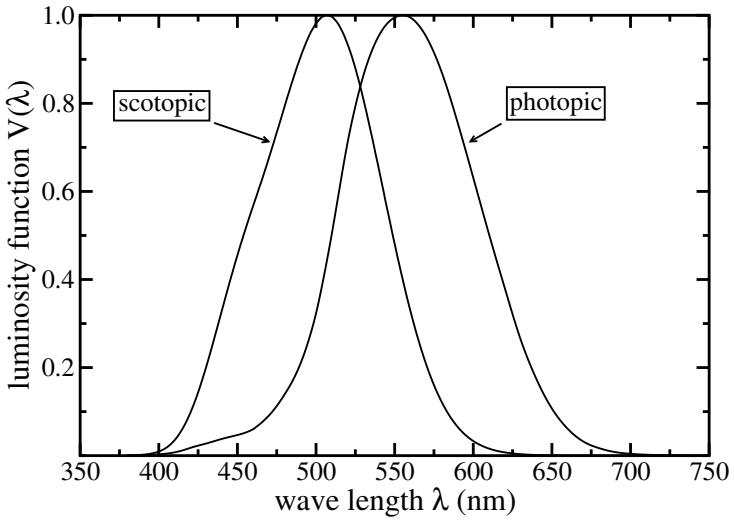

Fig. 1.1: *The measured* scotopic *and the* photonic *luminosity function. The scotopic luminosity function (adopted by* GIE *in 1951, [Wal45, Cra49]) shows the* brightness sensitivity *of the cones, i.e. for color seeing, whereas the* brightness sensitivity *of the rods, responsible for seeing in twilight, is given by the photopic luminosity function, standardized by* CIE, *1931, based on [GT23].*

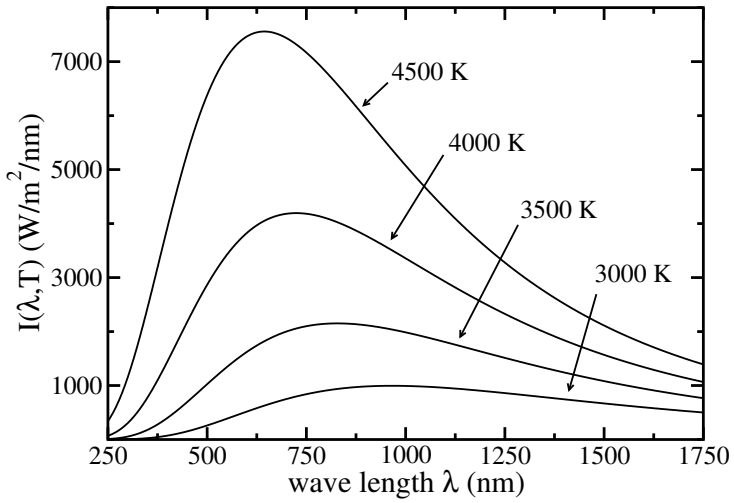

Fig. 1.2: *The temperature radiation, i.e. Planck's law, of a black body versus* λ *for various temperatures. It is remarkable that with increasing temperature, the maximum of the radiation is shifted towards decreasing wavelengths (*Wien's law*).*

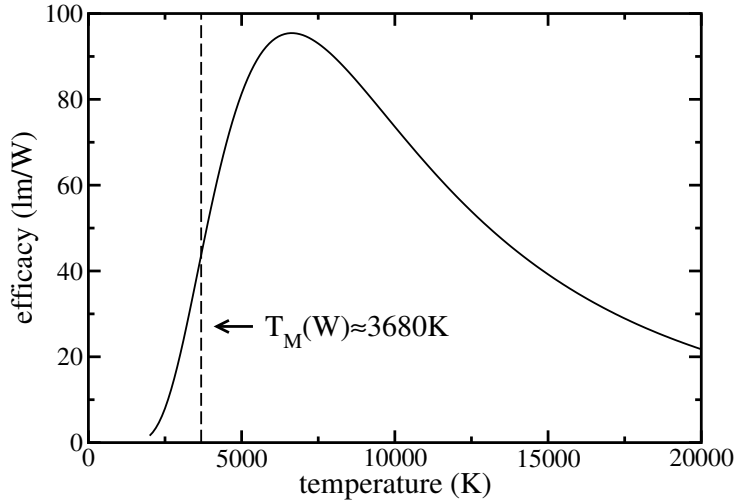

Fig. 1.3: *The* efficacy *of a* black body *versus temperature is shown. The efficacy refers to the amount of visible light (luminous flux in* lm*), as a ratio of the amount of power (in* W*) consumed to produce it. For comparison reasons, the melting point of tungsten is also shown (dashed vertical line).*

for the definition of the dimensionless *coefficient of emissivity*, generally a function of both, wavelength and temperature, and which formally describes the ratio of radiance of matter and black body. The coefficient of emissivity as a function of both, temperature and wavelength, is shown in Fig. 1.4 for tungsten.

At least for humans, *light* is only a very tiny part of the spectrum of electromagnetic waves as seen before. The visible spectrum ranges from wavelengths about $\lambda \approx 400$nm to 800nm as indicated by the luminosity functions, Fig. 1.1. This means, that for temperature radiation to be useful for illumination, one has to consider only a very limited range from the total emitted spectrum. Fig. 1.3 shows the *luminous efficacy*, i.e. the ratio of luminous flux to radiant flux. The luminous flux of a black body is the integral of Planck's curve over all wavelengths weighted by the *photopic luminosity function* $V_M(\lambda)$, whereas the unweighted integral gives the radiant flux:

$$E(\mathrm{lm/W}) = 683.002 \cdot \frac{\int_0^\infty V_M(\lambda) I(\lambda, T)\, d\lambda}{\int_0^\infty I(\lambda, T)\, d\lambda} \quad .$$

The numerical prefactor (683.002) accounts for the definition of lm as to be unity for a radiant energy of 1/683W at a frequency of 540THz, which corresponds to a standard air wavelength of 555.016nm rather than 555nm, which is the peak of the photopic luminosity curve $V_M(\lambda)$, and, therefore,

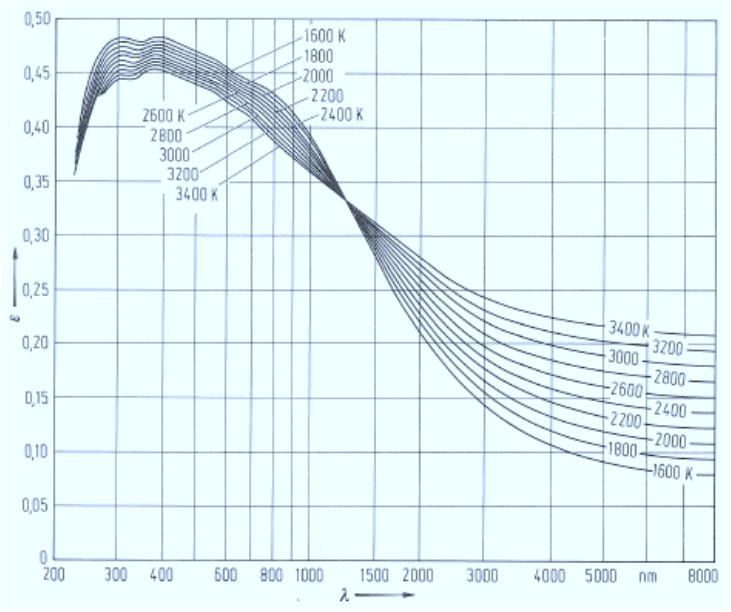

Fig. 1.4: *The* coefficient of emissivity *of tungsten as a function of temperature and wavelength is shown. Remarkable here is the fact, that tungsten radiates maximal in the visible region. [LS99]*

is responsible for the small deviation of the numerical prefactor from 683 as should be expected.

As can be seen in Fig. 1.4, the emissivity of tungsten shows its maximum in the visible region. This makes tungsten a candidate of choice for its use in lighting industry as this means, that the theoretical efficacy of tungsten is even superior to a black body radiator. Of course, mechanical stability at these high temperatures where the radiated "light output" is not negligible has to be guaranteed, also. That's why for incandescent lamps the melting point of any material used must not be exceeded or only be reached in "real" lamps for daily use. Tungsten is *the* metal with the highest melting point and lowest evaporation rate and vapor pressure at a given temperature in the periodic table, see Fig.1.5. These remarkable properties of tungsten are closely connected to the fact, that the binding energy of tungsten (8.9eV) is the highest among all transition metals. So, as far as its applicability for incandescent lamps is concerned, tungsten shows both, high mechanical stability at elevated temperatures and radiates predominantly in the visible spectrum. Furthermore, as a metal, it has a finite specific resistivity and, therefore, via direct current heating it can be easily used as a "converter" of electric energy to energy in form of visible light. Unfortunately, things are not that easy: tungsten is usually very brittle, which makes manufacturing

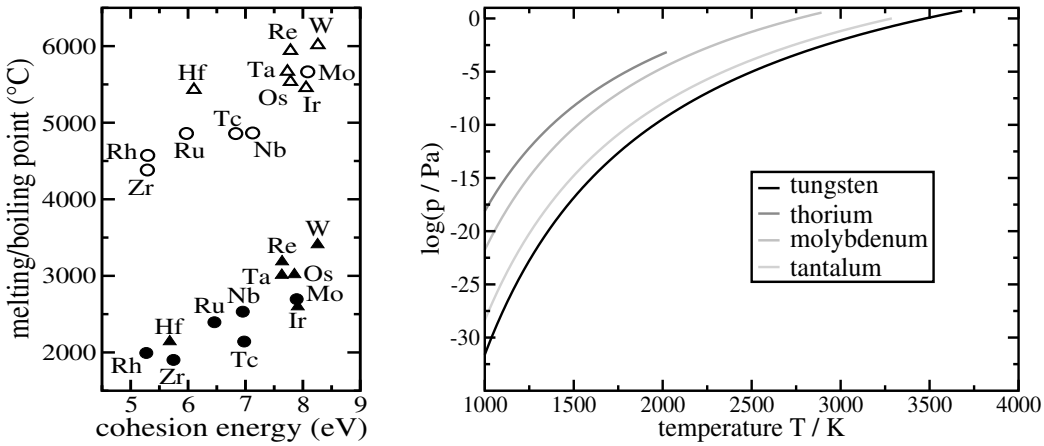

Fig. 1.5: *Melting and boiling points of various transition metals as a function of binding energy (left) and evaporation rates versus temperature are shown (right) [LS99]. Tungsten has the highest melting and boiling point and the lowest evaporation rates of all transition metals at least over a wide range of temperatures.*

of for instance coils not very comfortable. It was a powder processing route, which enabled industry to turn the elemental tungsten from the ore to one of the most important of industrial metals. *Tungsten*, an adaption of the Swedish *tung sten* (meaning "heavy stone"), as an element was first identified in 1781 by a Swedish chemist, K. W. Scheele, for whom the calcium tungstate mineral, scheelite was later named. "Heavy stone" for tungsten seems to be quite reasonable as its density ($19.254(\pm 0.005)\mathrm{g/cm^3}$ (25°C), from X-ray lattice parameter experiments) is exceeded only by metals of the platinum group and *rhenium*. For lighting industry, other properties of tungsten are likewise outstanding and important: especially its corrosion resistance but also its tensile strength (strongly depending on working conditions) is one of the highest across the periodic table. It was in the year 1913, when W. D. Coolidge tried to patent "Tungsten and Method of Making the Same for use as filaments of incandescent electric lamps and for other purposes" which was later-on ruled by court, that this was not valid as an invention. Nevertheless, in his "patent specification" he describes a powder metallurgical route towards "ductile" and compact tungsten filaments, which also nowadays forms the basis of modern tungsten forming parts and wire production. Very crudely, the manufacturing process is a succession of at least three stages starting with tungsten metal powder. The powder metallurgic stage comprises two crucial steps: *compaction* and *sintering*. One route to compact tungsten powder is to press it in rigid dies (uniaxial pressing). Typical compaction pressures are in the range of $200 - 400\mathrm{MPa}$. The

green density, i.e. the density of the compact, is in the range of $55 - 65\%$ of the theoretical density and depends upon the applied pressure, particle size of the powder, its size distribution, particle shape, and size of the compact. The resulting ingot is sintered afterwards. The sintering stage, is carried out in the temperature range of 2000°C up to temperatures near the melting point of tungsten. The necessary temperature is most often generated via direct current sintering in hydrogen atmosphere. The main aim of sintering is densification in order to provide the metal with the necessary physical and mechanical properties and a density which is suitable for subsequent thermo-mechanical processing. The density of the sinter ingot rises during sintering up to 90% of the theoretical density. After this stage, the ingot can be reduced in diameter via rolling and hammering processes. At a diameter small enough to be drawn, the material is further reduced in diameter with drawing the specimen meanwhile with circular shaped cross section through either hard metal or diamond dies, depending on the diameter range to be processed. Depending on its intended use, the probably most important step was not mentioned up to now: the *dope process*, where the overall properties of the tungsten product as the *working horse* in lamp applications are adjusted. The addition of small amounts of finely dispersed oxides, e.g. ThO_2, to metals, for increasing the high temperature strength or reducing the *work function*, i.e. the energy needed to extract an electron from the metal surface to infinity in vacuum, is a common practice in physical metallurgy. In the case of tungsten, this technology can be traced back to its early roots. In 1913, long before the mechanism of dispersion-strengthening were known, impact- and vibration-resistant filaments were produced based on thoriated tungsten. Whereas thoriated tungsten nowadays, since the invention of *non-sag* tungsten, where potassium additions turned out to be superior to thoria (ThO_2) as far as the resulting creep resistance is concerned, see Fig. 1.6, a crucial property for coiling applications, plays only a minor role as filament material in incandescent lamps, is nevertheless still alive as electrode material especially for high-wattage direct current cathodes in discharge lamps. The illumination principle of discharge lamps differs considerably to its incandescent counterpart: discharge lamps generate light with a electric current through gas- or metal vapor, e.g. mercury, in otherwise closed discharge vessels. The discharge in the plasma region is driven by a suitable voltage applied between the electrodes. The electrons emitted from the cathode are accelerated until, because of collisions with neutral or excited atoms in the plasma, "new" electrons are generated. The electrons continously gain energy from the external electric field applied. This heats the plasma considerably, so that, in a "burning" plasma always electrons, ions and neutral atoms are present in dynamic equilibrium. Due to this principle, the plasma has a *posi-*

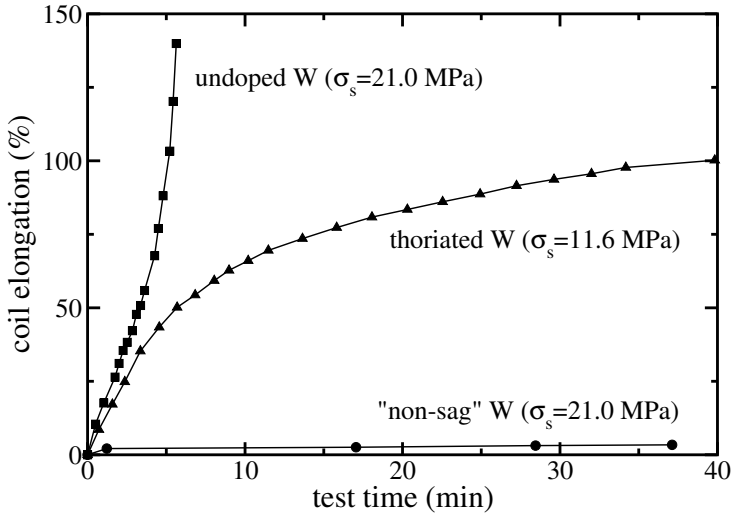

Fig. 1.6: *Creep curves for pure, i.e. undoped, tungsten, thoriated tungsten, and* non-sag*, i.e. potassium doped, tungsten wires at* 2500°C*, showing the outstanding creep resistance of* non-sag *tungsten. The curves show the response, i.e. the elongation versus time due to a constant shear stress (annotated values) applied to the coil.*

tive characteristic which means, in contrast to a "normal" metal, the electric conductivity of the plasma rises whenever the temperature increases. This makes the limitation of the total lamp current via some suitably chosen ballast of vital importance. In general, for thermionic cathodes to be able to operate, it is generally assumed, that the *Richardson-Dushman-Eq.*, which describes the emission current density of thermally activated electrons from metallic surfaces, holds:

$$j(T,\phi) = A \cdot T^2 \cdot e^{-\frac{e\phi_{eff}(E)}{k_B T}}$$

with $A = 1.2 \cdot 10^6 \mathrm{A/m^2/K^2}$, the elementary charge e and the electric field strength E. The *effective* work function $\phi_{eff}(E)$ is given by:

$$\phi_{eff}(E) = \phi - \sqrt{\frac{eE}{4\pi\epsilon_0}}$$

where ϵ_0 denotes the vacuum permittivity and $\phi = 4.5\mathrm{eV}$ the work function of *pure* polycrystalline tungsten surfaces without any electric field applied. The remaining term in ϕ_{eff} describes the *Schottky correction* which accounts for electric fields applied at the surface setting up a finite potential barrier for electrons to be circumvented via quantum mechanical tunneling processes.

At this point, the essential role of thoria comes into play: under working conditions, thoria is reduced and the released thorium atoms act as an electron emitter as soon as thorium atoms diffuse to the surface. It is assumed, that the reduction of thoria by tungsten according to

$$2\,W \;+\; x\,ThO_2 \rightarrow 2\,WO_x \;+\; x\,Th$$

is favored by the simultaneous evaporation of the tungsten oxide, because of its high vapor pressure. Thorium atoms are likewise not stable at the surface and, therefore, evaporate quickly at operating temperatures (approx. $3000K$). This means, that a constant diffusional flux of thorium atoms has to be maintained. Thorium atoms stretch the tungsten lattice considerably due to the size mismatch of tungsten and thorium atoms. Consequently, not negligible thorium fluxes can be maintained only by suitably adjusted microstructures as it is commonly assumed, that thorium atoms can only diffuse along grain boundaries or dislocation cores. To initiate this process, the electrodes have to be activated before use. This is done by rapid heating above 2000°C and subsequent activation annealing at $1500 - 1800$°C. Thorium is a radioactive element and a natural α-emitter. This has led to considerable efforts to replace thoria by other fine oxide dispersions. In order to fully replace thoria, the static as well as dynamic "interactions" of free thorium atoms with various defects, e.g. vacancies, dislocations or grain-boundaries, are important to "design" proper microstructures, i.e. microstructures which favor diffusional fluxes to the surface. Some more light in this widely unknown area shall be shed in this thesis.

As we are interested in atomic features in the wider sense, and we intend to approach the problems within a *molecular dynamics* scheme, we need more detailed knowledge about the atomic interactions between tungsten- and thorium- and tungsten-thorium atoms. As thorium is not soluble in the tungsten lattice very little is known about crystalline structures comprised by both tungsten and thorium. This makes the application of a very flexible method where nothing specific about the interatomic interactions is assumed necessary. The method of choice is based on the in the meanwhile famous *density functional theory* (DFT). Its presence in public consciousness was greatly extended as the Nobel prize in chemistry was given to *Walter Kohn* for his development of the DFT and to *John A. Pople* for his development of computational methods in quantum chemistry based on DFT in 1998. The basic ideas of the DFT will be outlined in chapter 2. The method we applied to hypothetic crystalline intermetallic ($B2$, $L1_2$) structures is the *full potential linearized plane-wave method* (FLAPW), a very flexible method without any assumptions about the crystal potential as described in chapter

3. As this method, while very flexible, is limited to very small systems comprising only a few atoms, we decided to derive the interatomic interaction according to a semi-classical scheme: the *embedded atom potential* (EAM). This scheme accounts for the fact, that, both, thorium as well as tungsten, are of metallic nature and, therefore, their properties are dominated by the metallic bonding. These EAM-derived potentials as well as the basics of the *molecular dynamics* method and some subtleties are given in chapter 5. Various applications of the EAM-potentials to zero-, one- and two-dimensional defects, i.e. vacancies, Th-impurities in tungsten crystals, dislocations and grain boundaries, are the topic of chapter 6. Finally, chapter 7, summarizes the main results of this thesis and gives some ideas for a follow-up project.

Chapter 2

Electronic Structure Calculations

One of the main aspects of this thesis is to derive interatomic interactions ready for use within a *molecular dynamics* scheme. The information necessary to accurately describe the response of one atom due to the presence of another atom is commonly assembled from the physical properties of alloys encountered in nature. For the system tungsten-thorium, however, such data of alloy properties are missing due to the insolubility of thorium in tungsten. One quite promising way to get appropriate data needs the freedom to generate "artificial" alloy data. This can be done applying methods based on *density functional theory* (DFT) to such (almost arbitrary) systems. The basics of the DFT will be presented in this chapter starting from the basic approach of a solid as an assembly of interacting electrons and nuclei [KG02].

2.1 The Many Body Problem

Chemical and physical properties in condensed matter are determined by the interplay of electrons and nuclei. The foundation of the theory of electronic structure of matter is the nonrelativistic Schrödinger equation for the many-electron wave function Ψ given through the Hamiltonian $\hat{\mathbf{H}}_{tot}$ [Koh99]:

$$\hat{\mathbf{H}}_{tot} := \hat{\mathbf{T}}_n + \hat{\mathbf{V}}_{nn} + \hat{\mathbf{H}}_e \tag{2.1}$$

with the kinetic energy of the nuclei (M_μ denotes the mass of nucleus μ)

$$\hat{\mathbf{T}}_n := -\sum_{\mu=1}^{M} \frac{\hbar^2}{2M_\mu} \nabla_\mu^2 \,, \tag{2.2}$$

the electrostatic *nucleus - nucleus* interaction

$$\hat{\mathbf{V}}_{nn} := \frac{1}{8\pi\epsilon_0} \sum_{\mu\neq\nu}^{M} \frac{Z_\mu Z_\nu}{|\mathbf{R}_\mu - \mathbf{R}_\nu|} \tag{2.3}$$

and the hamiltonian describing the influence of the electrons

$$\hat{\mathbf{H}}_e := -\frac{\hbar^2}{2m_e}\sum_{i=1}^{N}\nabla_i^2 - \frac{1}{4\pi\epsilon_0}\sum_{i=1}^{N}\sum_{\mu=1}^{M}\frac{e\,Z_\mu}{|\mathbf{r}_i - \mathbf{R}_\mu|} + \frac{1}{8\pi\epsilon_0}\sum_{i\neq j}^{N}\frac{e^2}{|\mathbf{r}_i - \mathbf{r}_j|} \tag{2.4}$$

where $\{\mathbf{R}_\nu\}$, $\nu = 1\cdots M$ is a set of M nuclear coordinates, and $\{\mathbf{r}_i\}$, $i = 1\cdots N$ is a set of N electronic coordinates. With $\hat{\mathbf{H}}_{tot}$ we describe the system by a number of nuclei and electrons interacting through coulomb (electrostatic) forces. Electrons are fermions, so that the total electronic wave function must be antisymmetric with respect to exchange of two electrons, according to the quantum mechanical theory of indistinguishable particles [Sch99]. Nuclei can be fermions, bosons or distinguishable particles, depending on the particular physical system under consideration. From a theoretical point of view, all necessary ingredients are well known and, in principle, all the properties can be derived by solving the following Schrödinger equation:

$$\hat{\mathbf{H}}_{tot}\Psi_i(\mathbf{r},\mathbf{R}) = E_i\Psi_i(\mathbf{r},\mathbf{R}) \tag{2.5}$$

or, to say it with P. M. Dirac [Dir29]:

> "The underlying physical laws necessary for the mathematical theory of a large part of physics and the whole of chemistry are thus completely known, and the difficulty is only that the exact application of these laws leads to equations much too complicated to be soluble."

So, in Dirac's opinion, chemistry had come to an end shortly after Schrödinger's equation for the electronic wave function Ψ had been put forward and spectacularly validated for small systems [Sch26]. Furthermore, he argued, that in practice, however, this problem is almost infeasible in a full quantum mechanical framework. Analytical solutions are limited to very small systems, even numerical solutions are available for only few particles. There are several reasons for this difficulty. First, this is in general a multicomponent many-body system, where each component (each nuclear species and the electrons) obeys a particular statistics. Moreover, the complete wave function cannot be easily factorized because of coulombic interaction. This means, that we have in general to deal with $(3(M+N))$ coupled degrees of freedom. Nevertheless, to perform such calculations, one has to fall back on a sensible approximation.

2.1.1 Adiabatic Approximation

The ratio of the masses of electrons and protons (the most unfavorable case) is of the order 1 in 2000. If electrons and nuclei could be treated as classical

particles, the equipartition theorem would be valid in equilibrium [Rei65]. This theorem states, that the energy for each degree of freedom is equal. If we denote for the moment the velocity of electron i with $\mathbf{v}_i$ and that of the nucleus μ with $\mathbf{v}_\mu$ than the ratio of the kinetic energies consequently must be one, or the mass ratio as defined above, must be inversely proportional to the ratio of the squared velocities. As a result, the ratio of the velocities of the nuclei and the electrons must be of the order $\sqrt{2000}$. One can therefore expect that the electrons are at each instant of time at their corresponding groundstate related to the instantaneous positions of the nuclei. In other words, as the nuclei follow their dynamics, the electrons immediately adjust their wave function according to the nuclear wave function.

All this can be cast in a formal mathematical framework by proposing a solution to Eq. (2.5) of the following form:

$$\Psi_i(\mathbf{r},\mathbf{R}) = \sum_q \Theta_{iq}(\mathbf{R})\Phi_q(\mathbf{r},\mathbf{R}) \tag{2.6}$$

where $\Phi_q(\mathbf{r},\mathbf{R})$ are the eigenstates of the electronic hamiltonian:

$$\hat{\mathbf{H}}_e\Phi_q(\mathbf{r},\mathbf{R}) = \epsilon_q(\mathbf{R})\Phi_q(\mathbf{r},\mathbf{R}) \tag{2.7}$$

with

$$\hat{\mathbf{H}}_e := \hat{\mathbf{T}}_e + \hat{\mathbf{V}}_{ee} + \hat{\mathbf{V}}_{ne}\,, \tag{2.8}$$

see also Eq. 2.4. Inserting the above ansatz into the full Schrödinger equation we obtain:

$$\begin{aligned}\left[-\sum_{\mu=1}^{M}\frac{\hbar^2}{2M_\mu}\nabla_\mu^2 + \hat{\mathbf{V}}_{nn} + \epsilon_p(\mathbf{R})\right]\Theta_{ip}(\mathbf{R}) &= E_i\Theta_{ip}(\mathbf{R}) \\ &+ \sum_q\sum_{\mu=1}^{M}\frac{\hbar^2}{2M_\mu}\left[\left\langle\Phi_p\left|\nabla_\mu^2\right|\Phi_q\right\rangle + 2\left\langle\Phi_p\left|\nabla_\mu\right|\Phi_q\right\rangle\cdot\nabla_\mu\right]\Theta_{iq}(\mathbf{R})\end{aligned} \tag{2.9}$$

which constitute an infinite set of coupled partial differential equations. The reduction of the full wave function to an expression of the type:

$$\Psi(\mathbf{r},\mathbf{R}) = \Theta_p(\mathbf{R})\Phi_p(\mathbf{r},\mathbf{R}) \tag{2.10}$$

is known as the *adiabatic* or *Born-Oppenheimer approximation* [BO27]. But when is it possible to neglect non-adiabatic couplings? From Eq. (2.9) follows the condition (at least for *non degenerate* electronic groundstates)

$$\left|\sum_{\mu=1}^{M}\frac{\hbar^2}{M_\mu}\left\langle\Theta_{ip}\left|\nabla_\mu\right|\Theta_{iq}\right\rangle\cdot\left\langle\Phi_p\left|\nabla_\mu\right|\Phi_q\right\rangle\right| \ll |\epsilon_p(\mathbf{R}) - \epsilon_q(\mathbf{R})| \tag{2.11}$$

or, equivalently [Mes61]:

$$\frac{m_e}{M_\mu}\left|\frac{\hbar\Omega_\nu}{\epsilon_p(\mathbf{R})-\epsilon_q(\mathbf{R})}\right| \ll 1 \tag{2.12}$$

where Ω_ν is the maximum frequency of rotation of the electronic wave function due to the nuclear motion and the energies in the denominator correspond to the electronic adiabatic eigenstates. Thus the smaller the ratio m_e/M_μ the better the adiabatic approximation.

2.1.2 Classical nuclei approximation

Neglecting the non-adiabatic couplings as discussed above results in a time dependent adiabatic Schrödinger equation for the nuclear wave function:

$$i\hbar\frac{\partial\Theta_p(\mathbf{R},t)}{\partial t} = \left(-\sum_{\mu=1}^{M}\frac{\hbar^2}{2M_\mu}\nabla_\mu^2 + \hat{\mathbf{V}}_{nn} + \epsilon_p(\mathbf{R})\right)\Theta_p(\mathbf{R},t)\,. \tag{2.13}$$

With *Ehrenfest's theorem* [Sch99] the following evolution equations for the mean values of position and momentum arise:

$$\begin{aligned} i\hbar\frac{d\langle\mathbf{R}_\mu\rangle}{dt} &= \langle[H,\mathbf{R}_\mu]\rangle = i\hbar\frac{\langle\mathbf{P}_\mu\rangle}{M_\mu} \implies M_\mu\frac{d\langle\mathbf{R}_\mu\rangle}{dt} = \langle\mathbf{P}_\mu\rangle \\ i\hbar\frac{d\langle\mathbf{P}\mu\rangle}{dt} &= \langle[H,\mathbf{P}_\mu]\rangle = -i\hbar\left\langle\nabla_\mu(\epsilon_p(\mathbf{R})+\hat{\mathbf{V}}_{nn})\right\rangle\,. \end{aligned} \tag{2.14}$$

When combined, we arrive at Newton's equation of motion

$$M_\mu\frac{d^2\langle\mathbf{R}_\mu\rangle}{dt^2} = -\left\langle\nabla_\mu(\epsilon_p(\mathbf{R})+\hat{\mathbf{V}}_{nn})\right\rangle\,. \tag{2.15}$$

In principle this equation is only valid for the mean value of the position operator. If the nuclear wave functions are strongly localized and there is no quantum phase coherence present (a discussion of the quantum to classical transition, i.e. the decoherence process can be found in [Zur91] and the references therein), the nuclear wave function is well approximated as an incoherent superposition of delta functions whose centers are located at the classical positions $\mathbf{R}_\mu^{cl}(t)$:

$$\Theta_p(\mathbf{R},t) = \Pi_\mu\delta(\mathbf{R}-\mathbf{R}_\mu^{cl}(t)) \tag{2.16}$$

In that case, $\langle\mathbf{R}_\mu\rangle = \mathbf{R}_\mu^{cl}(t)$ and $\langle\nabla\epsilon_p(\mathbf{R})\rangle = \nabla\epsilon_p(\mathbf{R}_\mu^{cl})$. Due to the fact, that the latter is strictly valid only for harmonic potentials and for delta functions, the leading error is expected to be proportional to the anharmonicity

of the potential and to the spatial extension of the wave packet. This approximation, relating the mean value with the cartesian coordinates of the corresponding classical particle, is commonly referred to as the *classical nuclei approximation*. Altogether one gets from Eq. (2.15):

$$M_\mu \frac{d^2\mathbf{R}_\mu^{cl}(t)}{dt^2} = -\nabla_\mu(\epsilon_p(\mathbf{R}_\mu^{cl}(t)) + \hat{\mathbf{V}}_{nn}) \tag{2.17}$$

where $\epsilon_p(\mathbf{R}_\mu^{cl}(t))$ is known as the p^{th} adiabatic *potential energy surface* (PES). With the *Hellmann-Feynman theorem* [Fey39]

$$\nabla_\mu \epsilon_p(\mathbf{R}) = \left\langle \Phi_p(\mathbf{r},\mathbf{R}) \left| \nabla_\mu \hat{\mathbf{H}}_e(\mathbf{R}) \right| \Phi_p(\mathbf{r},\mathbf{R}) \right\rangle \tag{2.18}$$

the final expression reads:

$$M_\mu \frac{d^2\mathbf{R}_\mu^{cl}(t)}{dt^2} = -\left\langle \Phi_p(\mathbf{r},\mathbf{R}) \left| \nabla_\mu (\hat{\mathbf{H}}_e(\mathbf{R}) + \hat{\mathbf{V}}_{nn}) \right| \Phi_p(\mathbf{r},\mathbf{R}) \right\rangle \tag{2.19}$$

The numerical integration of the Newtonian equation of motion receives the name *first-principles Molecular-Dynamics*, and $\epsilon_p(\mathbf{R})$ is the first-principles potential. In order to obtain $\epsilon_p(\mathbf{R})$ (and its gradient for the forces on the nuclei) it is necessary to solve the time-independent electronic Schrödinger equation (2.7). This is a field of its own, and has commonly termed *electronic structure calculation*. In a sense, electronic structure calculations based on the direct solution of the time-independent electronic Schrödinger equation is not feasible due to the enormous degrees of freedom (DOF) in most systems of interest. It's the *density functional theory* (DFT) which allows the reduction of the DOF to "its extreme", will be explained immediately.

2.2 Density Functional Theory

Density Functional Theory (DFT) is one of the most widely used methods for *ab initio* electronic structure calculations. Compared to the traditional way to introduce DFT, which is closely related to the historical chronology and starts with a proof of the interim famous *Hohenberg-Kohn theorem* [HK64] in succession the derivation of the *Kohn-Sham equations* [KS65], we present a primer which gives a quick insight into the origin of DFT. This is based on the mathematical works of E. H. Lieb [Lie83] and R. Fukuda [FKSY94]. Additional information can be found also in [Esc96]. The main benefit of DFT is the apodictic statement that the groundstate density can serve as a unique variable of the physical system under consideration determining all groundstate properties. Whereas the *Kohn-Sham equations* provide an

unambiguous mapping of the interacting many electron to a non-interacting particle system. Moreover it is a *theory*, there are no approximations (at least at that stage) at all, in clear contrast to e.g. the in quantum chemistry widely used *Hartree-Fock method*.

It should be noted that in spite of the fact that we formulate the non spin polarized and non relativistic theory, the whole apparatus of DFT and basically all arguments of the following can be easily extended to the spin-polarized relativistic case [MV79, KH77]. Moreover this theory is applied to the zero temperature case. For finite temperatures the original arguments are expanded by N. D. Mermin [Mer65].

2.2.1 Hohenberg-Kohn Theorem

Starting point for the following is the many body hamiltonian for the electronic subsystem, i.e. Eq. (2.4), in a more formal notation (with explicitly mentioning the dependence on the external potential $v(\mathbf{r})$):

$$\hat{\mathbf{H}}_{Coul}[v(\mathbf{r})] := \hat{\mathbf{T}} + \hat{\mathbf{V}} + \Lambda\hat{\mathbf{U}} \tag{2.20}$$

with

$$\hat{\mathbf{T}} := -\frac{1}{2}\sum_{i=1}^{N}\nabla_i^2 \tag{2.21}$$

as usual,

$$\hat{\mathbf{V}} := \int v(\mathbf{r})\hat{n}(\mathbf{r})d\mathbf{r} \qquad \hat{n}(\mathbf{r}) := \sum_{i=1}^{N}\delta(\mathbf{r}-\hat{\mathbf{r}}_i) \tag{2.22}$$

where $\hat{n}(\mathbf{r})$ denotes the local density operator and $v(\mathbf{r})$ the potential energy due to the atomic nuclei, i.e. $v(\mathbf{r}) = \sum_{\mu}^{M}\frac{Z_\mu}{|\mathbf{r}-\mathbf{R}_\mu|}$, and

$$\hat{\mathbf{U}} := \frac{1}{2}\int \frac{1}{|\mathbf{r}-\mathbf{r}'|}\hat{n}(\mathbf{r})\left(\hat{n}(\mathbf{r}) - \delta(\mathbf{r}-\mathbf{r}')\right)d\mathbf{r}d\mathbf{r}' \,, \tag{2.23}$$

where the second term in the bracket excludes the interaction of each electron with itself, $\Lambda = 1$ is a parameter introduced for later convenience. The trick starts with the observation that the groundstate energy $E[v(\mathbf{r})] := \left\langle \Phi \left| \hat{\mathbf{H}}[v(\mathbf{r})] \right| \Phi \right\rangle$ ($\Phi(\mathbf{r})$ being the (electronic) groundstate) is a concave functional of $v(\mathbf{r})$. Therefore

$$E[\alpha v_1(\mathbf{r}) + (1-\alpha)v_2(\mathbf{r})] \geq \alpha E[v_1(\mathbf{r})] + (1-\alpha)E[v_2(\mathbf{r})] \tag{2.24}$$

for $\alpha \in [0,1]$ holds, implying that $-E[v(\mathbf{r})]$ is necessarily a convex functional. For such functionals, a Legendre transform, a likewise convex functional, can be defined via [Esc96]:

$$F[n(\mathbf{r})] := \sup_{v \in X^*} \left\{ E[v(\mathbf{r})] - \int n(\mathbf{r}) v(\mathbf{r}) d\mathbf{r} \right\} \tag{2.25}$$

with some suitable chosen function spaces X and X^* denoting the corresponding dual space [Lie83]. The back transformation is given by

$$E[v(\mathbf{r})] := \inf_{n \in X} \left\{ F[n(\mathbf{r})] + \int v(\mathbf{r}) n(\mathbf{r}) d\mathbf{r} \right\} \tag{2.26}$$

The problem that remains, is determining a suitable set X for the admissible (groundstate) densities for the search as indicated above (Lieb's theory is also known as the *constrained search method*). For not too pathological densities ("v representability of n", i.e. n must be derivable from an external potential v by solving the many body Schrödinger equation), the functional $F[n(\mathbf{r})]$ can be identified with the well known *Hohenberg-Kohn free energy functional* $F_{HK}[n(\mathbf{r})]$. If the infimum in Eq. (2.26) exists and is an element of $X \equiv \mathcal{A}_N$ then the infimum is identical to a minimum:

$$E[v(\mathbf{r})] := \min_{n \in \mathcal{A}_N} \left\{ F_{HK}[n(\mathbf{r})] + \int v(\mathbf{r}) n(\mathbf{r}) d\mathbf{r} \right\} \tag{2.27}$$

An interesting consequence of Eq. (2.27) arises, if the functional derivative of $F_{HK}[n(\mathbf{r})]$ with respect of $n(\mathbf{r})$ exists:

$$v = -\frac{\delta F_{HK}[n]}{\delta n} \tag{2.28}$$

Under proper conditions this ensures a one to one relationship between v and n due to the generalized convexity and the *universality* of $F_{HK}[n]$, i.e. it is independent of the external potential v. In the framework of Legendre transforms presented above, one would say that v and n are conjugate variables.

For later purposes an appropriate decomposition of $F_{HK}[n]$ is given by:

$$F_{HK}[n] := T[n] + E_H[n] + E_{XC}[n] \tag{2.29}$$

where $T[n]$ denotes the kinetic energy of a *non-interacting* particle system with density n and $E_H[n]$

$$E_H[n] := \frac{1}{2} \iint \frac{n(\mathbf{r}) \cdot n(\mathbf{r}')}{|\mathbf{r} - \mathbf{r}'|} d^3r \, d^3r' \tag{2.30}$$

the classical *Hartree energy*, the electrostatic energy of a classical charge density n. $E_{XC}[n]$ comprises all remaining contributions to $F_{HK}[n]$, i.e. exchange and correlation terms, not contained in $T[n]$ and $E_H[n]$.

In summary, the two theorems as formulated by Hohenberg and Kohn [HK64] read as:

Theorem 1

$$v(\mathbf{r}) = v[n](\mathbf{r})$$

is a unique functional of the groundstate density $n(\mathbf{r})$

and

Theorem 2

$$E[v] = \min_{n \in \mathcal{A}_N} \left\{ F_{HK}[n] + \int n v \, d\mathbf{r} \right\}$$

i.e. the electronic groundstate energy is given by the minimum of a convex functional. This is the starting point for an effective and efficient procedure to calculate groundstate properties as will be shown in the following subsection, where we derive the meanwhile widely known *Kohn-Sham equations*.

2.2.2 The Kohn-Sham Equations

From the preceding subsection subjecting the Hohenberg-Kohn theorems we know that we have to calculate the minimum of

$$E_v[n] = T[n] + E_H[n] + E_{XC}[n] + \int n v \, d\mathbf{r} \tag{2.31}$$

under the constraint that the total number of electrons is N:

$$\int n(\mathbf{r}) \, d\mathbf{r} = N \tag{2.32}$$

in order to get the correct groundstate density:

$$\frac{\delta \left(E_v[n(\mathbf{r})] + \mu(N - \int n(\mathbf{r}) \, d\mathbf{r}) \right)}{\delta n(\mathbf{r})} = 0 \tag{2.33}$$

where μ denotes the Lagrange multiplier associated with the constraint. With an ansatz of non interacting orthonormal particle orbitals $\phi_i(\mathbf{r})$ for the electron density:

$$n(\mathbf{r}) := \sum_i \phi_i^*(\mathbf{r}) \phi_i(\mathbf{r}), \tag{2.34}$$

Eq. (2.33) is even fulfilled if the constraint is replaced by the orthonormality of the ϕ_i and the variation of (2.31) with respect of ϕ_i is zero:

$$\frac{\delta\left(E_v[n(\mathbf{r})] + \sum_{j=1}^{N} \epsilon_j (1 - \int \phi_j(\mathbf{r})^* \phi_j(\mathbf{r})\, d\mathbf{r})\right)}{\delta \phi_i^*(\mathbf{r})} = 0 \tag{2.35}$$

With the kinetic energy $T[n(\mathbf{r})]$ of a non-interacting particle system

$$T[n(\mathbf{r})] := -\frac{1}{2} \sum_{i=1}^{N} \int \phi_i^*(\mathbf{r}) \nabla^2 \phi_i(\mathbf{r})\, d\mathbf{r} \tag{2.36}$$

we arrive at the *Kohn-Sham equations*:

$$\left(-\frac{1}{2}\nabla^2 + v_{eff}(\mathbf{r})\right) \phi_i(\mathbf{r}) = \epsilon_i \phi_i(\mathbf{r})\,, \qquad v_{eff}(\mathbf{r}) := v(\mathbf{r}) + v_H(\mathbf{r}) + v_{XC}(\mathbf{r})\,, \tag{2.37}$$

with the *Hartree potential*

$$v_H(\mathbf{r}) := \int \frac{n(\mathbf{r}')}{|\mathbf{r} - \mathbf{r}'|}\, d^3 r' \tag{2.38}$$

and the *Exchange and Correlation potential*

$$v_{XC}(\mathbf{r}) := \frac{\delta E_{XC}[n]}{\delta n(\mathbf{r})}\,. \tag{2.39}$$

Despite the close resemblance to a conventional Schrödinger equation, there is an important difference: the effective potential $v_{eff}(\mathbf{r})$ depends itself on the groundstate density, which is closely related to the orbitals via Eq. (2.34). This gives rise to highly non-linear behavior, which usually is computationally treated within a *self consistent field cycle*.

The Self-Consistent-Field (SCF) Cycle

The most important and cumbersome element of electronic structure calculations of condensed matter as well as molecules is self-consistency, that is, deriving a self-consistent effective potential within the framework of density-functional theory. A computational scheme for the self-consistent field cycle is depicted in Fig. 2.1. The generally arbitrary starting density for the procedure, necessary for calculating the effective one-particle potential, is usually derived from the superposition of the electron densities of free atoms. The Kohn-Sham equations are solved and the highest occupied orbital and its Kohn-Sham eigenvalue, representing the Fermi energy, is determined. With the Kohn-Sham orbitals, the new density is generated and the cycle starts from the beginning. The story is aborted, when the changes of two subsequent charge densities or total energies are negligible.

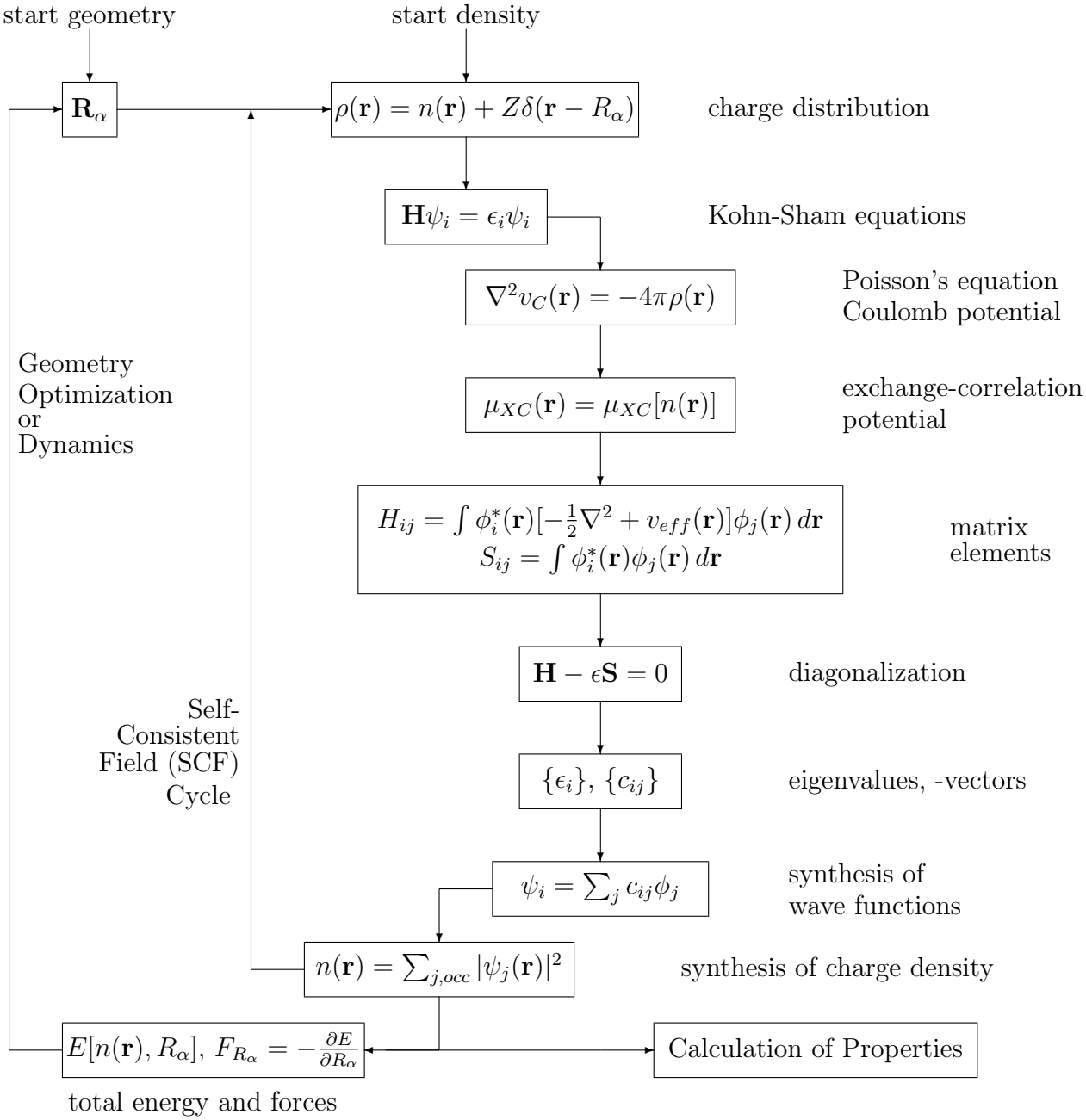

Fig. 2.1: *Scheme of a typical self consistent field cycle. Self-consistency is reached, when the error in charge density or total energy is below a certain predefined value.*

2.2.3 Exchange and Correlation Potential: Nature's Glue

In the Kohn-Sham density functional theory of groundstate electronic structure as presented above, all many body effects are hidden in the *Exchange and Correlation potential*, Eq. (2.39). Unfortunately this potential is not explicitly known and consequently must be of approximative nature. Considerable efforts are undertaken to construct such approximative potentials up to now. Although the corresponding energy E_{XC} provides typically not a large contribution to the total energy E, it is the principal ingredient of the glue that binds atoms together to molecules and solids. In the following section we describe briefly the *Local (Spin) Density Approximation* (L(S)DA), which has been already proposed in the seminal paper by Kohn and Sham [KS65], and serves as the basis for many successive approximations. One of the most popular representative of the *Generalized Gradient Approximations* (GGA) and that used in this work [PBE96] will be presented afterwards.

Local Spin Density Approximation (LSDA)

The spin polarized *homogeneous electron liquid* serves as a reference model system for which all the properties can be calculated (at least in principle) with arbitrary accuracy. It is defined as an interacting electronic system in a homogeneous, i.e. constant in space, positive charge density (contrary to the homogenous electron *gas* where there is no electron-electron interaction present). For the spin polarized system, we define the relative spin polarization ζ for the collinear spin situation, which relates the electron density n with its spin components $n_\uparrow$ and $n_\downarrow$, through:

$$\zeta := \frac{n_\uparrow - n_\downarrow}{n} \text{ , with } \qquad n := n_\uparrow + n_\downarrow \,. \tag{2.40}$$

The exchange- and correlation-energy E_{XC} of the inhomogeneous spin-polarized electron liquid reads as [Esc96]:

$$E_{XC}^{LSDA}[n_\uparrow, n_\downarrow] := \int \epsilon_{XC}\left(n(\mathbf{r}), \zeta(\mathbf{r})\right) n(\mathbf{r})\, d^3r \tag{2.41}$$

where

$$\epsilon_{XC}\left(n(\mathbf{r}), \zeta(\mathbf{r})\right) = \epsilon_X\left(n(\mathbf{r}), \zeta(\mathbf{r})\right) + \epsilon_C\left(n(\mathbf{r}), \zeta(\mathbf{r})\right) \tag{2.42}$$

denotes the exchange- and correlation-energy *per electron* of the homogeneous spin-polarized electron liquid.

In lowest order many body perturbation theory the exchange energy per electron ϵ_X of the homogenous electron liquid is obtained as [GMB57]:

$$\epsilon_X(n, \zeta) = -\frac{3}{4\pi}\left(3\pi^2 n\right)^{1/3} \frac{(1+\zeta)^{4/3} + (1-\zeta)^{4/3}}{2 r_s(n)} \tag{2.43}$$

where the *Wigner-Seitz-radius* $r_s(n)$ is defined as:

$$r_s(n) := \left(\frac{3}{4\pi n}\right)^{1/3} \tag{2.44}$$

On the basis of the study of Vosko, Wilk and Nussair [VWN80] the spin polarized correlation energy fulfills:

$$\epsilon_C(r_s,\zeta) = \epsilon_C(r_s,0) + \alpha_C(r_s)\frac{f(\zeta)}{f''(0)}(1-\zeta^4) + (\epsilon_C(r_s,1) - \epsilon_C(r_s,0))f(\zeta)\zeta^4 \tag{2.45}$$

with

$$f(\zeta) := \frac{(1+\zeta)^{4/3} + (1-\zeta)^{4/3} - 2}{2^{4/3} - 2} \quad \text{for} \quad \zeta \in [-1,1] \tag{2.46}$$

For $\epsilon_C(r_s,0)$, $\epsilon_C(r_s,1)$ and $-\alpha_C(r_s)$, Perdew and Wang used a uniform and simple parameterization [PW92]:

$$g(r_s) := -2A(1+\alpha_1 r_s)\ln\left(1 + \frac{1}{2A(\beta_1 r_s^{1/2} + \beta_2 r_s + \beta_3 r_s^{3/2} + \beta_4 r_s^{P+1})}\right) \tag{2.47}$$

with

$$g(r_s) := \begin{cases} \epsilon_C(r_s,0) \\ \epsilon_C(r_s,1) \\ -\alpha_C(r_s) \end{cases} \tag{2.48}$$

For the coefficients they specified:

	$\epsilon_C(r_s,0)$	$\epsilon_C(r_s,1)$	$-\alpha_C(r_s)$
P	1.00	1.00	1.00
A	0.031091	0.015545	0.016887
α_1	0.21370	0.20548	0.11125
β_1	7.5957	14.1189	10.357
β_2	3.5876	6.1977	3.6231
β_3	1.6382	3.3662	0.88026
β_4	0.49294	0.62517	0.49671

The corresponding spin dependent exchange and correlation *potential*, Eq. (2.39), is given by:

$$v_{XC\uparrow\downarrow}^{LSDA} := \epsilon_{XC}\left(n(\mathbf{r}),\zeta(\mathbf{r})\right) + n(\mathbf{r})\frac{\partial \epsilon_{XC}}{\partial n}\left(n(\mathbf{r}),\zeta(\mathbf{r})\right) \pm (1 \mp \zeta(\mathbf{r}))\frac{\partial \epsilon_{XC}}{\partial \zeta}\left(n(\mathbf{r}),\zeta(\mathbf{r})\right) \tag{2.49}$$

Generalized Gradient Approximation (GGA)

The *Generalized Gradient Approximation* seems to be a subtle improvement over LSDA for some properties, e.g. binding energies and bond lengths, of many physical systems. There are a lot of GGAs to choose from [LM81, PW86, Per86, Bec88], the one used in this work is that of Perdew, Burke and Ernzerhof [PBE96].

They derived the GGA for correlation in the form

$$E_C^{GGA}[n_\uparrow, n_\downarrow] := \int n(\mathbf{r})(\epsilon_C(r_s, \zeta) + H(r_s, \zeta, t))\, d^3r\,. \tag{2.50}$$

with $t := |\nabla n| / (2\phi(\zeta) k_s n)$ a dimensionless density gradient, the spin-scaling factor $\phi(\zeta) := [(1+\zeta)^{2/3} + (1-\zeta)^{2/3}]/2$, the Thomas-Fermi screening wave number $k_s := \sqrt{4k_F/\pi a_0}$, the Fermi wave number $k_F := \sqrt[3]{3\pi^2 n}$, the Bohr length $a_0 := \hbar^2/me^2$ and

$$H(r_s, \zeta, t)) := \frac{e^2}{a_0}\gamma\phi^3 \ln\left\{1 + \frac{\beta}{\gamma}t^2\left[\frac{1+At^2}{1+At^2+A^2t^4}\right]\right\} \tag{2.51}$$

where

$$A = \frac{\beta}{\gamma}\left(e^{-\epsilon_C^{LSDA} a_0/\gamma\phi^3 e^2} - 1\right)^{-1} \tag{2.52}$$

with $\beta = 0.031091$ and $\gamma = (1 - \ln 2)/\pi^2$.

For the exchange energy of the non spin-polarized case ($\zeta = 0$) their ansatz reads as:

$$E_X^{GGA}[n, \zeta = 0] := \int n(\mathbf{r})\epsilon_X^{LSDA}(n(\mathbf{r}))F_X(s)\, d^3r \tag{2.53}$$

with

$$F_X(s) := 1 + \kappa - \frac{\kappa}{1 + \mu s^2/\kappa} \quad \text{and} \quad \kappa = 0.804\,,\ \mu = 0.21951\,. \tag{2.54}$$

The likewise dimensionless density gradient s is defined as $s := |\nabla n| / (2k_F n)$.

The connection with the spin polarized case is given by the spin-scaling relationship [OP79]:

$$E_X^{GGA}[n_\uparrow, n_\downarrow] = \frac{1}{2}(E_X^{GGA}[2n_\uparrow, \zeta = 0] - E_X^{GGA}[2n_\downarrow, \zeta = 0]) \tag{2.55}$$

Of course the exchange- and correlation potential could be calculated using the defining equation, Eq. (2.39).

2.2.4 Periodic systems and the Supercell method

The quantum mechanical treatment of perfect crystals within Born-Oppenheimer approximation means solving the *Kohn-Sham equations* (2.37) in a *self-consistent cycle* due to its nonlinearity. The effective potential $v_{eff}(\mathbf{r})$ and therewith the Kohn-Sham hamiltonian shows necessarily the same periodicity as the underlying crystal lattice: a translation of the potential or hamiltonian by a lattice vector $\mathbf{R}$ leaves them untouched. In quantum mechanically terms this means, that the corresponding translation operator

$$\hat{\mathbf{T}}(\mathbf{R}) := exp(\frac{i}{\hbar}\mathbf{R}\cdot\hat{\mathbf{P}}) \quad \text{and} \quad \hat{\mathbf{P}} := \frac{\hbar}{i}\nabla \tag{2.56}$$

commutes with the Kohn-Sham hamiltonian. As a consequence, a solution of the Kohn-Sham equations of the form

$$\psi_n^{\mathbf{k}}(\mathbf{r}) = e^{i\mathbf{k}\cdot\mathbf{r}} w_{n\mathbf{k}}(\mathbf{r})\,, \quad \text{with} \quad w_{n\mathbf{k}}(\mathbf{r}+\mathbf{R}) = w_{n\mathbf{k}}(\mathbf{r})\,, \tag{2.57}$$

valid for each lattice vector $\mathbf{R}$ can be found, a fact, which is commonly referred to as *Bloch's theorem*. As is easily seen from Eq. (2.57) the Bloch wave number $\mathbf{k}$ can always be chosen within the first Brioullin zone. Generally, for a given wave number $\mathbf{k}$ there is a discrete set of Kohn-Sham single particle eigenenergies and can therefore be labeled $\epsilon_n^{\mathbf{k}}$. These give rise to the term *band structure*. But life would be rather boring, if only perfect crystals would exist and, indeed, the daily experience shows that total symmetry is more the exception than the rule. The question that arises is, how should we treat such defective systems? There are several workarounds for this problem. The easy way out from loss of periodicity is to restore it in an artificial way, i.e. to construct a supercell containing the defect with which one can fill up the whole space: the resulting structure is periodic again, with all beautiful consequences, i.e. the validity of Bloch's theorem. With this simple trick, perfect and defective crystals can be treated on the same footing.

Unfortunately, the (possibly enforced) periodicity of the structure imposes a penalty: whereas for finite Coulomb-systems the total energy is always well defined, it does not exist at all for periodic structures. The same holds for the energy density (groundstate energy per volume of the supercell) unless the supercell is perfectly neutral with zero dipolar moment [Esc96]. This involves serious problems in constructing supercells for e.g. surface problems, where the symmetry of the structure is broken due to the presence of the surface. In this case one has to enlarge the supercell and include a reflected image of the surface. This procedure removes a net dipolar moment for the cell and is therefore a suitable candidate for electronic structure calculations using DFT within the supercell method. Of course, in adopting this procedure one has

to ensure, that the two surfaces of the supercell do not interact, which makes the introduction of a more or less huge vacuum layer in-between necessary. The consequence is a great enlargement of a widely used planewave basis set, with all the negative influences on computational speed and resources.

Chapter 3

FLAPW method

There are basically only two methods to manage the calculation of the Kohn-Sham one-particle wave function in crystals, their essential difference lying in the relative emphasis placed on the importance of the two requirements the wave function must meet, i.e.

1. satisfying Kohn-Sham equations
2. satisfying Bloch's theorem

Modern trends are towards the second type of method, in which one begins with a formal expansion of the wave function such that Bloch's theorem is exactly satisfied from the outset. The most obvious expansion of this nature is the Fourier series, the coefficients in which are the momentum eigenfunctions. This plane-wave expansion has proven in practice to be very slowly convergent, a major reason for this being the necessary orthogonality of the wave functions of the outer electrons to the core functions, which enforces a very high resolution and, therefore, many plane waves with high wave numbers. Apart from the pseudopotential ansatz, it was Slaters proposal [Sla37] which changed this rather disappointing situation. His meanwhile widely used APW method uses a to the physical situation of electrons in crystals perfectly adapted basis set. Near the nuclei, the electrons feel an almost spherical atomic like potential whereas the impact on the electrons within the interstitial is rather weak and weak varying also: the famous *muffin tin* shape approximation for the crystal potential was born. The quality of this approximation depends mainly on the detailed structure of the underlying lattice. It turns out to be very good for close packed (fcc- and hcp-structures, with ideal c/a-quotient) materials. It is less suitable but still reasonable for bcc- and related structures (e.g. CsCl structure) [EK76], and becomes increasingly less reliable as the site symmetry and coordination decrease.

Before going into details of the *Full potential Linear Augmented Plane Wave* (FLAPW) method, we describe its predecessor, the *Augmented Plane Wave* (APW) method, to show the remaining problems and how to resolve them.

3.1 The APW method and its problems

In the following section we will limit ourselves to the nonrelativistic approximation and to the case of one atom per unit cell. Neither of these restrictions is necessary but is done to simplify the discussion. The starting point of the APW method is as implied from the considerations above a separation of space in non overlapping spheres (MTS), each containing a nucleus and in which the potential is assumed to be spherical symmetric, and the space in between, the interstitial region (I), where the potential is assumed to be approximately zero. Therefore, as mentioned, the more or less crude approximation of the crystal potential having muffin tin form reads as:

$$V(\mathbf{r}) := \sum_{\mathbf{R}} v(|\mathbf{r} - \mathbf{R}|), \tag{3.1}$$

where the v's are spherical within the sphere radii R_{MT} and zero outside, i.e.:

$$v(r) \equiv 0 \quad \text{for } r \geq R_{MT} \,. \tag{3.2}$$

A schematic view of this potential is given in Fig. 3.1. With $\mathbf{R}$ we denote the location of the nuclei comprising the solid. In using the muffin tin potential, it

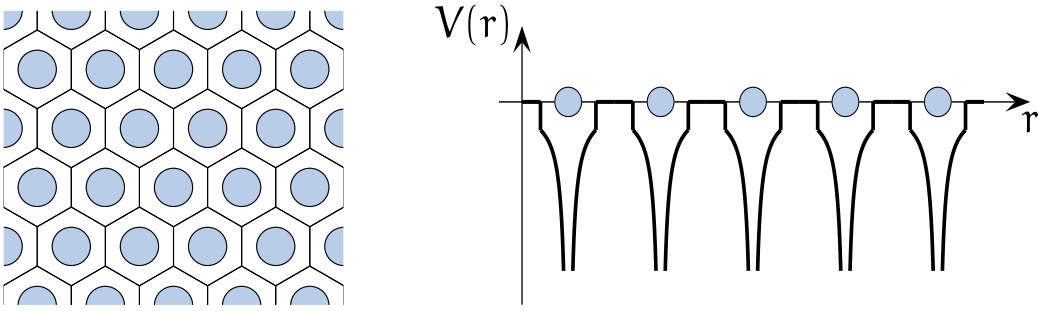

Fig. 3.1: *Muffin tin separation of space: the shaded area represents the spherical atomic-like potential (left) and a schematic muffin-tin potential plotted along a line of ions (right).*

is natural to use a plane wave expansion of the wave function in the interstitial region (I) where the potential is kept constant. On the other hand, the

natural expansion about a site within the muffin tin radius R_{MT} is of the form

$$\psi(\mathbf{r}) := \sum_{lm} c_{lm} R_l(r) Y_{lm}(\hat{\mathbf{r}}) \quad \text{for} \quad r \leq R_{MT} \tag{3.3}$$

where $rR_l(r)$ satisfies the radial Schrödinger equation

$$\frac{d^2}{dr^2}(rR_l) + \left(E - V(r) - \frac{l(l+1)}{r^2} \right) rR_l = 0\,. \tag{3.4}$$

and $Y_{lm}(\hat{\mathbf{r}})$ denotes a spherical harmonic in the direction variables of the vector $\mathbf{r}$. The basic idea of the APW method is to expand in functions composed of waves of the form of Eq. (3.3) near the nuclei and plane waves between them. One immediate advantage is that Bloch's theorem is automatically satisfied. Consequently there is a dual representation for the basis functions, the *augmented plane waves*,

$$\phi_{\mathbf{k_n},\mathcal{E}}(\mathbf{r}) := \begin{cases} e^{i\mathbf{k_n}\cdot\mathbf{r}} & \text{for} \quad \mathbf{r} \text{ in I}, \\ \sum\limits_{l=0}^{\infty} \sum\limits_{m=-l}^{l} A_{lm}(\mathbf{k_n}) Y_{lm}(\widehat{\mathbf{r}}_\nu) R_l(\mathcal{E}, r) & \text{for} \quad \mathbf{r} \text{ in Sphere at } \mathbf{R}_\nu^{\mathbf{MT}} \end{cases} \tag{3.5}$$

where $\mathbf{r}_\nu := \mathbf{r} - \mathbf{R}_\nu^{\mathbf{MT}}$. Generally there is a discontinuity of the APW at the sphere boundary. In the standard Slater scheme it is made continuous over the surface of the sphere. This is easily arranged by an appeal to the standard expansion theorem for a plane wave in spherical harmonics and spherical Bessel functions [Sch99]:

$$e^{i\mathbf{k_n}\cdot\mathbf{r}} = 4\pi \sum_{lm} i^l j_l(k_n r) Y_{lm}(\widehat{\mathbf{r}}) Y_{lm}^*(\widehat{\mathbf{k}}_n) \tag{3.6}$$

For the coefficients $A_{lm}(\mathbf{k_n})$ we get

$$A_{lm}(\mathbf{k}_n) = \frac{4\pi i^l}{\Omega^{1/2} R_l(R)} \sum_{\mathbf{G}_n} c_{\mathbf{G}_n} j_l(k_n R) Y_{lm}^*(\widehat{\mathbf{k}}_n) \tag{3.7}$$

A linear combination of the APW as defined above

$$\Psi_{\mathbf{k}}(\mathbf{r}) = \sum_{\mathbf{G_n}} \alpha_{\mathbf{G_n}} \phi_{\mathbf{k_n},\mathcal{E}}(\mathbf{r}) \tag{3.8}$$

serves as a putative solution of the Schrödinger equation. The sum over reciprocal lattice vectors is limited by a plane wave cutoff G_C, so that $|\mathbf{k} + \mathbf{G}| \leq G_C$. An increase of G_C results in a "more complete" basis set.

In practical calculations one has always to check, if the results are converged with respect to G_C to a satisfactory degree. The condition that the coefficients $\alpha_{\mathbf{G_n}}$ may be determined imposes a relationship between the energy eigenvalue $\mathcal{E}$ and the wave vector $\mathbf{k}$.

Calculating the expectation value of the Kohn-Sham operator with the muffin tin potential

$$H^{MT}\Psi_{\mathbf{k}}(\mathbf{r}) = \epsilon_{\mathbf{k}}\Psi_{\mathbf{k}}(\mathbf{r}) \quad \text{with} \quad H^{MT} := -\nabla^2 + \Phi^{MT}(\mathbf{r}) \tag{3.9}$$

and exploiting Ritz' variational principle [Sch99] with the ansatz above using the $\alpha_{\mathbf{G_n}}$ as variational parameters results in a matrix equation

$$\sum_m (H_{nm} + S_{nm} - \mathcal{E}O_{nm})\alpha_{\mathbf{G_m}} = 0 \tag{3.10}$$

with

$$H_{nm} := \int_\Omega \phi^*_{\mathbf{k_n},\mathcal{E}}(\mathbf{r}) H^{MT} \phi_{\mathbf{k_m},\mathcal{E}}(\mathbf{r})\, d\Omega \tag{3.11}$$

$$\begin{aligned} S_{nm} := -\frac{1}{2}\int_{\mathcal{S}} &(e^{i\mathbf{k_n}\cdot\mathbf{r}} + \sum_{l=0}^{\infty}\sum_{m=-l}^{l} A_{lm}(\mathbf{k_n}) Y_{lm}(\widehat{\mathbf{r}_\nu}) R_l(\mathcal{E}, r))^* \\ &(\frac{\partial}{\partial\rho} e^{i\mathbf{k_n}\cdot\mathbf{r}} - \frac{\partial}{\partial\rho}\sum_{l=0}^{\infty}\sum_{m=-l}^{l} A_{lm}(\mathbf{k_n}) Y_{lm}(\widehat{\mathbf{r}_\nu}) R_l(\mathcal{E}, r))\, d\mathcal{S} \end{aligned} \tag{3.12}$$

$$O_{nm} := \int_\Omega \phi^*_{\mathbf{k_n},\mathcal{E}}(\mathbf{r}) \phi_{\mathbf{k_m},\mathcal{E}}(\mathbf{r})\, d\Omega \tag{3.13}$$

and the corresponding secular equation which is well known from pseudopotential theory [Har66]:

$$det\,|H_{nm} + S_{nm} - \mathcal{E}O_{nm}| = 0\,, \tag{3.14}$$

a generalized algebraic eigenvalue problem determining the expansion coefficients $C^{i\mathbf{k}}_{\mathbf{G}}$ and one particle energies ϵ_i. The basis functions depend on ϵ_i, so that the eigenvalue problem, Eq. (2.37), is nonlinear with all problems arising with this nonlinearity. Furthermore the secular equation, Eq. (3.14), shows a singularity whenever a node of the radial function $R^\alpha_l(R^\alpha_{MT}, \epsilon^{\mathbf{k}}_i)$ happens to coincides with the muffin tin radius R^α_{MT} (c.f. Eq. (3.7)). Yet another drawback of the APW method is the fact that generally the basis functions are only continuous but not continuously differentiable at R^α_{MT}. This leads to a jump in the kinetic energy [Sla37] and the cumbersome calculation of the matrix elements S_{nm}, being not physical for the actual crystal potential.

A further difficulty with the APW method is that it is hard (but not impossible [EK76]) to extend it to use a general crystal potential, beyond the level of the *warped* muffin-tin approximation (general potential in the interstitial and a spherical potential inside the spheres).

In addition there is a so called asymptote problem: in Eq. (3.7) $R_l(R)$ appears in the denominator. However, there are in general values of the energy parameter $\mathcal{E}_l$ for which R_l vanishes on the sphere boundary. At these energies the plane waves and radial functions become decoupled. In the vicinity of this asymptote the relation between A_{lm} and $c_{\mathbf{G}}$ and thus the secular determinant are strongly varying. This leads to numerical difficulties when bands occur near an asymptote.

All these deficiencies of the APW method are lifted by a linearization first introduced by Andersen in 1975 [And75] traced back to the widely unnoticed suggestion of Marcus [Mar67] as will be outlined in the next section.

3.2 LAPW method

The common origin of all the difficulties within the APW method as sketched above is the energy dependence of the APW. Within the Linearized Augmented Plane Wave (LAPW) method, this energy dependence of the basis functions is avoided by determining the radial functions R_l^α for a fixed and suitably chosen energy value E_l^α

$$H_\alpha^{rad}(rR_l^\alpha(r_\alpha, E_l^\alpha)) = E_l^\alpha(rR_l^\alpha(r_\alpha, E_l^\alpha)) \tag{3.15}$$

where

$$H_\alpha^{rad} = -\frac{d^2}{dr^2} + \frac{l(l+1)}{r^2} + V(r) \tag{3.16}$$

(see also Eq. (3.4)). In the APW method $\mathcal{E}_l$ serves as a variational parameter which suitably chosen assists in getting the correct wave function. The lack in this variational freedom is partly compensated through the usage of the energy derivative of R_l [KA75, And75]. The obvious solution consists in using the Taylor expansion of $R_l^\alpha(r_\alpha, E_l^\alpha)$ around a fixed parameter E_l up to linear order within a muffin tin sphere:

$$R_l^\alpha(r_\alpha, E_l^\alpha + \delta) = R_l^\alpha(r_\alpha, E_l^\alpha) + \delta\dot{R}_l^\alpha(r_\alpha, E_l^\alpha) + o(\delta) \tag{3.17}$$

where

$$\dot{R}_l^\alpha(r_\alpha, E_l^\alpha) := \frac{\partial R_l^\alpha(r_\alpha, E)}{\partial E}\,|_{E=E_l} \tag{3.18}$$

For this to be true one has to ensure an energy independent normalization within the muffin tin, e.g.:

$$\int_0^R r^2 R_l^2 dr = 1 \tag{3.19}$$

The differential equation for the energy derivative $\dot{R}_l^\alpha(r_\alpha, E_l^\alpha)$ is obtained from Eq. (3.15) by a straightforward differentiation:

$$H_\alpha^{rad}\dot{R}_l^\alpha(r_\alpha, E_l^\alpha) - E_l^\alpha \dot{R}_l^\alpha(r_\alpha, E_l^\alpha) = R_l^\alpha(r_\alpha, E_l^\alpha) \tag{3.20}$$

Differentiating of the normalization condition (Eq. (3.19)) with respect to E_l, directly shows the orthogonality of $R_l^\alpha(r_\alpha, E_l^\alpha)$ and $\dot{R}_l^\alpha(r_\alpha, E_l^\alpha)$. The *augmented plane wave* within LAPW are given in close resemblance to the APW method

$$\phi_{\mathbf{k}_n}(\mathbf{r}) := \begin{cases} \Omega^{-1/2} e^{i\mathbf{k}_n \cdot \mathbf{r}} & \text{for} \quad \mathbf{r} \text{ in I}, \\ \sum_{l=0}^{\infty} \sum_{m=-l}^{l} (A_{lm} R_l^\alpha(r_\alpha, E_l^\alpha) + & \text{for} \quad \mathbf{r} \text{ in Sphere located at } \mathbf{R}_\alpha^{\mathbf{MT}} \\ \quad B_{lm} \dot{R}_l^\alpha(r_\alpha, E_l^\alpha)) Y_{lm}(\widehat{\mathbf{r}_\alpha}) & \end{cases} \tag{3.21}$$

where $\mathbf{k}_n := \mathbf{k} + \mathbf{K}_n$, with the reduced wave vector $\mathbf{k}$ and reciprocal lattice vector $\mathbf{K}_n$, Ω denotes the volume of the unit cell. In contrast to the conventional APW formalism, E_l^α is now kept constant. Note that the method permits different choices of the energy parameter for different angular momenta. E_l is set as the average band energy of momentum l within the α^{th} muffin tin sphere and can be approximately determined by the *Wigner-Seitz rule* [And73, And75, BSST90]. $\phi_{\mathbf{k}_n}(\mathbf{r})$ is constructed to be continuous with continuous derivative across the muffin tin sphere boundary with the utilization of the Rayleigh expansion, Eq. (3.6), for each angular momentum l. This results in

$$A_{lm}(\mathbf{k}_n) = 4\pi R^2 \Omega^{-1/2} i^l Y_{lm}^*(\hat{\mathbf{k}}_n) a_l \tag{3.22}$$

$$a_l = j_l'(k_n R)\dot{R}_l^\alpha(R_\alpha, E_l^\alpha) - j_l(k_n R)\dot{R}_l^{\alpha'}(R_\alpha, E_l^\alpha) \tag{3.23}$$

$$B_{lm}(\mathbf{k}_n) = 4\pi R^2 \Omega^{-1/2} i^l Y_{lm}^*(\hat{\mathbf{k}}_n) b_l \tag{3.24}$$

$$b_l = j_l(k_n R) R_l^{\alpha'}(R_\alpha, E_l^\alpha) - j_l(k_n R)\dot{R}_l^{\alpha'}(R_\alpha, E_l^\alpha) \tag{3.25}$$

In calculating the expectation value of the Kohn-Sham operator with the muffin tin potential with the trial solution

$$\Psi_{\mathbf{k}}(\mathbf{r}) = \sum_{\mathbf{K_n}} \alpha_{\mathbf{K_n}} \phi_{\mathbf{k_n}, E_l}(\mathbf{r}) \tag{3.26}$$

using $\alpha_{\mathbf{K_n}}$ as variational parameters, one arrives at the matrix equation

$$\sum_m (H_{nm} - \mathcal{E} O_{nm})\alpha_n = 0 \tag{3.27}$$

with

$$H_{nm} := \left\langle \phi^*_{\mathbf{k_n}}(\mathbf{r}) \middle| H^{MT} \middle| \phi_{\mathbf{k_m}}(\mathbf{r}) \right\rangle \tag{3.28}$$

$$O_{nm} := \left\langle \phi^*_{\mathbf{k_n}}(\mathbf{r}) \middle| \phi_{\mathbf{k_m}}(\mathbf{r}) \right\rangle \tag{3.29}$$

The overlap matrix is given by

$$O_{nm} = U(\mathbf{k_n} - \mathbf{k_m}) + \frac{4\pi R^4}{\Omega} \sum_l (2l+1) P_l(\hat{\mathbf{k}}_n \cdot \hat{\mathbf{k}}_m) o^l_{nm} \tag{3.30}$$

$$o^l_{nm} = a_l(k_n) a_l(k_m) + b_l(k_n) b_l(k_m) N_l \tag{3.31}$$

where $U(\mathbf{K})$ is the Fourier series transform of the Heavyside step function, which is zero inside the muffin tin and one outside,

$$U(\mathbf{K}) = \delta_{\mathbf{K}} - \frac{4\pi R^2}{\Omega} \frac{j_1(KR)}{K} \tag{3.32}$$

and the norm of $\dot{R}_l$ within the muffin tin sphere

$$N_l := \int_0^R r^2 \dot{R}_l \dot{R}_l dr \; . \tag{3.33}$$

For the hamilton matrix the result reads as:

$$H_{nm} = \mathbf{k}_n \mathbf{k}_m U(\mathbf{K}_n - \mathbf{K}_m) + \frac{4\pi R^4}{\Omega} \sum_l (2l+1) P_l (E_l o^l_{nm} + \gamma^l) \tag{3.34}$$

$$\begin{aligned} \gamma^l = {} & \dot{R}_l R'_l (j'_l(k_n R) j_l(k_m R) + j_l(k_n R) j'_l(k_m R)) \\ & - (\dot{R}'_l R'_l j_l(k_n R) j_l(k_m R) + \dot{R}_l R_l j'_l(k_n R) j'_l(k_m R)) \end{aligned} \tag{3.35}$$

In principle with standard matrix diagonalization techniques one can solve this electronic structure problem as shown. There is, however, one crucial disadvantage of the LAPW method as described above: the method relies on the replacement of the effective crystal potential with the simplified muffin tin potential. For materials for which the bonding character is mainly covalent, but also for metals with defects and transition metals this is not a very good approximation. Fortunately the LAPW method is easily extended to the *Full Potential* LAPW method (FLAPW) [KA75].

3.3 FLAPW method

In contrast to LAPW or APW method the full effective crystal potential is considered within the Full Potential Linearized Augmented Plane Wave (FLAPW) method [BSST90]. To correct for the full crystal potential, we write it as a sum of the underlying muffin tin potential and a non muffin tin contribution:

$$v_{eff}(\mathbf{r}) = v_{MT}(\mathbf{r}) + v_{NMT}(\mathbf{r}) \tag{3.36}$$

In close analogy to the basis function expansion (3.21) the non muffin tin contribution is represented as a superposition of plane waves in the interstitial and spherical harmonics within the muffin tin spheres:

$$v_{NMT}(\mathbf{r}) = \begin{cases} \sum_{\mathbf{K}\neq 0} v(\mathbf{K}) e^{i\mathbf{K}\mathbf{r}} & \text{for} \quad \mathbf{r} \in I \\ \sum_{\alpha} \sum_{L\neq 0,M} v^{\alpha}_{LM}(r_\alpha) Y_{LM}(\hat{\mathbf{r}}_\alpha) & \text{for} \quad \mathbf{r} \in MTS_\alpha \end{cases} \tag{3.37}$$

The functions $R^{\alpha}_{l}(\mathbf{r})$ and $\dot{R}^{\alpha}_{l}(\mathbf{r})$ to construct the basis are further-on calculated with the spheric symmetric part of $v_{eff}(\mathbf{r})$ within the α^{th} muffin tin sphere. Due to the presence of $v_{NMT}(\mathbf{r})$ additional terms arise in the hamilton matrix, Eq. (3.34):

$$\begin{aligned} H^{I}_{nm} &:= \left\langle \phi^{*}_{\mathbf{k_n}}(\mathbf{r}) \middle| \sum_{\mathbf{K}\neq 0} v(\mathbf{K}) e^{i\mathbf{K}\mathbf{r}} \middle| \phi_{\mathbf{k_m}}(\mathbf{r}) \right\rangle_I \\ &= \sum_{\mathbf{K}\neq 0} \int_I v(\mathbf{K}) e^{i(\mathbf{K}_m + \mathbf{K} - \mathbf{K}_n)\,\cdot\,\mathbf{r}} \end{aligned} \tag{3.38}$$

(the integration comprises only the interstitial region I in the integral above), the correction within the MTS reads as:

$$\begin{aligned} H^{NMT}_{nm} &:= \left\langle \phi^{*}_{\mathbf{k_n}}(\mathbf{r}) \middle| \sum_{\alpha} \sum_{L\neq 0,M} v^{\alpha}_{LM}(r_\alpha) Y_{LM}(\hat{\mathbf{r}}_\alpha) \middle| \phi_{\mathbf{k_m}}(\mathbf{r}) \right\rangle_{MTS} \\ &= \sum_{\alpha} \frac{(4\pi {R^{\alpha}_{MT}}^2)^2}{\Omega} e^{i(\mathbf{K}_m - \mathbf{K}_n)\,\cdot\,\mathbf{R}_\alpha} \\ &\cdot \sum_{lm} \sum_{l'm'} \sum_{L\neq 0,M} G(lLl', mMm') Y^{*}_{lm}(\hat{\mathbf{k}}_n) Y_{l'm'}(\hat{\mathbf{k}}_m) \\ &\cdot i^{l-l'} \int_0^{R^{\alpha}_{MT}} r^2 \cdot (a_l(k_n) R^{\alpha}_{l}(r_\alpha, E^{\alpha}_{l}) + b_l(k_n) \dot{R}^{\alpha}_{l}(r_\alpha, E^{\alpha}_{l})) v^{\alpha}_{LM}(r_\alpha) \\ &\cdot (a_l(k_m) R^{\alpha}_{l'}(r_\alpha, E^{\alpha}_{l'}) + b_{l'}(k_m) \dot{R}^{\alpha}_{l'}(r_\alpha, E^{\alpha}_{l'}))\, dr_\alpha \,, \end{aligned} \tag{3.39}$$

with the *Gaunt coefficients* defined as

$$G(lLl', mMm') := \int_S Y^*_{lm}(\hat{\mathbf{r}}) Y_{LM}(\hat{\mathbf{r}}) Y_{l'm'}(\hat{\mathbf{r}})\, dS \tag{3.40}$$

with the integration carried over the unit surface. $G(lLl', mMm')$ vanishes for some combination of (lLl', mMm'), depending of the symmetry of the system under consideration. In this respect, symmetry reduces substantially the computational demands.

The FLAPW method provides a very accurate and flexible method to calculate solid state properties. Due to the fact that it takes care for the full crystal potential, one obtains an exact (up to computational inefficiencies) charge density distribution throughout the crystal. With an accurate knowledge of the charge density, one can calculate the total energy within LDA or GGA of the assembly of nuclei and electrons to a very high degree. For the actual calculation of the groundstate energy a very efficient procedure of M. Weinert et al. [WWF82] is used.

The basic assumption, that there is no spill out of the core states in the interstitial region, is unfortunately sometimes a rather poor assumption, e.g. the high lying d-states in transition metals often show considerable overlap, even if the largest muffin tin sphere radii consistent with the structure are chosen. In particular, the LAPW method relies on the fact that the R^α_l and $\dot{R}^\alpha_l$ are orthogonal to any eigenstate that falls to zero at the sphere boundary, i.e. the underlying core states. The result of this overlap is that orthogonality of the valence wave function to the *semi core states* is not assured, unless the semi core state is treated within the valence window, i.e. by setting the relevant energy parameter to the energy of the semi core state. However, with this choice, the calculation is equivalent to a one window calculation in that there is poor variational freedom for that l character in the valence band [MH86, SK91]. To circumvent this problem, one could perform a so called *two window calculation*, where the valence states and the semi core states are treated on the same footing but in separate energy panels. This ensures the orthogonality of the semi core states to the deep lying core states, but not that of the semi core states to the valence states. Furthermore the computational cost of this *two window calculation* is almost twice the *one window calculation*. An elegant alternative is the utilization of the *local orbitals*, a concept based on the work of D. Singh [Sin91].

3.4 Local Orbitals

D. Singh introduced this extension of the LAPW method [Sin91, Sin94], where the LAPW basis set, Eq. (3.21), within the muffin tin sphere is ex-

panded through the introduction of **K**-independent basis set functions, the *local orbitals*:

$$\phi_{lm}^{LO}(\mathbf{r}) := (A_{lm}R_l(r, E_l^{val}) + B_{lm}\dot{R}_l(r, E_l^{val}) + C_{lm}R_l(r_\alpha, E_l^{sc}))Y_{lm}(\hat{\mathbf{r}}) \quad (3.41)$$

where E_l^{val} is the linearization energy of the valence state and E_l^{sc} that of the corresponding, i.e. shows the same l character, semi core state. The coefficients A_{lm}, B_{lm} and C_{lm} are fixed by ensuring that ϕ_{lm}^{LO} and its derivative at the muffin tin sphere boundary vanishes and its normalization within the muffin tin sphere.

Utilization of ϕ_{lm}^{LO} within a LAPW calculation, therefore, permits the treatment of two differing states with the same angular momentum l within the same energy panel. This assures automatically the orthogonality of both states. The presence of the local orbitals changes the total number of basis set functions and consequently the dimensions only in a negligible manner. Thus the computational costs is almost unchanged. We will use local orbitals for the tungsten 5s-, 5p- and 4f-orbitals and for the thorium 6s- and (just to enhance the flexibility of the basis) 7p-orbitals.

3.5 Brillouin zone Integration

The translational symmetry introduced with the supercell method results in a quantum number, the *supercell* or *crystal momentum* **k** (Eq. 2.57). The groundstate density $n(\mathbf{r})$ is calculated with Eq. (2.34) which using *Bloch's theorem* takes the form:

$$n(\mathbf{r}) := \sum_{\epsilon_n(\mathbf{k}) \leq E_F} \phi_{\mathbf{k}}^*(\mathbf{r})\phi_{\mathbf{k}}(\mathbf{r}) \quad (3.42)$$

where $\phi_{\mathbf{k}}(\mathbf{r})$ denote the *Kohn-Sham orbitals*, $\epsilon_n(\mathbf{k})$ n'th *Kohn-Sham eigenvalue* with crystal momentum **k** and E_F the eigenvalue of the highest occupied *Kohn-Sham orbital*, representing the *Fermi energy*. For infinite systems, the $\{\mathbf{k}\}$ are infinitely dense in reciprocal space and comprise the first Brillouin zone. Consequently, the groundstate density is given as the integral over the first Brillouin zone of the reciprocal space:

$$n(\mathbf{r}) = \sum_n \int_{BZ} \phi_n^*(\mathbf{r};\mathbf{k})\phi_n(\mathbf{r};\mathbf{k}) f(\epsilon_n(\mathbf{k}))\, d^3k\,, \quad (3.43)$$

where BZ is the first Brillouin zone, n the energy band index and $f(\epsilon_n(\mathbf{k}))$ the occupation number for the n'th energy surface in **k**-space:

$$f(\epsilon_n(\mathbf{k})) := \begin{cases} 1 & \text{if } \epsilon_n(\mathbf{k}) \leq E_F \\ 0 & \text{else} \end{cases} \quad (3.44)$$

For the Brillouin zone integration the following two methods are most widely used: the *tetrahedron method* and the *special-point scheme*. The special-point scheme is advantageous for insulating or semiconducting materials, and represents the Brillouin zone integration as a weighted sum over selected **k**-points. Today, the most widely used sets of special-points are those of *Monkhorst-Pack* [MP76, PM77], which consists of an equispaced grid in **k**-space. The tetrahedron method is more general in the sense, that it can be equally applied to insulators and metals. The idea of this method is to subdivide reciprocal space into tetrahedra, within which the band energies are linearized in **k** [LT72]. The linear approximation allows the integration to be performed analytically, taking into account the often complicated shape of the Fermi surface. In the present work, we use an improved tetrahedron method [BJA94] which reduces substantially the number of reciprocal space points necessary for a given accuracy. This *improved tetrahedron method* results in a weighting formula, converting the integral into a weighted sum over irreducible **k**-points $\mathbf{k}_j$ of the form:

$$n(\mathbf{r}) \approx \sum_{n,j} \phi_n^*(\mathbf{r};\mathbf{k}_j)\phi_n(\mathbf{r};\mathbf{k}_j)\,\omega_{n,j} \tag{3.45}$$

with:

$$\omega_{n,j} := \int_{BZ} \omega_j(\mathbf{k}) f(\epsilon_n(\mathbf{k}))\, d^3k\,. \tag{3.46}$$

$\omega_j(\mathbf{k})$ is given as:

$$\omega_j(\mathbf{k}) := \begin{cases} 1 & \text{for } \mathbf{k} = \mathbf{k}_j \text{ and its corresponding star} \\ 0 & \text{on all other } \mathbf{k}\text{-points on the grid} \end{cases} \tag{3.47}$$

The *star* of the irreducible $\mathbf{k_j}$ is defined as as the set of **k**-points which can be transformed into $\mathbf{k}_j$ with spacegroup operations. In-between the grid points $\omega_j(\mathbf{k})$ is defined to interpolate linearly. Starting point for the grid in **k**-space is an equispaced distribution of **k**-points. The number of **k**-points is then subsequently reduced applying the symmetry operations of the space-group [AC65a, AC65b, KS77]. After this procedure, the remaining **k**-points are used to create the tetrahedrons.

The number of tetrahedrons or, likewise, the number of irreducible **k**-points of the grid determines the accuracy of the integration over the first Brillouin-zone. In practical electronic structure calculations, therefore, this number is gradually increased until the integral (or its approximative equivalent) doesn't change anymore beyond a predefined threshold value.

Chapter 4

First principles calculations of the system W-Th

As will be carried out later (see chapter 5) a necessary ingredient in calculating interatomic potentials suitable to perform molecular dynamics are experimentally and/or theoretically derived data which characterize the interactions between the atoms. In this chapter we will utilize DFT calculations to get some insight into some physical properties, including elastic constants, phase stabilities and vacancy formation energies.

4.1 Elastic Constants

As outlined in the previous chapters DFT enables us to calculate the accurate total energy and charge density of an assembly of electrons and nuclei. If we limit ourselves to simple lattices, the internal lattice parameters will be fixed once we specify the volume of the unit cell. We can thus determine a set of total energies $E_i = E(V_i)$. In practice, we use several volumes which are within 10%-20% of the expected equilibrium volume. We then make a least squares fit of the set (V_i, E_i) to a form proposed by Murnaghan [Mur44] (see also appendix A):

$$E(V) - E(V_0) = \frac{B_0 V}{B_0'}\left(1 + \frac{1}{B_0' - 1}\left(\frac{V_0}{V}\right)^{B_0'}\right) - \frac{B_0 V_0}{B_0' - 1} \qquad (4.1)$$

where V_0, B_0 and B_0' are, respectively, the equilibrium volume, bulk modulus, and pressure derivative of the bulk modulus.

In this chapter we consider cubic lattices. It comprises the monatomic bcc and fcc lattices as well as the diatomic $B2$ (Pearson symbol: cP2) and $L1_2$

(Pearson symbol: cP4) structures. These structures are completely specified by one parameter, the volume of the unit cell V, or alternatively the cubic lattice constant a.

For the remaining elastic constants, we apply a slightly different procedure. If we strain the lattice by distorting the primitive vectors, we may obtain all the elastic constants C_{ij} [AM76]. But before we go into the specific details it is advisable to drop some preliminary remarks. In this context a solid is characterized by fixed neighborhood relations. Atoms will slightly change their relative positions upon stress, but they return to their original position when the stress is removed.

Deformations of a solid can be formally described by the *deformation* or *strain tensor* $\boldsymbol{\epsilon}$:

$$\boldsymbol{\epsilon} := \begin{pmatrix} \epsilon_{11} & \epsilon_{12} & \epsilon_{13} \\ \epsilon_{21} & \epsilon_{22} & \epsilon_{23} \\ \epsilon_{31} & \epsilon_{32} & \epsilon_{33} \end{pmatrix} \tag{4.2}$$

If a lattice is deformed such that the resulting structure remains a perfect lattice, the deformation is said to be *homogeneous* [BK54]. In this case $\boldsymbol{\epsilon}$ does not depend on the location. According to $\boldsymbol{\epsilon}$ given, the primitive lattice vectors $\{\boldsymbol{a_1}, \boldsymbol{a_2}, \boldsymbol{a_3}\}$ and therefore the total lattice are transformed to the new lattice vectors $\{\boldsymbol{a_1'}, \boldsymbol{a_2'}, \boldsymbol{a_3'}\}$:

$$\begin{pmatrix} \boldsymbol{a_1'} \\ \boldsymbol{a_2'} \\ \boldsymbol{a_3'} \end{pmatrix} = (\mathbf{1} + \boldsymbol{\epsilon}) \cdot \begin{pmatrix} \boldsymbol{a_1} \\ \boldsymbol{a_2} \\ \boldsymbol{a_3} \end{pmatrix} \tag{4.3}$$

where $\mathbf{1}$ is the 3×3 identity matrix. We need only to consider non-rotating strains, so we represent the strain by a symmetric tensor with six independent components (*Voigt-notation*):

$$\boldsymbol{\epsilon} := \begin{pmatrix} \epsilon_1 & \epsilon_6/2 & \epsilon_5/2 \\ \epsilon_6/2 & \epsilon_2 & \epsilon_4/2 \\ \epsilon_5/2 & \epsilon_4/2 & \epsilon_3 \end{pmatrix} \tag{4.4}$$

Therewith, the total energy changes by an amount:

$$E(\{\epsilon_i\}) - E(\{\epsilon_i = 0\}) = -p(V)\Delta V + \frac{V}{2} \sum_{ij}^{6} C_{ij}\epsilon_i\epsilon_j + O(\{\epsilon_i^3\}) \tag{4.5}$$

where V is the volume of the undistorted lattice, $p(V)$ is the hydrostatic pressure of the undistorted lattice at volume V, ΔV is the change in the volume of the lattice due to the strain (Eq. 4.4), and $O(\{\epsilon_i^3\})$ indicates that

the neglected terms in the polynomial expansion are cubic and higher powers of strains ϵ_i.

Owing to symmetry ($C_{ij} = C_{ji}$), there are only 21 independent elastic constants C_{ij} in Eq. (4.5). Lattice symmetries reduce this number down to three for the cubic lattices (e.g. C_{11}, C_{12} and C_{44}). In this case the bulk modulus B can be expressed with these constants as:

$$B = (C_{11} + 2C_{12})/3 \tag{4.6}$$

Apart from the bulk modulus B we need two more constants for a complete set. Mechanical stability of a cubic material (at least up to $O(\{\epsilon_i^3\})$) implies [BK54]:

$$B = (C_{11} + 2C_{12})/3 > 0, \tag{4.7}$$

$$C_{11} - C_{12} > 0, \tag{4.8}$$

$$C_{44} > 0 \tag{4.9}$$

Therefore the logical completions are the tetragonal strain modulus $C' := (C_{11} - C_{12})/2$ and the monoclinic strain modulus C_{44}.

Although the obvious method of computing C' uses the tetragonal strain, we prefer the volume conserving orthorhombic strain,

$$\epsilon_1 = \epsilon\,, \quad \epsilon_2 = -\epsilon\,, \quad \epsilon_3 = \epsilon^2/(1-\epsilon^2)\,, \quad \epsilon_4 = \epsilon_5 = \epsilon_6 = 0\,. \tag{4.10}$$

With this choice of strain, the total energy change is given by

$$\Delta E = 2VC'\epsilon^2 + O(\epsilon^4) \tag{4.11}$$

i.e. is an even function of ϵ and does not depend on the hydrostatic pressure p, resulting in fewer calculations necessary (e.g. only for positive ϵ). Although the orthorhombic strain yields to lower symmetry and thus needs more independent **k**-points for Brillouin zone averages than the tetragonal strain, we choose this method because of the reduction in the number of self-consistent calculations needed.

In close analogy, we use a volume conserving monoclinic strain for C_{44},

$$\epsilon_6 = \epsilon\,, \quad \epsilon_3 = \epsilon^2/(4-\epsilon^2)\,, \quad \epsilon_1 = \epsilon_2 = \epsilon_4 = \epsilon_5 = 0\,. \tag{4.12}$$

The total energy results in this case in

$$\Delta E = VC_{44}\epsilon^2/2 + O(\epsilon^3)\,. \tag{4.13}$$

To get B, C' and C_{44} we use the following procedure: as a first step, we calculate data pairs $\{V, E\}$ or $\{\epsilon, E\}$ for some V or ϵ, respectively, within DFT. The second step fits the resulting data points to Eqs. (4.1), (4.11) and (4.13).

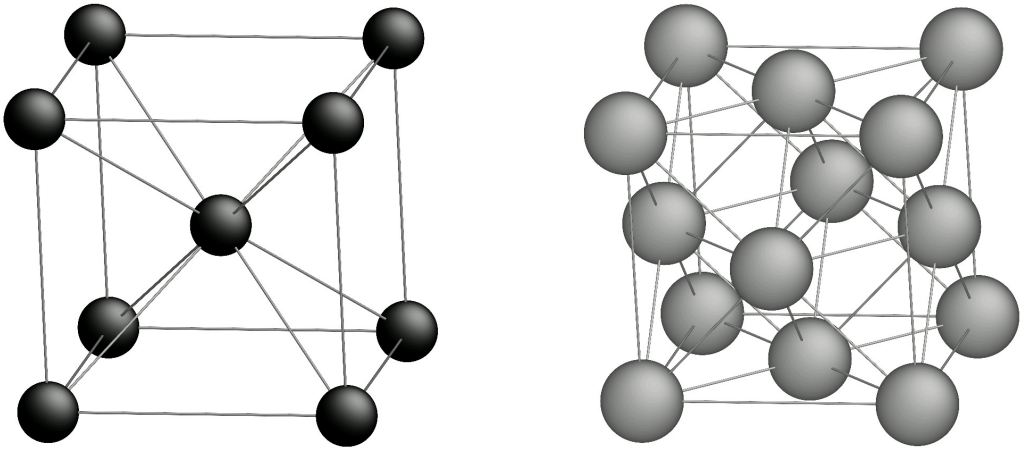

Fig. 4.1: *The conventional unit cell of W (left) and Th (right) at low hydrostatic pressure*

4.1.1 The monatomic metals Tungsten and Thorium

In order to test the treatment as introduced above and to determine the settings of the FLAPW method to get proper results, we studied the monatomic case of tungsten and thorium at first. Apart from the fact that the tungsten-thorium system plays an important role as basis material of gas discharge lamp electrodes, they are interesting for themselves.

Tungsten but also, in a wider sense, thorium belongs to the class of the so called *transition metals*. In a narrow sense, transition metals are elements with partly occupied 3d-, 4d- and 5d-shells, which form large periods in the periodic table. Sometimes this term is applied to all the elements with partly filled inner electron shells, including 4f (rare earths) and 5f (actinides). The electronic configuration of free tungsten atoms consists of a chemically inert Xe-core, a complete 4f-shell, 4 5d- and 2 6s-electrons, $[Xe]4f^{14}5d^{4}6s^{2}$ for short. In total it has 74 electrons. In a solid d- (and f-) states are generally very localized. The corresponding electrons are therefore strongly screened due to the presence of nearly delocalized s- and p- electrons resulting in a comparable weak overlap of d-states of neighboring atoms. This weak overlap generally implicates a narrow electronic d-bandwidth in band structure calculations. A narrow d-band is responsible for the occasional occurrence of magnetism in the d-rows (predominantly in the 3d-row) of the periodic table. Fortunately for our bandstructure calculations concerning tungsten there is no magnetic ordering (at least in the bcc structure), so there is no need for spin polarized calculations. This allows for using the maximum symmetry of the underlying bcc-lattice (Space group: $Im\bar{3}m$) which reduces

the computational costs to a minimum.

The electronic configuration of free thorium atoms is $[Rn]6d^27s^2$ with in total 90 electrons. It occupies a unique position in the periodic table as being a transition metal (in the wider sense) with strong s-d hybridization and on the threshold of being a regular 5f band light actinide element. Th is the only element which has an unoccupied 5f band as near as 1.5 eV above the Fermi level [SJ80] and at ambient condition with four valence electrons is regarded as a regular tetravalent transition metal in a row with e.g. titanium, zirconium and hafnium [JAEW95]. Interestingly enough, Th when compared to Ti, Zr and Hf should be expected to be a hcp metal. Since this is not the case, Th (at least under low pressure conditions) shows an fcc structure ($Fm\bar{3}m$), one should search for pressure induced crystallographic transitions to the hcp structure of Hf or Zr, as is well known for other groups of elements in the same row of the periodic table [Joh78, REJ75, JR75].

Computational Details

In the literature two forms of tungsten are referred to: the stable α-form and a (meta-)stable [HEB31] form called β-tungsten (crystal structure: $A15$, spacegroup symmetry: $Pm3n$ with eight atoms per unit-cell). If at all, β-tungsten seems to be stable at temperatures below $630°C$ [MHSN57] and high hydrostatic pressure. Furthermore, up to now, β-tungsten can be synthesized only in nanometer-scale (diameter of crystallites about $20nm$) and is mostly accompanied with the thermodynamic stable α-tungsten and some tungsten-oxides [Ley98].

The undistorted α-Tungsten lattice at low hydrostatic pressure belongs to the *body centered cubic* lattices (α-phase) with spacegroup symmetry $Im\bar{3}m$ [Hah96]. There is also strong evidence that there exist pressure induced structural phase transitions in tungsten. J. A. Moriarty [Mor92] showed with the aid of first-principles total-energy calculations a ultrahigh-pressure destabilization of the bcc structure of tungsten through a bcc→hcp phase transition at about 12.5 Mbar. Furthermore, he predicts a subsequent hcp→fcc transition at about 14.4 Mbar. The question of phase stability in tungsten was also addressed by Söderlind *et al.* [SAEJ94] within a LDA calculation with basically the same conclusions, but with a slightly different transition pressure for the bcc→hcp transition (9.2 Mbar). In the present work we take the bcc structure for granted.

For both the orthorhombic (4.10) for C' as well as the monoclinic strain (4.12) for C_{44} the distorted tungsten lattice becomes orthorhombic with spacegroups $Fmmm$, i.e. *face centered orthorhombic*, and $Immm$, i.e. *body centered orthorhombic*, respectively. There is only one inequivalent atom

present: its fractional coordinates are $(0,0,0)$ with the origin at the center of (mmm), site symmetry group (mmm) and eight (point) symmetry operations which leave the lattice invariant.

Without external stress applied and at low hydrostatic pressure, the lattice of thorium belongs to the *face centered cubic* lattices (commonly referred to as α-Thorium) with spacegroup symmetry $Fm\bar{3}m$ [Hah96]. There are experimental as well as theoretical results, which observe a fcc→bct (body centered tetragonal) transition at about 0.8-1.0 Mbar, unisono. The experiment was observed in the diamond-anvil cell by the energy-dispersive x-ray-diffraction (EDXD) technique using a synchrotron source [VA91]. The calculations were done using the *linear muffin-tin orbital* (LMTO-) method within the *atomic sphere approximation* [RGS92] and the full crystal potential [JAEW95], respectively, with remarkable agreement. Our considerations below base on the assumption of a low pressure fcc structure of thorium ("α-Th").
The calculations were done using the FLAPW method as introduced above in an implementation as supplied with the *WIEN97* package, version $WIEN97.8$, release 4/99 [BSL99].
The converged FLAPW parameters for tungsten and thorium are:

	SG	R_{MT} ()	E_{cut}^{wf} (Ry)	#k (BZ)	l_{wf}	l_{pot}	E_{cut}^{pot} (Ry)	LO
W	$Im\bar{3}m$	1.27	11.11	5000	12	5	196.0	5s, 5p, 4f
Th	$Fm\bar{3}m$	1.32	10.24	5000	12	5	196.0	6s, 6p

where SG is the spacegroup of the structure, R_{MT} the muffin-tin radius, E_{cut}^{wf} and E_{cut}^{pot} the wavefunction and potential cutoff, respectively, l_{wf} and l_{pot} the maximal angular momentum for the wavefunction and potential expansion within R_{MT}, and LO denotes the orbitals for which we apply Singh's local orbital concept [Sin91]. With #k we denote the total number of k-points in the first Brillouin zone used. The resulting *total density of states* (DOF) for the equilibrium configurations of W and Th is shown in Fig. 4.2. The transition to the shaded areas mark the *Fermi-Energy*, i.e. the highest occupied one-particle energy in groundstate. Especially the DOS of W shows the origin of the stability of the *bcc*-structure: the bimodal shape of the DOS of W, which is primarily a result of the d-states. There exists a pseudo-gap inmidst the d-band partial DOS. If the Fermi-Energy happens to coincide with this pseudo-gap, which is the case for approximately half-filled d-bands, than the binding energy is lower in this bimodal shape compared to an unimodular one. So, in this respect, the equilibrium *bcc*-structure is a consequence of the

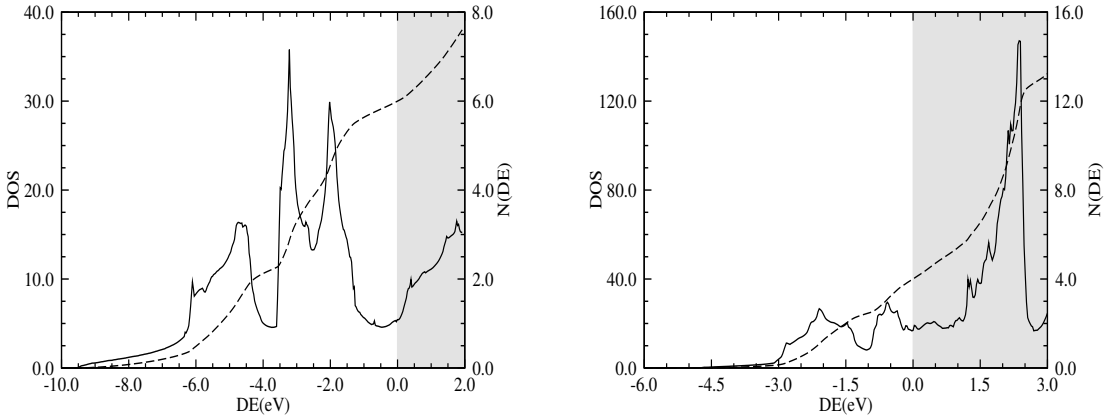

Fig. 4.2: *The Total Density of States (DOS) (scales on the left side) for W (left) and Th (right) as a function of the difference of the one-particle energy and the fermi-level (transition to shaded region) and the integrated DOS is shown (scales on the right side).*

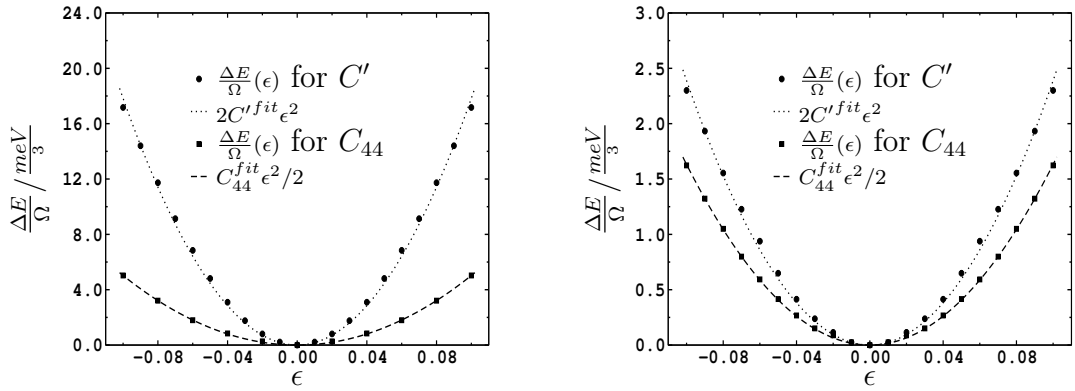

Fig. 4.3: *Calculated (dots) and fitted (line) values for the energy density as a function of strain ϵ for the monoclinic (C_{44}) and tetragonal (C') modulus of W (left) and Th (right)*

half-filling of the d-band. Furthermore, the metallic character of W and Th is clearly demonstrated, as the Fermi-Energy resides at non-zero DOS.

The bulk moduli of W and Th are derived using eleven Energy-Volume pairs (E_i, V_i) in the range from $\frac{V_i}{V_0} = 0.9$ to $\frac{V_i}{V_0} = 1.1$, where V_0 is the unit cell volume for which the energy takes its minimum ("equilibrium volume"). For each of the remaining elastic constants, i.e. C_{44} and C', six Energy-Strain-parameter pairs (E_i, ϵ_i), with ϵ_i varied from zero to 0.1 are used.

Figs. 4.3 show the resulting total energies for different strains applied and the curves fitted according to Eqs. (4.13) and (4.11), respectively. The nonlinear least square fits to the parabolae were done with the *Levenberg-Marquardt* method [Mar63].

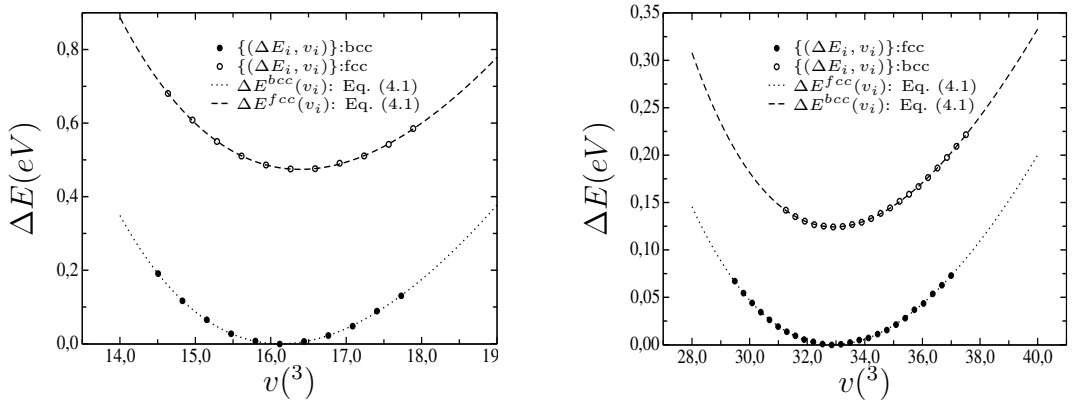

Fig. 4.4: *Calculated (dots) and fitted (lines) energy dependence of W and Th of volume per atom v. From these calculations bulk modulus as well as phase stability are derived.*

A thorough consideration of the bulk moduli of W and Th results in Fig. 4.4. Likewise, Eq. (4.1) was fitted using Levenberg and Marquardt's scheme.

Additionally, the *bcc-fcc phase stability* of W and Th is derived from the calculations. For this, we used the calculated groundstate energies per atom of W and Th in *bcc* as well as *fcc* structure. The result of the calculations are also depicted in Fig. 4.4. It comes as no surprise that the claimed equilibrium structures, *bcc* for W and *fcc* for Th, are the phases of lowest energy per atom among those compared. The difference in the groundstate energies results in $\Delta E^W_{fcc-bcc} = 0.475eV$ for W and $\Delta E^{Th}_{bcc-fcc} = 0.123eV$ for Th, respectively. The corresponding equilibrium volumes per atom are nearly uninfluenced and remain almost at their value in the equilibrium phases: $v^W = 16.13^3$ and $v^{Th} = 32.90^3$.

	$V_0(^3)$	$B(GPa)$	B'	$C_{44}(GPa)$	$C'(GPa)$
W	16.1305	310.439	4.0955	161.065	142.856
Th	32.9031	52.655	2.5454	52.304	19.144

Table 4.1: *The results of the fitting procedures for W and Th: the equilibrium volume per atom V_0, bulk modulus B and its derivative B' with respect to the hydrostatic pressure applied, tetragonal strain modulus $C' := (C_{11} - C_{12})/2$ and monoclinic strain modulus C_{44}.*

For completeness, we mention in Tab. 4.1 also the derivative of the bulk modulus with respect of hydrostatic pressure B', which is also a result of the fitting procedure to *Murnaghan's equation*, Eq. (4.1). A short summary

	V_0 (Å^3)	B (GPa)	C_{11} (GPa)	C_{12} (GPa)	C_{44} (GPa)	A
present work	32.2610	310.438	500.920	215.204	161.067	1.1280
TB [MP96]	30.9592	318.993	528.991	169.991	197.997	1.1031
Expt.	31.4648	310.374	522.390	204.374	160.827	1.0115

Table 4.2: *Comparison of results of our FLAPW calculations for tungsten with those of shock experiments and those of a tight-binding (TB) method [MP96]. The table shows the equilibrium volume of the unit cell V_0, the elastic constants for the body centered cubic (bcc) phase C_{11}, C_{12} and C_{44}, as well as the* anisotropy factor $A := \frac{2 \cdot C_{44}}{C_{11} - C_{12}}$.

of the results for W are presented in Tab. 4.2, where we also compared our results with those of a shock experiment and those calculated within a *tight-binding* procedure [MP96]. The *anisotropy factor* $A := \frac{2 \cdot C_{44}}{C_{11} - C_{12}}$ is also shown to be rather near to unity, quantifying the fact that tungsten is one of the elastically most isotropic element.

Up to now, we basically calculated only the elastic constants of the pure phases, that is, with the physical data derived so far, no interaction between W- and Th-atoms can be characterized. Therefore, in the next section we want to extend the ideas developed in the preceding paragraph.

4.1.2 The ordered intermetallic Tungsten-Thorium

One of the main aspects of this thesis is to derive interaction potentials suitable for molecular dynamics not only for the interplay of W- or Th-atoms with themselves, but also for the description of interacting W- and Th-atoms. Unfortunately, there are almost no data available, which could serve as a database against which models for the interatomic interaction could be fitted. This is not very astonishing due to the fact, that the $Th-W$ phase diagram shows almost no solubility of W in Th [MJLMK90, HA58]. Even less is known about the reversed case: up to now, there is no phase diagram for Th in W available.

Although the solubility of Th in solid W is very small it is not zero as measurements of diffusion and electrical resistivity clearly indicate [FYW33]. Additionally, there is evidence that there are no compounds in the $Th - W$ system [SR55]. Basing on this knowledge, we conclude, that considerable effort would be necessary to derive physical data from experiments for the sequencing fitting procedure.

However, in the preceding section, we used the FLAPW method with

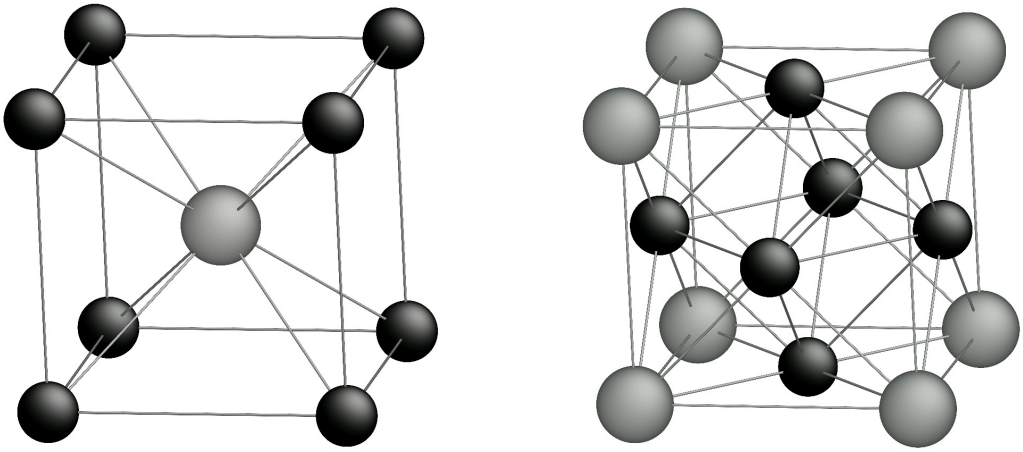

Fig. 4.5: *The conventional unit cell of W-Th in B2- (left) and $L1_2$- (right) structure. The B2 contains two atoms: Th at the position with fractional coordinates* $(0,0,0)$ *and W at* $(\frac{1}{2},\frac{1}{2},\frac{1}{2})$*, whereas the $L1_2$ contains four atoms: Th at the position with fractional coordinates* $(0,0,0)$ *and W at* $(\frac{1}{2},\frac{1}{2},0)$*,* $(\frac{1}{2},0,\frac{1}{2})$ *and* $(0,\frac{1}{2},\frac{1}{2})$

satisfactory results. So, why shouldn't we try to extend the ideas to ordered intermetallic compounds between W and Th despite the fact, that no such compounds exist in nature?

Well, let's start with a compound which is commonly referred to as $B2$ according to the nomenclature of the *Strukturbericht* with corresponding spacegroup symmetry $Pm\bar{3}m$, see the left-hand picture of Fig. 4.5. The unit-cell of this structure contains two atoms. For the calculations we chose the atom with fractional coordinates $(0,0,0)$ to be thorium and the atom with coordinates $(\frac{1}{2},\frac{1}{2},\frac{1}{2})$ to be tungsten. This structure is therefore composed of the same number of W- and Th-atoms.

Another structure, where this particle number symmetry is broken is the $L1_2$ (*Strukturbericht designation*) with the same spacegroup symmetry ($Pm\bar{3}m$) as $B2$. For an illustration see the right-hand picture of Fig. 4.5. In this structure we locate a Th-atom at the position with fraction coordinates $(0,0,0)$, whereas we want W-atoms at the remaining positions $((\frac{1}{2},\frac{1}{2},0)$, $(\frac{1}{2},0,\frac{1}{2})$ and $(0,\frac{1}{2},\frac{1}{2}))$. In total, the unit cell of $L1_2$ contains therefore 4 atoms.

As a next step we applied the same procedure as in the preceding section to derive bulk modulus, and tetragonal and monoclinic strain modulus. The converged parameters for the FLAPW calculations used are given in Tab. 4.3.

The results of the calculations are presented in Figs. 4.6. From the compilation in Tab. 4.4, derived from the fits to Eqs. (4.1, 4.11, 4.13), we can clearly see, that the structures $B2$ and $L1_2$ are not stable, because either C_{44}

		SG	R_{MT} ()	E_{cut}^{wf} (Ry)	#k (BZ)	l_{wf}	l_{pot}	E_{cut}^{pot} (Ry)	LO
$B2$		$Pm\bar{3}m$		11.11	3000	10	6	196.0	
	W		1.27						5s, 5p, 4f
	Th		1.43						6s, 6p
$L1_2$		$Pm\bar{3}m$		10.24	1000	10	6	100.0	
	W		1.32						5s, 5p, 4f
	Th		1.43						6s, 6p

Table 4.3: *Converged FLAPW parameters used for the elastic constants of the intermetallic compounds $B2$ and $L1_2$. R_{MT} denotes the radius of the muffin tin sphere, E_{cut}^{wf} and E_{cut}^{pot} the cutoff energy of the plane wave expansion of wave function and potential within the interstitial, l_{wf} and l_{pot} the expansion limit of the spherical harmonics of the wave function and potential within the muffin tin spheres.*

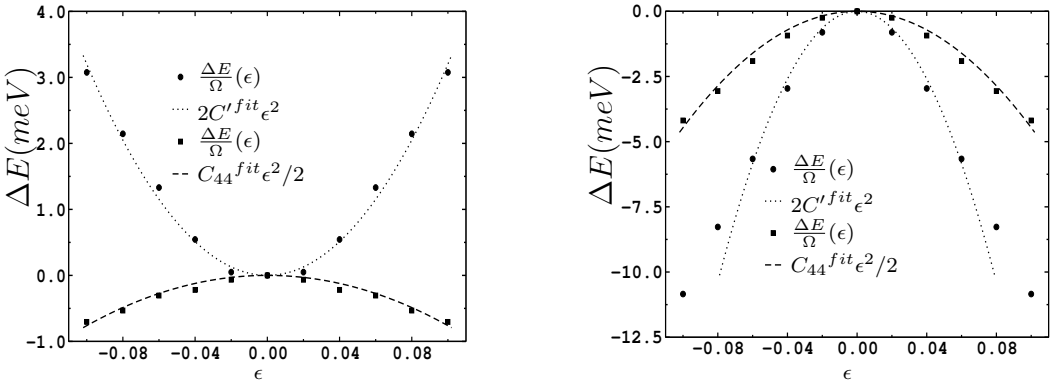

Fig. 4.6: *Calculated (dots) and fitted (line) values for the energy density as a function of strain ϵ for the monoclinic (C_{44}) and tetragonal (C') modulus of $W - Th$ assembled in $B2$- (left) and $L1_2$-structure (right)*

or C' have negative values [BK54].

4.2 Unrelaxed vacancy formation energy of Tungsten and Thorium

It's a matter of common knowledge, that point defects predominantly influence the thermodynamic and kinetic behaviour of metals. In this respect, the most important quantity seems to be the vacancy formation energy E_{vf}, as its value determines the equilibrium concentration of vacancies in bulk metal

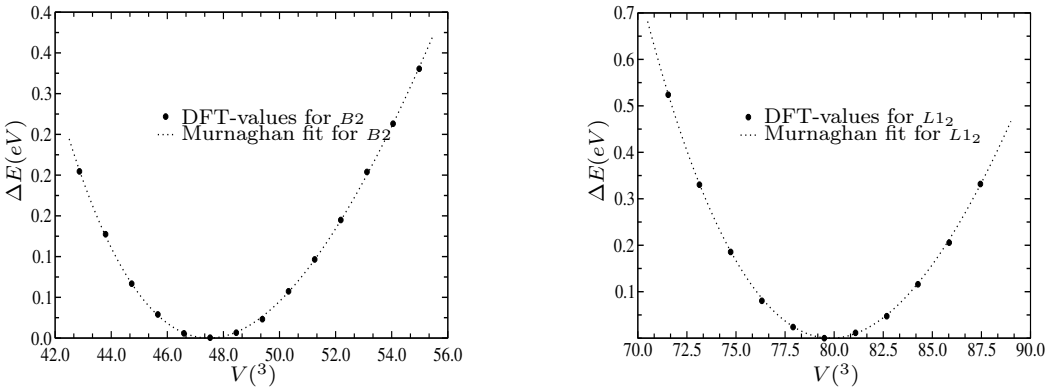

Fig. 4.7: *Calculated (dots) and fitted (line) values for total energy differences as a function of volume V of the $B2$- (left) and $L1_2$-unit cell (right).*

	V_0(Å^3)	B(GPa)	B'	C_{44}(GPa)	C'(GPa)
$L1_2$	79.834	166.3510	3.3954	−143.0143	−129.9582
$B2$	47.476	119.3696	5.0507	−24.4074	25.6577

Table 4.4: *Calculated values for $L1_2$ and $B2$: the equilibrium unit cell volume (V_0), bulk modulus (B), its pressure derivative B' and the remaining elastic constants (C_{44}, C')*

and contributes to the self-diffusion coefficient in the monovacancy mechanism, which is the main diffusion process at least in close-packed metals, but also in, e.g. bcc-Fe [FBEF93]. The activation energy for self-diffusion is calculated as the sum of vacancy formation energy and of the migration energy of the vacancy E_{vm}. The equilibrium concentration $c(T)$ of vacancies at temperature T is given as

$$c(T) \propto e^{-E_{vf}/(k_B T)} . \tag{4.14}$$

A similar expression holds for the self diffusion coefficient $D(T)$

$$D(T) \propto e^{-(E_{vf}+E_{vm})/k_B T} . \tag{4.15}$$

Experimentally the vacancy properties are very difficult to obtain, because very pure samples and a small concentration of thermal vacancies are required for reliable results. This is one reason for the fact, that the experimentally available data for tungsten and even more for thorium vary a lot [Sch87, KJBP84, SCPS75].

Later we will deal with diffusion phenomena of Th in W in more detail. Due to its importance for diffusion processes in metals, we used the FLAPW

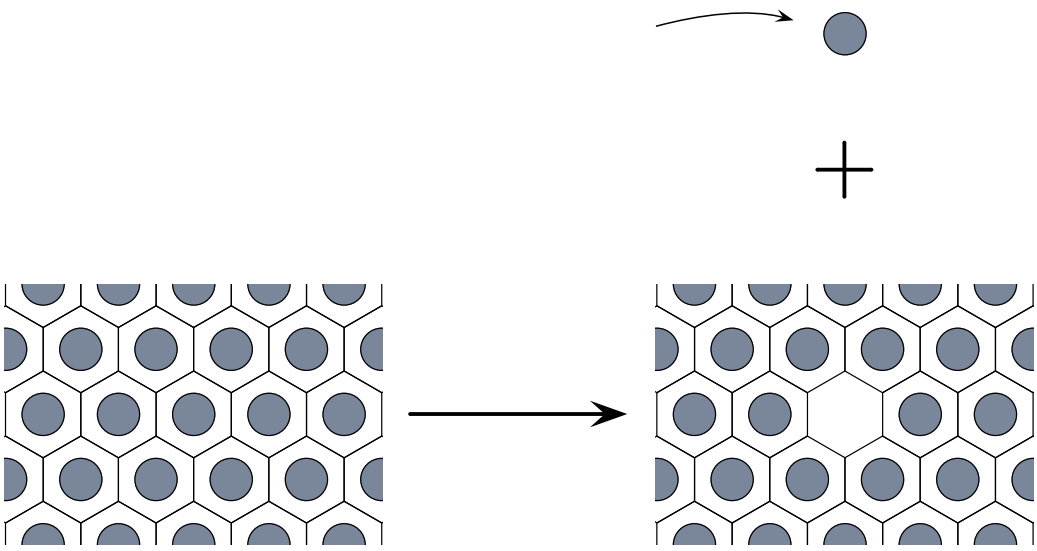

Fig. 4.8: *Schematic illustrating the geometry of a supercell used to evaluate the vacancy formation energy. The left side depicts an undisturbed lattice, whereas on the right the vacancy and, to keep the total number of atoms constant, an additional free atom.*

method to calculate the *un-relaxed vacancy formation energy* E_{vf}. This energy will be used to fit interatomic potentials. For the calculations we used a $2 \times 2 \times 2$-unit cell with the equilibrium lattice constants, $a_0 = 3.183$ for W and $a_0 = 5.087$ for Th, respectively. The unit cells therefore contain $N = 15$ $(bcc - W)$ and $N = 31$ $(fcc - Th)$ atoms. The vacancy formation energy E_{vf} (at $T = 0K$) is defined as the energy required to create a vacancy in the bulk. For a supercell of N atoms, E_{vf} is given by

$$E_{vf} = E(N-1) - \frac{N-1}{N} E(N) \tag{4.16}$$

where $E(N-1)$ is the total energy of the supercell containing $N-1$ atoms and a single vacancy, and $E(N)$ is the total energy of the bulk supercell containing N atoms. For a sketch of a supercell containing a vacancy see Fig. 4.8.

In our case, no atomic relaxations were considered. Atomic relaxations have the effect of reducing E_{vf}. There are two contributions to this relaxation energy. First, there is a relaxation associated with the overall volume change, a feature that can be exploited to determine the concentration of vacancies in real crystals. This effect could be captured in the calculations by allowing the supercell parameters to enter the calculation as a dynamical degree of

	SG	R_{MT} ()	E_{cut}^{wf} (Ry)	#k (BZ)	l_{wf}	l_{pot}	E_{cut}^{pot} (Ry)	LO
W(VF)	$P432$ 1b,3c,3d,8g	1.27	11.11	625	12	5	144.0	5s, 5p 4f
Th(VF)	$P432$ 1b,3c,3d,12i,12j	1.58	7.11	800	12	6	144.0	6s, 6p

Table 4.5: *Converged FLAPW parameters used for the calculation of the un-relaxed vacancy formation energy of W and Th.*

freedom. However, there are also local atomic relaxations in the vicinity of a vacancy. DFT calculations show [Phi01] that $\Delta E_{relax}/E_{vf} \approx 0.14$, revealing that the relaxation energy is only a minor fraction of the overall vacancy formation energy. For fitting purposes it is preferable not to use relaxed energies because the fitting procedure will become easier as will become evident in the next chapter. A comparison of E_{vf} of the present work with some values, already reported in literature, is given in Tab. 4.6.

	Present Work	Exp.	FP-LMTO (eV)	PP	PP-relaxed
W	3.85 (15)	4.6±0.8	3.53 (27)	3.68 (54)	3.44 (54)
Th	1.44 (31)	1.28±0.23	—	—	—

Table 4.6: *Comparison of some values of the vacancy formation energy E_{vf} of W and Th. The calculations in the present work are at fixed supercell size and without structural relaxation. The experimental data are from [Sch87] for W and from [KJBP84] for Th. The* Full Potential Linear Muffin Tin Orbital *calculations (FP-LMTO) are from [KPN95], the* Pseudo-Potential *calculations (PP) are those of [SWdG98]. All energies are given in eV*

We conclude this section with a remark on some empirical rules. There are two rules of thumb for the magnitude of the vacancy formation energies discussed in literature. First, a good estimate for E_{vf} should be derived from:

$$E_{vf} = -\frac{1}{3} E_{coh}\,, \tag{4.17}$$

where E_{coh} denotes the *cohesion energy* of the metal under consideration ($-8.9eV$ for W and $-6.2eV$ for Th). Another rule states that

$$E_{vf} = 10^{-3} T_m\, eV\, K^{-1} \tag{4.18}$$

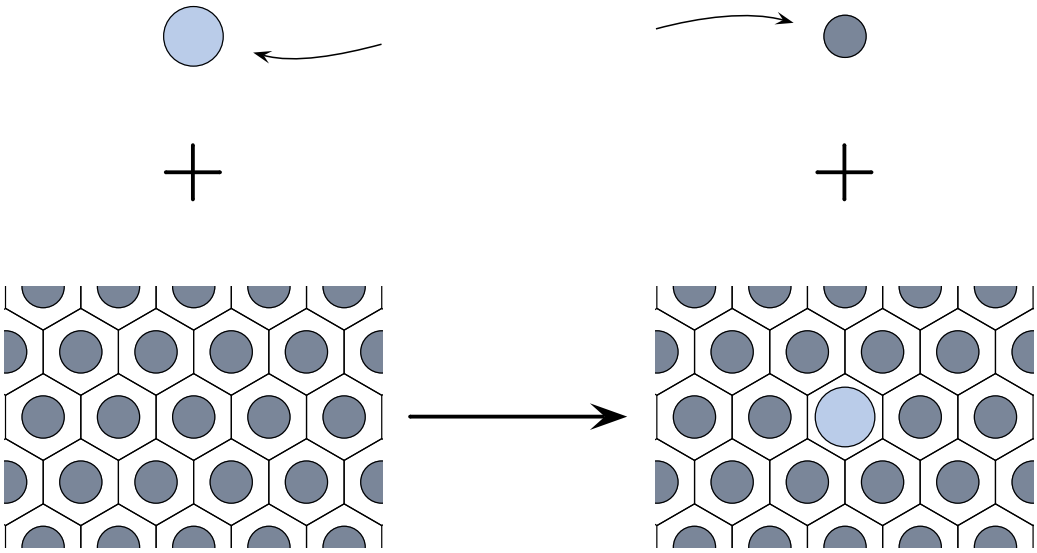

Fig. 4.9: *A sketch of the situations used for the definition of the* impurity formation energy E_{if}, *Eq.* (4.19). *Two situations were compared: a system consisting of an undisturbed tungsten bulk supercell together with a* free *thorium atom (left) and a supercell with one tungsten atom replaced by a thorium atom together with a* free *tungsten atom (right).*

with the melting temperature T_m of the elements ($3683K$ for W and $2020K$ for Th). Comparing our results or the experiments with these rules of thumb, we cannot state, that either one of the rules is preferable.

4.3 Un-relaxed impurity formation energy of Th in W

A furthermore very useful quantity, at least for the verification of the fitting process of interatomic potentials to follow, is the *un-relaxed impurity formation energy* E_{if}. A proper definition of E_{if} starts from a situation, where we have a disturbed tungsten bulk (N tungsten atoms interacting with one thorium atom) and an additional *free* tungsten atom and an undisturbed one *free* thorium atom and compare this total (potential) energy with the corresponding situation of is given by:

To properly define the *impurity formation energy* E_{if}, we decided to start from situations, which allow us to extract only the change in binding energy, which is just the energy, directly derivable from molecular dynamics calculations, as discussed later on. For this, the following two atomic situations as

sketched in Fig. 4.9, serve as starting point. The starting situation consists of a free tungsten atom in the presence of a disturbed tungsten bulk, i.e. with one tungsten atom substituted by a thorium atom. For E_{if}, the energy of the similar arrangement with a free thorium atom and an undisturbed tungsten bulk is to be subtracted:

$$\begin{aligned} E_{if} :=& E(N \cdot W, 1 \cdot Th) + E_f(W) - (E((N+1) \cdot W, 0 \cdot Th) + E_f(Th)) \\ =& E(N \cdot W, 1 \cdot Th) - (N+1) \cdot (E_f(W) + E_c(W)) + E_f(W) - E_f(Th) \\ =:& E_b(N \cdot W, 1 \cdot Th) - (N+1) \cdot E_c(W) \end{aligned} \tag{4.19}$$

where $E(N \cdot W, 1 \cdot Th)$ denotes the total energy of a cell containing N W-atoms and one Th-atom, $E_f(W)$, $E_f(Th)$ is the energy of a *free* W- or Th-atom, respectively. Together with the experimentally available cohesion energies, $E_c(W) = -8.9\text{eV}$ and $E_c(Th) = -6.2\text{eV}$, this allows us to calculate E_{if}. $E_b(N \cdot W, 1 \cdot Th)$ is the *binding energy* as given from e.g. interactomic potentials within molecular dynamics simulations. The cell energies $E(N \cdot W, 1 \cdot Th)$ and $E(N+1, 0)$ are determined for both, $N = 15$ and $N = 53$. These choices correspond to cells containing 2 and 3 bcc-unit cells in each space dimension, respectively. The lattice parameter of the supercell was chosen as a multiple of the equilibrium lattice constant of tungsten, i.e. $2 \cdot a_0$ or $3 \cdot a_0$, with $a_0 = 3.1834$. These supercells seem to be the smallest ones, to ensure that the interaction of the Th-atom with those of neighboring cells is negligible: as a rule of thumb, approximately three atomic layers in metals are necessary that neighboring Th-impurities do not affect each other and, therefore, can be treated as isolated, according to the very efficient electronic shielding of electrostatic charges in metals. Here, we have, depending on the situation, 3 or even 5 atomic layers between two Th-atoms. This should ensure that the electrostatic field of the Th-atoms do not interact.

For the calculation of $E((N+1) \cdot W, 0 \cdot Th)$, a cell containing only one symmetry equivalent atom would suffice in principle, as $E((N+1) \cdot W, 0 \cdot Th) = (N+1) \cdot E(W)$, where $E(W)$ denotes the energy per particle in tungsten bulk. As this is accompanied with a different set of FLAPW-basis functions as compared to a (symmetry broken) set, where we use a supercell containing 2 or 3 conventional bcc unit cells, we should expect different total energies per atom. In order to estimate this influence of the basis set chosen to the total energy per particle, we compared the energy per particle of the symmetry broken cases with 2 (five nonequivalent atoms per supercell) and 3 (eight nonequivalent atoms) bcc-unit cells in each space dimension, $E^{\{2\}}$ and $E^{\{3\}}$, with the corresponding energy per particle $E^{\{1\}}$ of a calculation using only one nonequivalent tungsten atom per supercell. The energies

such calculated are $E^{\{1\}} = -32332.236020\,\mathrm{Ry}$, $E^{\{2\}} = -32332.236138\,\mathrm{Ry}$ and $E^{\{3\}} = -32332.236140\,\mathrm{Ry}$. As all energies reported are well within the convergence criterion ($|\Delta E| \leq 10^{-4}\,\mathrm{Ry}$, where $|\Delta E|$ denotes the difference in total energy of the supercell between two subsequent iterations within a *SCF*-cycle), they can be considered equal, so that the influence of the broken symmetry in the calculations is negligible.

For E_{if}, we used the following variant of Eq. (4.19):

$$E_{if} = E(N \cdot W, 1 \cdot Th) - N \cdot E(W) - E(Th) - E_c(W) + E_c(Th) \qquad (4.20)$$

which is now entirely expressed in energies (apart from the experimentally derived *cohesion energies*, $E_c(W)$ and $E_c(Th)$, respectively) from *ab-initio* calculations. For Eq. (4.20), we made use of the relation $E_c(W) = E(W) - E_f(W)$ for tungsten and its equivalent for thorium. Finally, using Eq. (4.20), E_{if} is calculated to $E_{if}^{\{3\}} = 6.43\mathrm{eV}$ and $E_{if}^{\{2\}} = 6.80\mathrm{eV}$. The fact that both values are different, shows quite impressively, that the shielding of the conduction electrons is not that efficient as assumed. The assumption of isolated impurities in both cells is therfore not strictly valid. Strictly spoken, in order to get the impurity formation energy, one has to stretch the cells further on in order to increase the separation of thorium impurities in neighboring supercells. As in our case, E_{if} will only be used both, as a check and as a fitting parameter of the interatomic potentials for the system tungsten-thorium, $E_{if}^{\{3\}}$ should suffice for our purpose. As the values for E_{if} are huge and positive, it is clearly demonstrated, that, whenever one tries to generate thorium impurities in tungsten *bulk*, one has to tread this huge portion of additional energy, so that it is quite unlikely, that one would "see" a thermally induced thorium atom in tungsten bulk, i.e. the diffusional flux of thorium atoms in tungsten should be at most expected to be carried by lattice defects, a fact, which is experimentally also well-known [Lan34].

Chapter 5

Molecular Dynamics and Interatomic Interaction

Molecular Dynamics (MD) has a relatively long history starting with computations of classical phase space trajectories of a system of hard spheres [AW57, AW59]. Meanwhile, MD has evolved into an important and widely used theoretical tool that allows researchers in chemistry, physics and biology to model the detailed microscopic dynamical behavior of different types of systems, including gases, liquids, surfaces and clusters.

In a MD simulation, the classical equation of motion governing the microscopic time evolution of a many-body system are solved numerically subject to boundary conditions appropriate for the geometry or symmetry of the system. Thus, MD methodology is founded upon the basic principles of classical mechanics and can provide a window into the microscopic dynamical behavior of the individual atoms that make up a given system. From this information, the microscopic mechanisms of energy and mass transfer in chemical processes can be "observed", and dynamical properties such as rate constants and transport properties calculated. In addition to providing a microscopic dynamical picture, MD can also be employed as a means of sampling from a statistical mechanical ensemble and determining equilibrium properties. These properties include average thermodynamic quantities (pressure, temperature, volume, etc.), structure, and free energies along reaction paths.

A necessary ingredient to construct the phase space trajectory of a many-body system under consideration is a detailed knowledge of the interatomic interaction. Depending on the actual system of atoms, various models for this interaction are developed. An early, simple and yet powerful model is the two-parameter *Lennard-Jones* potential, which is a typical pairwise (or *two-body*) potential, i.e. depends only on the distance of two particles. Two-

body potentials suffer from some deficiencies, which make them unsuitable for metallic systems. A considerable improvement are the in the mid-eighties developed many-body (*Finnis-Sinclair-* or *Embedded-Atom-Model-*) potentials.

In this chapter, we first provide a short introduction of the MD methodology, together with a description of the implementation of the NPT-ensemble, i.e. an ensemble with constant particle number N, constant hydrostatic pressure P and constant temperature T, via the *Langevin-Piston-Method*, a method which incorporates deterministic and stochastic behavior. Furthermore, a detailed description of the *Embedded-Atom-Model* is presented afterwards.

5.1 Molecular Dynamics

Molecular Dynamics (MD) is employed to study the classical motion of a many-body system and extract from the dynamics experimental observables. As MD calculations provide a window into the detailed motion of individual atoms in a system, the microscopic mechanisms of energy and mass transfer can be investigated.

In order to introduce the basic principles of MD, we consider a system consisting of N particles moving under the influence of the internal forces acting between them. The spatial positions of the particles as functions of time will be denoted by $\mathbf{r}_1(t), \ldots, \mathbf{r}_N(t)$, and their velocities, $\mathbf{v}_1(t), \ldots, \mathbf{v}_N(t)$. If the forces, $\mathbf{F}_1(t), \ldots, \mathbf{F}_N(t)$, on the N particles are specified, then the classical motion of the system is determined by *Newton's second law*

$$m_i \ddot{\mathbf{r}}_i = \mathbf{F}_i, \tag{5.1}$$

where $m_1, \ldots, m_N$ are the masses of the particles. Since the forces on each particle is, in principle, a function of all of the N position variables, $\mathbf{F}_i = \mathbf{F}_i(\mathbf{r}_1, \ldots, \mathbf{r}_N)$, Eqs. (5.1) constitute in three spatial dimensions a set of $3N$ coupled second order differential equations. A unique solution to Eqs. (5.1) is obtained by choosing a set of initial conditions, $\{\mathbf{r}_1(0), \ldots, \mathbf{r}_N(0), \mathbf{v}_1(0), \ldots, \mathbf{v}_N(0)\}$. Newton's equations completely determine the full set of positions and velocities as functions of time and thus specify the *classical state* of the system at time t.

5.1.1 A Variable Cell Method

For the following it is useful to adopt the *Lagrangian* formulation of classical point mechanics. Consistent with *Hamiltons principle of stationary action*,

Eqs. (5.1) can be rewritten as

$$\frac{d}{dt}\left(\frac{\partial \mathcal{L}}{\partial \dot{\mathbf{r}}_i}\right) - \frac{\partial \mathcal{L}}{\partial \mathbf{r}_i} = \mathbf{0}, \tag{5.2}$$

the *Euler-Lagrange equations of motion* and $\mathcal{L} = \mathcal{L}(\{\mathbf{r}_i\}, \{\dot{\mathbf{r}}_i, \})$, the *Lagrange function*, defined through

$$\mathcal{L}(\{\mathbf{r}_i\}, \{\dot{\mathbf{r}}_i\}) = T(\{\mathbf{r}_i\}, \{\dot{\mathbf{r}}_i\}) - V(\{\mathbf{r}_i\}, \{\dot{\mathbf{r}}_i\}), \tag{5.3}$$

where we assumed, that the forces on the particles can be derived from the potential $V(\{\mathbf{r}_i\})$, i.e. $\mathbf{F}_i = -\frac{\partial V(\{\mathbf{r}_i\})}{\partial \mathbf{r}_i}$. T denotes the total kinetic energy of the system, i.e.

$$T(\{\mathbf{r}_i\}, \{\dot{\mathbf{r}}_i, \}) = \sum_{i=1}^{N} \frac{1}{2} m_i \dot{\mathbf{r}}_i \cdot \dot{\mathbf{r}}_i \,. \tag{5.4}$$

In order to circumvent the limitation of ordinary MD to the micro-canonical (NVE) ensemble, in which the number of particles, the volume and the total energy are conserved, one has to derive in some sense new equations of motion. The first proposal stems from H. C. Andersen [And80], who initialized with his work a number of possible generalizations and improvements for his set of equations of motion for an interacting N-particle system describing an isenthalpic-isobaric ensemble. Following Andersen's idea, M. Parrinello and A. Rahman [PR80] used scaled particle coordinates and velocities defined by $\mathbf{r}_i =: \mathbf{h}\mathbf{r}_i^s$ and $\mathbf{v}_i := \dot{\mathbf{r}}_i =: \mathbf{h}\mathbf{v}_i^s$, with $\mathbf{h} := (\mathbf{a}, \mathbf{b}, \mathbf{c})$ and $\mathbf{a}, \mathbf{b}, \mathbf{c}$ are the in general time dependent edges of the MD cell. The Lagrangian driving the system is assumed to be given through

$$\mathcal{L} := \sum_{i\alpha\beta} \frac{m_i}{2} (h_{\alpha\beta} \dot{r}_{i\beta}^s)^2 - V(\{\sum_{\beta} h_{\alpha\beta} r_{i\beta}^s\}) + \sum_{\alpha\beta} \frac{W_\beta}{2} \dot{h}_{\alpha\beta}^2 - P \det(h_{\alpha\beta}) \tag{5.5}$$

where P denotes the external pressure to be balanced. Latin indices count particles, i.e. $i = 1 \ldots N$, and greek ones correspond to the spatial degrees of freedom, i.e. $\alpha, \beta = 1 \ldots 3$. The corresponding equations of motion result in

$$m_i \ddot{\mathbf{r}}_i^s = \mathbf{h}^{-1} \mathbf{f}_i - m_i \mathbf{g}^{-1} \dot{\mathbf{g}} \mathbf{r}_i^s \tag{5.6}$$

$$W_\beta \ddot{h}_{\alpha\beta} = \sum_{\gamma} (\Pi_{\alpha\gamma} - P) \sigma_{\gamma\beta} \tag{5.7}$$

where $\sigma := (\mathbf{b} \times \mathbf{c}, \mathbf{c} \times \mathbf{a}, \mathbf{a} \times \mathbf{b})$, Π denotes the symmetrized stress tensor:

$$\mathbf{\Pi} := \frac{1}{\Omega} \sum_i (m_i (\mathbf{h}\dot{\mathbf{r}}_i^s)(\mathbf{h}\dot{\mathbf{r}}_i^s)^T + \mathbf{f}_i \mathbf{r}_i^T) \,, \tag{5.8}$$

$\Omega := det(\mathbf{h})$ is the volume of the MD cell and $\mathbf{g} := \mathbf{h}^T\mathbf{h}$. Here, we introduced two minor, yet important, generalizations to the original scheme: first, we associated with each box dimension a separate "box mass" W_β in order to respond independently to the box forces introduced with the stress tensor Eq. (5.8). These "box masses" W_β are additional degrees of freedom, which should be chosen carefully in order to enable the system to respond as quickly as possible to the external pressure and therefore to reach the equilibrium situation very fast, and also as slow as necessary for the trajectory generated to become as close as possible to the true one. The second generalization concerns the interatomic potential: in the original scheme, the authors assumed pair potentials, whereas the equations of motion, Eqs. (5.6) and (5.7), are more general, and permit for instance the widely used *embedded atom* potentials.

It is clear, that large W_β means a heavy, slow cell. In the limiting case, infinite W_β reverts to constant-volume dynamics. Whereas a small W_β means fast motion of the cell vectors. A thorough examination of the volume fluctuations results in a relation between the "box masses" W_β and the time scale of the fluctuations of the box dimensions (with period T_0) [NK83]:

$$T_0 = 2\pi \left(\frac{W_\beta}{3LB} \right) \tag{5.9}$$

where L denotes a typical length of the MD cell and B the bulk modulus of the system under consideration.

For the following, we restrict the dynamics to orthorhombic MD cells.

The equations of motion, Eqs. (5.6), (5.7) and (5.8), for the case of a orthorhombic cell (with cell dimensions $L_\alpha, (\alpha = 1 \ldots 3)$) reduce to:

$$m_i \ddot{r}^s_{i\alpha} = \frac{f_{i\alpha}}{L_\alpha} - 2m_i \frac{\dot{L}_\alpha}{L_\alpha} \dot{r}^s_{i\alpha} \tag{5.10}$$

$$W_\alpha \ddot{L}_\alpha = \frac{\Omega}{L_\alpha} \left(\Pi_{\alpha\alpha} - P \right) \tag{5.11}$$

and

$$\Pi_{\alpha\alpha} = \frac{1}{\Omega} \sum_i \left(m_i (L_\alpha \dot{r}^s_{i\alpha})^2 + f_{i\alpha} (L_\alpha r^s_{i\alpha}) \right), \tag{5.12}$$

respectively.

Completing, the Lagrangian generating Eqs. (5.10), (5.11) and (5.12) is

given through:

$$\mathcal{L}(\{r^s_{i\alpha}\},\{\dot{r}^s_{i\alpha}\},\{L_\alpha\},\{\dot{L}_\alpha\}) := \sum_{\substack{i=1\ldots N\\ \alpha=1\ldots 3}} \frac{m_i}{2}(L_\alpha \dot{r}^s_{i\alpha})^2 - V(\{L_\alpha r^s_{i\alpha}\}) + \sum_{\alpha=1\ldots 3} \frac{W_\alpha}{2}\dot{L}^2_\alpha - P\prod_{\alpha=1\ldots 3} L_\alpha \quad (5.13)$$

In unscaled coordinates, this set of equations results in:

$$m_i \ddot{r}_{i\alpha} = f_{i\alpha} + m_i \frac{\ddot{L}_\alpha}{L_\alpha} r_{i\alpha} \quad (5.14)$$

$$W_\alpha \ddot{L}_\alpha = \frac{\Omega}{L_\alpha}(\Pi_{\alpha\alpha} - P) \quad (5.15)$$

with

$$\Pi_{\alpha\alpha} = \frac{1}{\Omega}\sum_i \left(m_i(\dot{r}_{i\alpha} - \frac{\dot{L}_\alpha}{L_\alpha} r_{i\alpha})^2 + f_{i\alpha} r_{i\alpha} \right) \quad , \quad (5.16)$$

and

$$\mathcal{L}(\{r_{i\alpha}\},\{\dot{r}_{i\alpha}\},\{L_\alpha\},\{\dot{L}_\alpha\}) := \sum_{\substack{i=1\ldots N\\ \alpha=1\ldots 3}} \frac{m_i}{2}(\dot{r}_{i\alpha} - \frac{\dot{L}_\alpha}{L_\alpha} r_{i\alpha})^2 - V(\{r_{i\alpha}\}) + \sum_{\alpha=1\ldots 3} \frac{W_\alpha}{2}\dot{L}^2_\alpha - P\prod_{\alpha=1\ldots 3} L_\alpha \quad (5.17)$$

In principle, we were now in a position to perform molecular dynamics calculations with Eqs. (5.14, 5.15 and 5.16) in a NPH-ensemble, i.e. constant particle number, pressure and *enthalpy* [PR81]. One can easily construct the corresponding Hamiltonian following the usual rules of mechanics. Since the system is not subject to time dependent external forces this is a constant of motion:

$$\mathcal{H} := \sum_{\substack{i=1\ldots N\\ \alpha=1\ldots 3}} \frac{m_i}{2} v^2_{i\alpha} + V(\{r_{i\alpha}\}) + \sum_{\alpha=1\ldots 3} \frac{W_\alpha}{2}\dot{L}^2_\alpha + P\Omega\,. \quad (5.18)$$

For a system in equilibrium at temperature T, the kinetic box degrees of freedom contribute an energy $3/2k_BT$ and the particle ones $3N/2k_BT$ to the total energy. Thats why to an accuracy of $1:N$ the constant of motion $\mathcal{H}$ is nothing but the *enthalpy* H:

$$H := E + P\Omega\,, \quad (5.19)$$

with

$$E := \sum_{\substack{i=1\ldots N \\ \alpha=1\ldots 3}} \frac{m_i}{2} v_{i\alpha}^2 + V(\{r_{i\alpha}\})\,. \tag{5.20}$$

Unfortunately, a peculiarity of these equations of motion prevents us from its implementation, as will be shown and discussed in the next section.

5.1.2 The Langevin Piston

A drawback with the variable cell method just introduced arises from Eq. (5.11) being a second order differential equation. The resulting decay of the volume fluctuations may not be monotonic, but instead the system may contain a "ringing" with a frequency proportional to $\sqrt{1/W_\beta}$ [NK83] (see also Eq. (5.9)). The system dynamics therefore depends on the "piston masses" W_β. In order to eliminate these unwanted and unphysical behavior, Berendsen and co-workers developed a constant pressure technique, the *weak coupling pressure control algorithm*, which also treated the volume as a dynamical variable, but their equation describing the volume evolution was first order [BPvG$^+$84] and therefore suppresses ringing of the system. In both Parrinello-Rahman's and Berendsen's method, the control of system's temperature is optional (depending on the choice of isothermal (NPT) or isenthalpic (NPH) ensemble). On the contrary, a constant temperature method must be used with the weak coupling pressure control algorithm. As can be shown [FZPB95], the motion of the piston degree of freedom is dissipative, and therefore the energy dissipated by the piston must be returned to the system or else the temperature of the particles decreases over the course of the simulation. To maintain a constant temperature, Berendsen and coworkers proposed a weak coupling temperature control algorithm where a uniform velocity rescaling is applied [BPvG$^+$84]. Unfortunately, this simple rescaling procedures do not generate a proper (NPH) or (NPT) ensemble [Hoo85, Nos84]. An easy to implement, yet powerful method was first proposed by Schneider and Stoll [SS78] and later on by Andersen [And80]. The basic idea was to consider equations similar to Langevin's equation for Brownian dynamics for some additional degrees of freedom. Further improvements for generating trajectories from a (NPT) ensemble applicable for molecular dynamics simulations were presented by Feller *et. al.* [FZPB95]. Within this scheme, which is also based on Andersen's extended system method, the deterministic equations of motion for the piston degrees of freedom are replaced by a Langevin equation. They argued that a sensible choice of the collision frequency eliminates the unphysical "ringing" of the volume associated with the piston mass. So, undesirable dependencies of the system properties of the

mass of the piston are avoided. Kolb *et. al.* [KD99] extended this method in thermostatting each particle degree of freedom individually. For this reason, local instabilities arising from discretization errors, are efficiently corrected for, without spreading throughout the system.

In this work we slightly generalized the idea of Kolb *et. al.* [KD99] in replacing the canonical equations of motion of *each* degree of freedom in the system, including the three box dimensions, by a Langevin stochastic process. Within this scheme the equations of motion, Eq. (5.14) and Eq. (5.15) are changed to:

$$m_i \ddot{r}_{i\alpha} = f_{i\alpha} + m_i \frac{\ddot{L}_\alpha}{L_\alpha} r_{i\alpha} - m_i \gamma_0 \dot{r}_{i\alpha} + m_i \sqrt{2D_i}\, \Gamma(t) \tag{5.21}$$

$$W_\alpha \ddot{L}_\alpha = \frac{\Omega}{L_\alpha} \left(\Pi_{\alpha\alpha} - P\right) - W_\alpha \gamma_B \dot{L}_\alpha + W_\alpha \sqrt{2D_\alpha}\, \Gamma(t)\,, \tag{5.22}$$

where the stochastic force $\Gamma(t)$ is characterized as *Gaussian White Noise*:

$$\langle \Gamma(t) \rangle = 0\,, \tag{5.23}$$

$$\langle \Gamma(t)\Gamma(t') \rangle = \delta(t - t')\,. \tag{5.24}$$

γ_0 and γ_B are friction coefficients which have to be chosen carefully for the particles as well as for the box dimensions. The diffusion constants D_i and D_α are determined by applying a form of the *Fluctuation-Dissipation Theorem*, see Appendix E:

$$D_\alpha := \frac{k_B T}{W_\alpha} \gamma_B \qquad , \qquad D_i := \frac{k_B T}{m_i} \gamma_0\,. \tag{5.25}$$

Unfortunately, Eqs. (5.21 and 5.22) exhibit *non-markovian* character. However, the markovian character of these equations can be reestablished by introducing two additional stochastic variables (the velocities $v_{i\alpha}$ of the particles and V_α of the box dimensions):

$$\dot{r}_{i\alpha} = v_{i\alpha} \tag{5.26}$$

$$m_i \dot{v}_{i\alpha} = f_{i\alpha} + m_i \frac{\dot{V}_\alpha}{L_\alpha} r_{i\alpha} - m_i \gamma_0 v_{i\alpha} + m_i \sqrt{2D_i}\, \Gamma(t) \tag{5.27}$$

and

$$\dot{L}_\alpha = V_\alpha \tag{5.28}$$

$$W_\alpha \dot{V}_\alpha = \frac{\Omega}{L_\alpha} \left(\Pi_{\alpha\alpha} - P\right) - W_\alpha \gamma_B V_\alpha + W_\alpha \sqrt{2D_\alpha}\, \Gamma(t)\,. \tag{5.29}$$

To solve the original second order equations of motion, the implementation of the usually very efficient *six'th order predictor-corrector scheme* as discussed by Gear [Gea66, Gea71] can not be used, because of its tendency to "wipe out" the strong "oscillations" of the force term due to the presence of noise. In order to circumvent this problem, a suitable integration scheme was implemented, closely resembling the well-known *Velocity Verlet Algorithm*, for details see Appendix E.

An integration step for a small time step δt for the particles is then given by:

$$r_{i\alpha}(t+\delta t) = r_{i\alpha}(t) + c_{01}v_{i\alpha}(t)\delta t + c_{02}f_{i\alpha}(t)\delta t^2 + \delta r_{i\alpha}\,, \tag{5.30}$$

$$v_{i\alpha}(t+\delta t) = c_{00}v_{i\alpha}(t) + c_{02}f_{i\alpha}(t+\delta t)\delta t + (c_{01}-c_{02})f_{i\alpha}(t)\delta t + \delta v_{i\alpha}\,. \tag{5.31}$$

Here, we used the shorthand notations:

$$c_{00} := e^{-\gamma_0\delta t} \qquad c_{01} := \frac{1-c_{00}}{\gamma_0\delta t} \qquad c_{02} := \frac{1-c_{01}}{\gamma_0\delta t} \tag{5.32}$$

$\delta r_{i\alpha}$ and $\delta v_{i\alpha}$ are random numbers with a joint probability distribution $P(\delta r_{i\alpha}, \delta v_{i\alpha})$:

$$P(\delta r_{i\alpha}, \delta v_{i\alpha}) = \frac{1}{2\pi\sqrt{|det(\mathbf{C_i})|}} e^{-\frac{(\delta r_{i\alpha},\delta v_{i\alpha})\mathbf{C_{i\alpha}}^{-1}\binom{\delta r_{i\alpha}}{\delta v_{i\alpha}}}{2}}\,, \tag{5.33}$$

a bivariate Gaussian distribution with *covariance matrix* (for *each* particle) $\mathbf{C_i}$:

$$\mathbf{C_i} := D_i \begin{pmatrix} \frac{2\gamma_0\delta t - 3 + 4e^{-\gamma_0\delta t} - e^{-2\gamma_0\delta t}}{\gamma_0^3} & \frac{1-2e^{-\gamma_0\delta t}+e^{-2\gamma_0\delta t}}{\gamma_0^2} \\ \frac{1-2e^{-\gamma_0\delta t}+e^{-2\gamma_0\delta t}}{\gamma_0^2} & \frac{1-e^{-2\gamma_0\delta t}}{\gamma_0} \end{pmatrix}. \tag{5.34}$$

A convenient way to accomplish the generation of random variables (for a short introduction of random variables and stochastic processes, see Appendix B) $\delta r_{i\alpha}$ and $\delta v_{i\alpha}$ with joint probability Eq. (5.33) is given by a straightforward *Cholesky Decomposition* of the covariance matrix $\mathbf{C_i}$. Details can be found in Appendix E.

But, why do the trajectories generated with the equations of motion, Eq. (5.21) and (5.22), really represent a (NPT) ensemble? A partial answer to this question is given with the *uniqueness-theorem for "linear" thermal baths* [Rei01], which states, that for any "linear" thermal bath, the form of the dissipation term and the bath temperature uniquely fix all statistical properties of the noise, without referring to any microscopic details of the bath. As a consequence, any linear thermal bath can be imitated by a harmonic oscillator bath model and the noise statistics is always Gaussian. A

straightforward calculation starting from a particle coupled linearly to a oscillator bath leads to the *generalized nonlinear Langevin equation* [Cha87], first derived by R. Zwanzig [Zwa61] (for a short derivation see Appendix D). The *Kramers-Moyal expansion* of the transition probability of the process generated by the generalized nonlinear Langevin equation can be shown to end after second order, meaning that the n-th Kramers-Moyal coefficient $D^{(n)}$ is identical to zero for $n \geq 3$. In this case, the Kramers-Moyal expansion is identical to the *Fokker-Planck equation*. The stationary solution of the Fokker-Planck equation can be identified with the phase space distribution function. It's an easy task to show, that the distribution function for the (NPT) ensemble is indeed a solution of the Fokker-Planck equation. The trajectories therefore really represent the (NPT) ensemble [KD99].

For the implementation of this scheme, one is faced with the problem to generate Gaussian noise. This is efficiently arranged with utilization of the *Box-Mueller algorithm* [Knu69, FGRV88], see also Appendix C.

Solving the equations of motions as presented above provides an efficient scheme for producing particle and box trajectories of a (NPT) ensemble. Yet, one is faced with a remaining challenge: as we want to describe metallic systems, the application of a two-body interaction scheme is not possible without neglecting important contributions to the total energy of a many body system. To overcome this problem, we will describe an interaction scheme, the *Embedded Atom Method* (EAM), in the next section which resolves most of the drawbacks of the conceptionally simpler two body potentials without tremendously increasing the computational needs. But before, as we are also interested in free energy and free enthalpy differences, we introduce some subtleties connected to "computing" such quantities in the next subsection.

5.1.3 Free Enthalpy and the Overlapping Distribution Method

According to the second law of thermodynamics, the equilibrium of a closed system with internal energy E, volume V, and particle number N, is characterized by a maximum of its entropy S. From this, it is easy to derive the corresponding equilibrium conditions for systems that can exchange heat, volume or particles with a reservoir. In particular, if a system is in contact with a heat bath, such that its temperature T, volume V and particle number N is fixed, than the *Helmholtz Free Energy* (or simply *Free Energy*) $A(N, V, T) \equiv E - TS$ is at a minimum in equilibrium. Analogously, for a system of N particles at constant temperature T and pressure P, the *Gibbs Free Energy* (or *Free Enthalpy*) $G(N, P, T) \equiv A + PV$ is at a minimum. Usu-

ally, under laboratory conditions, we can observe differences in $G(N, P, T)$. In fact, phase diagrams are a direct consequence of these measurements. On a computer, free enthalpy differences can be determined only by a procedure analogous to calorimetry, i.e., by establishing a reversible path between the system of interest and some reference system of known free enthalpy. This *computer calorimetry* enables one to study a much wider class of reference systems and reversible paths, as one is not restricted to adopt "realistic" situations, i.e. changing only the in the laboratory accessible thermodynamic variables, but one can also alter the hamiltonian of the systems of interest. It is the latter, which we will make use of, extensively. There are several methods available to compute free energy or free enthalpy differences. One widely used method is the *thermodynamic integration* [Fre85, BD89] or its successor, the *Adiabatic Switching Method* [WR90], which resides on the fact, that if an ergodic Hamiltonian is changing slowly in time, its energy shell is an adiabatic invariant: even though the energy changes, an initial surface of constant energy is mapped into a continuous family of surfaces, each of which is also of constant energy. This enables a direct dynamical calculation of the entropy, and therefore also the corresponding free energies of the systems under consideration. However, the results from these methods rely heavily on the proper choice of a "switching function", which is *a priori* unknown. Another idea to calculate the configurational entropy, and with it the free energy differences, of at least simple fluids starts from an entropy expansion in one- and two-body contributions, and now includes three-body contributions as well [BE89, BE90], which offers some technical difficulties and which are not easy to overcome. From a computational point of view, much more easy to handle is the *Overlapping Distribution Method* [Ben76].

For an instructive introduction, it is useful to define the following (normalized) distributions $f_{\alpha/\alpha'}(\Delta)$ to get an enthalpy difference Δ along a trajectory of a MD course with potential energy $\tilde{U}_\alpha$ or $\tilde{U}_{\alpha'}$, respectively:

$$f_{\alpha/\alpha'}(\Delta) := \left\langle \delta(\Delta - (\tilde{U}_\alpha - \tilde{U}_{\alpha'})) \right\rangle_{\alpha/\alpha'} , \tag{5.35}$$

where with $\tilde{U}_\alpha$ we introduced a shorthand notation for:

$$\tilde{U}_\alpha := U_\alpha - P\Omega , \tag{5.36}$$

with a parameter dependent potential energy U_α, pressure P and (instantaneous) volume of the simulation cell Ω. Free enthalpy differences between systems driven by potentials with two different parameters α and α' are given by:

$$\Delta G := G_\alpha - G_{\alpha'} = -k_B T \cdot \ln\left(\frac{Q_\alpha}{Q_{\alpha'}}\right) \tag{5.37}$$

where Q_α and $Q_{\alpha'}$ denote the corresponding partition functions

$$Q_\alpha \propto \int e^{-(\sum_i \frac{p_i^2}{2m_i}+\tilde{U}_\alpha)/k_BT}\, d^{3N}r\, d^{3N}p\, d\Omega \tag{5.38}$$

for a N-particle system. Together with Eq. (5.35), ΔG can be calculated by:

$$\Delta G = -k_BT \cdot \ln\left(\frac{f_{\alpha'}(\Delta)}{f_\alpha(\Delta)} e^{-\beta\Delta}\right). \tag{5.39}$$

and, as usual, $\beta = \frac{1}{k_BT}$.

With $\langle \ldots \rangle_{\alpha/\alpha'}$ we denote the averaging over the trajectory generated with potential energy U_α or $U_{\alpha'}$, respectively. Eq. (5.39) shows, that each point in the overlap region of f_α and $f_{\alpha'}$ results in an estimation of the free enthalpy difference, hence the name *Overlapping Distribution Method*.

A subtle refinement of this method, and the one excessively used in this work, is the *Acceptance Ratio Method* [Ben76]. For this, we start from the following identity:

$$\begin{aligned}
\Delta G &:= -k_BT \cdot \ln\left(\frac{q_\alpha}{q_{\alpha'}} \cdot \frac{\int w(\{\mathbf{r}_i\},\Omega) e^{-\beta(\tilde{U}_\alpha+\tilde{U}_{\alpha'})}\, d^{3N}r\, d\Omega}{\int w(\{\mathbf{r}_i\},\Omega) e^{-\beta(\tilde{U}_\alpha+\tilde{U}_{\alpha'})}\, d^{3N}r\, d\Omega}\right) \\
&= -k_BT \cdot \ln\left(\frac{\left\langle w(\{\mathbf{r}_i\},\Omega) e^{-\beta\tilde{U}_\alpha}\right\rangle_{\alpha'}}{\left\langle w(\{\mathbf{r}_i\},\Omega) e^{-\beta\tilde{U}_{\alpha'}}\right\rangle_{\alpha}}\right) \\
&= -k_BT \cdot \ln\left(\frac{\frac{1}{n_{\alpha'}}\sum_j^{n_{\alpha'}} w(\{\mathbf{r}_i(t_j)\},\Omega(t_j)) e^{-\beta\tilde{U}_\alpha(\{\mathbf{r}_i(t_j)\},\Omega(t_j))}}{\frac{1}{n_\alpha}\sum_j^{n_\alpha} w(\{\mathbf{r}_i(t_j)\},\Omega(t_j)) e^{-\beta\tilde{U}_{\alpha'}(\{\mathbf{r}_i(t_j)\},\Omega(t_j))}}\right)
\end{aligned} \tag{5.40}$$

where $q_\alpha \propto \int e^{-(\tilde{U}_\alpha)/k_BT}\, d^{3N}r\, d\Omega$ denotes the *configurational* part of the partition function and $w(\{\mathbf{r}_i\},\Omega)$ is an arbitrary function of particle coordinates and cell volume. In the last line of Eq. (5.40) we replaced the integral over the configurations with a discrete averaging over (statistically independent) configurations taken along a trajectory at various instances of time t_j. Of course, this requires the *ergodicity theorem* to be valid. n_α denotes the number of configurations used for averaging. For each choice of $w(\{\mathbf{r}_i\},\Omega)$ we get an estimation for the free energy difference ΔG. Eq. (5.39) can be considered as a special case of Eq. (5.40) with $w := \delta(\Delta - (\tilde{U}_\alpha - \tilde{U}_{\alpha'}))e^{\beta\tilde{U}_\alpha}$. Minimization of the variance of Eq. (5.40) with respect of $w(\{\mathbf{r}_i\},\Omega)$ together with the constraint of a likewise arbitrary normalization constant, which is chosen to be:

$$\int w(\{\mathbf{r}_i\},\Omega) e^{-\beta(\tilde{U}_\alpha+\tilde{U}_{\alpha'})}\, d^{3N}r\, d\Omega = const. \tag{5.41}$$

yields:

$$w(\{\mathbf{r}_i\},\Omega) \propto \big(\frac{q_\alpha}{n_\alpha} e^{-\beta\tilde{U}_{\alpha'}} + \frac{q_{\alpha'}}{n_{\alpha'}} e^{-\beta\tilde{U}_\alpha}\big)^{-1} \tag{5.42}$$

at least for sufficiently large samples, such that the *Central Limit Theorem* can be applied. Inserting Eq. (5.42) into Eq. (5.40) finally yields:

$$\Delta G = -k_B T\big[\ln\big(\tfrac{\sum_{\alpha'} f(\beta\tilde{U}_\alpha - \beta\tilde{U}_{\alpha'} - C)}{\sum_\alpha f(\beta\tilde{U}_{\alpha'} - \beta\tilde{U}_\alpha + C)}\big) - C + \ln\tfrac{n_\alpha}{n_{\alpha'}}\big] \tag{5.43}$$

where we introduced the yet undetermined constant C:

$$C := \ln\frac{q_{\alpha'} n_\alpha}{q_\alpha n_{\alpha'}} \tag{5.44}$$

and the *Fermi function* $f(x) := (1+e^x)^{-1}$ for brevity. On the other hand, this choice of C means also:

$$\Delta G = -k_B T(\ln\tfrac{n_\alpha}{n_{\alpha'}} - C)\,. \tag{5.45}$$

Clearly, Eq. (5.43) and Eq. (5.45) are consistent only if

$$\sum_{\alpha'} f(\beta\tilde{U}_\alpha - \beta\tilde{U}_{\alpha'} - C) = \sum_\alpha f(\beta\tilde{U}_{\alpha'} - \beta\tilde{U}_\alpha + C)\,. \tag{5.46}$$

In principle, the set of (nonlinear) equations, Eqs. (5.43) and (5.45), have to be iterated until self-consistency is arrived, because both right hand sides depend via C on the quantity $\ln\frac{q'_\alpha}{q_\alpha}$ which is proportional to ΔG, the very quantity which should be calculated. In practice, although, C will be treated as an adjustable parameter, that is varied, until Eq. (5.46) is satisfied. ΔG then follows immediately from Eq. (5.45).

5.2 The Embedded Atom Method

In principle, from the standpoint of microscopic theories, the computation of the total potential energy of a many-body system (in this respect also called *configurational energy*) requires a description not only in terms of the atomic positions but also in terms of the electronic degrees of freedom, as is evident from the considerations in chapter 2. So, a proper starting point for deriving an atomic interaction scheme should be the total many-body Hamiltonian, Eq. (2.1), and trying to remove the electronic degrees of freedom from the total energy of the system. This means that the exact total energy is replaced by an approximate surrogate via:

$$E_{exact}(\{\mathbf{R}_i\}) \to E_{approx}(\{\mathbf{R}_i\}) \tag{5.47}$$

where $\{\mathbf{R}_i\}$ denotes the set of atomic positions. Perhaps the simplest example of simplifying the total energy is via an approximation of the form:

$$E_{approx}(\{\mathbf{R}_i\}) = \frac{1}{2}\sum_{ij} V(R_{ij})\,. \tag{5.48}$$

$V(R)$ is some properly chosen function, the *pair potential*, and $R_{ij} := |\mathbf{R}_i - \mathbf{R}_j|$. Unfortunately, the pair potential ansatz suffers from some serious drawbacks especially for transition metals:

- Transition metals rarely obey the *Cauchy condition* [Car90]. For cubic crystals *Cauchy's condition* can be summarized as:

  $$C_{12} = C_{44}$$

  which is a direct consequence of a central pair potential assumption [BK54]. This relation is often violated by 30% or more within transition metal systems.

- The *cohesion energy per atom* E_c^a (equals the energy difference of the bonded and the free atom state per atom) depends **non-linearly** on the coordination number Z. From tight-binding arguments one can conclude an approximately square root dependency [FS84]:

  $$E_c^a \sim \sqrt{Z}$$

  whereas a description via central pair potentials and nearest-neighbor interaction assumed a **linear** dependency of E_c^a on Z would be predicted.

- As a rule of thumb, the vacancy formation energy is $E^{vf} \approx E_c^a/2$ for most transition metals, whereas the pair potential assumption implies $E^{vf} \approx E_c^a$.

These problems are lifted, among others [FS84, JNP87, ETP86, TB85, RGL89], within the nowadays widely used *embedded atom method* (EAM) [DB84], which will be briefed in the next section.

5.2.1 The Cohesion Energy for Pure Elements

Jacobsen *et al.* [JNP87] discussed the derivation of the binding energy in their *effective medium theory* based on the ansatz of the total charge density

$$\rho(\mathbf{r}) = \sum_i \Delta\rho_i(\mathbf{r})\,, \tag{5.49}$$

i.e. as a superposition of induced densities $\Delta\rho_i(\mathbf{r})$ centered at sites i, and the variational principle of density functional theory. The result is that the binding energy is given by

$$E_c = \sum_i E_i(\bar{\rho}_i) + E_{ov} + E_{1e}\,. \tag{5.50}$$

$E_i(\bar{\rho}_i)$ is the energy of embedding the ith atom in a neutral sphere in which the average electron density is $\bar{\rho}_i$. The embedding density $\bar{\rho}_i$ is defined by the charge density tails of the neighboring atoms. The second term, E_{ov}, is called the overlap energy. It describes the electrostatic repulsion that occurs when neutral spheres are forced to overlap. Finally, E_{1e} is called the one-electron energy. This term becomes important in cases where the local density of states in the metal is not free-electron like. Thus it seems reasonable to neglect this term for sp-bonded (*simple*) metals but not for transition metals. In the case of transition metals, it is more sensible to start with a tight binding model of the solid, and to abandon the concept of embedding the atom in a homogeneous electron gas. The EAM [DB84] is an empirical implementation of Eq. (5.50) for the binding energy of the metal as a sum of two terms. Unfortunately on the first sight, they neglected in their ansatz the one-electron energy which is of utmost importance for the description of transition metal systems. The EAM-ansatz for the cohesion energy of an assembly of N atoms therefore reads[DB84]

$$E_c = \sum_i F_i \left(\sum_{j(\neq i)} \Delta\rho_j(R_{ij}) \right) + \frac{1}{2} \sum_{\substack{i,j \\ (j\neq i)}} \phi_{ij}(R_{ij}) \tag{5.51}$$

where F is the embedding energy, $\Delta\rho_j$ is a spherically averaged atomic density, and ϕ_{ij} is an electrostatic two-body potential. The background density for each atom is determined by evaluating at its nucleus the superposition of atomic density tails from the surrounding atoms. Indeed, the theoretical justification [Daw89] of Eq. (5.51) from DFT starts with an electron density in the solid, which is not far from a superposition of single-atom densities. This seems to be well-justified at least for early and late transition metals. Closely related to the EAM, and actually the justification for us to use the EAM-ansatz, even for tungsten and thorium, are the considerations following Finnis and Sinclair [FS84, FS86]. Their N-body potentials correspond

to a *second moment approximation* (SMA) to tight-binding theory [PSD88]. In tight binding theory [Har80], atom-based orbitals are assumed to interact via a simple one-electron Hamiltonian. Diagonalizing the Hamiltonian matrix for the system leads to a set of orbital energy levels which can be populated with electrons and summed to obtain the total binding energy. With the *local density of states* (LDOS) $d_i(E)$ the contribution of the ith atom to the binding energy $E_c^{(i)}$ is given by

$$E_c^{(i)} = 2 \int_{-\infty}^{E_F} d_i(E)(E - \epsilon_i)\, dE\,. \tag{5.52}$$

To proceed, Finnis and Sinclair used a well-known remarkable theorem [CL68] which allows one to calculate the moments of the LDOS from the topology of the local atomic environment without knowing the functional form of the LDOS in advance. The moments of the LDOS characterize its shape. The zeroth moment of the LDOS is one owing to the normalization of the basis states. The first moment corresponds to the center of gravity of the LDOS and the second moment is a measure of its width. So, to mimic the actual LDOS, one goes on with its second moment approximation, which finally leads to

$$E_c^{(i)} \propto \sqrt{\mu_i^{(2)}} \tag{5.53}$$

where $\mu_i^{(2)}$ denotes the second moment of $d_i(E)$. It is also a consequence of the above mentioned theorem of moments that $\mu_i^{(2)}$ can be expressed as a sum of pair contributions:

$$\mu_i^{(2)} = \sum_{j \neq i} \beta^2(R_{ij})\,. \tag{5.54}$$

$\beta^2(R_{ij})$ is an averaged square of the transfer integral between atomic states of atoms i and j. To account for core-core interactions one has to add a repulsive pairwise contribution, so that within SMA the total cohesive energy per atom is given by:

$$E_c^{FS} = -A \sum_i \sqrt{\sum_{j(\neq i)} \beta^2(R_{ij})} + \frac{1}{2} \sum_{\substack{i,j \\ (j \neq i)}} \phi_{ij}(R_{ij}) \tag{5.55}$$

This approach is assumed to be primarily suitable for transition metal systems due to the fact that it resides on the proper second moment (which means essentially its width) of the LDOS. It is just the d- and f-states that produce narrow bands and therefore the second moment of the LDOS is a

proper means to reflect this fact. If we would identify the square root with the embedding function of EAM the functional forms of the two approaches would be identical. That's why we will use the EAM despite the fact that the transition metals do not belong to the materials class for that EAM is originally derived for.

To summarize, our model for the total cohesive energy of a pure, i.e. no alloy, intermetallic or impurities, metallic solid composed of N particles is described by

$$E_c = \frac{1}{2} \sum_{\substack{i,j \\ (j \neq i)}}^{N} \phi(R_{ij}) + \sum_{i}^{N} F(\bar{\rho}_i) \,, \tag{5.56}$$

where $\bar{\rho}_i$ is given by

$$\bar{\rho}_i = \sum_{j(\neq i)} \rho(R_{ij}) \,. \tag{5.57}$$

Within the spirit of EAM (or likewise *effective medium theory* [JNP87]) $\rho(R_{ij})$ describes the contribution of the jth atom to the total electron density at site i.

Ansatz Eq. (5.56) together with Eq. (5.57) is computationally only slightly more intense than a purely pair potential assumption. But even if there is only a small additional effort modeling systems within EAM it would be a waste of (computational) time if there are no further advantages of EAM compared to pair potentials. We will see in a few moments, that all the disadvantages of the pair potentials mentioned above are lifted. Of course there is also a major drawback: the conceptionally simpler pair potentials are in most cases much more easily to derive and to fit on actual material properties than our EAM-ansatz, as will be outlined in one of the next sections. This is basically a consequence of the up to now unspecified *embedding function* $F(\rho)$. This function is necessarily of nonlinear character, otherwise we would generate a pair potential with all its drawbacks.

We want to model not only pure systems, but also the interaction of tungsten with some thorium-impurities as mentioned in the outline above. Thats why we have to digress a little bit and describe the changes necessary in the model if we would consider systems containing more than only one type of atoms, before we discuss the fitting procedure to fix the model in detail.

5.2.2 A generalization: the Cohesion Energy for Alloys

It is our intention to simulate not only systems composed of only one type of atoms. To incorporate the effects of some additional elements into our EAM

model, we have to note that both the pure pair potential interaction and the contribution to the total electron density at some site will be altered if there are some impurities present. Furthermore, the weighing of the total electron density at the site of a impurity via the embedding function should change also. In total this means, that our model for systems containing impurities or likewise for alloys has to be extended and is described by the following ansatz:

$$E_c = \frac{1}{2} \sum_{\substack{i,j \\ (j \neq i)}}^{N} \phi_{t_i t_j}(R_{ij}) + \sum_{i}^{N} F_{t_i}(\bar{\rho}_i) \,, \tag{5.58}$$

and

$$\bar{\rho}_i = \sum_{j(\neq i)} \rho_{t_j}(R_{ij}) \,, \tag{5.59}$$

where t_i and t_j denote the type of atom i or j, respectively. This slight generalization of notation in the total energy expression Eq. (5.58) together with Eq. (5.59) has some far reaching consequences for the efforts for generating the functions necessary for the model: for a binary alloy with atom types say A and B, the complete EAM expression requires definitions for ϕ_{AA}, ϕ_{AB}, ϕ_{BB}, ρ_A, ρ_B, $F_A(\bar{\rho})$, and $F_B(\bar{\rho})$. In general, one has to specify $\frac{N_T(N_T+1)}{2}$ pair potentials, N_T density contributions and N_T embedding functions, when N_T denotes the number of different species in the system.

5.2.3 Fitting the Potentials

To mimic the classical electrostatic interaction between two spherical atomic charge densities, the pairwise potential ϕ_{MM} is taken to be of Morse form [VC87]:

$$\phi_{MM}(r) := D_{MM}\big(1 - e^{-\alpha_{MM}(r - R_{MM})}\big)^2 - D_{MM} \,, \tag{5.60}$$

where MM denotes WW, $ThTh$ or WTh, respectively. The three parameters D_{MM}, R_{MM} and α_{MM}, define the depth, the distance to the minimum, and a measure of the curvature near the minimum. In order to define the density function ρ_M, we start from the radial density of the hydrogenic $4s$ orbital [Sch90]:

$$\rho_H^{4s}(r) \sim (r^3 - 24r^2 + 144r - 192)^2 e^{-r/2} \,. \tag{5.61}$$

We expect from our ansatz for the electron density to increase for systems under compression. This requires, that we will only use the monotonically decreasing part with respect of r in Eq. (5.61). Thats why we reduce the expression for the density to leading order in r:

$$\rho_M(r) := r^6\big(e^{-\beta r} + 2^9 e^{-2\beta r}\big) \,. \tag{5.62}$$

M means W or Th, respectively. β is an adjustable parameter. The second term is added to ensure that $\rho_M(r)$ decreases monotonically with r over the whole range of possible interaction distances. The prefactor 2^9 of the second term is the relative normalization factor for a $4s$ orbital with a doubled exponent. This ansatz was shown to be flexible enough to describe pure *fcc*- [VC87, FBD86] including some alloys, as well as some pure *bcc*-metals [HVC88, AF90]. Even more, there were some efforts to describe covalent materials [Bas87] as well as liquid transition metals [Foi85] within an EAM scheme. To be suitable for use in molecular dynamics and molecular statics simulations, the interatomic potentials and, for force calculations, its first derivatives with respect to nuclear coordinates, should be continuous at all geometries of the system. This is accomplished by forcing $\phi_{MM}(r)$, $\phi'_{MM}(r)$, $\rho_M(r)$, and $\rho'_M(r)$, where as usual the inverted comma denotes differentiation with respect of r, to go smoothly to zero at a cutoff distance r_{cut}, which is used as an additional parameter in the fitting procedure. Voter *et al.* [CSV89] managed this cutting using the following functional form for smoothing:

$$f_{smooth}(r) := f(r) - f(r_{cut}) + \frac{r_{cut}}{m}\left[1 - \left(\frac{r}{r_{cut}}\right)^m\right]\frac{df(r)}{dr}\Big|_{r=r_{cut}}, \qquad (5.63)$$

where $f(r)$ means $\phi_{MM}(r)$, $\phi'_{MM}(r)$, $\rho_M(r)$, and $\rho'_M(r)$, respectively, and $m = 20$, which turns out to be a proper choice for thorium and thorium-tungsten interaction potentials. For pure tungsten, we instead follow [AF90] and the arguments therein, who used $m = 1$ and who claimed that for fitting purposes, at least for the *bcc* phase of vanadium, this choice seemed to be the most successful one, an observation which we made during the fitting procedure, too.

Up to now, the *embedding functions* $F_W(\bar{\rho})$ and $F_{Th}(\bar{\rho})$ are completely unspecified. One of the cleanest routes to determining embedding functions is by invoking the *universal binding energy relation* found by Rose *et al.* [RSGF84]. On the basis of a vast collection of experimental data as well as first-principles calculations of a wide range of materials, it was found that the total energy at zero temperature as a function of lattice parameter may be fitted to

$$E_M^R(a_M^*) = -E_M^c(1 + a_M^*)e^{-a_M^*} \qquad (5.64)$$

with the scaled lattice parameter a_M^*:

$$a_M^* := \sqrt{\frac{9B_M\Omega_M}{E_M^c}}\left(\frac{a_M}{a_{M0}} - 1\right). \qquad (5.65)$$

B_M denotes the bulk modulus, Ω_M the volume per atom, E_M^c the cohesion energy with the lattice at equilibrium at zero temperature, a_{M0} the equilibrium

lattice constant and M, as in the preceeding sections, W or Th. This form of the total energy suggests a strategy for constructing embedding functions via the following procedure:

- For a given crystal lattice structure (with a scaled lattice parameter a_M^*) of a pure metal and a given set of trial parameters we start calculating the density $\bar{\rho}_i$ at a typical lattice site i with Eqs. (5.62), (5.63) and (5.57).

- The next step determines the pair potential contribution per atom E_i^P to the total energy via

$$E_i^P := \frac{1}{2} \sum_{j(\neq i)}^{N} \phi(R_{ij}) \,. \tag{5.66}$$

- To derive the embedding energy $F(\bar{\rho}_i)$ for $\bar{\rho}_i$, we then equate Rose's universal binding energy relation, Eq. (5.64), and our expression for the total energy, Eq. (5.56), to get:

$$F(\bar{\rho}_i) = E_M^R(a_M^*) - E_i^P \,. \tag{5.67}$$

Unfortunately, our cutting and smoothing procedure of the potential functions with Eq. (5.63) has a severe consequence: it is just the cutting procedure, which enables us to calculate the total energy per atom with a simulation cell of *finite* dimensions because pairs of atoms, which are far enough apart do not contribute any energy to the total energy, but according to Eq. (5.64), as the lattice is expanded to the point where the nearest neighbor distance R_{NN} is equal to r_{cut}, the density and pair interaction will be zero, but the total energy is not. This means, that the embedding function at zero density is nonzero and the functions will not reasonably handle the case of an atom moving away from the solid. To handle this, the universal binding energy relation, Eq. (5.64), was modified so that $E_M^R(a_{Mcut}^*) = 0$, where a_{Mcut}^* is the scaled lattice constant such that R_{NN} equals r_{cut}. In this work, we used a corrected version of the cutting procedure as the one indicated in ([AF90]).

The modified universal binding energy relation was designed to preserve the correct equilibrium properties, i.e. the lattice constant, the bulk modulus and the cohesion energy in equilibrium should remain unaltered. This is accomplished by the following transformation:

$$E_M^{RC}(a_M^*) = -E_M^c \frac{g(a_M^*\sqrt{1-\epsilon_M}) - \epsilon_M}{1-\epsilon_M} \,, \tag{5.68}$$

where we introduced a new parameter ϵ and, for notational reasons, the function $g(a_M^*) := (1 + a_M^*)e^{-a_M^*}$. ϵ is chosen such that $E_M^{RC}(a_{Mcut}^*) = 0$ at a_{Mcut}^* and results in a highly nonlinear equation which we solve within a self-consistent cycle:

$$\epsilon = g(a_{Mcut}^* \sqrt{1 - \epsilon}) \,. \tag{5.69}$$

The procedure to determine $F(\bar{\rho})$ ensures a *perfect* fit to the lattice constant a_{M0}, cohesion energy E_M^{coh} and bulk modulus B_M of the perfect equilibrium lattice. Furthermore, to fully specify the potentials, we need to fix the five parameters D_{MM}, R_{MM}, α_{MM}, β_M and r_{cut}, apart from the cutting parameter ϵ, which will be determined self consistently and r_{cut} which is chosen, such that its value is between the second and third neighbor shell of the perfect lattices in order to ensure that the potentials to be generated are able to distinguish between the *hexagonal close-packed* and *face-centered cubic* structures, see Tab. 5.1. Additionally, it can be shown [Joh88] that a cutoff radius r_{cut} smaller than second neighbor shell is not able to describe all the elastic properties accurately, due to the fact that the restriction to nearest neighbor interaction implies an *anisotropy factor* of two, which is not true for most transition metals (e.g. for tungsten this factor is almost one).

	bcc	fcc	hcp
first shell	8	12	12
second shell	6	6	6
third shell	12	24	2

Table 5.1: *Number of neighbors of an atom in the* body-centered cubic *(bcc),* face-centered cubic *(fcc) and* hexagonal close-packed *(hcp) structure. Whereas the neighbor shells in bcc and fcc already differ in the first shell, fcc and hcp show up to and including the second shell equal coordination numbers. To distinguish between fcc and hcp structures with an short range interaction potential one therefore has to extend the range of the potential beyond the second neighbor shell.*

Whereas five parameters have to be determined to fix the embedded atom potentials for the pure metals, one needs to fix one more pair potential ϕ_{MM} for unlike interacting atoms. In order to get a more reliable description for the interaction of thorium and tungsten atoms, we furthermore improve the flexibility of the ansatz using the following two scaling relationships which keep the energy of the pure metals unaffected but changes the behavior of alloys [Joh88]:

$$\rho_M(r) \to s_M \rho_M(r) \tag{5.70}$$

$$F(\bar{\rho}) \to F(\bar{\rho}/s_M) \tag{5.71}$$

and

$$\phi_{MM}(r) \to \phi_{MM}(r) - 2g_M\rho_M(r) \tag{5.72}$$

$$F(\bar{\rho}) \to F(\bar{\rho}) + g_M\bar{\rho}\,, \tag{5.73}$$

where we introduced two new parameters s_M and g_M for each constituent with which we optimize the alloy fit without affecting the single component potentials. As can be easily shown, the parameters s_W and s_{Th} cannot be chosen independently from each other because only the *relative* scaling of the density functions $\rho_M(r)$ affects the alloy energy [Vot94].

The potentials for the pure metals, thorium and tungsten, are fitted against the properties as shown in Tab. 5.2, whereas for the tungsten-thorium interaction the elastic properties derived from *ab initio* calculations as presented before are used, see Tab. 5.3.

The fitting was accomplished in minimizing squared deviations. For the multidimensional minimization the very robust *downhill simplex method* [NM65] was implemented. One advantage of this method is that it requires only *function* evaluations, not derivatives as in e.g. *conjugate gradient methods*. The downhill simplex method relies on two basic "movements" of a *simplex* in N-dimensional space (i.e. a geometrical figure, consisting of $(N+1)$ vertices and all their interconnecting line segments, polygonal faces, etc.): *reflections* about a face and *contractions* or *expansions* about a vertex of the simplex. These movements are driven towards the (global or local) minimum. It is not surprising, especially for the tungsten-thorium interaction, that there are more than one local minimum where this procedure is endangered to be trapped. To ensure a "good" (i.e. global) minimum, it is favorable to begin with a simplex which is assumed to be as close as possible to the destination, the desired (global) minimum. For this, we started with a simplex one vertex of which is chosen as the set of parameters fitted to an analytically nearest neighbor model of Johnson, see [Joh88] for the pure and [Joh89] for the alloy systems, where we used the ansatz for the pair interaction between tungsten and thorium atoms derived from the tungsten-tungsten and thorium-thorium interactions:

$$\phi_{WTh}(r) := \frac{1}{2}\left(\frac{\rho_{Th}(r)}{\rho_W(r)}\phi_{WW}(r) + \frac{\rho_W(r)}{\rho_{Th}(r)}\phi_{ThTh}(r)\right). \tag{5.74}$$

A comparison of the starting potential for the tungsten-thorium cross potential with its fitted counterpart and the fitting result can be found in Fig. 5.1. For the fitting procedure, it turned out to be essential for a reasonable fit to start with comparable density functions, $\rho_W(r)$ and $\rho_{Th}(r)$. This

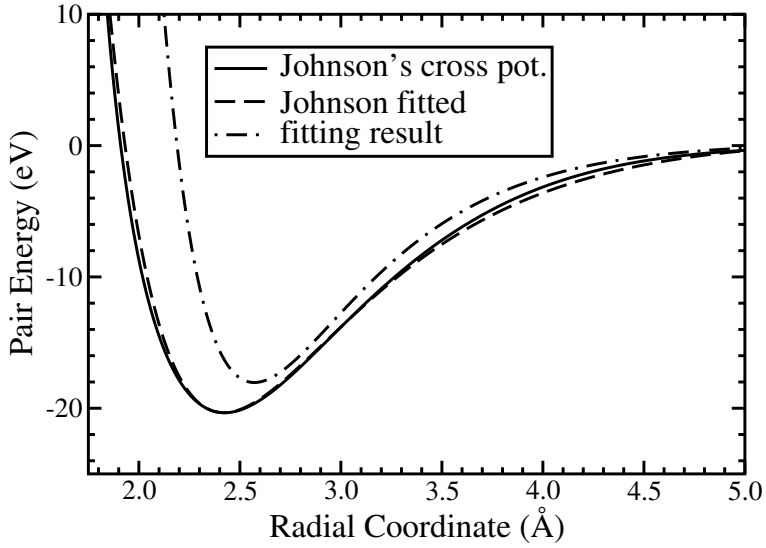

Fig. 5.1: *To improve the fitting procedure, we start the fitting of the tungsten-thorium cross potential with a fit of Eq. (5.60) together with Eq. (5.63) against Johnson' suggestion for a cross potential based on the pair potentials of the pure systems, Eq. (5.74). Johnson' cross potential (straight) for the tungsten-thorium system together with its fitted counterpart (dashed) and the result of the fitting procedure (dash-dotted) is shown.*

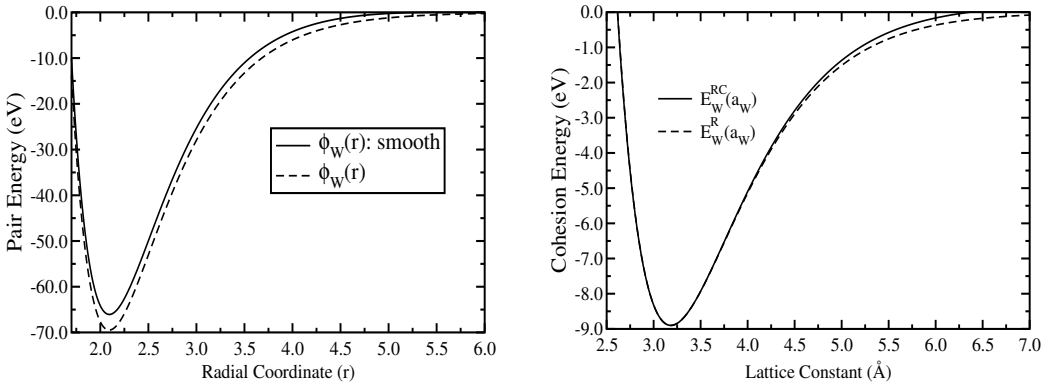

Fig. 5.2: *The influence of the cutoff procedure, Eq. (5.63) is shown for the tungsten-tungsten pair potential, Eq. (5.60), as an example and the result of Eqs. (5.64) and (5.68) for cutting the* universal binding energy function *[RSGF84] adapted to pure tungsten in the* bcc*-phase.*

was accomplished using the scaling property, Eq. (5.70), after fitting the pure potentials.

The functional dependencies for the elastic constants, C_{11}, C_{12} and C_{44}, used in the fitting procedure are given as

$$C_{11} = [B_{11} + F'(\bar{\rho})W_{11} + F''(\bar{\rho})(V_{11})^2]/\Omega_0 \tag{5.75}$$
$$C_{12} = [B_{12} + F'(\bar{\rho})W_{12} + F''(\bar{\rho})(V_{11})^2]/\Omega_0 \tag{5.76}$$
$$C_{44} = [B_{12} + F'(\bar{\rho})W_{12}]/\Omega_0 \tag{5.77}$$

with

$$B_{11} = \frac{1}{2}\sum_m (\phi''(r^m) - \phi'(r^m)/r^m)\frac{(r_1^m)^4}{(r^m)^2} \tag{5.78}$$
$$B_{12} = \frac{1}{2}\sum_m (\phi''(r^m) - \phi'(r^m)/r^m)\frac{(r_1^m)^2(r_2^m)^2}{(r^m)^2} \tag{5.79}$$
$$W_{11} = \sum_m (\rho''(r^m) - \rho'(r^m)/r^m)\frac{(r_1^m)^4}{(r^m)^2} \tag{5.80}$$
$$W_{12} = \sum_m (\rho''(r^m) - \rho'(r^m)/r^m)\frac{(r_1^m)^2(r_2^m)^2}{(r^m)^2} \tag{5.81}$$
$$V_{11} = \sum_m \rho'_m(r^m)(r_1^m)^2/r^m\,, \tag{5.82}$$

where r_1^m and r_2^m denote the first and second component of the position vector to the mth neighbor and r^m the distance to the mth neighbor shell. The lattice constants for the alloy systems are ensured by the equilibrium condition of zero stresses σ_{11}:

$$\sigma_{11} = 2(A_{11} + F'(\bar{\rho})V_{11})/\Omega_0 \equiv 0 \tag{5.83}$$

with

$$A_{11} = \frac{1}{2}\sum_m \phi'(r^m)(r_1^m)^2/r^m\,. \tag{5.84}$$

The result of the fitting process is shown in Fig. 5.3 and Fig. 5.4 together with the influence of the various cutoff procedures, Fig. 5.2. The parameters for the potentials are summarized in Tab. 5.4. Together with the potential parameter just derived all possible interactions on the atomic scale within this classical description between tungsten atoms, thorium atoms and those of tungsten with thorium are fixed. In the upcoming chapter, we will make use of these potentials first to check them against experimental data on perfect tungsten and thorium crystals and then to predict the behavior

Property	Tungsten		Thorium	
	ab initio	calc.	*ab initio*	calc.
a_0(Å)	3.18		5.08	
E_c(eV)	−8.9		−6.2	
B(GPa)	310		53	
C_{11}(GPa)	501	504	78	80
C_{12}(GPa)	215	214	40	39
C_{44}(GPa)	161	161	52	52
$E_v^f(eV)$	3.85	3.85	1.44	1.44
$E^{stab}(eV)$	0.475	0.382	0.123	0.080

Table 5.2: *Metal properties as used in the fitting procedure for the potentials of the pure systems. According to the way the embedding function $F(\bar{\rho})$ is determined the values for the equilibrium lattice constant a_0, the cohesion energy E_c and the bulk modulus B for thorium and tungsten are matched exactly. Also for the pure metals, the values to be fitted are* ab initio *derived as presented before, apart from the* cohesion energies E_c *of thorium and tungsten, which are experimental values. Additionally, we included the resulting values of the fitting procedure in the table for comparison.*

Property	Tungsten-Thorium	
	ab initio	calc.
a_0^{B2}(Å)	3.62	3.62
B^{B2}(GPa)	119	119
$a_0^{L1_2}$(Å)	4.31	4.31
B^{L1_2}(GPa)	166	166
$\sigma_{11}^{B2}(a_0^{B2})$ (GPa)	0	$-9.1 \cdot 10^{-4}$
$\sigma_{11}^{L1_2}(a_0^{L1_2})$ (GPa)	0	$2.3 \cdot 10^{-4}$

Table 5.3: *Metal properties as used in the fitting procedure for the potentials of the alloy ($B2$, $L1_2$) systems. All data are* ab initio *derived. The data include the lattice constants of the $B2$ and $L1_2$ structure at equilibrium, a_0^{B2} and $a_0^{L1_2}$, and its bulk moduli, B^{B2} and B^{L1_2}. There is an extraordinary agreement between the* ab initio *data and the fitted ones. Furthermore, we show also the stresses, $\sigma_{11}^{B2}(a_0^{B2})$ and $\sigma_{11}^{L1_2}(a_0^{L1_2})$, remaining in the structures, if we assume that the equilibrium lattice constants are the* ab initio *ones. Ideally, these figures should be zero, which would mean perfect agreement between the fitted and* ab initio *lattice constants.*

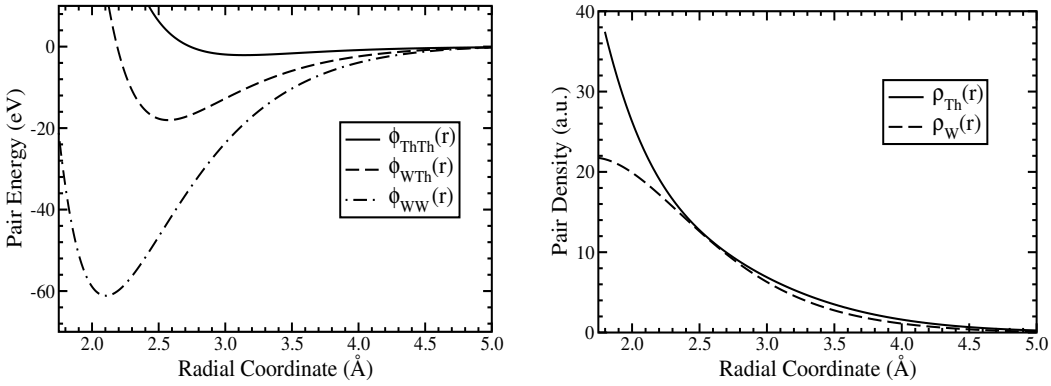

Fig. 5.3: *Results of the fitting processes. The pair (left) and the density interactions (right) for the system $W - Th$ as functions of the radial distance are shown.*

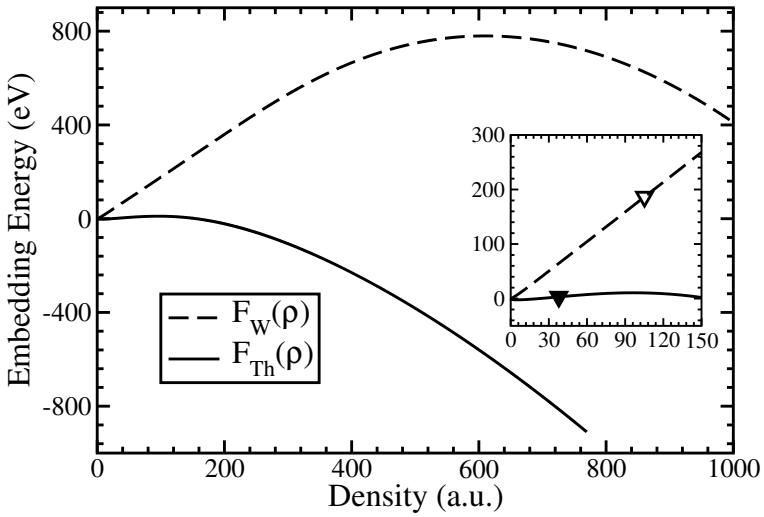

Fig. 5.4: *Resulting embedding energies for W and Th per atom in eV as functions of the density in arbitrary units are shown. Essentially, the non-linearity of these functions is responsible for the many-body effects, especially for the non-zero Cauchy-Relation, because,as shown in the text, any linear dependency of the embedding functions can be absorbed in the pair potentials. The insert shows the low-density dependency of the embedding energies. The open down triangle marks the embedding contribution to the total energy per atom for tungsten at equilibrium and the closed down triangle its corresponding counterpart for thorium.*

	D_{MM}	R_{MM}	α_{MM}	β_M	r_{Mcut}	s_M	g_M
$W-W$	69.4813	2.0917	1.6323	1.8156	5.5138	1.0000	-0.1318
$Th-Th$	2.3907	3.1126	1.6974	3.1316	6.6951	109.0667	-0.0244
$W-Th$	18.3215	2.5716	1.8020		5.4934		

Table 5.4: *Fitted parameters to fix the interatomic interaction between W- and Th-atoms.*

of defective systems, i.e. containing vacancies, impurities dislocations and grain boundaries. We will also have a glimpse into the *thermodynamics* of assembly of atoms and try to derive *entropies* and *free energies* using the *overlapping distribution method*, as described in this chapter.

Chapter 6

Applications of the EAM Potentials

Now, as we derived the preliminaries and necessary ingredients for molecular dynamics simulations, we want to apply this knowledge to get specific properties of pure tungsten crystals and crystals containing thorium-impurities. Among others, we are interested in static defect energies, enthalpies and structures. These include the relaxed vacancy formation in tungsten with and without thorium atoms in its neighborhood. Moreover, to get some hints towards self diffusion as well as diffusion of thorium atoms through bulk tungsten, the migration barrier of atoms in the presence of vacancies shall be calculated.

6.1 Phonon Dispersion for Tungsten and Thorium

As a fist check of the potentials just derived, we want to calculate the *phonon dispersion* and the corresponding *density of states* in comparison with experimental results. The *dynamical matrix* is given by [Phi01]:

$$\mathcal{D}_{\alpha\beta}(\mathbf{q}) := \sum_{j\neq 0} \mathcal{K}_{0j}^{\alpha\beta}\left(e^{i\mathbf{q}\cdot\mathbf{R}_{j0}} - 1\right) \tag{6.1}$$

where $\mathcal{K}_{ij}^{\alpha\beta}$ represents the *force constant matrix* (calculated at the equilibrium positions of the atoms):

$$\mathcal{K}_{ij}^{\alpha\beta} := \frac{\partial^2 E_{tot}}{\partial R_{i\alpha}\partial R_{j\beta}} = -\frac{\partial F_{i\alpha}}{\partial R_{j\beta}} \tag{6.2}$$

and $\mathbf{q}$ the *wave vector* (restricted to the first Brillouin zone), $\mathbf{R}_{j0} := (\mathbf{R}_j - \mathbf{R}_0)$ and $\mathbf{R}_0$ denotes the location of an arbitrarily chosen reference atom.
The force constant matrix for an arbitrary configuration energy is given by:

$$\mathcal{K}_{ij}^{\alpha\beta} = \sum_m (\delta_{ij} - \delta_{mj})(\delta_{\alpha\beta} - \widehat{\mathbf{R}}_{im}^{\alpha}\widehat{\mathbf{R}}_{im}^{\beta})\, E'(im)/R_{im} + \sum_{mn} \widehat{\mathbf{R}}_{im}^{\alpha}\widehat{\mathbf{R}}_{jn}^{\beta}\, E''(im;jn) \quad (6.3)$$

where we introduced the notations $E'(im)$ and $E''(im;jn)$, proportional to the symmetrized first and second derivative of the configuration energy with respect to the particle distances R_{im} and R_{jn}, respectively:

$$E'(im) := \left(\frac{\partial E}{\partial R_{im}} + \frac{\partial E}{\partial R_{mi}}\right) \quad (6.4)$$

$$E''(im;jn) := \left(\frac{\partial^2 E}{\partial R_{im}\partial R_{jn}} + \frac{\partial^2 E}{\partial R_{im}\partial R_{nj}} + \frac{\partial^2 E}{\partial R_{mi}\partial R_{jn}} + \frac{\partial^2 E}{\partial R_{mi}\partial R_{nj}}\right) \quad (6.5)$$

and

$$\widehat{\mathbf{R}}_{im}^{\alpha} := \frac{(\mathbf{R}_i - \mathbf{R}_m)_\alpha}{R_{im}} \quad , \quad R_{im} := |\mathbf{R}_i - \mathbf{R}_m| \quad (6.6)$$

For the EAM-potentials of a monoatomic and ideal crystalline system, i.e. equivalent atomic positions and at least inversion symmetry, we get:

$$\begin{aligned}\mathcal{K}_{ij}^{\alpha\beta} = \sum_m (\delta_{ij} - \delta_{mj}) \Big[&(\delta_{\alpha\beta} - \widehat{\mathbf{R}}_{im}^{\alpha}\widehat{\mathbf{R}}_{im}^{\beta})\left(\phi'(R_{im}) + 2F'(\bar{\rho}_i)\rho'(R_{im})\right)/R_{im} \\ &+ \widehat{\mathbf{R}}_{im}^{\alpha}\widehat{\mathbf{R}}_{im}^{\beta}\left(\phi''(R_{im}) + 2F'(\bar{\rho}_i)\rho''(R_{im})\right)\Big] \\ &+ F''(\bar{\rho}_i)\sum_m (1-\delta_{im})(1-\delta_{jm})\widehat{\mathbf{R}}_{im}^{\alpha}\widehat{\mathbf{R}}_{jm}^{\beta}\,\rho'(R_{im})\rho'(R_{jm})\,. \end{aligned} \quad (6.7)$$

The corresponding dynamical matrix, Eq. (6.1), therefore, is given by

$$\begin{aligned}\mathcal{D}_{\alpha\beta}(\mathbf{q}) = \sum_{j\neq 0} \Big[&(\delta_{\alpha\beta} - \widehat{\mathbf{R}}_{0j}^{\alpha}\widehat{\mathbf{R}}_{0j}^{\beta})\left(\phi'(R_{0j}) + 2F'(\bar{\rho}_0)\rho'(R_{0j})\right)/R_{0j} \\ &+ \widehat{\mathbf{R}}_{0j}^{\alpha}\widehat{\mathbf{R}}_{0j}^{\beta}\left(\phi''(R_{0j}) + 2F'(\bar{\rho}_0)\rho''(R_{0j})\right)\Big]\left(1 - e^{i\mathbf{q}\cdot\mathbf{R}_{0j}}\right) \\ &- F''(\bar{\rho}_0)\sum_{m\neq 0}\widehat{\mathbf{R}}_{0m}^{\alpha}\rho'(R_{0m})\,e^{i\mathbf{q}\cdot\mathbf{R}_{0m}}\sum_{j\neq 0}\widehat{\mathbf{R}}_{0j}^{\beta}\rho'(R_{0j})\,e^{i\mathbf{q}\cdot\mathbf{R}_{0j}}\,. \end{aligned} \quad (6.8)$$

From the functional dependencies of the force constant matrix, Eq. (6.7), it is evident, that the range of the force constants is beyond the cutoff radii,

i.e. twice the cutoff radius of the density potential, due to the nonlinearity of the embedding function.

The phonon dispersion relation, i.e. the relationship between the vibrational frequency ω and wave vector $\mathbf{q}$, is determined by:

$$\det \left| \mathcal{D}_{\alpha\beta}(\mathbf{q}) - m\omega^2 \delta_{\alpha\beta} \right| = 0 \tag{6.9}$$

From its definition, Eq. (6.1), it is clear that the dynamical matrix is symmetric. Another, more straightforward, way to derive the same information, i.e. the phonon dispersion, starts with Eq. (6.2). This force constant matrix is most easily derived from a *molecular statics*, i.e. $T = 0$K, calculation in deducing the changes of the forces on the particles in shifting a reference particle slightly off of its equilibrium position,

$$\mathcal{K}_{ij}^{\alpha\beta} = -\frac{\partial F_{j\beta}}{\partial R_{i\alpha}} \approx -\frac{\Delta F_{j\beta}}{\Delta R_{i\alpha}} \,. \tag{6.10}$$

The result for both approaches for tungsten as well as thorium is shown in Fig. 6.1. The phonon dispersion relations are determined along high symmetry lines in an irreducible wedge of the Brillouin zones of tungsten (bcc-lattice) and thorium (fcc-lattice). Also shown is the phonon density of states (PDOS) derived from a special point set constructed according to a description of Monkhorst and Pack [MP76]. It is given by

$$\rho(\omega) := \sum_i \delta(\omega - \omega_i) \tag{6.11}$$

and, for pictorial reasons, a subsequent convolution with a normalized Gaussian to smooth the resulting density, i.e.

$$\bar{\rho}(\omega) := \sqrt{\frac{\mu}{\pi}} \int_0^\infty \rho(\omega') e^{-\mu(\omega-\omega')^2} \, d\omega' = \sqrt{\frac{\mu}{\pi}} \sum_i e^{-\mu(\omega-\omega_i)^2} \tag{6.12}$$

and a proper choice of μ. The differences between both approaches are very small both for tungsten as well as for thorium and do exist at all because of the approximation of the partial derivatives in Eq. (6.10) by finite differences and it can also be shown that the cutoff procedures of the potential functions, which are responsible for a proper calculation of the forces on the particles, have a very sensitive influence on the forces and therefore also on the resulting dispersion relations. Altogether, this shows that the force calculation in the molecular dynamics package does a good job and, therefore, gives some confidence on future results to be derived. Also shown in Fig. 6.1 are experimental values for the dispersion, [RSP73, BJ03, LB76, LTM02],

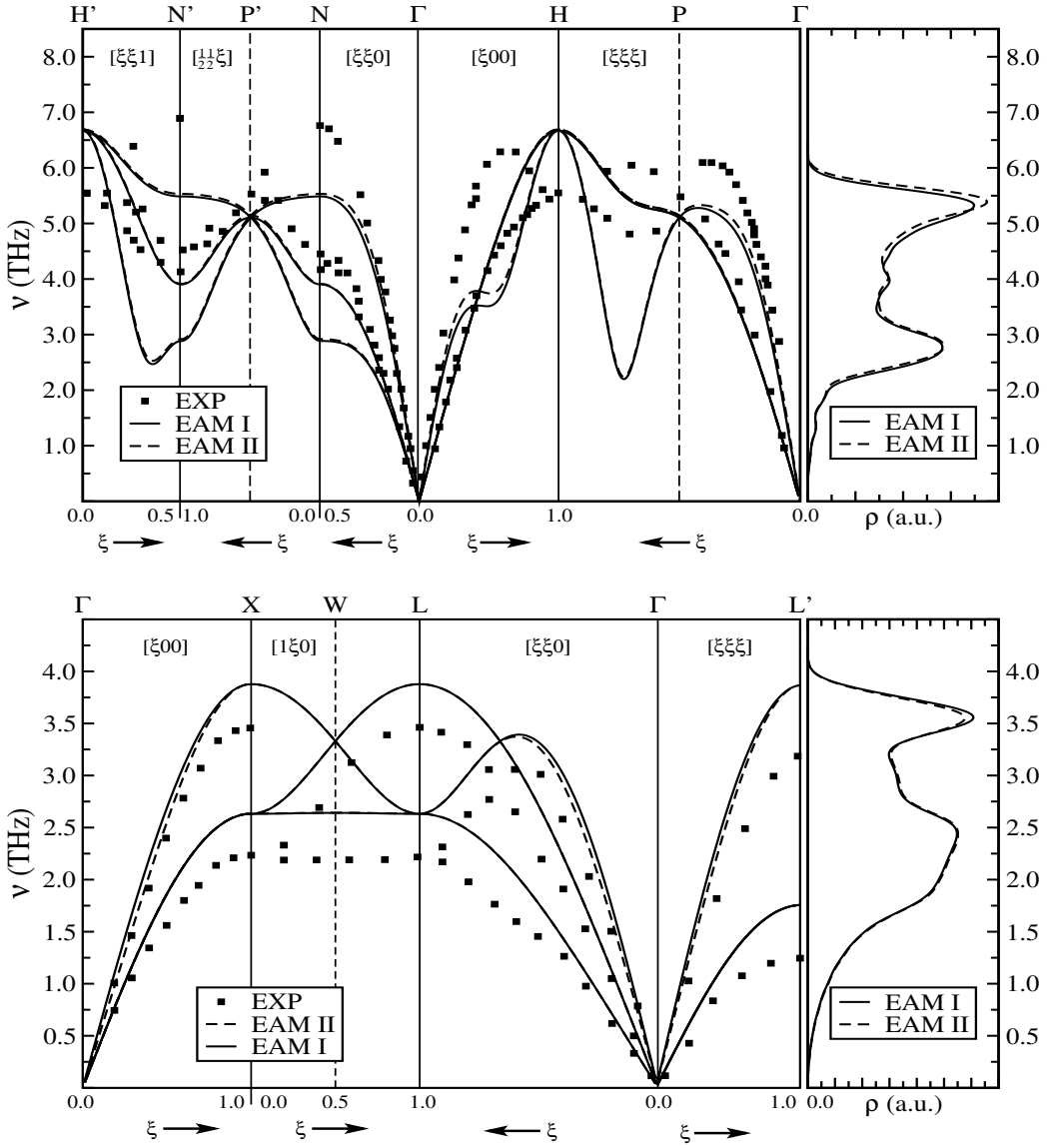

Fig. 6.1: *Phonon dispersion of tungsten (above) and thorium (below) derived using Eq. (6.1) (EAM I) and Eq. (6.10) (EAM II) together with the corresponding phonon density of states (PDOS, on the right). The PDOS are calculated using special point sets in the irreducible wedge of the Brillouin zone according to the description of* Monkhorst-Pack *[MP76]. These sets are composed of 285 symmetry reduced points for the bcc-lattice of tungsten and 344 symmetry reduced points for the fcc-lattice of thorium. All frequencies are given by* $\omega = 2\pi\nu$*. For pictorial reasons, the PDOS are smoothed by a convolution with a Gaussian.*

derived from neutron diffraction studies. The qualitative behavior of the theoretical dispersion relations is nearly identical to the experimental ones. The differences in the actual values, however, are not only due to deficiencies in the model. They are partly connected to a well known lowering of the phonon frequencies due to an increased weakening of the lattices with increasing temperatures. The experiments are done at room temperatures, whereas the theoretical curves are responses of the systems at $T = 0$K. The overall good agreement of the experimental and theoretical data is rather surprising due to the fact, that the potential functions are fitted, among others, against the elastic constants, which are closely related to the zone center behavior of the dispersion relations and can also serve as a proper check of the fitting process. Furthermore, this agreement over the whole zone is evidence, that the EAM-scheme provides a physically reasonable description of the vibrational excitation of transition metals [DH85].

Another approach towards the PDOS can be derived from a molecular dynamics run. It is easy to show that there exists a fundamental relationship between the PDOS and the single-particle velocity autocorrelation function (VACF), defined by:

$$C_{vv}(t) := \frac{\langle \mathbf{v}_i(0) \cdot \mathbf{v}_i(t) \rangle}{\langle \mathbf{v}_i(0) \cdot \mathbf{v}_i(0) \rangle} \,, \tag{6.13}$$

where $\langle \ldots \rangle$ means phase space averaging in this ensemble. Keeping this notation in mind, and taking the *classical equipartition theorem* into account, we get the following simple relation:

$$\rho(\omega) \propto \int_0^\infty cos(wt) C_{vv}(t)\, dt \,, \tag{6.14}$$

i.e. the phonon density of states is proportional to the *Fourier Cosine Transform* of the velocity autocorrelation function.

An example of $C_{vv}(t)$ for different temperatures as derived from a typical MD run is shown in Fig. 6.2. It is typical within MD runs, that the correlations between the particle velocities are damped out the quicker the higher the applied temperatures, a fact, which is clearly demonstrated on the left of Fig. 6.2. The normalized *Fourier Cosine Transforms* are shown on the right of Fig. 6.2. The strong peaks are lowered in favor of the frequencies in-between. Also, the spectra are shifted towards higher frequencies with temperature, a rather astonishing result, as one is tempted to assume, that higher temperatures mean "weaker" lattices, because of the increasing distance between the atoms. This is not solely a result of the anharmonic parts of the interatomic potentials as can be easily demonstrated: we scaled the "frozen" lattice of a tungsten cube according to the equilibrium lattice

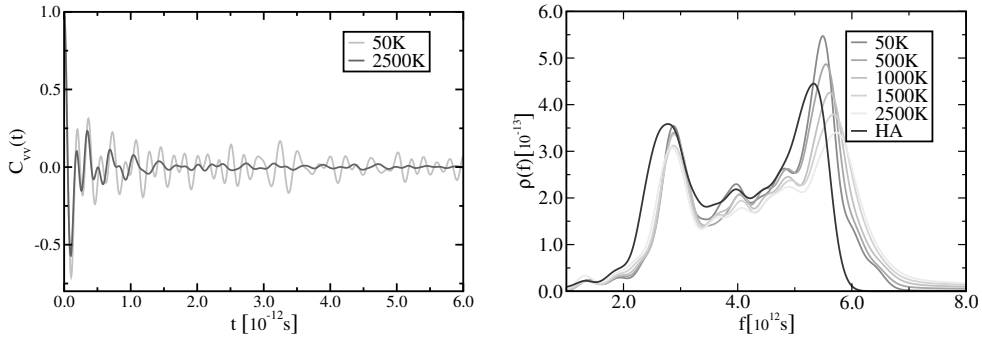

Fig. 6.2: *A typical result of a MD run for the* velocity autocorrelation function *(VACF), Eq. (6.13), of tungsten for the temperatures* $T = 50\text{K}$ *and* $T = 2500\text{K}$ *is shown (left). The corresponding phonon densities as derived from Eq. (6.14) for different temperatures are depicted (right). Also, the "dynamical" density of phonons is compared with its counterpart in harmonic approximation (HA), i.e. derived using Eq. (6.1). The strong influence of the anharmonic parts of the interatomic potentials for tungsten can be seen notedly.*

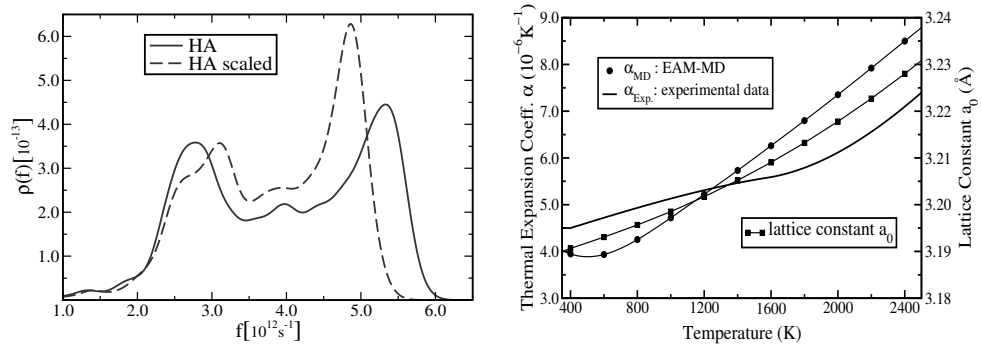

Fig. 6.3: *The smoothed* density of states *(in the harmonic approximation) for the vibrational modes is shown for tungsten for an unstrained and a strained lattice, which corresponds to the (strained) lattice constant of a crystal at temperature* $T = 2000\text{K}$ *(left). Also shown is the temperature dependence of the* linear expansion coefficient *derived from a MD-simulation course and compared to experimental data [TKT75] (right).*

constant of tungsten at $T = 2000\text{K}$ ($a_0(T = 2000\text{K}) = 3.2179\text{Å}$). In the harmonic approximation, the *DOS* of the vibrational modes exhibit most of the properties observed at the DOS derived from the VACF, especially the shift of the high frequency cutoff in the spectrum due to widening of the crystal lattice is obvious, whereas the low frequency cutoff seems to be nearly unaffected by the lattice scaling, see Fig. 6.3. A proper means to indicate the anharmonic effects of the interatomic potentials is the *linear thermal expansion coefficient* α, defined via [AM76]:

$$\alpha = \frac{1}{3\Omega}\left(\frac{\partial\Omega}{\partial T}\right)_P \tag{6.15}$$

and can be shown to be closely related to the vibrational modes ω_i [AM76]:

$$\alpha = \frac{1}{3B}\sum_i \left(-\frac{\partial}{\partial\Omega}\hbar\omega_i\right)\frac{\partial}{\partial T}(e^{\beta\hbar\omega_i} - 1)^{-1}\,, \tag{6.16}$$

where Ω, B, P, denote atomic volume, bulk modulus and hydrostatic pressure, respectively, and $\beta = 1/k_B T$. The thermal expansion coefficient α equals zero for purely harmonic crystals. That's, because the stiffness matrix of an harmonic crystal is per definition independent of any changes in volume and, therefore, the vibrational modes do not change also. $\alpha \neq 0$, therefore, is a direct consequence of the anharmonic energy contributions. A comparison of both, experimental and MD derived data for tungsten is also shown in Fig. 6.3. Now, as we got some confidence of the interatomic potentials as derived from *ab initio* calculations, we try to get some more information about tungsten and thoriated tungsten crystals. To start with, we will calculate the *excess volume* of a tungsten vacancy and of a thorium impurity, and, among others, some defect enthalpies in the upcoming section.

6.2 Excess Volume of point defects: W-Vacancy and Th-Impurity

A consistent definition of the term *excess volume* V_{ex} starts with following relation:

$$V_{ex} \equiv V(\text{with defect}) - V(\text{without defect})\,, \tag{6.17}$$

where V(with/without defect) denotes the simulation cell volume with or without defect, respectively. The excess volume as a function of simulation cell dimension that defined is given in Figs. 6.4 for a single W-vacancy and a Th-impurity. The values are converged for cubic simulation cells greater

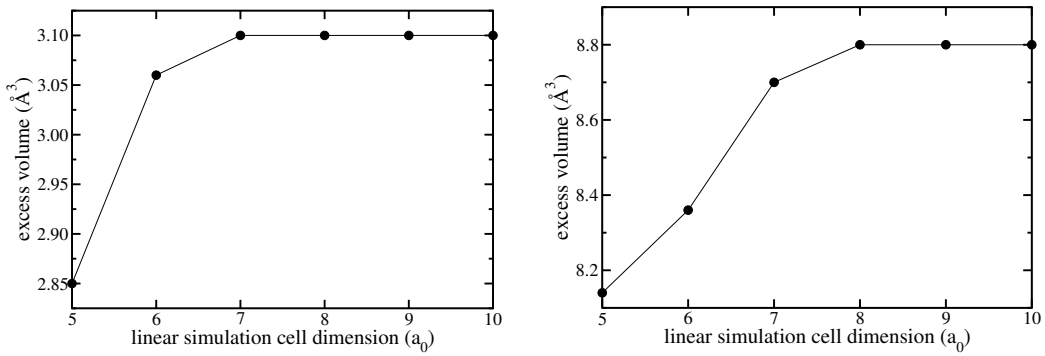

Fig. 6.4: *The* excess volume*, i.e. the change in volume of a W-crystal with a W-Vacancy (left) and a Th-Impurity (right) is shown as a function of the linear cell dimension.*

than 686 atoms (linear box dimension $L \sim 7a_0$) for the W vacancy and 1024 atoms ($L \sim 8a_0$) for the cell containing a Th impurity. The fact that bigger cells are necessary for the Th impurity compared to the vacancy resides on the bigger cutoff lengths for the potentials of W-Th than those of the W-W potentials. The Th-atom is "bigger" than the W-atom. This results in a dilated simulation cell containing a Th impurity. But, it is remarkable, that the presence of a vacancy yields likewise to an increase of volume.

6.3 Grain Boundary Formation

All MD simulation runs are done with a time step of $dt = 2 \cdot 10^{-15} s$. This corresponds to about 1/60 of the period of the oscillation with highest frequency, which can be easily estimated to be $T_S = h/(k_B \Theta_D)$, where Θ_D denotes the *Debye-Temperature* (for Tungsten: 400K, for Thorium: 163K). 135000 time steps were performed, which results in a total simulation time of about $500ps$ per run. The edges of the cell in this simulation were "frozen". The frozen edges of of the cell were chosen such that atoms neighboring the frozen ones, do not "feel" the presence of a surface, i.e. the distance of those atoms is chosen at least two times the cutoff of the potentials. The effect of this boundary zone is twofold: first, the movements of the closest atoms is damped, and, second, the elastic stress coming up with those frozen regions hinder the grain boundaries to fluctuate thermally to a great extent due to restoring forces on the grain boundaries.

6.3.1 Grain Boundary Structure and Energy

A *grain boundary* is the interface where two single crystals of different orientation join in such a manner that the material is continuous across the interface. Far away from the boundary, in the single crystals, the atoms are located at positions of the undisturbed crystal lattice. At the boundary, however, the atoms must be displaced from the positions which they would occupy in the perfect crystal. Therefore, the energy of the atoms in the boundary is necessarily higher than it would be for the atoms in the undisturbed crystal lattice. From this, it can be concluded, that one can associate a definite amount of energy per grain boundary area with the grain boundary itself.

Grain boundaries are of utmost importance for plastic deformation of the sample as it generally serves as sink or source for dislocations, which are primarily responsible for plasticity or even fracture and cleavage.

In this section, we try to shed some light into the complicated structures and associated energies of some specific grain boundaries. For this we introduce the concept of the *Coincidence Site Lattice* (CSL). CSL are periodic in space, with is of great advantage within MD simulations, as periodic boundary conditions can be applied and surface effects be neglected. A CSL arises quite naturally from studies of the symmetry of *dichromatic patterns* [SB95], which itself belongs to the methodology of *bicrystallography*, and which provides a systematic enumeration and classification of plane interfaces in crystals.

As the two crystals sharing the same interface are rotated against each other, there exists a rotation operation, which maps the atomic positions of one crystal on top of the other. For certain *misorientations*, however, it happens for some atoms of the two lattices to coincide. This coinciding lattice points then form itself a three dimensional lattice, the CSL. One can show [Gri76] that for a CSL to exist in cubic structures, one necessarily needs rotation matrices with purely rational entries. This can be summarized in the following form of the associated *Rodriguez Vector*,

$$\rho^R = \frac{m}{n} \left[HKL\right] , \tag{6.18}$$

where m, n are integers and $[HKL]$ describes the rotation axis with *Miller indices* H, K, L in one of the lattices. According to *Frank* [Fra88], the *Rodriguez Vector* associated with an arbitrary rotation around unit axis $\hat{\rho}$ and angle Θ is given by

$$\rho^R := \hat{\rho} \tan \frac{\Theta}{2} \tag{6.19}$$

For CSL it is convenient to introduce another figure: the integer number q of unit cells of the original lattice comprising the unit cell of the CSL. For cubic lattices q is given by [SB95]:

$$q = n^2 + m^2 \left(H^2 + K^2 + L^2\right) , \tag{6.20}$$

with n, m, H, K, L from Eq. (6.18).

In the following, we will restrict our considerations to *symmetrical tilt* and *symmetrical twist* CSL grain boundaries. Tilt boundaries are defined with a rotation around an axis lying in the grain boundary plane, whereas for twist boundaries the rotation axis is perpendicular to the grain boundary.

The simulations are done using approximately 20.000 atoms periodically arranged as induced by the specific CSL under consideration.

With $\Sigma q(hkl)$ we denote a symmetrical grain boundary with a common boundary plane (hkl) and CSL quotient q as introduced above, Eq. (6.20). Together with Eq. (6.20), for a given q we extract the possible combinations of m and n for a given rotation axis $[H\,K\,L]$. For tilt boundaries, we chose a rotation axis $[0\,0\,1]$ and a grain boundary plane of the form $(h\,k\,0)$ whereas for the twists we use a rotation axis $[1\,0\,0]$ and a boundary plane $(1\,0\,0)$. The parameters necessary to identify a unique boundary for the boundaries under investigation are summarized in Tab. 6.1. The simulation cells were

Θ	Σ	h	k	Θ	Σ	h	k	Θ	Σ	h	k
9.527	145	12	1	10.389	122	11	1	11.421	101	10	1
12.680	82	9	1	14.250	65	8	1	16.260	50	7	1
18.925	37	6	1	20.610	125	11	2	22.620	26	5	1
25.058	85	9	2	28.072	17	4	1	30.510	130	11	3
31.891	53	7	2	33.398	109	10	3	36.870	10	3	1
39.966	137	11	4	41.112	73	8	3	43.603	29	5	2
46.397	58	7	3	47.925	97	9	4	48.888	146	11	5
53.130	5	2	1	58.109	106	9	5	59.490	65	7	4
61.928	34	5	3	64.011	89	8	5	67.380	13	3	2
69.984	149	10	7	71.075	74	7	5	73.740	25	4	3
75.750	130	9	7	77.320	41	5	4	79.611	61	6	5
81.203	85	7	6	82.372	113	8	7	83.267	145	9	8

Table 6.1: *The parameters used which uniquely determine the symmetrical tilt and twist boundaries are shown. For the tilt boundary only h and k and for twists m and n need to be specified. The resulting boundaries are therefore $\Sigma q(hk0)$ for the tilts and $\Sigma q(100)$ for the twists, respectively.*

"quenched" to 0K for the system to end up in a state of a local minimum of

the potential energy. During this quenching, the cell dimensions as well as all atomic coordinates were allowed to relax. The resulting *grain boundary energies*, i.e. the energy difference of cell with and without grain boundary referred to the grain boundary area, are shown in Fig. 6.5. For both cases, the pronounced increase of the energies for small tilt and twist angles is clearly demonstrated, a fact which can be understood using Read and Shockley's analysis [RS50] based on dislocation theory. Unlike the computer simulations of Wolf [Wol89] on twist grain boundaries in Cu and Au using Lennard-Jones and EAM potentials, however, do not show the pronounced cusps related to low-Σ boundaries as visible in Fig. 6.5, whereas newer calculations [Wol90b, Wol90a] confirm this picture.

6.3.2 A closer look: the $\Sigma 5$ STGB

The geometric construction of a CSL boundary sometimes enforces atoms to get much closer together compared to bulk atoms such that the grain boundary energy per area is much more enhanced than observed in nature. Necessarily, this means that a substantial relaxation has to occur in order to get a "natural" Σ boundary. These "high energy" sites have to be relaxed at first by moving them apart. The corresponding change of grain boundary energy per area versus shifting distance away from the grain boundary plane is shown in Fig. 6.6. The resulting structures are shown in Fig. 6.7. Including all atoms in the relaxation process destroys the bcc-lattice symmetry which is persistent in either grain, i.e. on either side of the grain boundary. The resulting fully relaxed $\Sigma 5(310)[001]$ grain boundary is shown in Fig. 6.8. The atomic volumes and its dependencies of the distance of the grain boundary plane as a result of a *Voronoi tesselation* of the atomic coordinates of the simulation cell can be seen in Fig. 6.9. As expected, both, the highest as well as the lowest values for the volumes are on the grain boundary plane. This influences diffusional aspects and will become clear soon, see 6.4.

One should expect some systematic correlation between "atomic" volumes and "atomic" energies as we fitted the cohesion energy against the *universal binding energy function (UBEF)*, Eq. (5.64). The result for the edge dislocation is shown in Fig. 6.10, which shows, that here the atomic interactions can not be described as simply "volume dependent", sometimes assumed for atomic interaction potentials.

Generally, as we also did up to now, one is interested in the grain boundary structure of lowest possible potential energy. This structure is usually referred to as the global minimum energy for that particular grain boundary. However, there may be several other minimum energy structures that are structurally different from the global minimum but that may have energies

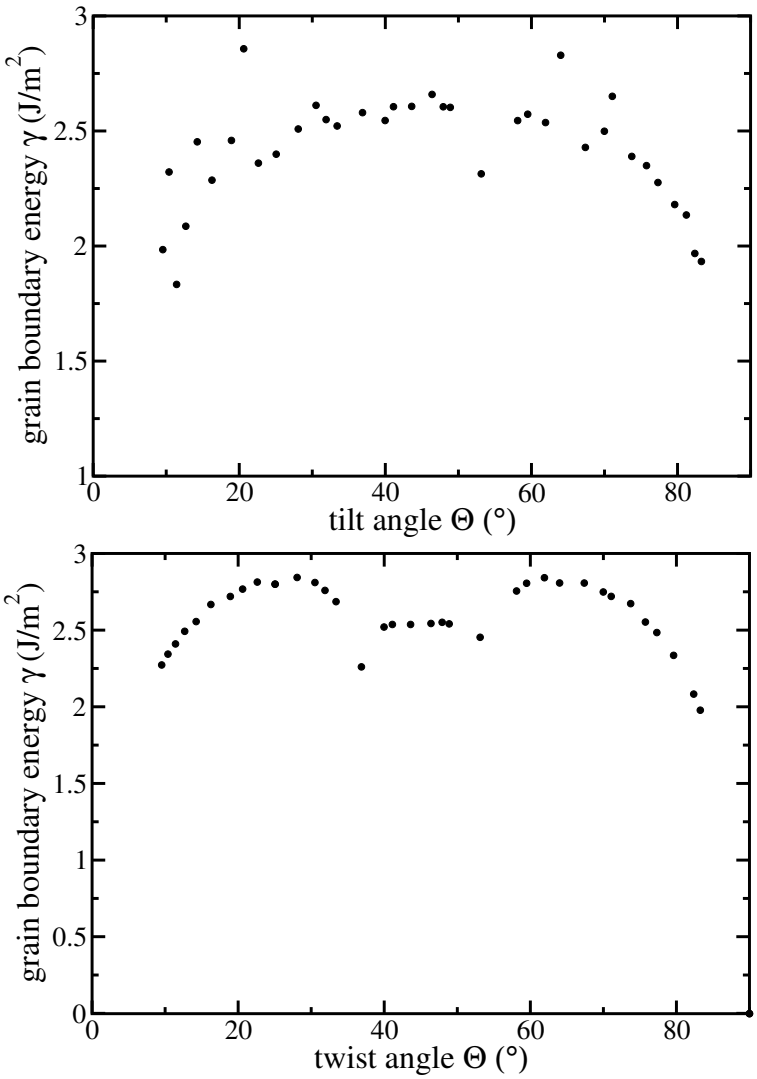

Fig. 6.5: *Grain boundary energy versus tilt and twist angle, respectively, for various* Σ *grain boundaries.*

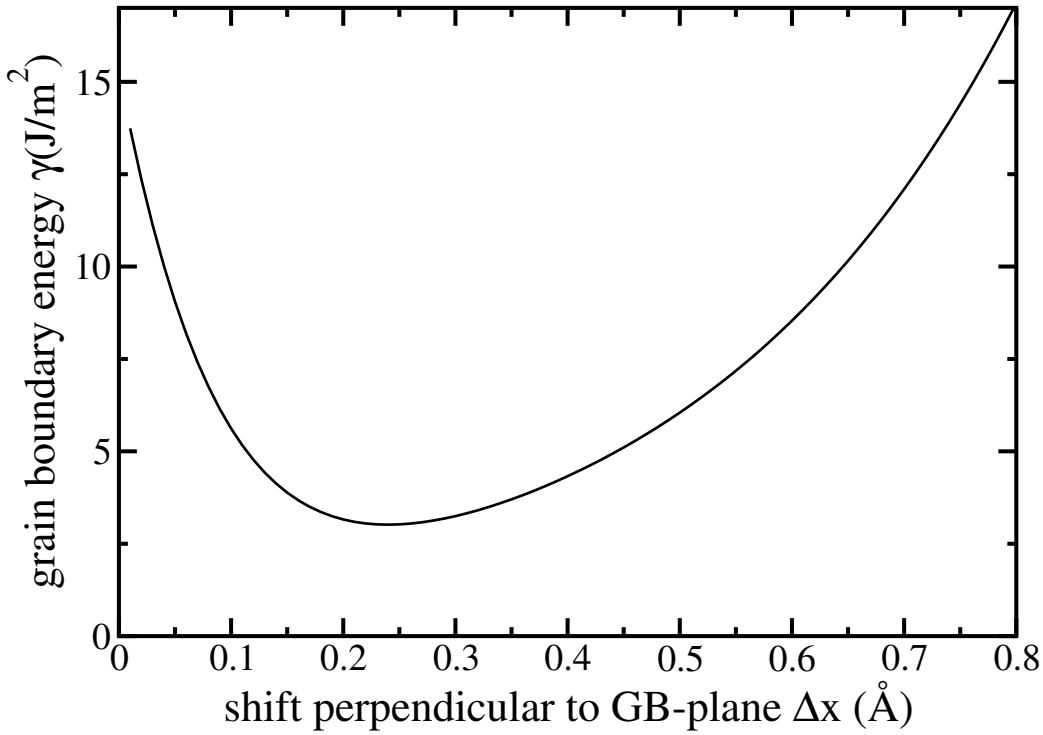

Fig. 6.6: *The grain boundary energy per area is shown vs. shifting the "high energy" sites (see text) perpendicular to the grain boundary plane of an otherwise undisturbed cell*

.

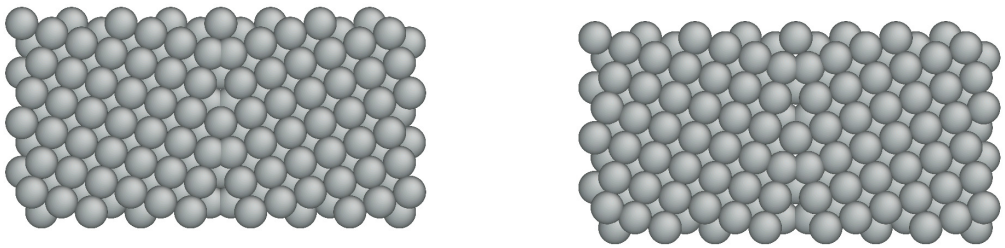

Fig. 6.7: *The structure of the* $\Sigma 5(310)[100]$ *grain boundary before (left) and after (right) the relaxation of the "high energy" sites.*

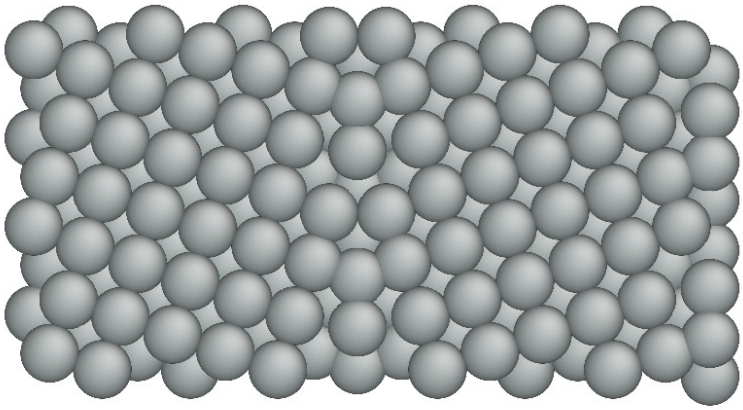

Fig. 6.8: *The fully relaxed, i.e. after quenching as described in the text, structure of the* $\Sigma 5(310)[100]$ *grain boundary.*

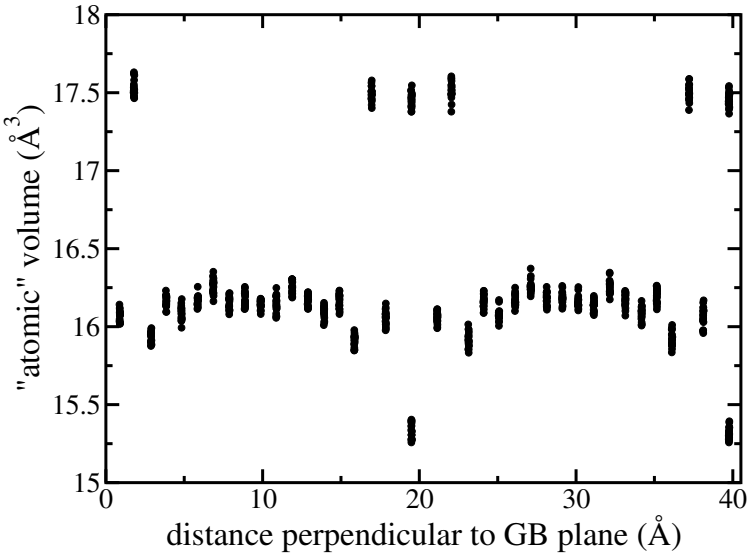

Fig. 6.9: *The fully relaxed and subsequently quenched structure of the* $\Sigma 5(310)[100]$ *grain boundary. A voronoi tessellation is used to generate the "atomic" volumes.*

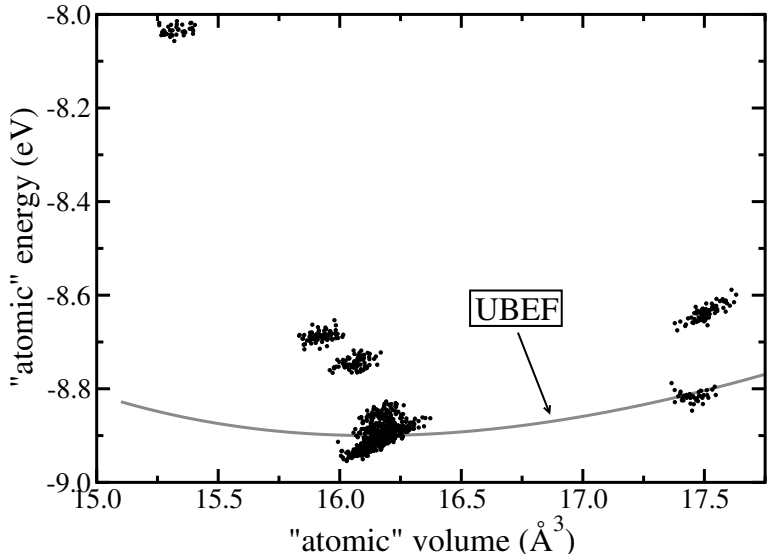

Fig. 6.10: *The relationship of the "atomic" volume versus the corresponding "atomic" energies for the quenched structure of a* $\Sigma5(310)[100]$ *grain boundary is shown.*

that are not much higher than the global minimum. These 'local minima' structures may then play a major role in the actual structure in a real material. This structural multiplicity was found in many metals and compounds and is reviewed for example by Balluffi and Sutton [SB95]. A simple way to check this possible existence of multiplicities is given by the concept of γ*-surfaces*. This concept, originally derived for dislocations [Vit68], was later-on extended to grain boundaries [MF98]. The basic idea of the γ-surface is to shift the crystals on either side of the grain boundary relative to one another by a vector $\mathbf{u}_0$ in the plane and to record the grain boundary energy. Here, we allowed the system to "breath", i.e. the atoms may relax perpendicular to the grain boundary plane. The grain boundary energy $\gamma(\mathbf{u}_0)$ as function of the shift vector $\mathbf{u}_0$ along a periodic unit zone within the grain boundary plane yields the γ-surface. The result of this procedure for the $\Sigma10(310)$ symmetrical tilt grain boundary is given in Fig. 6.11, where the energies are referred to the unshifted situation. In this very case, there arise three additional (local) minima in the γ-surface. One of which, in the middle of the scanned zone, seems to be a low energy grain boundary structure. This, however, corresponds to an symmetry related configuration to the beginning ($\mathbf{u}_0 = \mathbf{0}$) of the zone. The other local minima near the beginning and the end of the scanned zone are likewise symmetry related to one another. Their

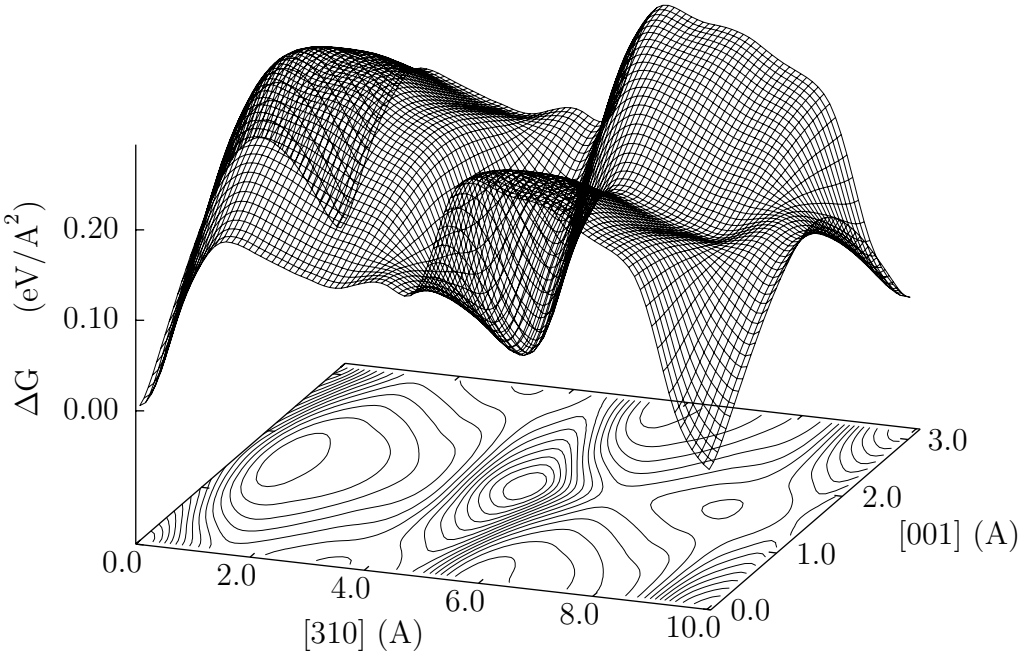

Fig. 6.11: *The* γ-surface *of a* $\Sigma 10(310)$*-tilt grain boundary. The energies per area are measured from the unshifted value, i.e. the shift vector* $\mathbf{u}_0 = \mathbf{0}$*. Three additional local minima are detected. One of which (in the middle of the scanned zone) is symmetry related to the unshifted situation. The remaining two are also symmetry related to one another, but their energy per area is about* $0.16\text{eV}/\mathring{A}^2$ *higher than unshifted.*

grain boundary energy is about $0.16\text{eV}/\mathring{\text{A}}^2$ higher than the unshifted situation. This huge energy difference to the global minimum makes the existence of such grain boundaries in real matter rather unlikely.

As mentioned, grain boundaries are supposed to serve as "short circuits" for self diffusional flux due to their loose and wide structures. For tungsten, self diffusion through the bulk is experimentally given by:

$$D(T) = D_l \exp(-Q/k_B T) \tag{6.21}$$

where k_B denotes *Boltzmann's constant* and T the *Kelvin* temperature scale, as usual. The pre-exponential factor and the activation energy Q are determined via sectioning to [AKK65]:

$$D_l = 4.28 \cdot 10^{-3}\text{m}^2/\text{s} \quad Q_l = 6.639\text{eV} \tag{6.22}$$

The corresponding data for grain boundary diffusion are [BSS81]:

$$\delta D_b = 2.30 \cdot 10^{-12}\text{m}^3/\text{s} \quad Q_b = 3.946\text{eV} \tag{6.23}$$

where δ denotes a typical width of the grain boundary. An estimated width δ for the $\Sigma 5$ GB for instance from inspection of Fig. 6.9 gives about 10Å. A comparison of the diffusional constants D at temperatures of interest in lighting applications, $T = 3000$K,

6.3.3 Segregation of Th on W-Grain Boundaries

It is well known, that different solute atoms present in multicomponent systems often tend to adsorb on crystalline interfaces, thereby building up interface "excess" concentrations. A grain boundary moves with a velocity $\mathbf{v}$ in response to a net *driving force* $\mathbf{P}$. It is generally assumed, that $\mathbf{v}$ is proportional to $\mathbf{P}$, the constant of proportionality being the *mobility*, M, of the boundary:

$$\mathbf{v} = M\,\mathbf{P} \tag{6.24}$$

This type of relationship is predicted by *reaction rate theory* if the mobility is independent of the driving force and if $\mathbf{P} \ll k_B T$, and should be independent on the details of the mechanism of boundary migration [Tur51]. Most theories of the effects of solutes on boundary mobility are based on that proposed by *Lücke and Detert* [LD57]. This theory was further developed by *Cahn* [Cah62]and, later-on, by *Lücke and Stüwe* [LS71]. The *Cahn-Lücke-Stüwe* (CLS) model is based on the concept, that atoms near a grain boundary has a different energy E_s to one in the interior of the grain due to the different local atomic environment and, therefore, E_s depends on the relative position of grain boundary and solute atom. The index s in E_s indicates the dependency of the cell energy on site s in the matrix. This is responsible for a net *force* between boundary and solute atom ($F \propto \nabla E$). A consequence of this force is that the overall recrystallization behavior is altered in the presence of solutes in the matrix, a fact, which results in an increased *recrystallization temperature*, i.e. the the onset temperature of recrystallization, of Th-doped tungsten materials compared to pure tungsten, and also shows, that the mobility M in Eq. (6.24) depends heavily on the concentration of Th-impurities. According to the CLS model, the solute concentration in the vicinity of the grain boundary is given by

$$c_s = c_0 \exp\left(-\frac{E_s}{k_B T}\right) \tag{6.25}$$

where c_0 denotes the equilibrium solute concentration.

In order to estimate E_s, we used the following procedure: we started with a relaxed simulation cell containing 1024 tungsten atoms arranged such that a $\Sigma 5$ STGB is present in the middle of the cell, see Fig. 6.9. As we assume,

that the Th-atom is considerably "thicker" (see, for instance, the difference in nearest neighbor distance in the pure materials) than a W-atom, we can safely expect, that the Th-atom when in tungsten bulk, will occupy a lattice site and will not stay at an interstitial. To estimate the *segregation energy* of a Th-atom on the Σ5-STGB we calculate the energy difference between the relaxed cell with Th-atom on the grain boundary and the Th-atom in the interior of the grain, far away from the boundary plane. All calculations were done with our *Langevin piston* at zero temperature and pressure, i.e. the cell dimensions may relax to their equilibrium values.

site s	2	3	4	5	6	7	8	9	10
E^s_{seg}(eV)	0.40	−0.19	−0.53	−0.10	−1.30	0.05	−0.19	−0.03	0.00

Table 6.2: *The* segregation energies $E^s_{seg} := E_s - E_{10}$*, where* E_s *denotes the cell energy with a Th-impurity located on site* s*, as determined from a MD simulation for a segregated Th-impurity on a* Σ5 *STGB. Here, we assumed, that site* 10 *is sufficiently away from the grain boundary plane and, therefore, can be considered as "bulk like".*

The nomenclature of the various sites on the grain boundary is the same as for the vacancy diffusion, considered in the upcoming section 6.4 and is given in Fig. 6.12. The results of this procedure are shown in Tab. 6.2. It's interesting to see, that here the segregation energies are correlated in a sense with the "atomic" volumes as derived for the relaxed pure grain boundary structure, as shown in Fig. 6.9: the highest segregation energy (0.40eV) results, when the Th-atom occupies the lattice site with the smallest "volume", site 2, and, likewise, the lowest segregation energy (−1.30eV) with Th on site 6, the site with the greatest "volume".

6.4 Vacancy Diffusion along the Σ5 STGB

Diffusional aspects are important, both, for the principal operating mechanism of some electric discharge lamps as the diffusional Th current in W is crucial for proper operation, i.e. no flickering of the discharge region on the W surface, as well as for the long term stability of tungsten coils under steady stresses imposed e.g. via the gravitational forces, as macroscopic creep mechanisms are mainly influenced via atomic diffusional processes.

Diffusion along grain boundaries is orders of magnitude faster than through the bulk of the crystal. From e.g. phenomenological continuum arguments [Phi01],

it is easy to derive an equation of motion, the *diffusion equation*, for the probability $P(\mathbf{x}, t)$ to find a diffusing atom at $\mathbf{x}$ at time t:

$$\frac{\partial}{\partial t} P(\mathbf{x}, t) = D \nabla^2 P(\mathbf{x}, t) \,, \tag{6.26}$$

where D is the temperature and, in general, space dependent *diffusion constant*. Its temperature dependence generally follows an *Arrhenius* type of equation:

$$D(T) = D_0 e^{-E/k_B T} \,, \tag{6.27}$$

E denotes the corresponding *activation energy*. For Th in W it was found [Lan34] that the grain boundary diffusion constants were 10^3 times those of volume diffusion in the temperature range between 1900K and 2400K. Also, the activation energy for boundary diffusion E_b was reported to be considerably smaller than that of the volume diffusion E_c: $E_b/E_c \approx 0.75$. The following Arrhenius parameters were evaluated for grain boundary diffusion of Th in W:

$$D_{b0} = 7.41 \cdot 10^{-5} \mathrm{m}^2/\mathrm{s} \,, \; E_b = 3.903 \mathrm{eV} \,. \tag{6.28}$$

Even at the melting point of W, $T_m \approx 3680$K, the diffusion constant is $D \approx 3.4 \cdot 10^{-12} \mathrm{m}^2/\mathrm{s}$. From an elementary treatment of *Brownian motion* one gets the famous connection between diffusion constant and atomistic jumping processes:

$$D = \frac{1}{6} \beta^2 \Gamma \,, \tag{6.29}$$

where β is a typical jumping distance and Γ the jumping frequency. Without assuming a particular mechanism, it is plausible, that β is about an interatomic distance in a lattice (for *bcc*-W ~ 2.76Å). From these assumptions, the jump frequency can be estimated to $\Gamma \sim 2.6 \cdot 10^8/\mathrm{s}$. That is, each thorium atom changes its position about 260 million times per second. This seems to be very often, but compared to typical vibrational frequencies for instance of about 5.0THz of tungsten atoms, shows, that only in one oscillation of about $2 \cdot 10^4$ a positional change can be expected.

As noticed already, MD Simulations are limited to time scales very small in macroscopic sense: the duration of a typical trajectory can be traced rarely beyond the *pico second* limit. This means, that for a diffusional jump of a thorium atom to occur within a calculated trajectory of $\sim$ 1ps, we would need at least about 10^4 equivalent thorium atoms (as impurities in tungsten bulk, as we are interested in Th diffusion in W). With conventional MD methods, this seems to be infeasible.

For an atom to migrate, it is essential to surmount energetic barriers composed by the atomic environment. The height of these barriers depend

heavily on the local structure and therefore hinge on the position of the diffusing atom before the jumping process and the site towards which the atom jumps onto. The corresponding energy barriers are given in Tab. 6.4. The barriers are determined within an either static or totally relaxed environment. For the simulation, a vacancy mechanism is assumed. For this, we introduced a vacancy on a site removing the corresponding atom. One atom in the vacancy's neighborhood is chosen to "jump". This atom is then gradually moved towards the vacancy. Whether a diffusion jump is slow enough so that a totally relaxed environment of the diffusing atom is a proper assumption or that fast, that the environment is not aware of the jumping atom changing its position is not well known. That's why two different procedures are applied determining the upcoming energy barriers: for the static environment, no positional changes of the neighborhood are allowed, i.e. the neighboring atoms are "frozen" for the simulation course, and the opposite one, where we shift the diffusing atom "over the barrier" and at each instant of time let the environment totally relax on a plane containing the diffusing atom perpendicular to the shifting direction. For the simulation a $\Sigma 5(310)$ symmetrical tilt grain boundary is used. The nomenclature of the sites is shown in Fig. 6.12.

As a by-product of this procedure, we also get the *vacancy formation energies* E_{vf}^{s}, where s indicates the different sites "occupied" by the vacancy. The numbering of the sites is the same as shown in Fig. 6.12. In order to derive E_{vf}^{s} for the different sites, we assume, that site $s = 10$ is "bulk like", i.e. $E_{vf}^{10}(static) = 3.86\text{eV}$ and $E_{vf}^{10}(relaxed) = 3.59\text{eV}$. This was a result of a simple procedure: we used a bulk cell with 2000 tungsten atoms and removed one atom. With ("relax") and without ("static") relaxation, the difference in cell energy with vacancy and undisturbed bulk denotes E_{vf}^{10}. To calculate E_{vf}^{s} for other sites, the following idea was applied: assume a hopping sequence for the vacancy from a "bulk like" site, e.g. $s = 10$, to a site s located on the grain boundary. Then, whenever the energy of the total cell, i.e. including the grain boundary, increases, E_{vf}^{s} grows by the same amount. The result of this procedure is shown in Tab. 6.3 for both, the relaxed and the "frozen" hopping sequence. Fig. 6.14 shows a detailed analysis of the energy barriers for a migrating vacancy located within the bulk (bcc) lattice, when "jumping" to a nearest neighbor position, i.e. in $\langle 1\,1\,1 \rangle$ direction. Here, various situations are shown: the vacancy "feels" a totally relaxed lattice at each instant of the jumping event ("relaxed"), the vacancy is relaxed but the jumping process occurs much faster as the lattice is able to respond to ("static"), and, the vacancy itself "hops" from position to position in a quick sequence, so that the surrounding atoms do not even "see" the vacancy ("frozen"). The corresponding barrier heights

range from approx. 2.5eV to approx. 3.3eV, an energy range which is possibly surmounted by thermally "activated" atoms. In literature the next-to-nearest neighbor jumps, i.e. in $\langle 1\,0\,0 \rangle$ direction, are considered as possible in bcc-lattices. Here, the energy barriers range from approx. 4.7eV for the totally relaxed situation to approx. 15.2eV for the "frozen" case, which is definitely beyond the scope to be crossed thermally.

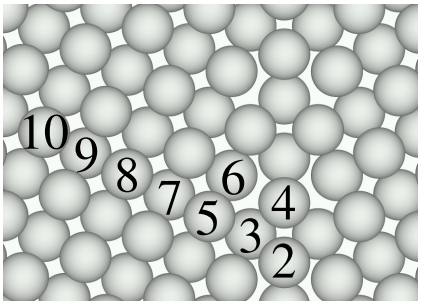

Fig. 6.12: *The nomenclature used to study the diffusional barriers. Only symmetrically non equivalent sites are numbered.*

site s	2	3	4	5	6	7	8	9	10
$E^s_{vf}(rel)$(eV)	1.87	3.13	3.26	3.15	2.63	3.68	3.55	3.62	3.57
$E^s_{vf}(stat)$(eV)	2.12	3.57	3.70	3.47	3.33	3.97	3.86	3.91	3.86

Table 6.3: *The* vacancy formation energies *determined from MD simulations in either totally relaxed ($E^s_{vf}(rel)$) or static ($E^s_{vf}(stat)$) situations.*

6.5 Edge Dislocation Structure and Energy

Dislocation Dynamics is of primary interest especially in bcc metals, as plastic deformation, at least at intermediate temperatures, is carried through the specific motion of dislocations. Dislocations are stress states which are concentrated along lines, i.e. are one dimensional in nature. In general we distinguish between *edge* and *screw* dislocations.

6.5.1 Single Edge Dislocations

A single edge dislocation was constructed within an parallelepiped-shaped simulation box. The simulation cell we used was spanned by the bcc lattice

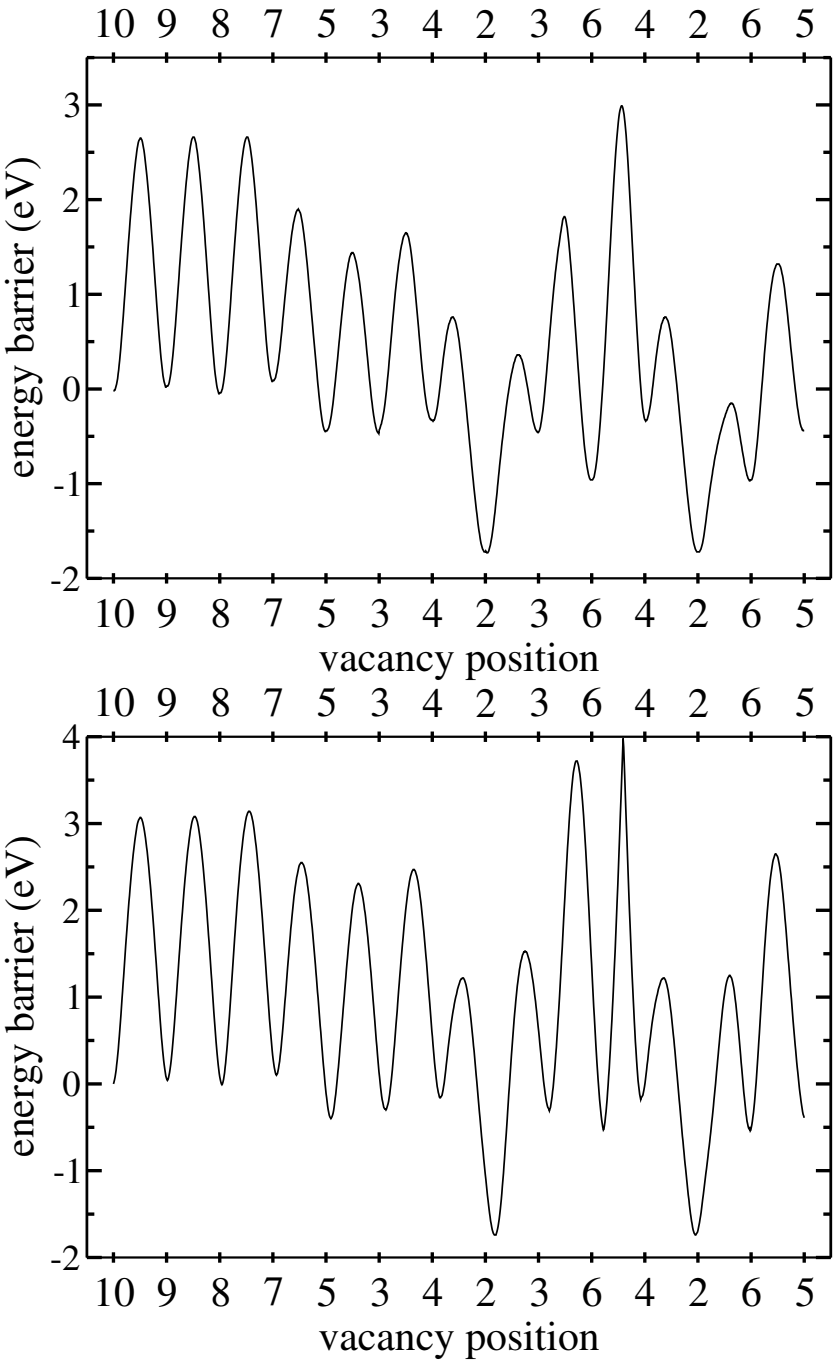

Fig. 6.13: *Energy barriers for a migrating vacancy. The energy landscape a vacancy has to surmount along its journey through the crystal along a* $\Sigma 5$ *grain boundary is illustrated. The energy of a totally relaxed lattice for the migrating vacancy (above) and of a static lattice where only the "jumping" atom is allowed to relax in the plane perpendicular to the transition path (below) is compared.*

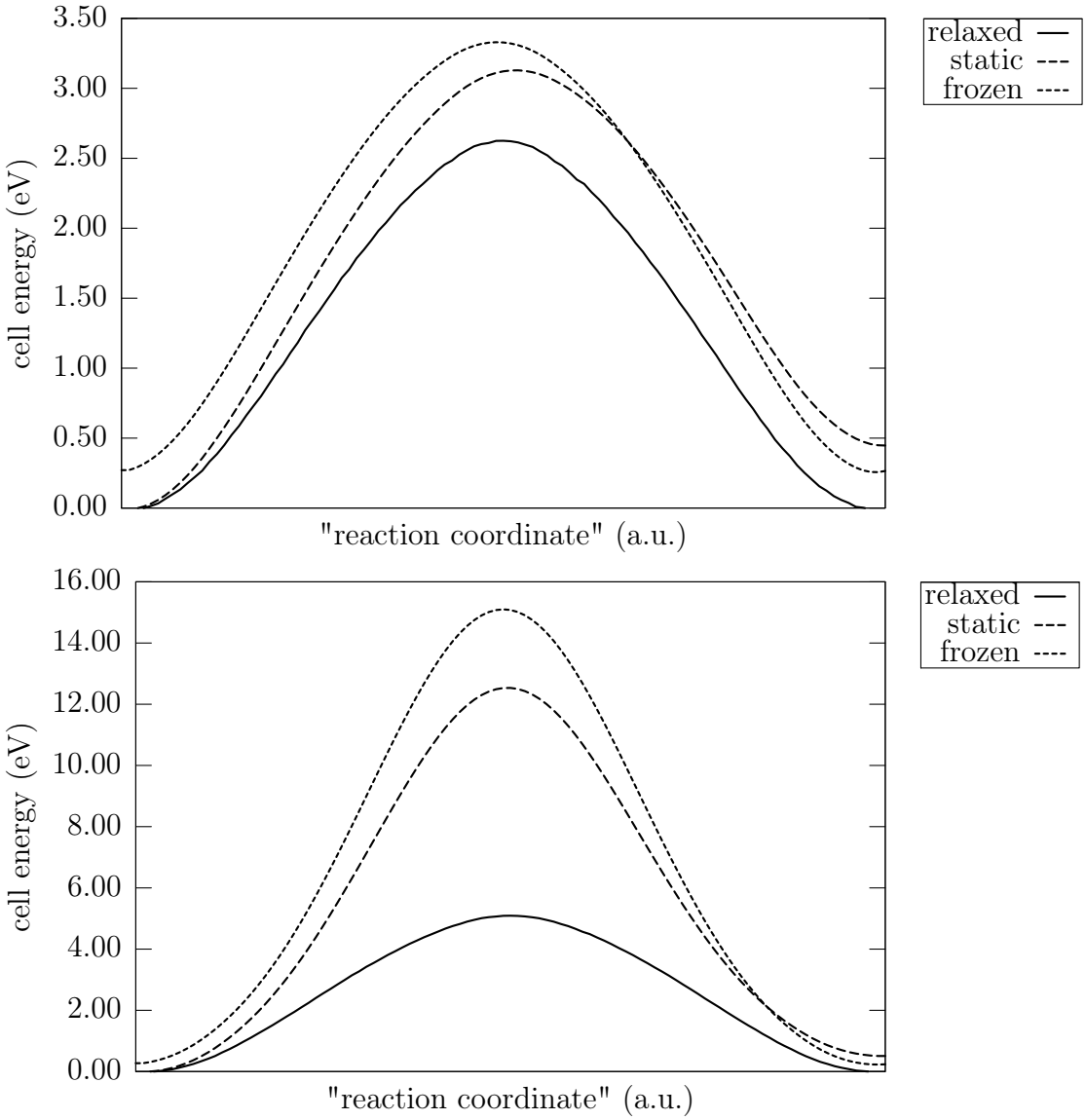

Fig. 6.14: *Energy barriers for a migrating vacancy located inmidst the bulk (bcc) lattice, when "jumping" to a nearest neighbor position, i.e. in* $\langle 1\,1\,1 \rangle$ *direction are depicted. Various possible situations are shown: the vacancy is located within a totally relaxed lattice at each instant of the jumping event ("relaxed"), the vacancy is relaxed but the jumping process occurs much faster as the lattice is able to respond to ("static"), and, the vacancy itself "hops" from position to position in a quick sequence, so that the surrounding atoms do not even "see" the vacancy ("frozen"). Furthermore, sometimes the next-to-nearest neighbor jumps, i.e. in* $\langle 1\,0\,0 \rangle$ *direction, are discussed as possible in bcc-lattices. The corresponding energies for these cases are presented, too (right).*

site	→	site	E_{rel}^{mb}(eV)	E_{stat}^{mb}(eV)	site	→	site	E_{rel}^{mb}(eV)	E_{stat}^{mb}(eV)
2	→	3	2.09	3.27	3	→	2	0.82	1.82
2	→	4	2.48	2.96	4	→	2	1.10	1.38
2	→	6	1.57	2.99	6	→	2	0.81	1.76
3	→	4	2.08	2.77	4	→	3	1.98	2.63
3	→	5	1.91	2.60	5	→	3	1.88	2.70
3	→	6	2.27	4.03	6	→	3	2.78	4.25
4	→	6	3.31	4.16	6	→	4	3.95	4.50
5	→	6	1.76	3.04	6	→	5	2.28	3.19
5	→	7	2.35	2.95	7	→	5	1.81	2.44
7	→	8	2.58	3.04	8	→	7	2.70	3.14
8	→	9	2.71	3.09	9	→	8	2.63	3.03
9	→	10	2.63	3.03	10	→	9	2.67	3.07

Table 6.4: *The energy barrier a vacancy "feels" during the transition between two neighboring sites. The barriers are determined within MD simulations in either totally relaxed (E_{rel}^{mb}) or static (E_{stat}^{mb}) situations.*

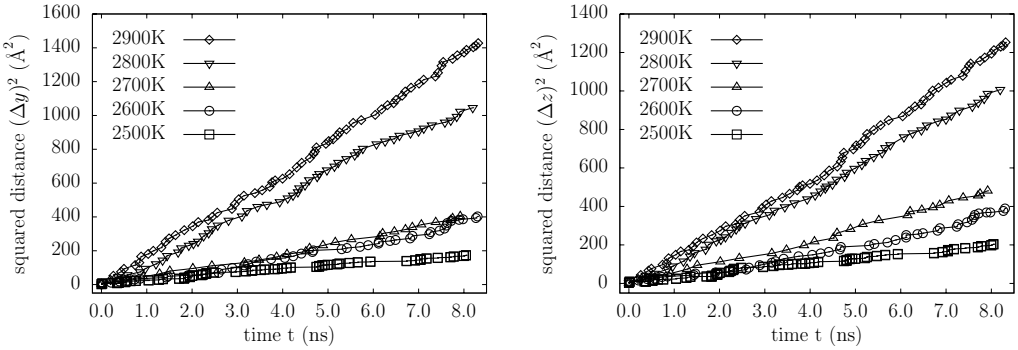

Fig. 6.15: *The squared jumping distance versus time for different temperatures along a* $\Sigma 5$ *symmetrical tilt grain boundary is shown (left: projections of the jumps along the grain boundary perpendicular to the tilt axis; right: projections along the tilt axis). The simulation box contained 2000 tungsten atoms and system trajectory is followed for approx.* 8ns.

D^B (Å^2/ns)	2500K	2600K	2700K	2800K	2900K	D_0^B (Å^2/ns)	Q^B (eV/K)
D_y^B	11.17	21.62	24.25	65.47	84.53	$3.3 \cdot 10^{-2}$	3.21
D_z^B	12.66	21.02	29.32	60.52	72.79	$7.0 \cdot 10^{-3}$	2.85

Table 6.5: *The diffusion constants as derived from an MD simulation of 2000 tungsten atoms with a vacancy inserted in the simulation box inmidst a* $\Sigma 5$ *grain boundary for various temperatures are shown. From these data fitted against* $D^B = D_0^B \cdot \exp(-Q^B/k_B T)$ *the effective activation energy* Q^B *and pre-exponential factor* D_0^B *are derived.*

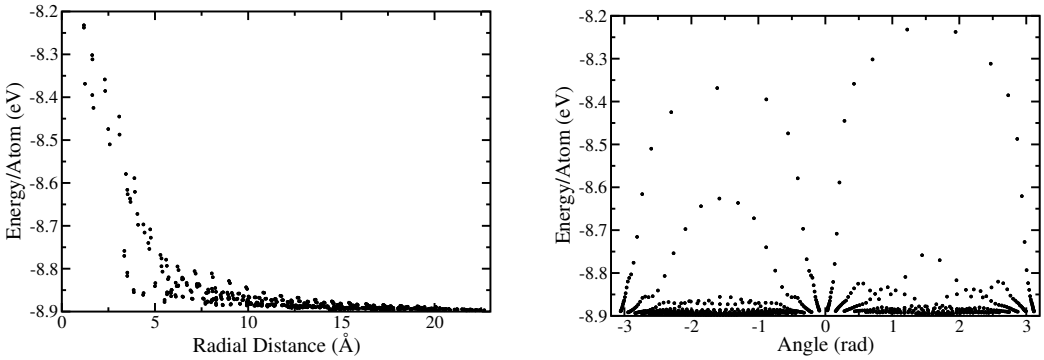

Fig. 6.16: *Energy per atom vs. radial distance (left) from and angle (right) around the dislocation line for an edge dislocation with Burgers vector* $\mathbf{b} = \frac{1}{2}[111]$ *in a tungsten crystal.*

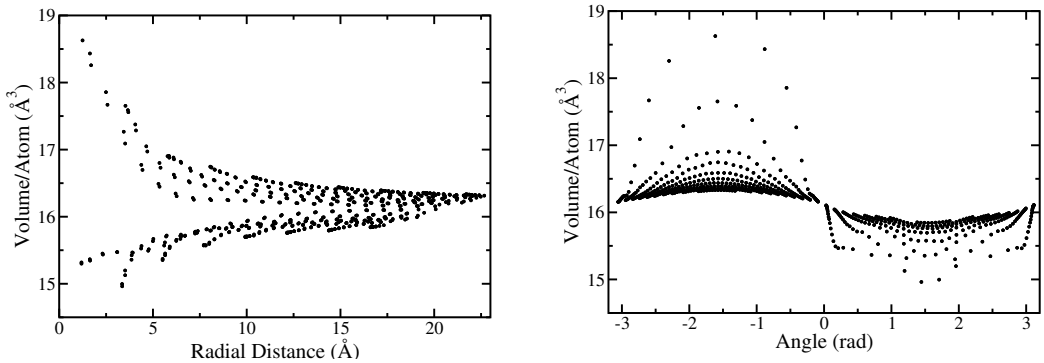

Fig. 6.17: *"Atomic" volume vs. radial distance (left) from and angle (right) around the dislocation line for an edge dislocation with Burgers vector* $\mathbf{b} = \frac{1}{2}[111]$ *in a tungsten crystal. The volumes are generated via a* Voronoi *tessellation.*

T (K)	site	τ_{Dwell}^{total} (ps)	# visits	τ_{Dwell}^{avg} (ps)
2500	6	$1.601 \cdot 10^{1}$	16	$1.001 \cdot 10^{0}$
	2	$8.004 \cdot 10^{3}$	55	$1.455 \cdot 10^{0}$
	3	$2.608 \cdot 10^{1}$	40	$6.52 \cdot 10^{-1}$
2600	4	$4.5 \cdot 10^{0}$	13	$3.462 \cdot 10^{-1}$
	6	$2.091 \cdot 10^{1}$	30	$6.971 \cdot 10^{-1}$
	2	$8.135 \cdot 10^{3}$	104	$7.822 \cdot 10^{1}$
	3	$4.163 \cdot 10^{1}$	63	$6.608 \cdot 10^{-1}$
2700	5	$5.621 \cdot 10^{1}$	3	$1.874 \cdot 10^{1}$
	6	$2.023 \cdot 10^{1}$	37	$5.469 \cdot 10^{-1}$
	2	$8.205 \cdot 10^{3}$	131	$6.263 \cdot 10^{1}$
	3	$7.063 \cdot 10^{1}$	98	$7.207 \cdot 10^{-1}$
2800	4	$8.654 \cdot 10^{0}$	45	$1.923 \cdot 10^{-1}$
	5	$3.27 \cdot 10^{1}$	5	$6.54 \cdot 10^{0}$
	6	$2.722 \cdot 10^{1}$	63	$4.321 \cdot 10^{-1}$
	2	$8.173 \cdot 10^{3}$	252	$3.243 \cdot 10^{1}$
	3	$9.789 \cdot 10^{1}$	151	$6.483 \cdot 10^{-1}$
2900	4	$1.283 \cdot 10^{1}$	71	$1.807 \cdot 10^{-1}$
	5	$3.64 \cdot 10^{1}$	7	$5.201 \cdot 10^{0}$
	6	$4.591 \cdot 10^{1}$	84	$5.465 \cdot 10^{-1}$
	2	$8.096 \cdot 10^{3}$	318	$2.546 \cdot 10^{1}$
	3	$1.37 \cdot 10^{2}$	175	$7.83 \cdot 10^{-1}$

Table 6.6: *The* total dwell time τ_{Dwell}^{total} *and the* averaged dwell time τ_{Dwell}^{avg} *for temperatures from* 2500K *to* 2900K *and for the sites occupied by the vacancy along the trajectory inserted inmidst the* $\Sigma 5$ *symmetrical tilt grain boundary at the very beginning are shown. Only those lattice sites visited by the vacancy are given.*

vectors $\mathbf{X} \propto [111]$, $\mathbf{Y} \propto [1\bar{1}0]$ and $\mathbf{Z} \propto [11\bar{2}]$. The box size was chosen to contain approximately 50000 atoms. It contains a crystallite in which a perfect edge dislocation line oriented along $\mathbf{Z}$ and with Burgers vector $\mathbf{b} = \frac{1}{2}[111]$ is introduced as follows:

In contrast to a pure *screw* dislocation, a *edge* dislocation results in a displacement field, which has compressive as well as dilated spatial regions even from a pure elastic continuum approach, i.e. even without taking anharmonic interaction energies of the atoms into account. The *atomic volumes* versus an coordinate along the cell constructed is shown in Fig. 6.19. The relative change in volume for the case of an edge dislocation in an isotropic

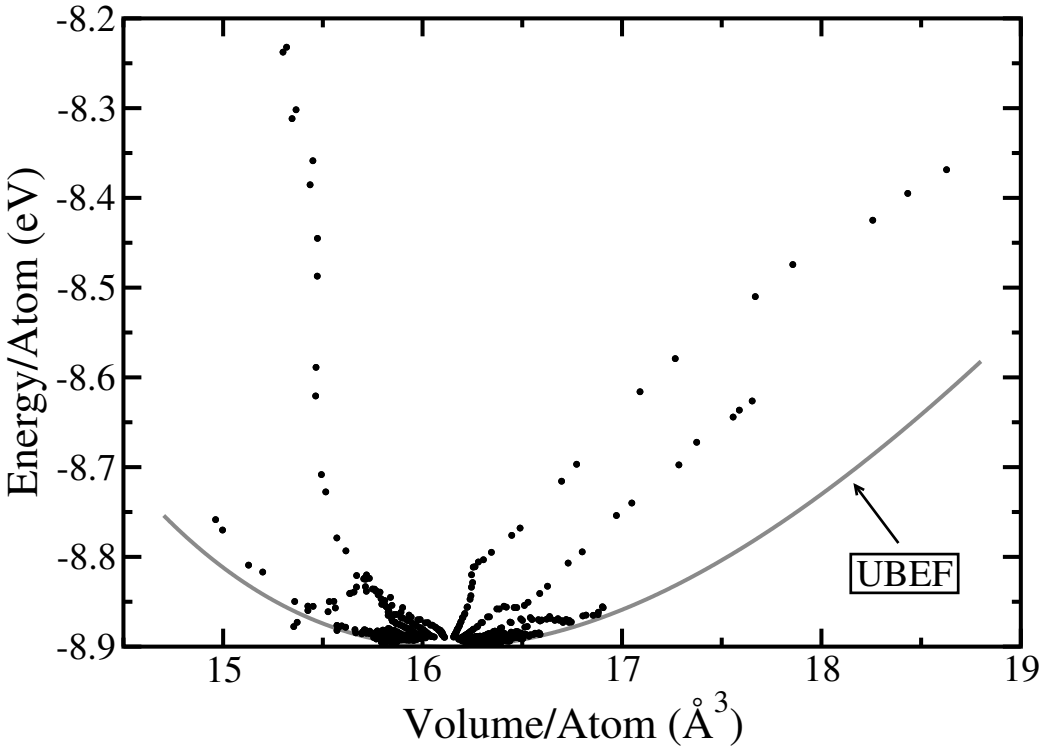

Fig. 6.18: *Energy per atom versus "atomic" volume. Also shown is the* universal binding energy function *(UBEF), (5.64), for comparison reasons, see text.*

medium is given from continuum theory as:

$$\frac{dV}{V} = -\frac{b\sin(\phi)(1-2\nu)}{2\pi(1-\nu)r} \tag{6.30}$$

where b denotes the magnitude of the *Burger's vector* and ν the *Poisson's number* of the elastic medium.

The influence of segregated Th-atoms on the structure of edge dislocations was determined as follows: as Th atoms would produce very large strains in the bulk lattice when placed on interstitial sites, they are supposed to occupy regular sites located at the dislocation core. Therfore, in a pure system containing an edge dislocation we removed one W atom and replaced it by a Th atom. The simulation cell is subdivided in 48 slabs in $[1\bar{1}0]$-direction and slabs 1, 2, 47 and 48 are kept fixed in space. Slabs 1 and 2 are then shifted by $\Delta x = \sqrt{3}a_0/2 \cdot (\frac{1}{2})^9$ in [111]-direction and at the same time slabs 47 and 48 are shifted about the same amount in the opposite direction. This results in a tilted simulation box with pure shear strains and corresponding stresses.

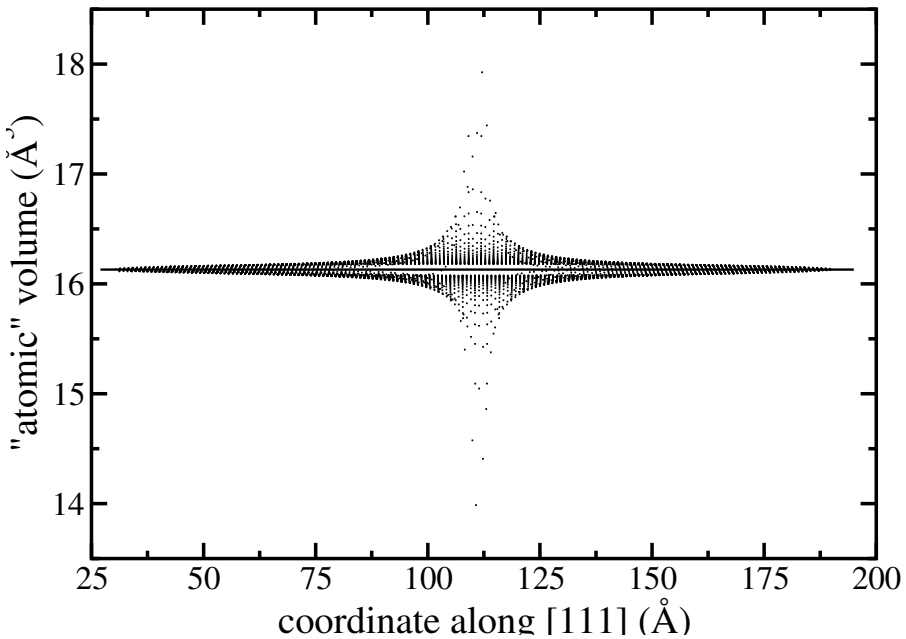

Fig. 6.19: *"atomic volumes", i.e. volumes as calculated from a* Voronoi tessellation *of the coordinates of the atoms in the simulation cell along the* $\mathbf{X} \propto [111]$*-direction, i.e. in direction of the* Burgers vector*, for an edge dislocation are shown.*

This straining procedure, for the definition of quantities and a schematic illustration, see Fig. 6.21, can be described by the deformation tensor

$$\epsilon_{ij} := \frac{\Delta x}{H}(\delta_{1i}\delta_{2j} + \delta_{2i}\delta_{1j}) \equiv \epsilon(\delta_{1i}\delta_{2j} + \delta_{2i}\delta_{1j}) \tag{6.31}$$

in the orientation spanned by $[1\,1\,1]$, $[1\,\overline{1}\,0]$ and $[1\,1\,\overline{2}]$. The energy density generated by straining as described, therefore, is given as

$$e = \sigma_{12}\,\epsilon \tag{6.32}$$

The stress component, therefore, we are interested in is

$$\sigma_{12} = \frac{\partial e}{\partial \epsilon}\,. \tag{6.33}$$

The strain at which the edge dislocation starts to separate from the Th impurity is calculated as $\epsilon^m = 5.19 \cdot 10^{-3}$. The corresponding maximum shear stress component, therefore, is given by $\sigma_{12}^m = 3.94 \cdot 10^{-5}/5.19 \cdot 10^{-3}\mathrm{eV/\AA}^3 = 7.59\mathrm{meV/\AA}^3 = 1.22\mathrm{GPa}$. With *Hooke's law* and the deformation tensor as defined above, the energy density is also given by:

$$e = 2\,\epsilon^2\,c_{1212} \tag{6.34}$$

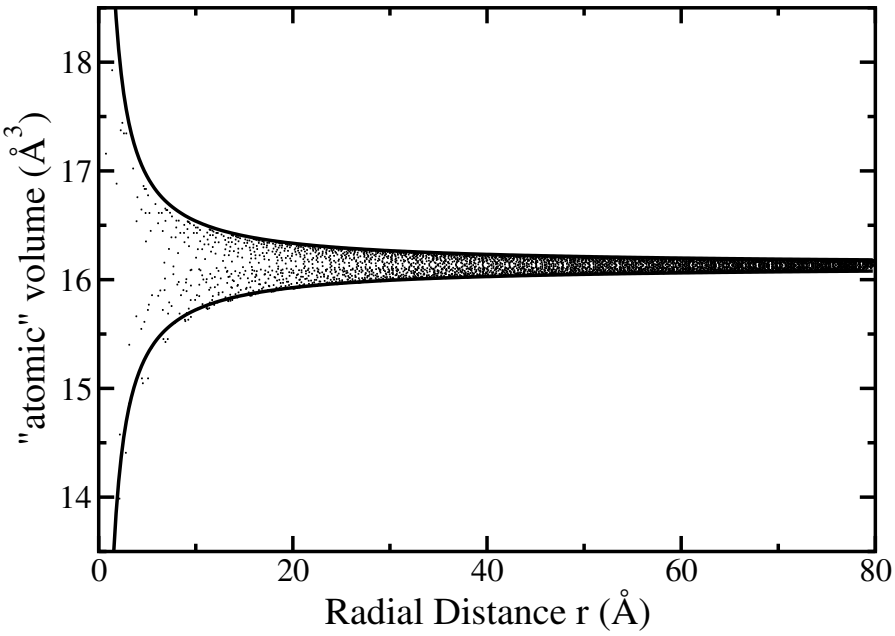

Fig. 6.20: *"atomic volumes" from a* Voronoi tessellation *versus distance from the dislocation line together with the continuum theoretic approach, Eq. (6.30).*

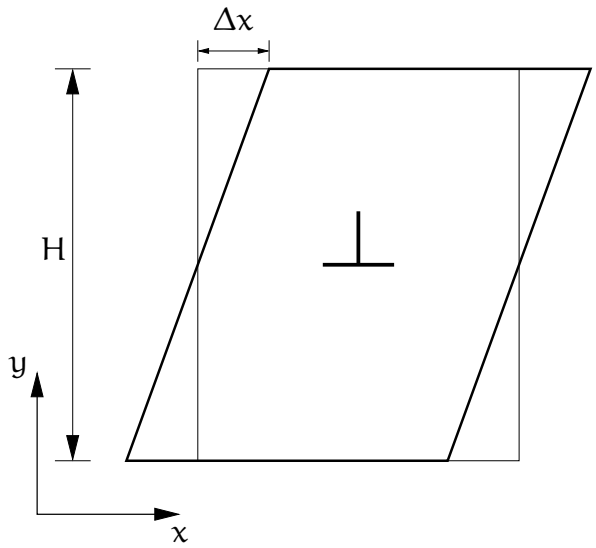

Fig. 6.21: *The straining procedure of a simulation box containing a single edge dislocation as described by Eq. (6.31) is shown schematically. This straining results in a pure shear of the y-plane, i.e. the glide plane of the dislocation chosen, in x-direction.*

where c_{1212} denotes the elastic constant in the coordinate system as specified. Fitting the energy vs strain curve results in $c_{1212} = 0.74\text{eV}/\text{Å}^3 = 119\text{GPa}$. Due to the overwhelming majority of tungsten atoms, c_{1212} should not be affected very much due to the presence of Th impurities in the simulation cell, so that c_{1212} should also be a good guess for simulation cells without Th impurities. The corresponding simulations without Th impurities, i.e. pure tungsten, shows a maximum strain of $\epsilon^m = 1.44 \cdot 10^{-4}$. This results in a maximum stress, the *Peierls stress*, of

$$\sigma_P = 2\,\epsilon^m\, c_{1212} = 0.21\text{meV}/\text{Å}^3 = 34\text{MPa} \tag{6.35}$$

at which the dislocation starts to glide. σ_P is much smaller, more than one order of magnitude, compared to the thoriated case. This shows once again the tendency of thorium in tungsten to enhance significantly the recrystallization temperature to surmount σ_P.

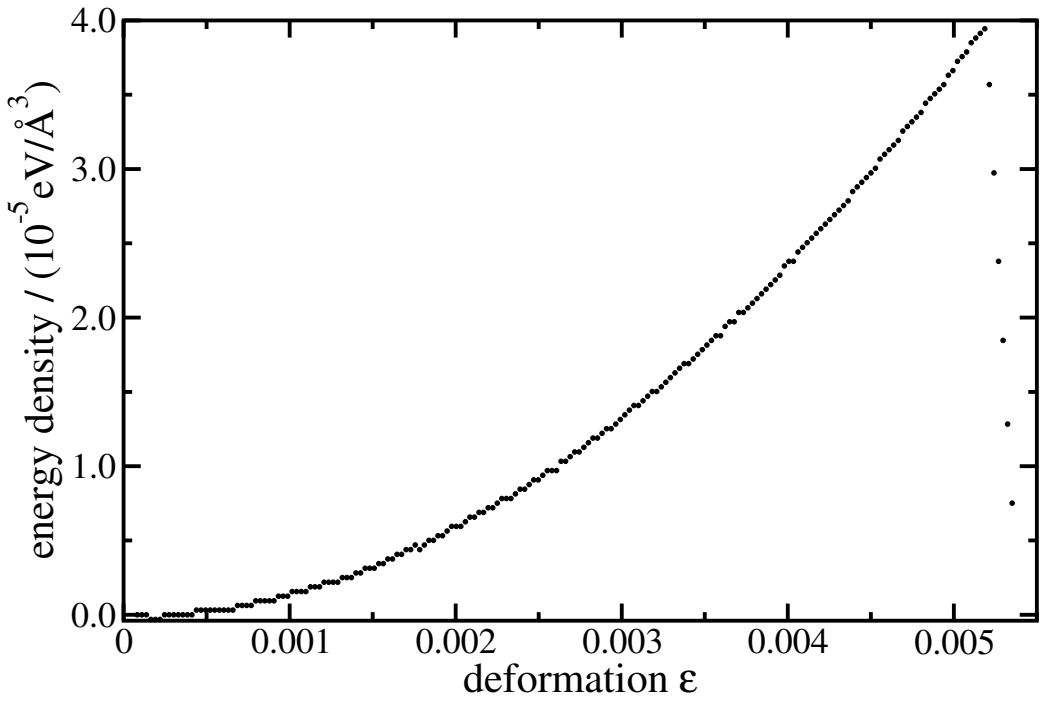

Fig. 6.22: *The energy density versus deformation for a simulation cell containing en edge dislocation and Th impurities along the dislocation line.*

The force on an isolated Th-atom can be calculated using Haasen-Fleischer's theory. For this we set an Th-atom near the glide plane of an edge dislocation. The energies of the cells are calculated and the Th-atom is shifted

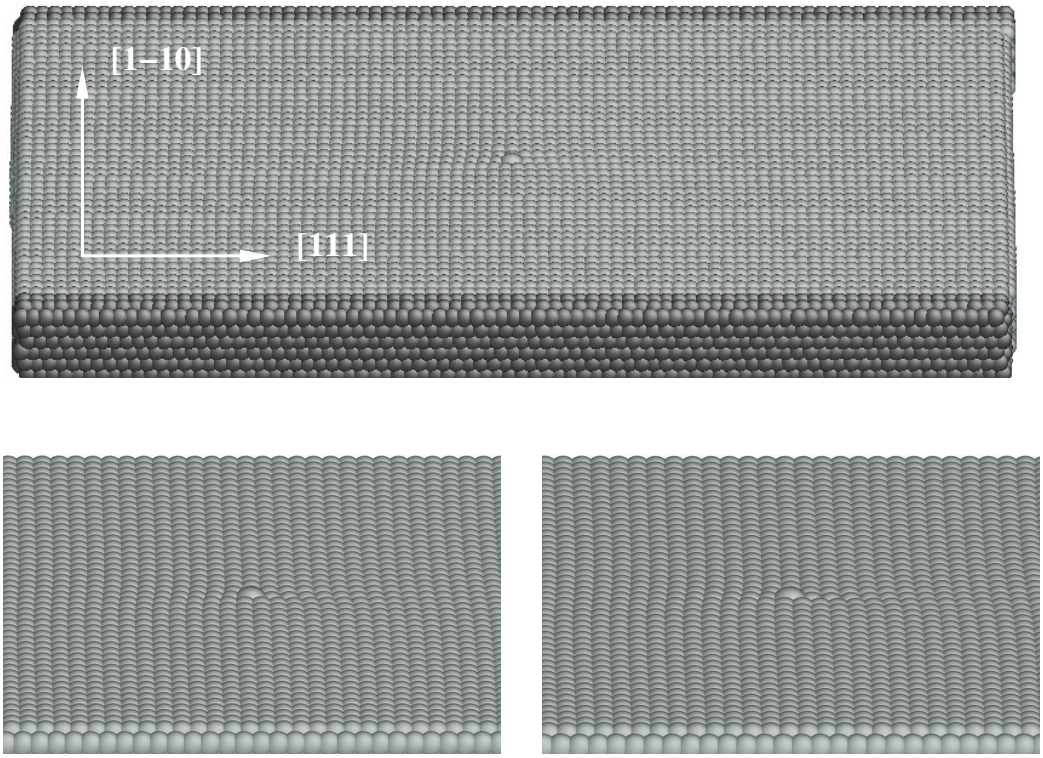

Fig. 6.23: *The simulation cell containing an edge dislocation is shown (above). The cell contains approximately 50000 atoms. Periodic boundary conditions are chosen in* $[11\overline{2}]$*-direction, whereas the remaining orthogonal directions (*[111], $[1\overline{1}0]$*) are dealt as free surfaces. The shaded regions are kept fixed during relaxation of the cell. The "thicker" atom marks the thorium atom. Its position is chosen on the dislocation core. Also shown are two snapshots of the atomic configurations immediately before (lower left) and after (lower right) the unsnapping of the dislocation off the thorium atom (see text).*

along [111]-direction. The resulting energies are fitted against

$$e = a_0/(1 + a_2|x - a_1|^{a_3}) \tag{6.36}$$

with

$$a_0 = -0.75eV; \quad a_1 = 10.3502; \quad a_2 = 0.23564; \quad a_3 = 2.23941; \tag{6.37}$$

and shown in Fig. 6.24. Also, the *configurational force* between Th atom and dislocation line is calculated as the derivative of Eq. (6.36). From Fig. 6.24 it can be seen that there is strong tendency of a Th impurity to trap the

dislocation line, i.e. it needs additional energy to release the dislocation line once trapped. The tendency to trap decreases with increasing distance of the Th atom from the glide plane. Moreover, the width of the "trapping region", i.e. the region on the glide plane with attractive forces on the dislocation line increases with increasing distance of the Th atom from the glide plane.

6.6 Screw Dislocation Structure and Energy

For a *screw* dislocation, the *Burgers vector* and the dislocation line direction are *collinear*. It is interesting to note, that in a *bcc* lattice, a screw dislocation with *Burgers vector* $\mathbf{b} = \frac{a_0}{2}[1\,1\,1]$ have high as well as low energy positions due to the geometry of the underlying lattice, which is also the origin for the high *Peierls* potential [Suz68]. Fig. 6.25 shows two alternative configurations of a screw dislocation yielding different line energies. An undisturbed bcc lattice is shown in (a), viewing direction is the [1 1 1] direction. The numerals indicate atomic positions as projected onto the (1 1 1) plane and their heights in [1 1 1] direction in units of the nearest neighbor distance. It can be seen in (a) that the atoms in neighboring triangular [1 1 1] atomic rows form a spiral configuration and its winding direction changes alternately as shown at **A** and **B**. The result of the superposition of the perfect strain field of a screw dislocation as given within isotropic elasticity theory (b) at **A** or **B**, results in atomic positions as shown in (c) and (d), respectively. The atomic positions of the dislocation at **A** shows the same spiral arrangement of neighboring [1 1 1] rows as in the undisturbed lattice, whereas the dislocation at **B** shifts atoms in neighboring [1 1 1] rows onto the same plane, therefore reducing the interatomic distance and, as a consequence, increases the line energy considerably. Thus, the dislocation core energy should be considerably higher for the dislocation at **B** compared to the one at **A**. This yields for a moving screw dislocation alternately to high and low line energies with distance from ridge to ridge of $(2\sqrt{2}/3)b$ and equals the distance between subsequent *Peierls potential barriers*.

In order to calculate the *Peierls stress* for the screw dislocations, we use the following setup: First, a cell oriented along $\mathbf{X} = 52[1\,\bar{1}\,0]$,$\mathbf{Y} = 30[1\,1\,\bar{2}]$ and $\mathbf{Z} = 6[1\,1\,1]$ was constructed. Inside a cylinder with radius $R = 26 \cdot a_0 \cdot \sqrt{2}$ a screw dislocation with *Burgers vector* $\mathbf{b} = a_0/2[1\,1\,1]$ with displacement field $u_z = b\Theta/2\pi r$ was established. After relaxing the structure inside the cylinder, the atoms in the outermost shell of the cylinder with a thickness of 15Å was fixed in space. The resulting structure served as the starting point for the simulations, see Fig. 6.26.

The following procedure is quite similar to the one used for the *Peierls*

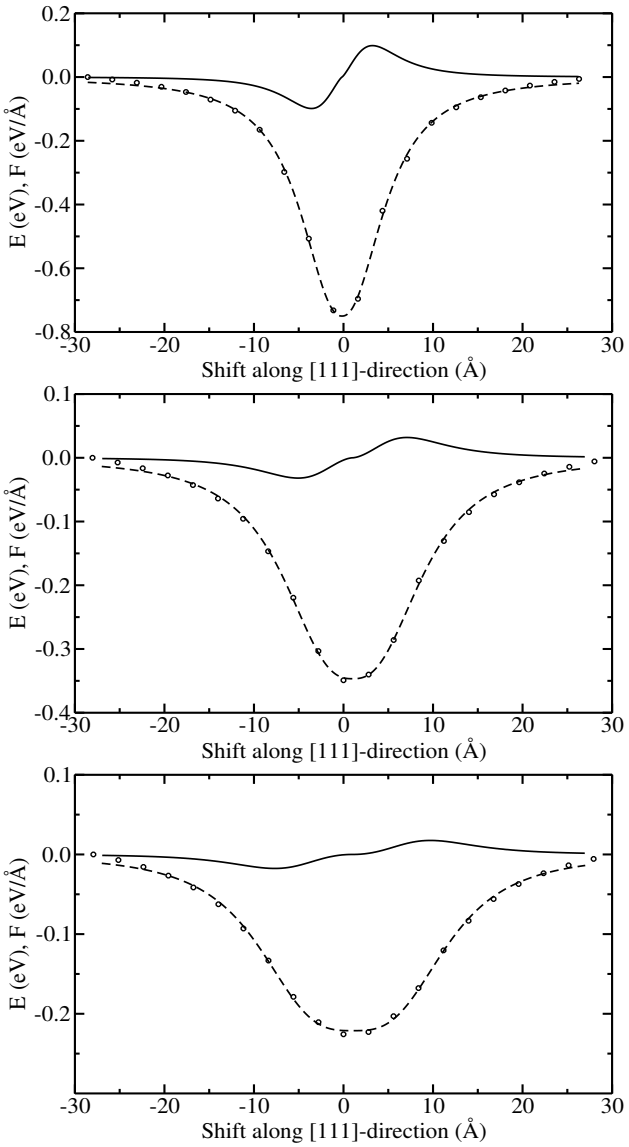

Fig. 6.24: *The change in energy (dashed) and the corresponding "force" (solid) between dislocation and Th atom located on a lattice plane parallel to the glide plane of a* $\frac{1}{2}[1\,1\,1]$ *edge dislocation is shown. The "force" was calculated as the derivative of the cell energy with respect to the shift of the Th atom in direction of the Burgers vector. The figures from top to bottom show the influence of a dislocation line passing a Th atom located on lattice planes with increasing distance to the glide plane.*

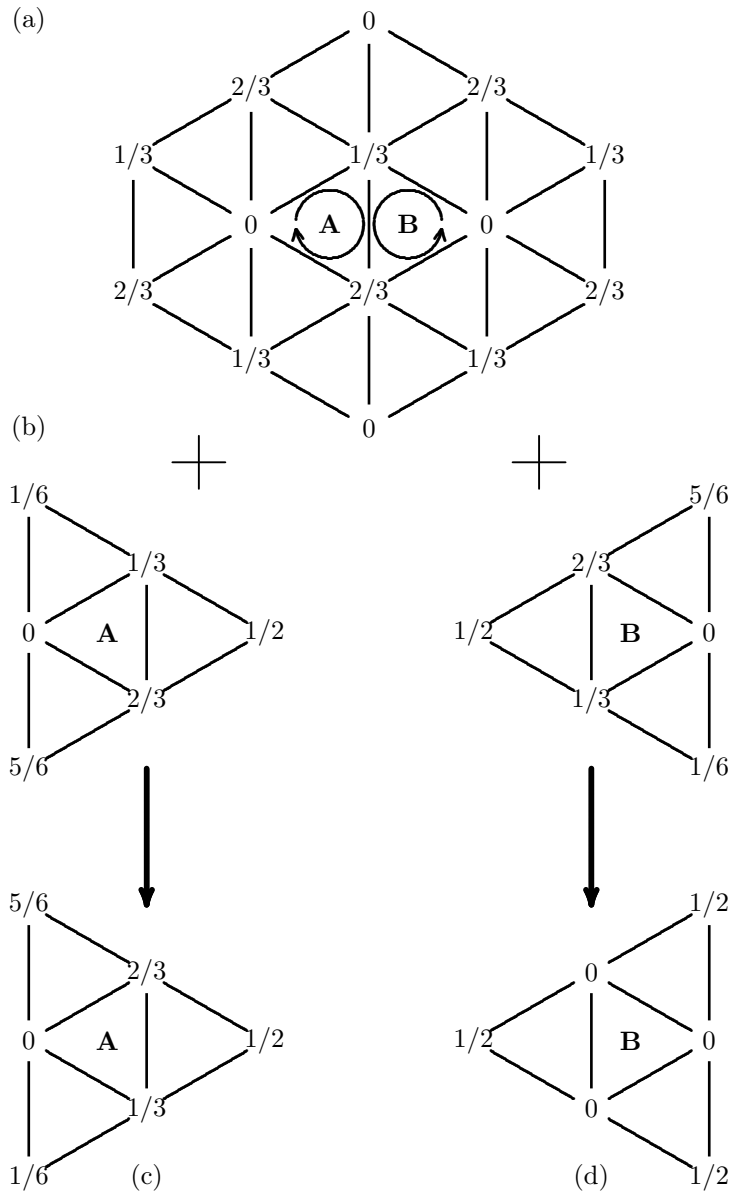

Fig. 6.25: *Changes of the atomic positions when a screw dislocation is introduced at position A or B in the perfect* bcc *lattice.(a) sketches the perfect lattice (the lattice is oriented with* $[1\,1\,1]$ *normal to the paper plane). The numerals at the atomic positions indicate the height of the atoms in* $[1\,1\,1]$ *direction in units of the nearest neighbor distance. (b) the strain field of a screw dislocation (*$\mathbf{b} \propto [1\,1\,1]$*) according to elasticity theory. (c) and (d) show the results after inserting the screw dislocation in the undisturbed lattice [STY91]*

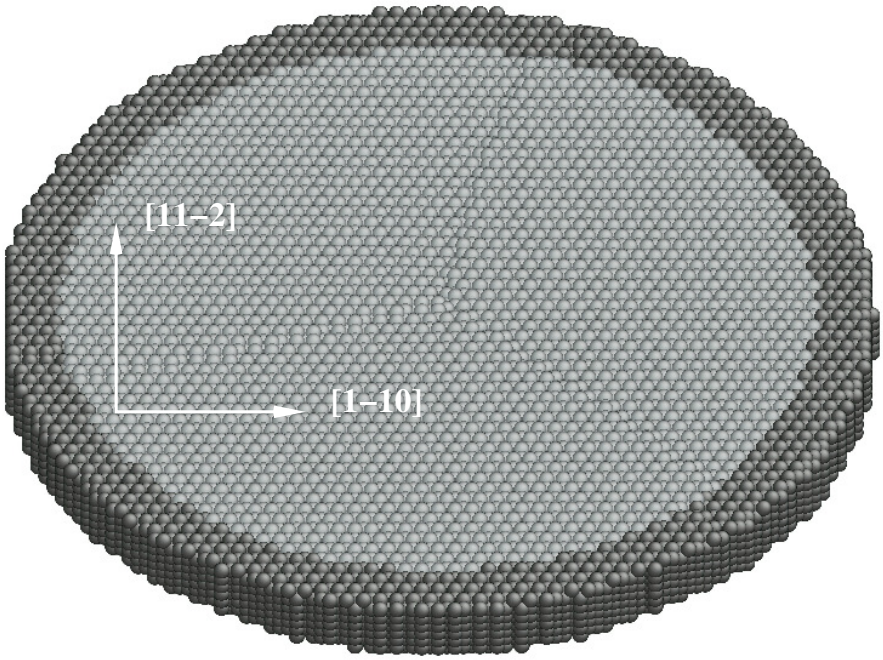

Fig. 6.26: *The relaxed starting cell, i.e. the structure which served as starting point for the MD simulations of the screw dislocation.*

stress of the edge dislocation: The cylinder was then strained in various steps and the corresponding energy density was recorded. The results for different glide planes are given in Figs. 6.27 and 6.28. The strain tensor used was this time given by

$$\epsilon_{ij} := \epsilon(\delta_{2i}\delta_{3j} + \delta_{3i}\delta_{2j}) \tag{6.38}$$

and the corresponding linear elastic energy density

$$e = 2\,\epsilon^2\,c_{2323} \tag{6.39}$$

where, as usual, c_{2323} denotes the elastic constant involved in this straining procedure. The fitting results in $c_{2323} \approx 153$GPa. The corresponding *Peierls stress* is calculated to $\sigma_P \approx 2.20$GPa. The interaction of a Th impurity atom

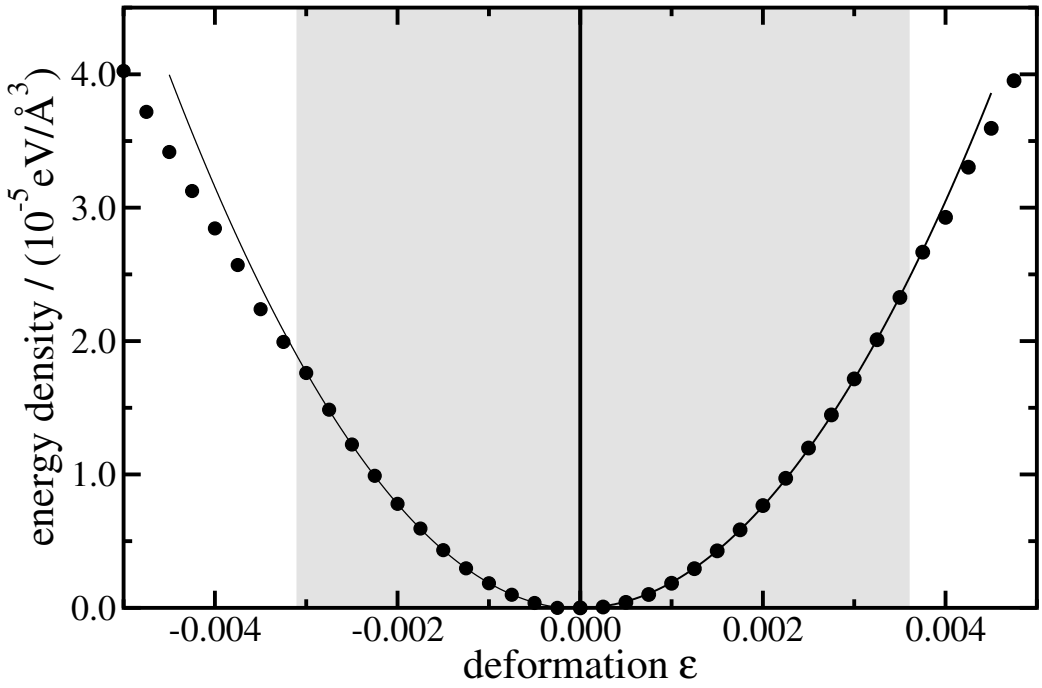

Fig. 6.27: *Energy density vs. lattice strain of a screw dislocation with* Burgers vector $b \propto [1\,1\,1]$ *and slip plane* $(1\,1\,2)$. *The points are the results from the MD simulation and the shaded region marks those points used to fit against* $e = 2\,\epsilon^2\,c_{2323}$. *For positive deformations* $\epsilon \gtrsim 3.6 \cdot 10^{-3}$ *and negative deformations* $\epsilon \lesssim -3.1 \cdot 10^{-3}$ *there is a more and more pronounced deviation from the fitted parabola (solid line).*

with a screw dislocation is at its maximum when the impurity is located in the dislocation core. To estimate the influence of a Th impurity on the the glide movement of the screw dislocation, we therefore put an atom in-midst the dislocation core and increased the stress on the dislocation with the straining procedure introduced above. The result is shown in 6.29. The stress at which the dislocation starts to move can be estimated to be $\sigma^m \approx 2.51$GPa and, therefore, the influence of the impurity atom on the drag of the dislocation is only small compared to the comparable situation in edge dislocations. In this sense, edge and screw dislocations behave quite differently in the presence of Th impurity atoms.

Plastic deformation is accompanied with moving dislocations. The onset of this movement should depend solely on the *critical resolved shear stress* for a given *slip system*, and, therefore, should be a function of applied external stress and inclination of the glide plane within the given stress state. From a continuum theoretical standpoint, it should be independent of the *direction* of

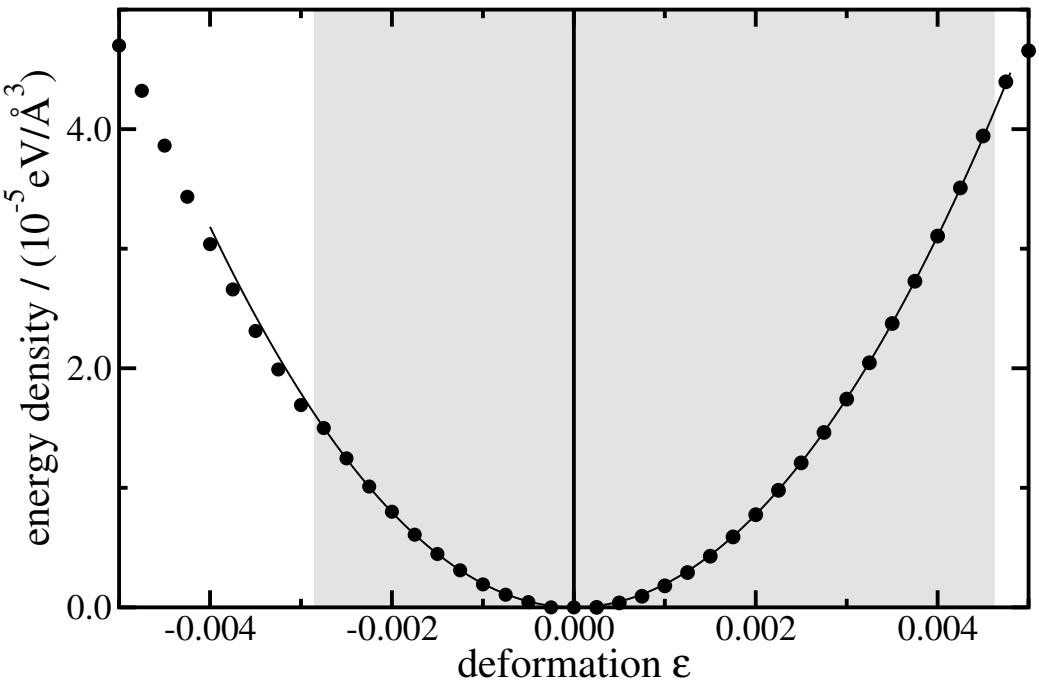

Fig. 6.28: *Energy density vs. lattice strain of a screw dislocation with* Burgers vector $b \propto [1\,1\,1]$ *and slip plane* $(1\,1\,0)$. *The points are the results from the MD simulation and the shaded region marks those points used to fit against* $e = 2\,\epsilon^2\,c_{2323}$. *For positive deformations* $\epsilon \gtrsim 4.6 \cdot 10^{-3}$ *and negative deformations* $\epsilon \lesssim -2.9 \cdot 10^{-3}$ *there is a more and more pronounced deviation from the fitted parabola (solid line).*

slip, i.e. the onset of shear deformation of a single crystal should not depend on pushing or pulling as long as we do not change the loading axis (*Schmid's law*). Things changes, when we take the discrete matter into account: the local environment, i.e. the atomic configuration, of a dislocation can change considerably with the viewing direction perpendicular to the dislocation line. This means, that there are chances, that *Schmid's law* is violated in "real" crystals. In order to check this for tungsten, we repeat the deformation procedure described above, but with "inverted" deformation tensor:

$$\epsilon_{ij} := -\epsilon(\delta_{2i}\delta_{3j} + \delta_{3i}\delta_{2j}) \tag{6.40}$$

When *Schmid's law* would be strictly valid, than the "Peierls stress" for this changed sign deformation should be unaffected. The result can be seen in Fig. 6.27 and 6.28. A slight asymmetry is visible, i.e. the Peierls stress in *forward*, i.e. positive sign, direction needs higher onset stress compared to its *backward* counterpart. The calculated difference is about $\Delta\sigma_P = 0.11$GPa.

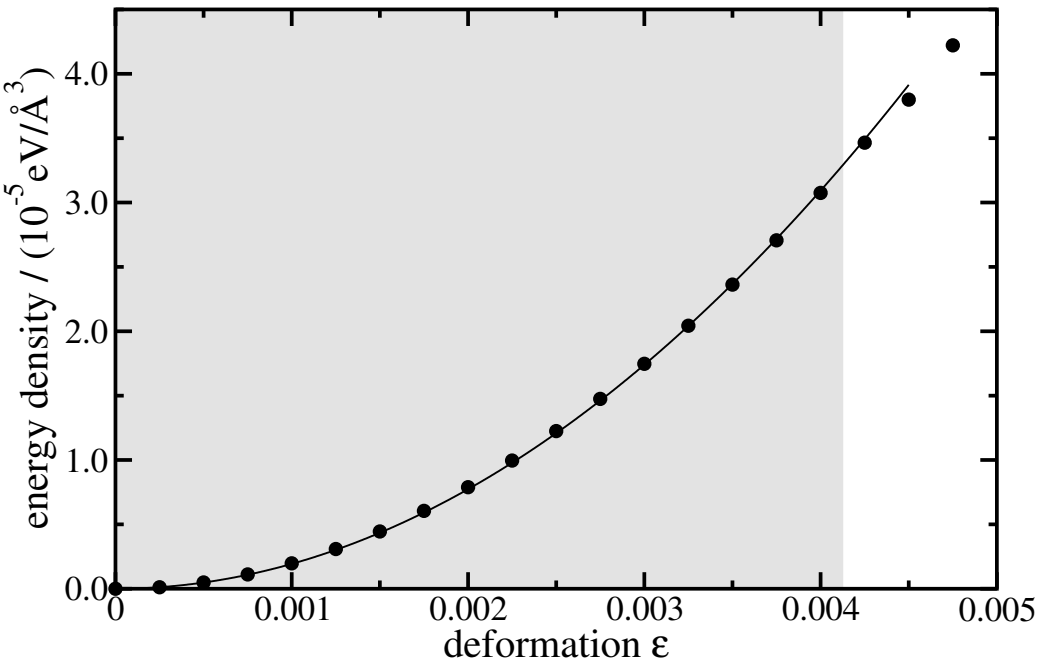

Fig. 6.29: *Energy density vs. lattice strain of a screw dislocation with* Burgers vector $b \propto [1\,1\,1]$ *and slip plane* $(1\,1\,2)$. *The interaction of the screw dislocation and a Th impurity atom is simulated by locating a Th atom in-midst the dislocation core. The points are the results from the MD simulation and the shaded region marks those points used to fit against* $e = 2\,\epsilon^2\,c_{2323}$. *For deformations* $\epsilon \gtrsim 4.1 \cdot 10^{-3}$ *there is a more and more pronounced deviation from the fitted parabola (solid line).*

To explain this at a first glance counter intuitive result, the *sessile dislocation model*, also called the *pseudo Peierls mechanism* [STY91], is sometimes used. Within this model, the dislocation core plays the dominant role: due to the threefold symmetry for this kind of screw dislocation core, there is no mirror symmetry plane containing the dislocation line perpendicular to the slip direction (in practice, $\propto [1\,1\,0]$ or $\propto [1\,1\,2]$), see Fig. 6.30. The core structure of a relaxed dislocation can be readily depicted within a *differential displacement* (DD) map [VPB70]. The DD map of the relaxed tungsten $1/2[1\,1\,1]$ screw dislocation is shown in Fig. 6.31.

6.7 A Dislocation of mixed type

Up to now, we considered only dislocations of either pure screw or pure edge type. But, it is a priori not clear, whether these pure dislocations are in a

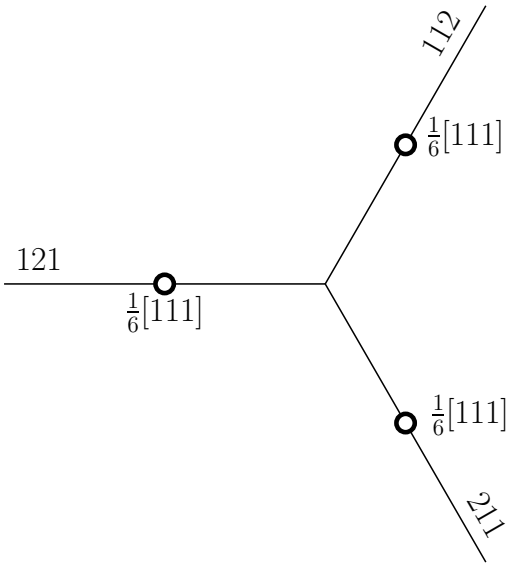

Fig. 6.30: *The commonly assumed threefold splitting of a* $\frac{1}{2}[1\,1\,1]$ *screw dislocation core is sketched. The splitting of the core should result in three* $\frac{1}{6}[1\,1\,1]$ partial dislocations*, where the partials reside on three* 120°*-rotated* $(1\,1\,2)$ *planes. This splitting serves as an explanation of the for bcc-metals quite common violation of* Schmid's law*, which states, that the* Peierls stress *should be independent of "forth" or "backward" shear. This violation is considered to be a result of the broken symmetry of the splitted core: in order to move, the "extended" core has to constrict on the glideplane before a movement of the dislocation can occur. This constriction needs almost surely different stresses in "forth" and "backward" direction.*

sense preferred over a dislocation of mixed type, i.e. with screw as well as edge components. In order to shed some light on a mixed dislocation, we study the well-known [Old86] 71°-dislocation and compare the results with the corresponding ones of the pure dislocations. For the construction of the simulation cell containing this type of dislocation, we follow closely the recipe in [Old86] and the procedure used therein is briefly summarized here. The *Burgers vector* of the 71°-dislocation is assumed to be $\mathbf{b} = a_0/2[1\,1\,1]$, the dislocation line $\mathbf{s}$ shall point into the $[\overline{1}\,\overline{1}\,1]$-direction. The glide plane coincides with the $(\overline{1}\,1\,0)$ plane. With these assumptions, the angle between $\mathbf{b}$ and $\mathbf{s}$ equals $\arccos(1/3) \approx 70°30'$. Furthermore, periodicity along the dislocation line is assumed. For the simulation cell, we make use of the following coordinate system: $X \propto [1\,1\,2]$, $Y \propto [\overline{1}\,1\,0]$ and $Z \propto [\overline{1}\,\overline{1}\,1]$. With these conventions, the Z-axis points along the dislocation line and the Burgers vector resides in the $Y - Z$ plane. For the construction of the edge component

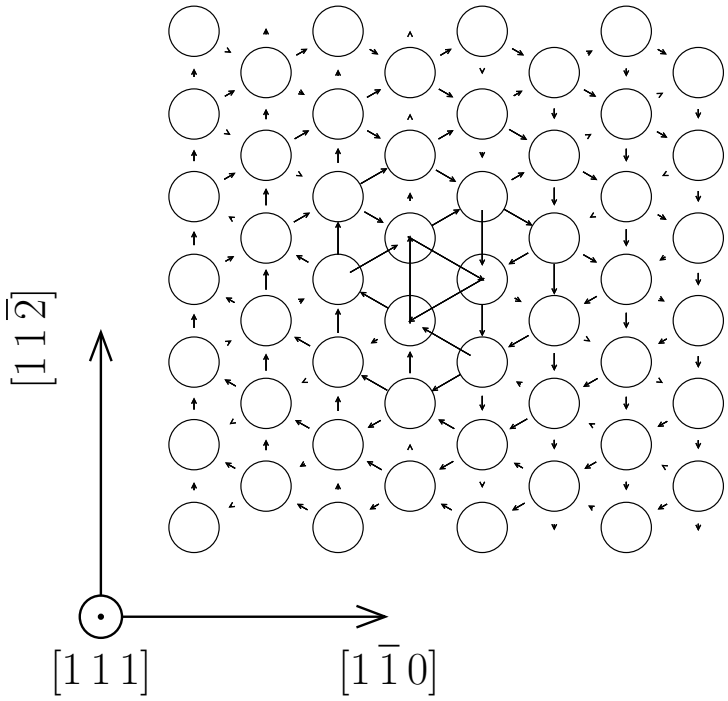

Fig. 6.31: *A* differential displacement map *of the* $a0/2[111]$ *screw dislocation. The lengths of the arrows indicate the relative displacement of neighboring atoms connected by the arrow. The arrow points to a neighbor. [VPB70]*

of the dislocation, we have to ensure, that atoms do not come too close to one another, so that we have to remove a suitably chosen halfplane. This halfplane is normal to the edge component (the X-axis) and starts at the dislocation line. This halfplane has to be swept in normal direction for a distance of one Burgers vector. The atoms in the "sweeping" region then have to be removed. The displacements for screw and edge components are then simply added independently. Therefore, the displacements are given by [Cah70]

$$\begin{aligned} u_x &= \frac{b_e}{2\pi}\left(\frac{xy}{2(1-\nu)(x^2+y^2)} - \Theta\right) \\ u_y &= \frac{b_e}{2\pi}\left(\frac{y^2}{2(1-\nu)(x^2+y^2)} - \frac{1-2\nu}{4(1-\nu)}\ln(\frac{x^2+y^2}{b_e^2})\right) \\ u_z &= \frac{b_s}{2\pi}\left(\frac{\pi}{2} - \Theta\right) \end{aligned} \tag{6.41}$$

where x and y denote the projections of coordinates of the distance of the particle from the dislocation line onto the X- and Y-directions, respectively,

and Θ is the angle between Y-axis and the projection of the particle coordinates onto the $Y - X$ plane. b_e and b_s are the edge and screw components of the Burgers vector, respectively, ν, as usual, is the Poisson number of tungsten ($\nu \approx 0.28$). The geometry of this mixed dislocation within the *bcc*-lattice of tungsten should leave the twofold symmetry axis along the Y-axis untouched. Applying the displacements, Eqs. (6.41), however, destroys this twofold symmetry and has to be restored afterwards. This was done by rotating the atom positions around the Y-direction, calculating the corresponding displacements, rotating the calculated displacements back and, finally, using the arithmetic mean between displacements and rotated ones. Using the procedure as introduced above, it turned out, that two energetically totally different dislocation cores can be constructed: a very high energy core (as used in the theoretical considerations in [Old86]) and a comparably low energy core. The core energy E_{dc} of the dislocations is defined as the difference between the *excess energy* E_{ex} and the *elastic energy* E_{el} per length of the dislocation line,

$$E_{dc} := E_{ex} - E_{el} \tag{6.42}$$

where the excess energy E_{ex} is given by

$$E_{ex} := E_{tot} - N \cdot E_{coh} \tag{6.43}$$

with the total energy of the simulation cell E_{tot} of N atoms in total and the cohesion energy per atom E_{coh}. The corresponding line energies and the detailed procedures to derive them are presented in the upcoming section, see section 6.8 and Tab. 6.7, therein.

The elastic energy E_{el} within a hollow cylinder of outer radius R and inner radius r_0 is well known to diverge, both, approaching the dislocation line (i.e. $r_0 \to 0$) and departing to infinity (i.e. $R \to \infty$)[HL82]:

$$E_{el} = \frac{\mu}{4\pi}\left(b_s + \frac{b_e}{1-\nu}\right)\ln\left(\frac{R}{r_0}\right) \tag{6.44}$$

This divergence in the total energy is addressed in the next section.

6.8 The dislocation line energy: a comparison

In this section, we try to estimate a property of dislocations which is assumed to be independent of the cell volume containing the dislocation: the *dislocation core energy* E_{dc}. A general result from isotropic elastic theory states, that the strain energy per dislocation length within a cylinder of radius R

generated by a straight dislocation arranged along the cylinder axis is given by [HL82]:

$$E(R, r_c) \propto \ln\left(\frac{R}{r_c}\right) . \tag{6.45}$$

Eq. (6.45) shows that $E(R, r_c) \to \infty$ whenever $r_c \to 0$ or $R \to \infty$, and therefore explains the fact, that the total strain energy depends on the simulation cell chosen. To get a cell independent property, we utilize the strain energy in the following form:

$$E(R, r_c) = C(\ln(R) - \ln(r_c)) + E_{dc}(r_c) \tag{6.46}$$

with a suitably chosen constant C. Generally, the result of a MD simulation is the cell energy or the energy per atom. In order to derive the strain energy, it is of crucial importance, to know the cohesion energy E_c, i.e. the energy difference at zero temperature of an atom in an ideal bulk system and a free atom without further bindings to other atoms, accurately. Due to the fitting procedure for the interatomic potential, one cannot assume, that the fitted value for the cohesion energy ($E_c^f = -8.9\text{eV}$) is the exact value for the actual atomic assembly in a MD simulation to arbitrary digits. The actual value of the cohesion energy serves as the zero point for the strain energy. Therefore, as a first step, we had to derive the cohesion energy from an optimization procedure as follows: We constructed a straight dislocation within a cylinder of a typical radius $R_c \approx 220\text{Å}$ according to isotropic elasticity theory as already described. Atoms within an outer ring of width 15Å were held fixed to mimic an infinite isotropic elastic region containing the dislocation. The width of the ring was chosen such that the non-fixed atoms closest to the fixed ring don't suffer from the outer surface of the cylinder. After relaxing the remaining atoms for $t_{relax} \approx 4\text{ps}$ at a temperature of $T = 10^{-3}\text{K}$ we arrived at a steady state of the assembly from which we recorded the energy for each individual atom. The cohesion energy E_c was determined iteratively: Assuming that the exact E_c is not known, we start from the obviously quite reasonable approximation $E_c^f = -8.9\text{eV}$. We then adjusted the cohesion energy such that the fitted (minimizing the least squares error using the *Levenberg-Marquardt* scheme [GM78]) strain energy relation

$$E^S(R, r_c) = E(R, r_c) - N(R)E_c - \frac{\Delta E_c}{\Omega}\pi R^2 = C(\ln(R) - \ln(r_c)) + E_{dc}(r_c) \tag{6.47}$$

yields $\Delta E_c \sim 0$. $N(R)$ denotes the total number of atoms in the cylinder of radius R and $E^S(R, r_c)$ its strain energy per dislocation line length. r_c was fixed to the magnitude b of the burgers vector which seems to be a quite common choice, despite the fact, that the elastic region starts about $4 \cdot b$, which

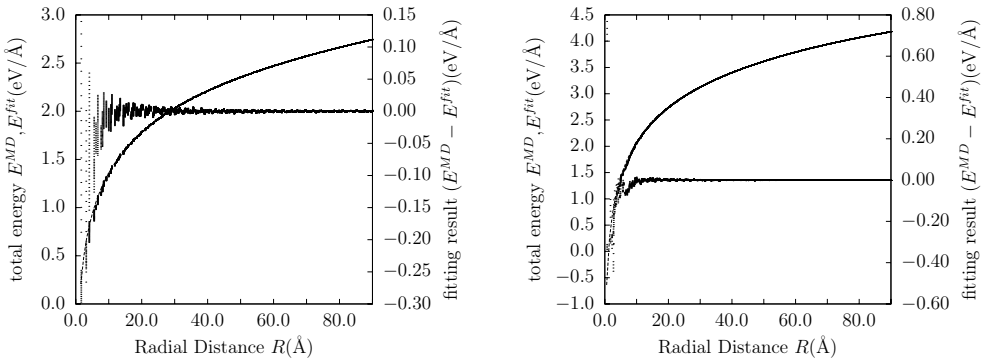

Fig. 6.32: *The fitting results as described in the text are shown for the pure* screw *(left) and the pure* edge *(right) dislocation. The scale on the left present the fitted equation together with the data fitted on. The data represent the result of the MD relaxation of a cylindrical cell containing the straight (either screw or edge) dislocations. The right axis shows the corresponding deviations between fit and data.*

dislocation	C (eV/Å)	$E_{dc}(b)$ (eV/Å)	ΔE_c (eV)	μ^* (GPa)
screw	0.610771	0.570498	$2.86 \cdot 10^{-5}$	161.8
edge	0.957555	0.844626	$-4.34 \cdot 10^{-7}$	182.6
mixed (low)	0.933877	0.857551	$-1.94 \cdot 10^{-5}$	183.8
mixed (high)	0.920740	0.877063	$-1.21 \cdot 10^{-6}$	181.2

Table 6.7: *The results of the fitting process of Eq. (6.47) against the MD data of a straight dislocation within a cylinder embedded in an isotropic elastic solid.*

was used to fit Eq. (6.47) against the $E(R, r_c)$ data. The last term righthand of Eq. (6.47) arises due to deviations of the assumed cohesion energy from the true one, i.e. $\Delta E_c \approx 0$ means that E_c coincides almost precisely with the exact cohesion energy. The cohesion energy for all simulations of the different dislocations thus determined resulted in $E_c = -8.89990$eV. A by-product of the fitting scheme described, is the dislocation line energy $E_{dc}(r_c)$. Because of the arbitrariness of the partitioning of space through the specific choice of r_c, E_{dc} is not a physical quantity in the sense, that it cannot be defined or measured uniquely. To make this parameter meaningful, r_c must of course be specified, also. As mentioned, here for comparison reasons, we used $r_c = b$, the magnitude of the Burgers vector. The overall results from the fitting procedure are shown in Figs. 6.32 and 6.33.

Remarkable from the fitting is the very small deviation of the calculated cohesion energy, despite the fact, that we used differently oriented crystals and yet isotropic elasticity theory for the construction of the dislocation. The shear constant was calculated using the following relation for the constant

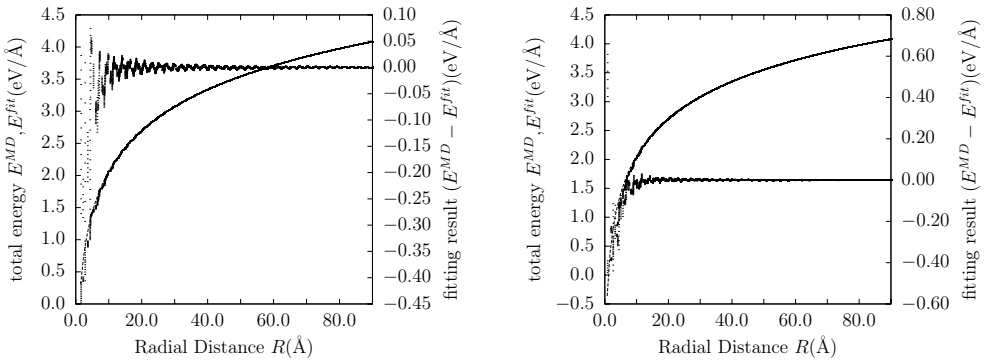

Fig. 6.33: *The fitting results as described in the text are shown for two dislocations of mixed type as described in the text (*low energy *on the left,* high energy *on the right). The scale on the left present the fitted equation together with the data fitted on. The data represent the result of the MD relaxation of a cylindrical cell containing various straight dislocations. The right axis shows the corresponding deviations between fit and data.*

C [HL82]:

$$C \approxeq \frac{\mu^* b^2}{4\pi} \left(\cos^2 \beta + \frac{\sin^2 \beta}{1-\nu} \right) \tag{6.48}$$

The shear constant so derived shows a pronounced increase as soon as there is some non zero edge component, probably a consequence of the anharmonic interatomic interactions. First of all, anharmonicity results in a non zero overall volume change due to the presence of edge dislocations. The fact that the cohesion energy remains almost unaffected irrespectively of the presence of a screw or edge dislocations seems to indicate, that the volume change is not responsible for the change in shearing behavior, because any overall volume change should change the calculated cohesion energy dramatically. Also, the dislocation core energies derived show a remarkable difference between edge (and mixed) and screw dislocations: E_{dc} tends to increase whenever a edge component is present. The total energy per dislocation line length $E(R)$ for $R = 90$Å as can be seen from Figs. 6.32, 6.33 are approximately 2.74eV, 4.18eV, 4.09eV and 4.08eV, for screw, edge, mixed (low) and mixed (high), respectively.

6.9 The Stacking Fault Energy (SFE)

Now, as we addressed different aspects of line defects, i.e. dislocations, in crystalline tungsten, we turn to another likewise important concept, especially for plasticity: the *stacking fault energy.* Any rearrangement of the

sequence of parallel planes in a crystal results in a stacking fault. The corresponding change in energy per area is consequently called *stacking fault energy*. To determine the stacking fault energy, we first calculate the γ-*surface*. For this, we divide a tungsten crystal in two halves and slide them relative to each other by a vector $\mathbf{u}_0$. The cell energy per unit area measured from the cell energy of the undisturbed crystal, i.e. $\mathbf{u}_0 = \mathbf{0}$, is called the *generalized stacking fault energy* $\gamma(\mathbf{u}_0)$. As we consider periodic aggregates of atoms, $\gamma(\mathbf{u}_0)$ is a periodic function of the shift vector $\mathbf{u}_0$ and it is sufficient to scan an *irreducible zone* of all shifts possible. For our purposes, we calculate $\gamma(\mathbf{u}_0)$ in starting with a properly chosen crystalline cell. As we are primarily interested in stacking faults along the most important *glide planes* of tungsten, i.e. $(1\,\bar{1}\,0)$ and $(1\,1\,\bar{2})$, the orthorhombic cell axes were chosen as $\mathbf{X} = 7[1\,\bar{1}\,0]$,$\mathbf{Y} = 4[1\,1\,\bar{2}]$ and $\mathbf{Z} = 3[1\,1\,1]$ for both, the $(1\,\bar{1}\,0)$- and $(1\,\bar{1}\,0)$-glide plane. The cell axes within the glide plane were periodic, whereas the cell along the glide plane normal had a free surface, i.e. no periodicity. For all subsequent shifts along the glide plane, the atoms were allowed to relax in glide plane normal direction and fixed perpendicular to it. All calculations were carried out at zero temperature and pressure using our *Langevin piston method*. We scanned the glide plane on a regular grid with shift vectors $\mathbf{u}_0(m,n) = (m\mathbf{Y} + n\mathbf{Z})/16$ and $\mathbf{u}_0(m,n) = (m\mathbf{X} + n\mathbf{Z})/16$, $0 \le m, n \le 16$, for the glide plane $(1\,\bar{1}\,0)$ and $(1\,1\,\bar{2})$, respectively. The energy per unit area was recorded. The results of this procedure are shown in Fig. 6.34. As the minima of the γ-surface for the $(1\,\bar{1}\,0)$-plane are aligned

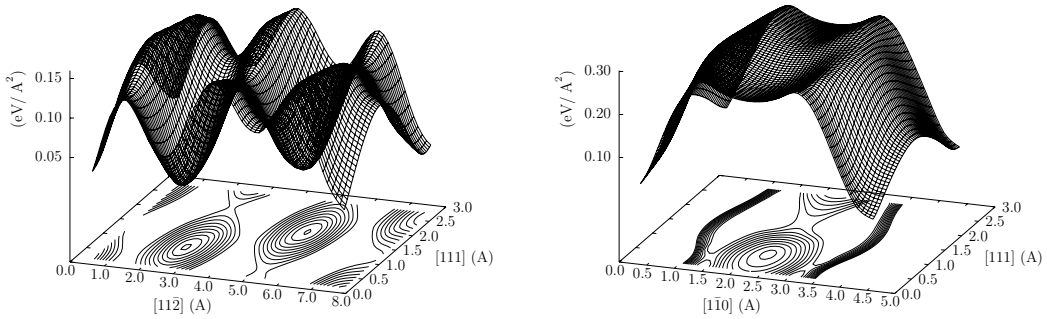

Fig. 6.34: *The gamma surface for a relaxed "stacking fault" on either* $(1\,\bar{1}\,0)$- *(left) or* $(1\,1\,\bar{2})$*-plane (right). The atoms in the simulation cells were allowed to relax along the direction perpendicular to the stacking fault plane.*

along $\frac{m}{2}[1\,1\,\bar{1}]$ with $m = 0, 1, 2$ and, therefore, coincide with "regular" lattice points, a stacking fault cannot exist at all on this plane. For the $(1\,1\,\bar{2})$-plane things are different: a possible stacking fault could exist with Burgers vector $\mathbf{b}_{sf} = \frac{1}{6}[1\,1\,1] + \frac{1}{2}[1\,\bar{1}\,0] = \frac{1}{6}[4\,\bar{2}\,1]$. The corresponding *stacking fault*

energy $\gamma(\mathbf{b}_{sf}) \approx 0.23\text{eV}/\text{Å}^2$. For the symmetry equivalent planes ($(1\,1\,\overline{2})$, $(1\,\overline{2}\,1)$ and $(\overline{2}\,1\,1)$) we get the following Burgers vectors for the corresponding partial dislocations:

$$\mathbf{b}_{sf}^1 := \frac{1}{6}[1\,1\,1] + \frac{1}{2}[1\,\overline{1}\,0] = \frac{1}{6}[4\,\overline{2}\,1] \tag{6.49}$$

$$\mathbf{b}_{sf}^2 := \frac{1}{6}[1\,1\,1] + \frac{1}{2}[\overline{1}\,0\,1] = \frac{1}{6}[\overline{2}\,1\,4] \tag{6.50}$$

$$\mathbf{b}_{sf}^3 := \frac{1}{6}[1\,1\,1] + \frac{1}{2}[0\,1\,\overline{1}] = \frac{1}{6}[1\,4\,\overline{2}] \tag{6.51}$$

The sum of these partials results in the Burgers vector of an undissociated (screw) dislocation, so that the following variant of *Sleeswyk's reaction* can be formulated:

$$\sum_{i=1}^{3} \mathbf{b}_{sf}^i = \frac{1}{2}[1\,1\,1] =: \mathbf{b} \tag{6.52}$$

However, a simple estimation of the expected equilibrium separation of the stacking fault planes [Haa78] makes a splitting of a screw dislocation into partials very unlikely due to the also observed very high *stacking fault energy* $\gamma(\mathbf{b}_{sf}) \approx 0.23\text{eV}/\text{Å}^2$.

6.10 Free Enthalpy with MD

In this section we will present some applications of the *Overlapping Distribution Method* as described in section 5.1.3. We start with the calculation of the free enthalpy of the pure tungsten lattice in the *bcc* phase as a function of temperature at zero pressure. This is done by a switching procedure in which a system of tungsten atoms, interacting through the *EAM* potentials as derived earlier, is turned into a system of independent identical three-dimensional harmonic oscillators, i.e. an *Einstein solid*. The vacancy formation enthalpy in pure tungsten, most important for diffusional fluxes, is calculated using a similar procedure, where gradually an atom, or its interaction energy with its environment, is "switched off". Within the same approach, we derive the enthalpy of solution of thorium in tungsten.

6.10.1 Lattice Formation Enthalpy

The process of formation of vacancies in tungsten, and in crystalline materials in general, is of considerable interest. Besides the significant role vacancies play in the transport of matter within a crystal through diffusion mechanisms, they effect mechanical properties through their interaction with

extended defects such as dislocations and stacking faults. In order to gain a better understanding of the influence of mono-vacancies on the structural properties of crystalline materials, knowledge of the thermodynamic parameters involved in their formation is indispensable.

We start with the well posed "reference state" of a system of harmonic oscillators oscillating with the same frequency ω_E, i.e. an *Einstein solid*. For the *Einstein solid* the *free energy* per degree of freedom as a function of temperature is a well known quantity [Boe83]:

$$A_{vib} = \frac{\hbar\omega_E}{2} + k_B T \ln(1 - e^{-\frac{\hbar\omega_E}{k_B T}}) \,. \tag{6.53}$$

In principle, the frequency of the oscillators can be chosen arbitrarily. But in order to get reliable results, this should be chosen sensible, as the results depend heavily on the "overlaps" of the corresponding distributions, see section 5.1.3. A rough choice for the oscillator frequency can be extracted from the phonon density of states (PDOS), Fig. 6.1. For tungsten one can guess a *Einstein frequency* f_E between 3THz and 6THz. A more accurate procedure is provided by inspection of the velocity autocorrelation function (VACF), Eq. (6.13), for very short times [AT87]:

$$C_{vv}(t) = 1 - \frac{1}{2}(\omega_E t)^2 + O(t^3) \,. \tag{6.54}$$

A fit of the parabola in Eq. (6.54) against $C_{vv}(t)$ is shown in Fig. 6.35. The *Einstein frequency* as indicated by the quadratic fitting of the VACF results in $f_E \approx 5.0$THz, which fits perfectly well into the range extracted from the PDOS.

We are mainly interested in calculating ensemble averages within MD. As we assume the *ergodic theorem* to be valid for the systems under consideration, we calculate averages along trajectories sampling the many-particle phase space. As the trajectories generated within MD are necessarily finite, the calculated averages are itself varying quantities. For this reason, we have to digress a little bit, and explore the sampling problem with correlated data. Assumed that we want to calculate the ensemble average of a phase space function $A(\Gamma)$, an *observable*, we start with a single trajectory $\Gamma(t_i)$ generated with MD, where t_i denotes an instance of time and $\Gamma(t_i)$ the corresponding phase space point. An estimation for the ensemble average $\langle A \rangle^{est}$, therefore, is given by:

$$\langle A \rangle^{est} = \frac{1}{N} \sum_i A(\Gamma(t_i)) \,, \tag{6.55}$$

with $N := |\{t_i\}|$, i.e. the total number of instances of time. As we consider *finite* trajectories, the calculated mean, Eq. (6.55), varies from trajectory

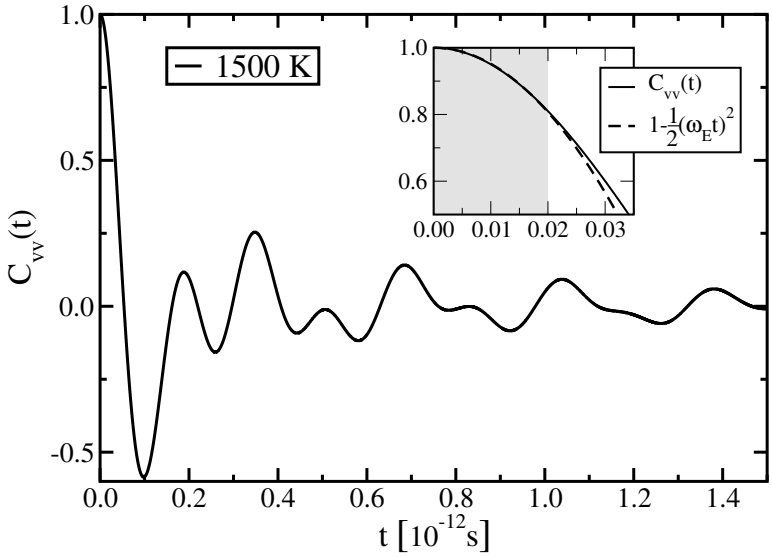

Fig. 6.35: *The (normalized)* velocity autocorrelation function *(VACF) is shown for a micro-canonical system of* 1024 *particles interacting with the EAM-potentials for tungsten at an average temperature of about* 1500K. *The insert shows the VACF for short times together with a fit against its expected short time behavior, Eq. (6.54). The grey-shaded area marks the fitted region. The fit gives an angular* Einstein frequency *of about* $\omega_E \approx 3.1 \cdot 10^{13} s^{-1}$*, which corresponds to a frequency of* $f_E \approx 5.0 \cdot 10^{12} s^{-1}$.

to trajectory. The squared width of the variations can be easily estimated assumed that the $A(\Gamma(t_i))$ are uncorrelated to each other:

$$\sigma^2(\langle A \rangle^{est}) = \frac{1}{N} \sigma^2(A)\,, \tag{6.56}$$

where

$$\sigma^2(A) = \frac{1}{N} \sum_i (A(\Gamma(t_i)) - \langle A \rangle^{est})^2\,. \tag{6.57}$$

Generally, of course, subsequent phase space points are not uncorrelated. The correlations persist for some characteristic time [Ben76, AT87], the *correlation time* τ_A. To get rid of spurious correlations between data points, one defines the *statistical inefficiency*

$$s_A = \lim_{N_b \to \infty} \frac{N_b \sigma^2(\langle A \rangle_b^{est})}{\sigma^2(A)}\,. \tag{6.58}$$

$N_b = N/n_b$ is an arbitrarily chosen block length, n_b equals the number of

blocks spanning the complete trajectory. $\sigma^2(\langle A\rangle_b^{est})$ is given by

$$\sigma^2(\langle A\rangle_b^{est}) = \frac{1}{n_b}\sum_{b=1}^{n_b}(\langle A\rangle_b^{est} - \langle A\rangle^{est})^2\,, \tag{6.59}$$

where

$$\langle A\rangle_b^{est} = \frac{1}{N_b}\sum_{i=1}^{N_b} A(\Gamma(t_i))\,, \tag{6.60}$$

i.e. the mean in each block. It can be shown [AT87], that $s_A \equiv 2\tau_A$. So, for efficient sampling, one should generate data points separated in time by at least the correlation time, one or two times τ_A. Unfortunately, τ_A is not known beforehand, before an actual simulation run is calculated. To avoid excessive strain of the computer storage, one should store a data point after approximately s_A MD-steps for a typical system. Fig. 6.36 shows the statistical inefficiency s_A for a micro-canonical trajectory generated by a system containing 1024 particles at a mean "temperature" of about 1500K. The time step chosen was $\Delta t = 2\cdot 10^{-16}s$. For each step the potential energy per particle was stored to get a reliable estimation for the block length and the correlation time for the potential energy. From Fig. 6.36 one extracts a block length of about 145. This gives an estimated correlation time of about $\tau_{E_{pot}} \approx 1.45\cdot 10^{-14}s$. $\tau_{E_{pot}}$ is nearly independent of the size of the system, i.e. the number of particles. Furthermore, it turned out to be nearly unaffected by the temperature in the range considered. Efficient sampling, therefore, means to store and use energy values separated in time by at least $\tau_{E_{pot}}$.

To calculate the free enthalpy per particle for the lattice, we will use the *Overlapping Distribution Method* as introduced in section 5.1.3. For this, we generate trajectories in the NVT ensemble, i.e. fixed number of particles, volume and temperature. After simulating an unperturbed system for a time duration of about $\tau_{E_{pot}}$, we gradually switch the interaction potential towards one, where the interaction energy between the particles is slightly reduced and, at the same time, we introduce a harmonic force acting on the particles. This is accomplished by scaling the EAM potentials for tungsten

$$\begin{aligned}\phi_\alpha(r) &:= \alpha\cdot\phi_{WW}(r)\\ F_\alpha(\rho) &:= \alpha\cdot F_W(\rho)\end{aligned} \tag{6.61}$$

with a scaling parameter $\alpha \in [0,1]$. This simple scaling ensures, that the interaction energy due to the EAM model of the particles is reduced to zero when α vanishes. In order to get an Einstein solid, we apply a harmonic

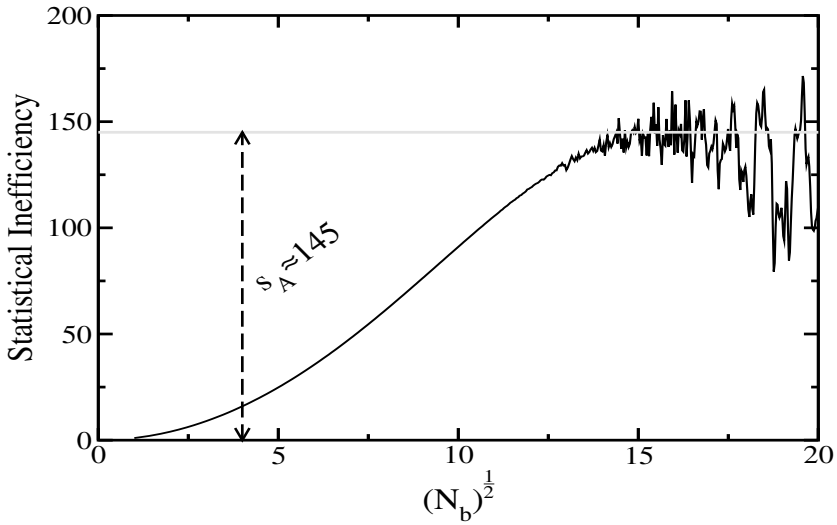

Fig. 6.36: *The* statistical inefficiency *as a function of* $\sqrt{N_b}$ *is shown. This figure is extracted from the data of a micro-canonical simulation of a system containing 1024 particles, relaxed at a temperature* $T = 1500$K. *The time step for the simulation was chosen to be* $2 \cdot 10^{-16} s$. *The block length to ensure uncorrelated data is shown to be approximately* $N_b \approx 145$.

force on each particle:

$$F_\alpha^h(\mathbf{r_i}) := -(1-\alpha) m_W \omega_E^2 (\mathbf{r_i} - \mathbf{r_i^0}) \tag{6.62}$$

where m_W denotes the mass of a tungsten atom, r_i and r_i^0 the actual position and the position of the origin of the harmonic force, respectively. ω_E is the Einstein frequency as derived above. Fig. 6.37 shows examples of the scaled potentials for various choices of α. The transformations Eq. (6.61) and (6.62) ensure a smooth transition from a system of interacting tungsten atoms to a system of oscillators, i.e. an Einstein solid.

The potential energy, therefore, for a system of particles is given by:

$$E_\alpha = \sum_i F_\alpha\Big(\sum_{j(\neq i)} \Delta\rho_j(R_{ij}) \Big) + \frac{1}{2} \sum_{\substack{i,j \\ (j\neq i)}} \phi_\alpha(R_{ij}) + \sum_i \Big((1-\alpha) m_W \omega_E^2 R_{i0}^2 + (1-\alpha) E_{coh} \Big) \tag{6.63}$$

where the last term ensures, that the system of non interacting harmonic oscillators for $\alpha = 0$ has the proper cohesion energy per atom E_{coh}. The time step for the simulations is chosen to be $\Delta t = 2 \cdot 10^{-15} s$, which is small enough

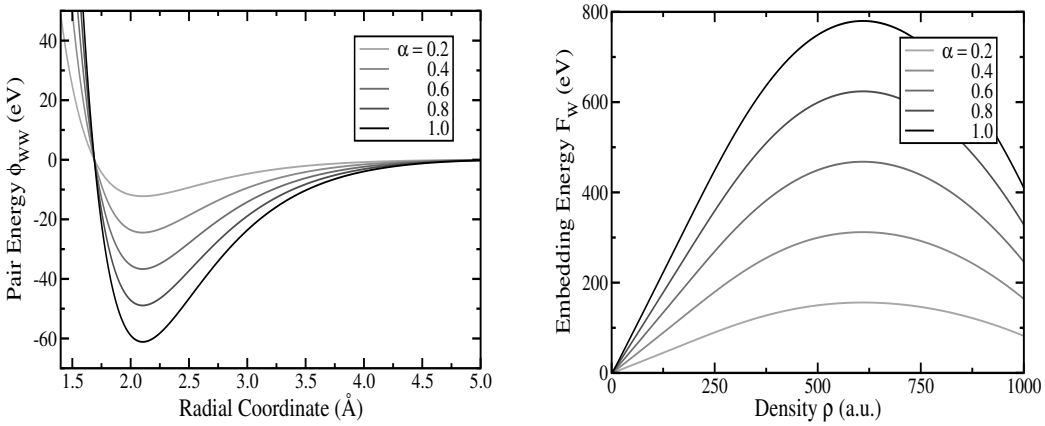

Fig. 6.37: *The scaled functions $F_W(\rho)$ and $\phi_{WW}(r)$ for tungsten are shown according to the transformation Eq. (6.61). for various choices of α. The result of these transformations is a smooth transition between the W-W interaction and an "harmonic lattice", i.e. a lattice, where each particle is bound to a purely harmonic force*

to generate cell energies which remain constant in the NVE ensemble along the simulated trajectories and, on the other hand, not too small to generate a reasonable amount of uncorrelated data within a given CPU time.

In order to make use of the *Overlapping Distribution Method* we calculated the trajectories of a system of 250 particles for a time duration of 2^{17} time steps after relaxing it for another 2^{12} steps for each temperature and choice of α. The temperatures were varied between 400K to 2000K. α was chosen between zero and one with step $\Delta\alpha = 0.1$. Taking the typical correlation time of about 2^4 time steps into account, this procedure results in a total number of 2^{13} uncorrelated instances of the trajectories. Furthermore, to ensure good starting values for the self-consistent cycle necessary to solve Eqs. (5.45) and (5.46) the free enthalpy differences for each transition from α to $\alpha + \Delta\alpha$, we use the following simple expressions for enthalpy differences $\Delta A := A(\alpha') - A(\alpha)$:

$$\Delta A_+ := -k_B T \ln \left\langle e^{-\beta(V(\alpha')-V(\alpha))} \right\rangle_\alpha \tag{6.64}$$

and

$$\Delta A_- := -k_B T \ln \left\langle e^{\beta(V(\alpha')-V(\alpha))} \right\rangle_{\alpha'}^{-1} \tag{6.65}$$

where $\langle \ldots \rangle_{\alpha/\alpha'}$ denotes averaging over the trajectory, generated with (total) interaction potential $V(\alpha)$ or $V(\alpha')$, respectively (see also section 5.1.3). As starting point for the iterative solution of Eq. (5.46) we used the arithmetic

mean of ΔA_+ and ΔA_-. Fig. 6.38 shows an example of the normalized densities $f_{\alpha/\alpha'}$, Eq. (5.35), for $\alpha = 0.4$ and $\alpha = 0.5$ and the free enthalpy differences and total free enthalpies per atom for tungsten.

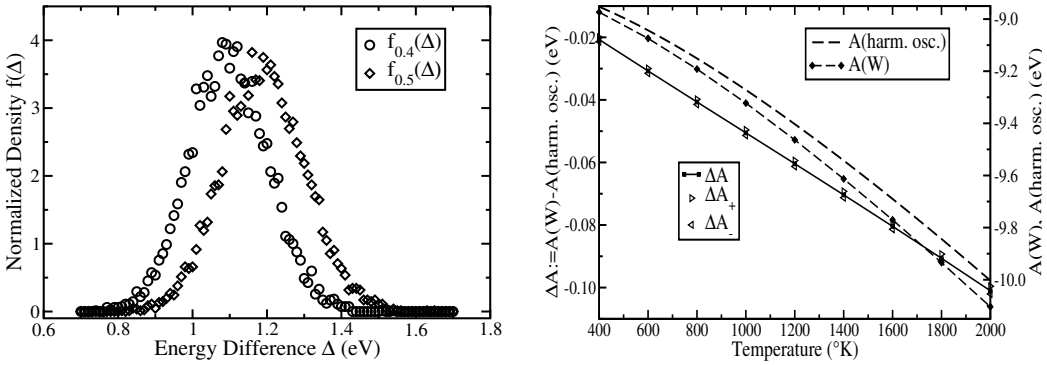

Fig. 6.38: *Left: An example for the normalized densities $f_{\alpha/\alpha'}$, Eq. (5.35), for $\alpha = 0.4$ and $\alpha = 0.5$ for a simulation of 250 particles at $T = 1000$K and fixed, but equilibrated volume. For the densities shown, a total of 8192 uncorrelated configurations for each choice of α were evaluated. Right: The resulting free energy differences calculated via self-consistently solving Eqs. (5.43) and (5.45), together with the free energy of a system of harmonic oscillators, Eq. (6.53), as a function of temperature is shown. The "bracketing" values of the free energy differences, ΔA_+ and ΔA_- are calculated with Eqs. (6.64) and (6.65).*

In order to check our result obtained so far, we exploit the following simple thermodynamic relationship for the *heat capacity per atom* c_P (at constant hydrodynamic pressure $P = 0$):

$$c_P = T\left(\frac{\partial S}{\partial T}\right)_{PN} = \left(\frac{\partial H}{\partial T}\right)_{PN} \tag{6.66}$$

with enthalpy $H = E + PV$, which in case of $P = 0$ is numerically equal to the internal energy E. We used the entropy S derived with the overlapping distribution method and the corresponding internal energies E directly from the MD runs to derive c_P. In order to enhance the accuracy of the partial derivative of S in Eq. (6.66), we fitted the function

$$f(T) = a_0 \ln(T + a_1) + a_2 \tag{6.67}$$

against the entropy data as a function of temperature within a least square procedure. The parameters obtained this way are $a_0 = 3.10353$, $a_1 = 17.816$ and $a_2 = -13.8537$. $c_P(T)$ obtained via the definitions, Eq. (6.66), and

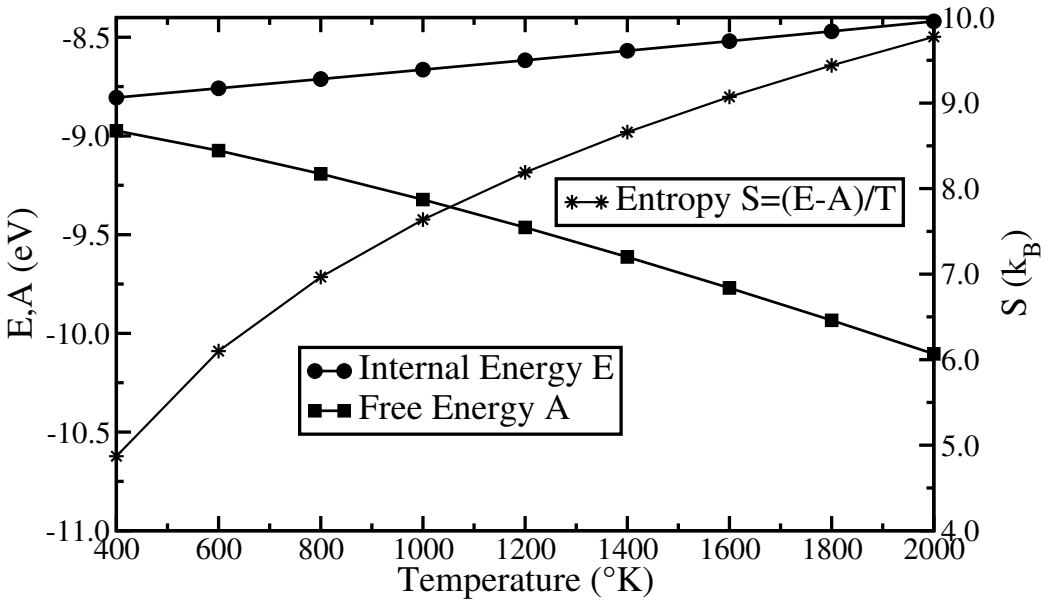

Fig. 6.39: *The* internal energy E*,* free energy A *and* entropy S *per atom for a tungsten lattice as a function of temperature* T *between* 400K *and* 2000K *is shown.*

its comparison with experimental data [WC84] is given in Fig. 6.40. The results show a remarkable agreement firstly between the two approaches, and secondly, an also reasonable conformity with experimental data. Finally, we also computed the entropy difference $\Delta S(T) := S(T) - S(400\text{K})$ from:

$$\Delta S(T) := \int_{400\text{K}}^{T} \frac{c_P(T')}{T'}\, dT' \,. \tag{6.68}$$

A rather good agreement between the different approaches is observed. We also see a slight enhancement with the data obtained from the *Overlapping Distribution Method (ODM)* compared to the more direct procedure calculating first the enthalpy. The very high computational costs in applying the *ODM* seem to ban its application and, instead, to prefer the usage of the direct approach as indicated above. But one should note, that for the knowledge of the total (vibrational) entropy it is necessary to get at least one entropic reference point. To get this point, the *ODM* should be used. The differences to the result for a system of noninteracting harmonic oscillators, $c_P = 3k_B \approx 2.58 \cdot 10^{-4}$eV/K (*Dulong and Petit law*), is not a consequence of the electronic contribution to the specific heat being not present in the classical interaction schemes suitable for molecular dynamics, because the

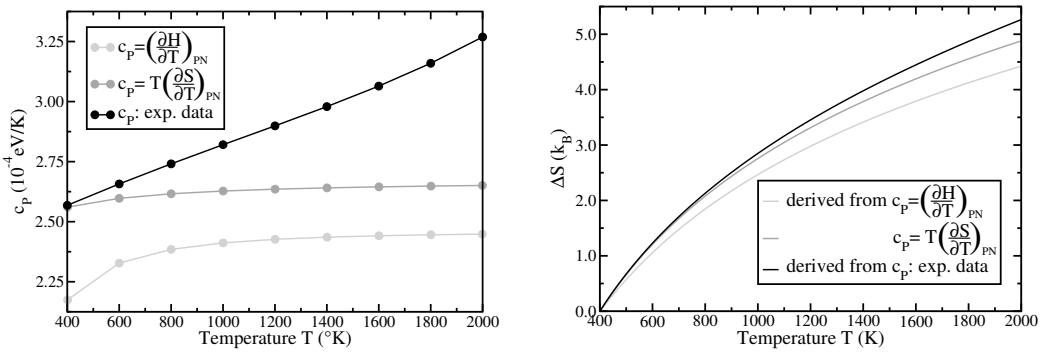

Fig. 6.40: *left:* $c_P(T)$ *for tungsten for a temperature range between* 400K *and* 2000K *as derived from Eqs. (6.66). right:* $\Delta S(T)$ *resulting from* $\Delta S(T) := \int_{400\mathrm{K}}^{T} \frac{c_P(T')}{T'}\, dT'$ *is shown.*

temperature T_0 [AM76] above which the phonon contribution exceeds the electronic contribution is typically only a few percent of the Debye temperature, as can be seen from

$$T_0 = \left(\frac{5}{24\pi^2} \frac{Z \cdot \theta_D^3}{T_F} \right)^{\frac{1}{2}} \approx 26\mathrm{K} \tag{6.69}$$

where the valency $Z \approx 6$, the Debye temperature $\theta_D \approx 400$K, and the *Fermi Temperature* $T_F \approx 116000$K. At temperatures high enough, the anharmonic effects could become important, which are not included in the classical result of *Dulong and Petit*.

To clarify the influence of anharmonicity of the interaction potentials for c_P, we did some test calculations first for a system of independent Einstein oscillators and successively include some anharmonic contributions with potential energies chosen according to the following scheme:

$$V_\alpha(x) := V_E(x) + \alpha V_E(x)^n\,, \text{ with } V_E(x) := \frac{m_W \omega_E^2}{2} x^2\,, \tag{6.70}$$

with x labeling the deviation from the corresponding origin, and m_W, ω_E are mass of a tungsten atom and *Einstein frequency*, respectively, as mentioned above and derived from Fig. 6.35.

Clearly, for $\alpha = 0$ we have the situation of noninteracting harmonic oscillators (for each degree of freedom), oscillating with the same frequency, ie. an *Einstein solid*. The forces, therefore, are given by:

$$F_\alpha(x) = -\frac{\partial V_\alpha(x)}{\partial x} = (1 + n\alpha V_E(x)^{n-1}) F_E(x)\,, \text{ with } F_E(x) := -m_W \omega_E^2 x\,. \tag{6.71}$$

This model system enables us in a simple manner to derive the anharmonic effects on c_P. For this, we generate a series of trajectories for varying temperatures and anharmonicity factors α. Furthermore, the "strength" of the anharmonicity can be triggered with a proper choice of the exponent n. So, additionally, we performed our calculations for different choices of n, too. All our test calculations are done coupled to a thermal bath, in order to generate trajectories from a canonical ensemble, applying our *Brownian thermostat* as already described. The models consist of 1024 particles each of mass m_W of a tungsten atom. The temperatures are varied between 400K and 2000K in steps of 200K. We took two different choices of n: $n = 2$ and $n = 3$. α is changed so that the mean potential energy change is about 10%, 20% and 30%, respectively. To ensure this last criterion, we apply the *generalized equipartition theorem* (see e.g. [Mün69]):

$$\left\langle q_k \frac{\partial H}{\partial q_k} \right\rangle = k_B T \tag{6.72}$$

$$\left\langle p_k \frac{\partial H}{\partial p_k} \right\rangle = k_B T \,, \tag{6.73}$$

where H denotes the total system Hamiltonian and q_k, p_k a generalized coordinate and momentum, respectively, and $\langle \ldots \rangle$ means averaging in the canonical ensemble. In our case, H is given by:

$$H_\alpha := \sum_i (\frac{1}{2} m_W \dot{x_i}^2 + V_\alpha(x_i)) \tag{6.74}$$

where the sum extends over all *degrees of freedom*. Applying Eq. (6.72) to the system Hamiltonian, Eq. (6.74), gives:

$$\langle E_{kin} \rangle = \frac{N k_B T}{2} \tag{6.75}$$

$$\langle E_{pot} \rangle = \frac{N k_B T}{2} - \alpha(n-1) \left\langle \sum_i V_E(x_i)^n \right\rangle . \tag{6.76}$$

Here $E_{kin} := \sum_i \frac{1}{2} m_W \dot{x_i}^2$ denotes the total kinetic anergy , whereas $E_{pot} := \sum_i V_\alpha(x_i)$ is its potential counterpart. N is the total number of degrees of freedom. To derive Eq. (6.75), we used the fact, that in *Eulerian nomenclature*, E_{kin}, as well as the harmonic part of E_{pot} are homogeneous functions of second order in $\dot{x_i}$ and x_i, respectively, and that $\langle \ldots \rangle$ is a linear operator.

Therefore, the mean total energy results in:

$$\langle E_{tot} \rangle := \langle E_{kin} \rangle + \langle E_{pot} \rangle = N k_B T - \alpha(n-1) \left\langle \sum_i V_E(x_i)^n \right\rangle , \tag{6.77}$$

which shows, that for a given temperature and $\alpha > 0$ and $n > 1$, the anharmonic contribution reduces the mean total energy of the system, as $\langle \sum_i V_E(x_i)^n \rangle > 0$, compared to the purely harmonic situation. Suppose now, that we want to reduce the mean potential energy by a given fraction χ. Simple analysis of Eq. (6.76) shows that a good guess for α at temperature T and with anharmonicity exponent n is, therefore, given by:

$$\alpha = \frac{\chi}{n-1} \left(\frac{k_B T}{2} \right)^{1-n} \tag{6.78}$$

where we made use of the approximation $\langle V_E(x_i)^n \rangle \approx \langle V_E(x_i) \rangle^n = (k_B T/2)^n$.

The results are shown in Fig. 6.41. Clearly, for the purely harmonic case, the specific heat is independent of temperature and equals $c = 3k_B$ per particle. The deviations from this classical result are the stronger the more the anharmonicity (triggered via exponent n) increases. But one also recognizes, that the deviations of $c = 3k_B$ are of negative sign, which is in clear contrast to our result from the tungsten calculations, see Fig. 6.40, where the deviations from the experimental values are of positive sign. This indicates, that the missing anharmonicity alone in the potentials created cannot explain the observed behavior.

When dealing with classical interaction potentials for molecular dynamics simulations, one necessarily has to cut off the interaction at some chosen distance. Particles whose distances is beyond this cutoff do not recognize each other. Unfortunately, this could be a principle source of error in the specific heat calculations. In order to clarify this point, we tried the following approach: we generated two simple *Lennard-Jones* potentials, a LJ-(12,6) and a LJ-(12,4) pair potential, fitted against the bulk modulus and the cohesive energy of bcc-tungsten, and varied the cutoff through shifting the potential and set to zero, whenever the potential rises above zero. The LJ-(12,6) and the LJ-(12,4) potentials are given by:

$$\phi(r) := 4\epsilon \left[\left(\frac{\sigma}{r} \right)^{12} - \left(\frac{\sigma}{r} \right)^{6} \right] \quad \text{and} \quad \phi(r) := 4\epsilon \left[\left(\frac{\sigma}{r} \right)^{12} - \left(\frac{\sigma}{r} \right)^{4} \right], \tag{6.79}$$

where we introduced two more parameters σ and ϵ, which are to be determined. It is easy to derive the following useful relations for the unknowns σ and ϵ:

$$r_0 = \left(\frac{2A_{12}}{A_6} \right)^{\frac{1}{6}} \sigma \quad , \quad E_0 = -\frac{A_6^2 \epsilon}{2A_{12}} \quad \text{and} \quad B_0 = \frac{9\epsilon}{2\sigma^3} A_{12} \left(\frac{2A_6}{A_{12}} \right)^{\frac{5}{2}}, \tag{6.80}$$

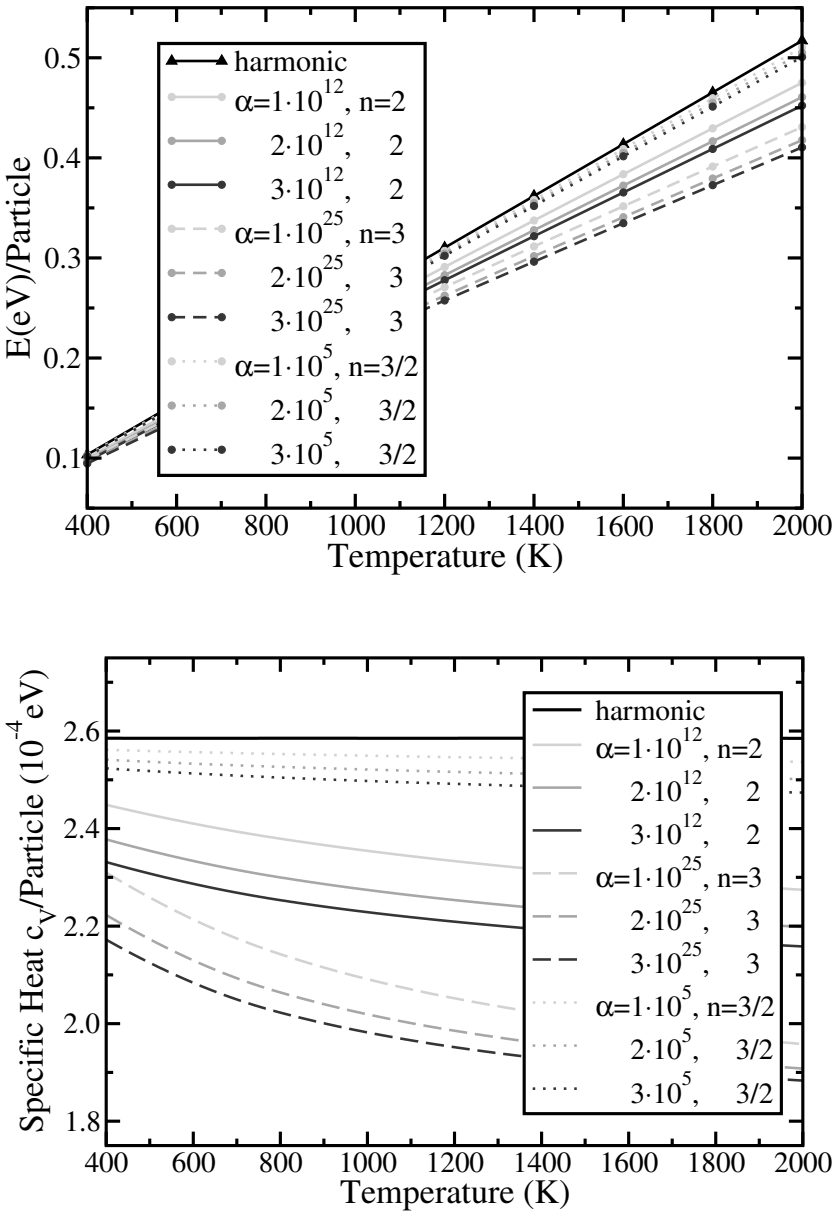

Fig. 6.41: *Results from the model calculations to estimate the influence of the anharmonicity of the interaction potentials on c_P or c_V. The total energy $E := E_{tot}$ (above) and the resulting* specific heat c_V *versus temperature for different* anharmonicity factors α*, Eq. (6.78), and exponents n are shown.*

and

$$r_0 = \left(\frac{3A_{12}}{A_4}\right)^{\frac{1}{8}} \sigma \quad , \quad E_0 = -\frac{4\epsilon}{3}\sqrt{\frac{A_4}{3A_{12}}} \quad \text{and} \quad B_0 = \frac{4\epsilon}{\sigma^3}\frac{4A_4}{3^{11/8}}\left(\frac{A_4}{A_{12}}\right)^{\frac{7}{8}} , \tag{6.81}$$

where r_0, E_0 and B_0 are *nearest-neighbor distance* in equilibrium, cohesive energy and bulk modulus, respectively. The dimensionless constants A_6 and A_{12} depend on the crystal structure. They are defined by the sums of the inverse 6th and 12th powers of the distance from a given Bravais lattice point to all others, where the unit of distance is taken to be the distance to the nearest neighbors. For the *bcc*-lattice they are given by [AM76]:

$$A_4 := 22.64, \quad A_6 := 12.25 \quad \text{and} \quad A_{12} := 9.11\,. \tag{6.82}$$

For determination of ϵ and σ, we decided to fit against the bulk modulus and the equilibrium nearest neighbor distance $r_0 = a_0\sqrt{3}/2$, with B_0 and a_0 from Tab. 5.2, as the total energy per particle in the lattice, the cohesion energy, is changed anyway via the shifting procedure of the potential as described above, as for a N-particle system, shifting of the potential together with the cutoff procedure mentioned is equivalent to shifting the total energy of the system. The fitted values for σ and ϵ are accordingly given by:

$$\text{LJ-(12,6):} \quad \sigma = 2.580\,\text{Å} \quad \text{and} \quad \epsilon = 0.474\,\text{eV}\,. \tag{6.83}$$

$$\text{LJ-(12,4):} \quad \sigma = 2.693\,\text{Å} \quad \text{and} \quad \epsilon = 0.213\,\text{eV}\,. \tag{6.84}$$

The cutoff is varied between fourth and sixth nearest neighbor distance.

In summary, the potentials in use become:

$$\phi_\delta(r) := 4\epsilon\left[\left(\frac{\sigma}{r}\right)^{12} - \left(\frac{\sigma}{r}\right)^{6}\right] + \delta\,, \tag{6.85}$$

for the LJ-(12,6) (the LJ-(12,4) is constructed analogously),where δ is chosen, such that the cutoff, i.e. the distance r_c beyond which $\phi_\delta(r) \equiv 0$, falls midway between the third and fourth, the fourth and the fifth, and, the fifth and the sixth neighbor shell. In particular, Tab. 6.8 shows the results, i.e. the shifting parameter δ for the cutoff r_c chosen.

With the shifted potentials, we generated trajectories and calculated the specific heat per particle as done with the EAM potentials. The results are shown in Fig. 6.42 and Tab. 6.9. As the energy versus temperature curves show to a very good approximation a almost linear dependency, we approximated the specific heat of the model system with a linear regression analysis and a variant of Eq. (6.66) applicable for c_V. From the values for c_V

Cutoff between	3-4	4-5	5-6
r_c (Å)	4.890530084	5.396436012	5.940303985
$\delta_{(12,6)}$ (eV)	0.040055831	0.022408353	0.012661784
$\delta_{(12,4)}$ (eV)	0.077756139	0.052691718	0.035961129

Table 6.8: *Parameter δ to fix the Lennard-Jones potential for a given cutoff. The figures in the top row show the neighbor shells between which the cutoff r_c is chosen. δ denotes the resulting shift of the Lennard-Jones potential which ensures $\phi_\delta(r)$ being zero at r_c.*

potential	LJ-(12,4)			LJ-(12,6)		
cutoff between shell	3-4	4-5	5-6	3-4	4-5	5-6
specific heat $c_V(10^{-4}\text{eV/K})$	2.52	2.47	2.52	2.47	2.46	2.49

Table 6.9: *Specific heat c_V per particle for Lennard-Jones potentials LJ-(12,4) and LJ-(12,6), respectively. The data are derived from Fig. 6.42 via $c_V = \left(\frac{\partial E}{\partial T}\right)_{VN}$. As the $E(T)$ behave linear to a good approximation, the specific heats are determined by linear regression of $E(T)$ and thus are valid for at least a temperature range of* 400K *to* 2000K.

in Tab. 6.9 we see, if ever, only a very small influence of the cutoff distances on c_V.

To summarize, neither the anharmonicity nor the neglected neighborhood due to the finite cutoff distance of the potentials seems to have any major influence on the specific heat of the many particle system.

Fig. 6.44 shows the comparison of the *universal binding energy relation* for tungsten, Eq. (5.64), and the result of a model calculation containing 1024 tungsten atoms interacting with the EAM-potentials connected to a heat bath at a temperature of 1000K and 2000K. The bulk modulus, extracted from Fig. 6.44, decreases from 331GPa at 1000K down to 311GPa at 2000K, a trend which corresponds well to the experimental data, albeit the absolute values are about 12% to high.

Up to now, we considered the body centered cubic tungsten lattice. We now want to supplement the calculations of the *lattice formation enthalpy* above by the equivalent simulations at the face centered cubic thorium lattice. The results for the *velocity autocorrelation function* of a thorium atom equilibrated at $T = 1500$K in the equilibrium lattice is shown in Fig. 6.47. Also shown is the fitted short term parabola to extract the *Einstein frequency* f_E, which results to $f_E \approx 2.9 \cdot 10^{12} s^{-1}$, almost a factor of two lower than its counterpart for tungsten. This clearly reflects the fact, that the elastic con-

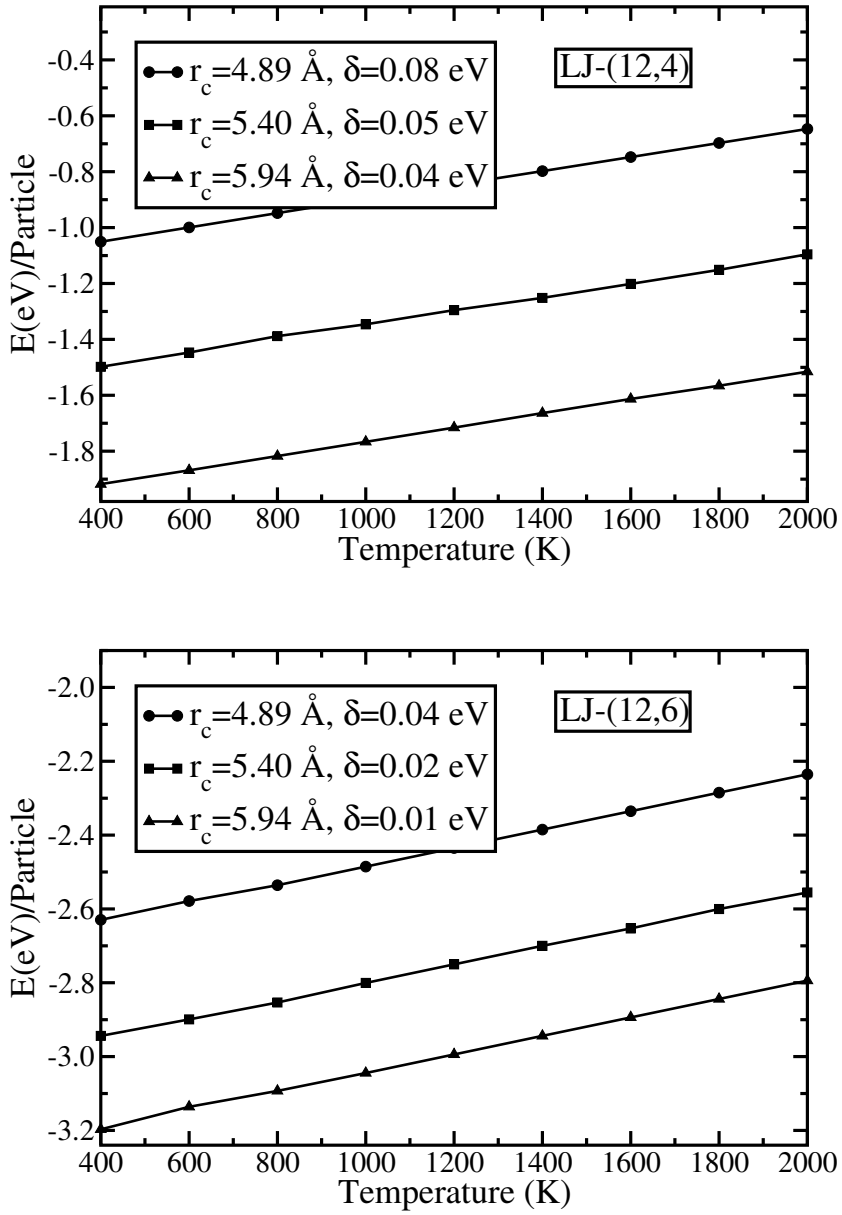

Fig. 6.42: *Energy (at constant* volume*) for a system of 1024 particles interacting via a (12,4)*-Lennard-Jones *(above) and (12,6)*-Lennard-Jones *(below) pair potential. The potential is shifted with an additive constant δ and set to zero whenever the shifted potential would become positive. Shifting of the potential therefore results in adjusting the cutoff distance r_c. The specific heat $c_V = \left(\frac{\partial E}{\partial T}\right)_{VN}$ can be calculated with linear regression as E versus T seems to be linear to a very good approximation.*

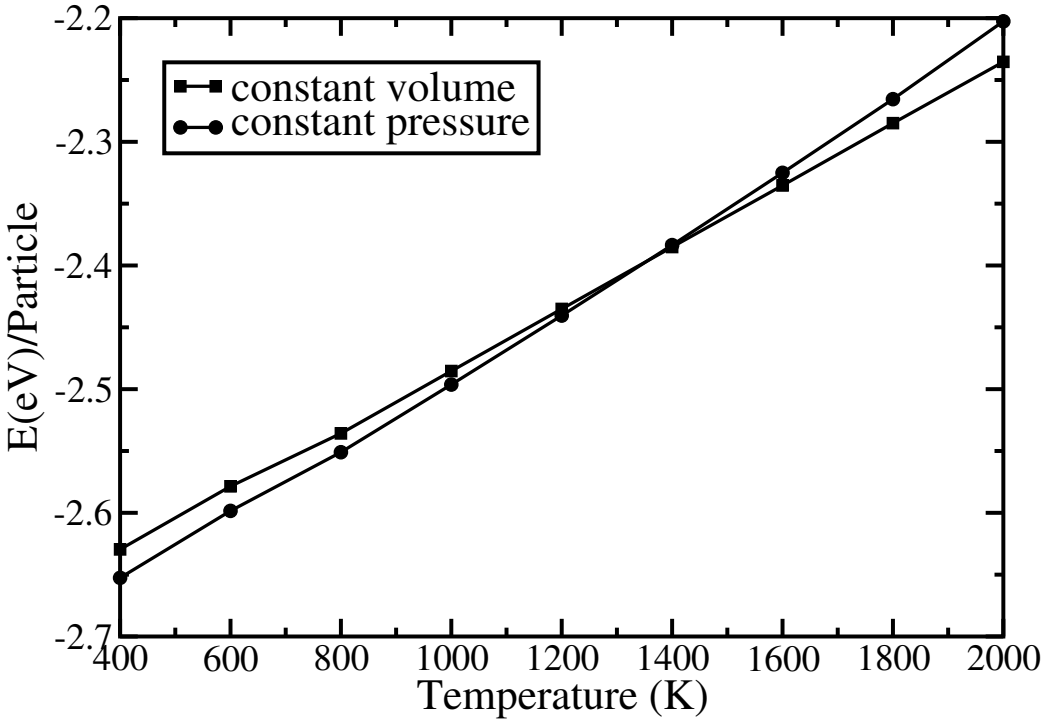

Fig. 6.43: *Energy at constant* pressure *as well as at constant* volume *for a system of 1024 particles interacting via a (12,6)*-Lennard-Jones *pair potential. The potential is shifted with an additive constant* $\delta = 0.04$eV *and set to zero whenever the shifted potential would becomes positive. Shifting of the potential, therefore, results in adjusting the cutoff distance to* $r_c = 4.89\mathring{A}$. *The specific heat per particle* $c_P = \left(\frac{\partial H}{\partial T}\right)_{PN}$ *and* $c_V = \left(\frac{\partial E}{\partial T}\right)_{VN}$ *derived from linear regression of the total energy data are* $c_P = 2.80 \cdot 10^{-4}$eV/K *and* $c_V = 2.47 \cdot 10^{-4}$eV/K.

stants of tungsten are considerably greater than those of thorium, i.e. the tungsten lattice is much stiffer than that of thorium. As it is advantageous to start simulations with the lattice constants of the corresponding temperatures, we also calculated the equilibrium lattice constants, and, from this, the *linear expansion coefficient*, from a MD-simulation and compared the result with experimental data. The simulation results are shown in Fig. 6.48. All simulations were performed with a cubic simulation cell containing 2048 particles and with the *Langevin piston* for thermostatting and volume equilibration. There are some considerable differences in the simulation results compared to the experimental ones: The simulations overestimate the experimentally available data by a factor of roughly two in the temperature range up to 1300K. The reason for this is not clear, and probably has its origin in

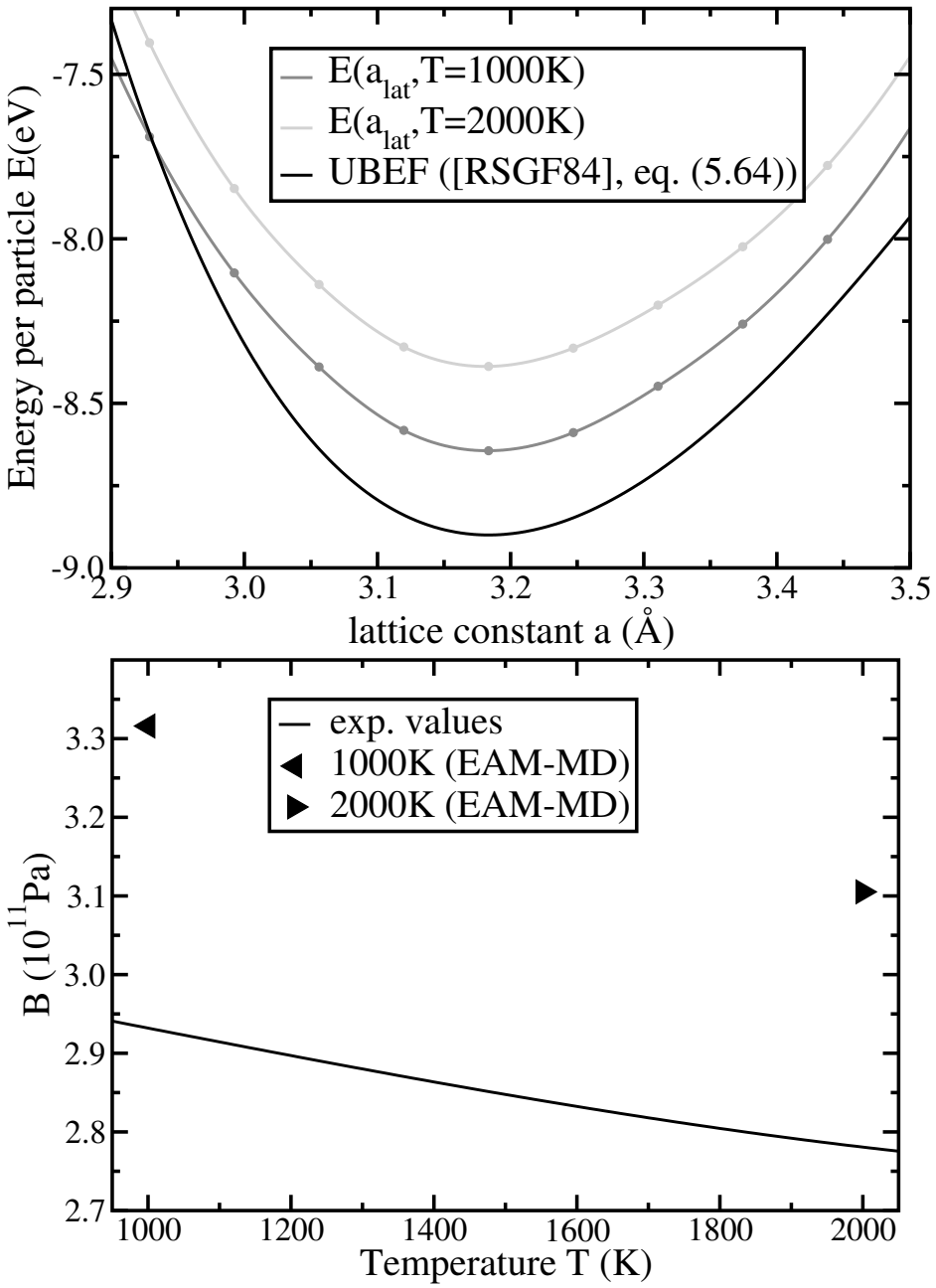

Fig. 6.44: *Energy per particle versus lattice parameter for a system of 1024 tungsten atoms interacting via the EAM-potential. The* universal binding energy function (UBER)*, Eq. (5.64) for tungsten in comparison to the total energy results derived at* $T = 1000\text{K}$ *and* $T = 2000\text{K}$ *is shown (above). Also, the derived* bulk moduli *at both temperatures and corresponding experimental values [LS99] are depicted (below).*

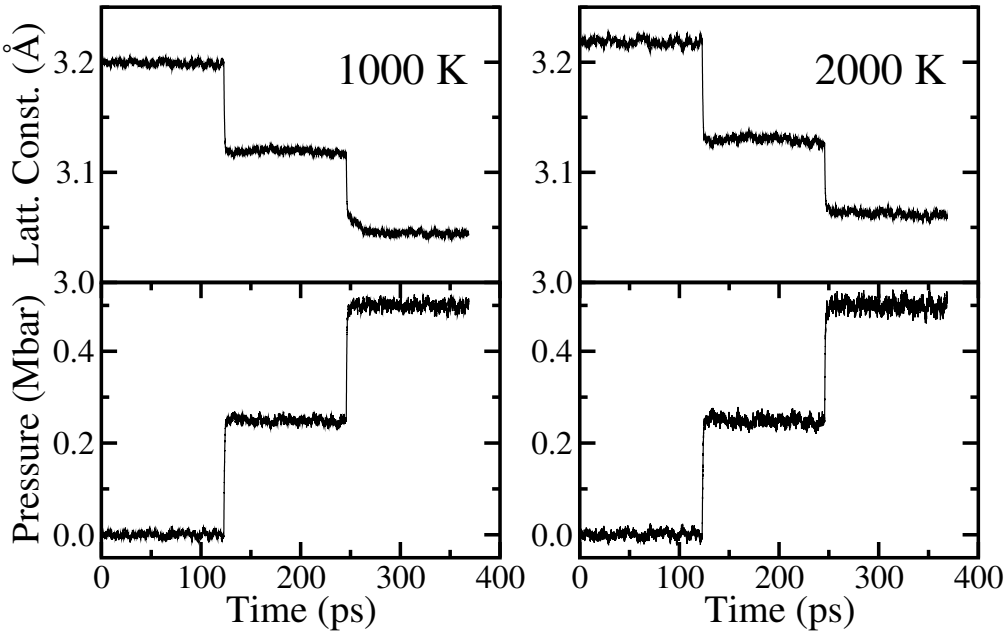

Fig. 6.45: *The lattice constant and hydrostatic pressure for a system of 1024 tungsten particles interacting via EAM potentials versus time for two different temperatures (*1000K *and* 2000K*) is shown. At certain instances of time the externally applied pressure on the system is increased. The parameters of the thermo- and barostat ("system mass" and friction coefficients) were adjusted so that the particle system could respond very quickly to the sudden increase of pressure.*

the electronic degrees of freedom, not properly accounted for within the semi-empirical EAM-potentials. The entropy together with the energy and free energy per atom as derived with the ODM are shown in Fig. 6.49, revealing qualitatively the same features as the corresponding results of the tungsten lattice. Finally, armed with the knowledge of entropy and energy per atom, we also calculated the specific heat at zero pressure utilizing Eqs. (6.66) for thorium. The corresponding results are shown in Fig. 6.50, where a remarkable coincidence of simulation and experimental data is obvious.

6.10.2 Vacancy Formation Free Enthalpy

The Gibbs free energy of formation g^{vf} of a mono-vacancy is defined as

$$g^{vf} := G(N, p, T, n = 1) - G(N, p, T, n = 0)\,. \tag{6.86}$$

Here N represents the number of atoms present in the system which is supposed to be large, p the pressure, T the absolute temperature, and n the

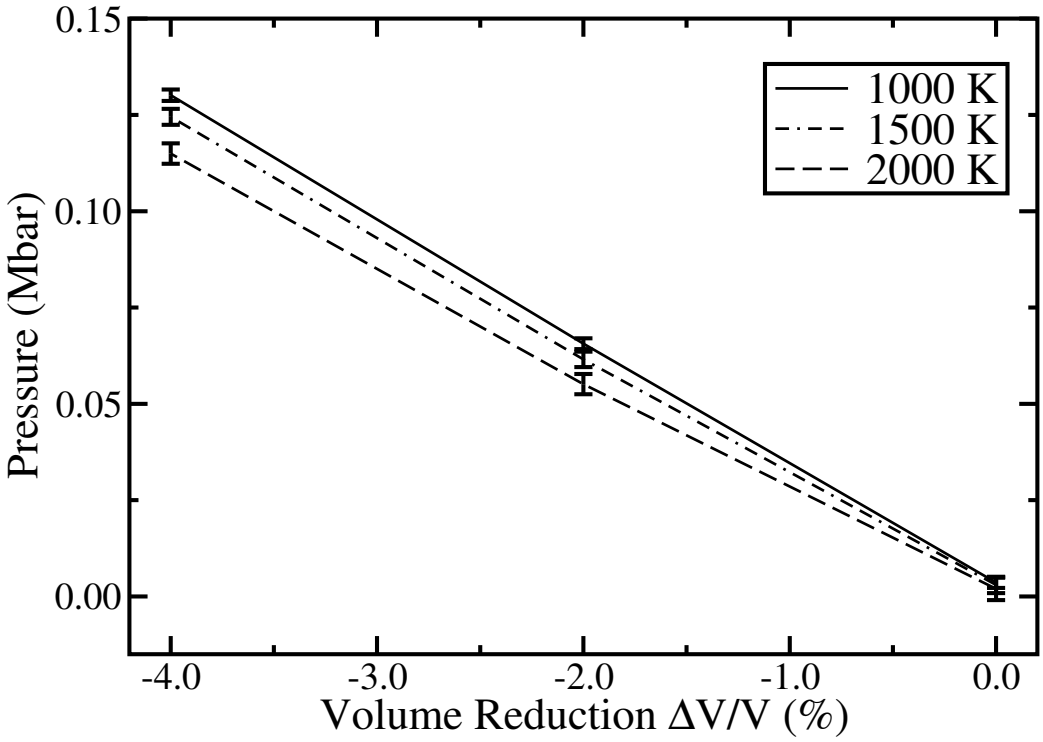

Fig. 6.46: *The change in hydrostatic pressure of a system of tungsten particles is shown as a function of relative volume reduction. The temperature dependent bulk moduli are determined to* $B(1000\,\mathrm{K}) = 3.1628\,\mathrm{Mbar}$, $B(1500\,\mathrm{K}) = 3.0381\,\mathrm{Mbar}$ *and* $B(2000\,\mathrm{K}) = 2.8250\,\mathrm{Mbar}$, *respectively.*

number of vacant lattice sites. In order to compute this formation energy we have to design a sequence of varying potentials transforming the thermodynamic state of the system according to

$$(N, p, T, 0) \to (N, p, T, 1)\,. \tag{6.87}$$

In practice it is not feasible to construct such sequences suitable for MD simulation. The reason for this is that the introduction of a vacant lattice site, maintaining the fixed number of atoms, results in symmetry alterations that cannot be represented in a computational cell subject to periodic boundary conditions. Because of this we cannot determine the vacancy formation parameters directly. Instead, one constructs a sequence of potentials, that represent transformations

$$(N, p, T, 0) \to (N-1, p, T, 1)\,, \tag{6.88}$$

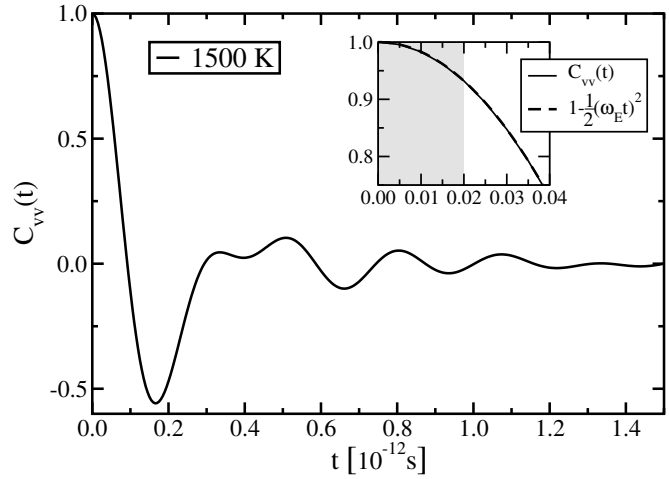

Fig. 6.47: *The (normalized)* velocity autocorrelation function *(VACF) is shown for a micro-canonical system of* 2048 *particles interacting with the EAM-potentials for thorium at an average temperature of about* 1500K. *The insert shows the VACF for short times together with a fit against its expected short time behavior, Eq. (6.54). The grey-shaded area marks the fitted region. The fit gives an angular* Einstein frequency *of about* $\omega_E \approx 1.8 \cdot 10^{13} s^{-1}$, *which corresponds to a frequency of* $f_E \approx 2.9 \cdot 10^{12} s^{-1}$.

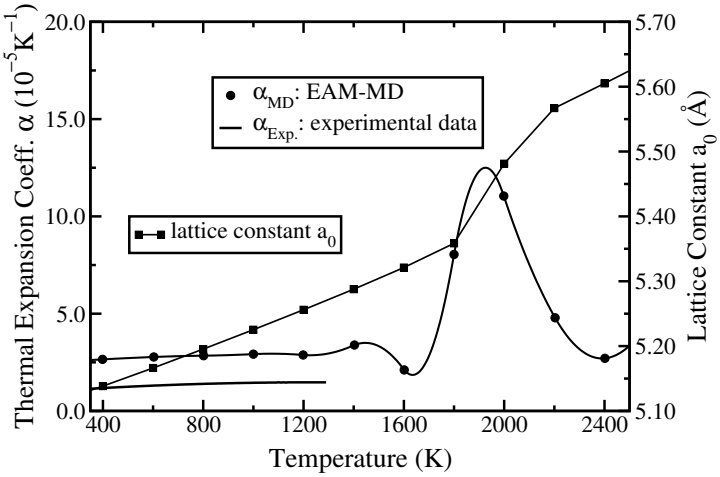

Fig. 6.48: *The temperature dependence of the equilibrium lattice constant* a_0 *of the thorium lattice and the corresponding* linear expansion coefficient *derived from a MD-simulation course together with experimental data [TKT75] is shown.*

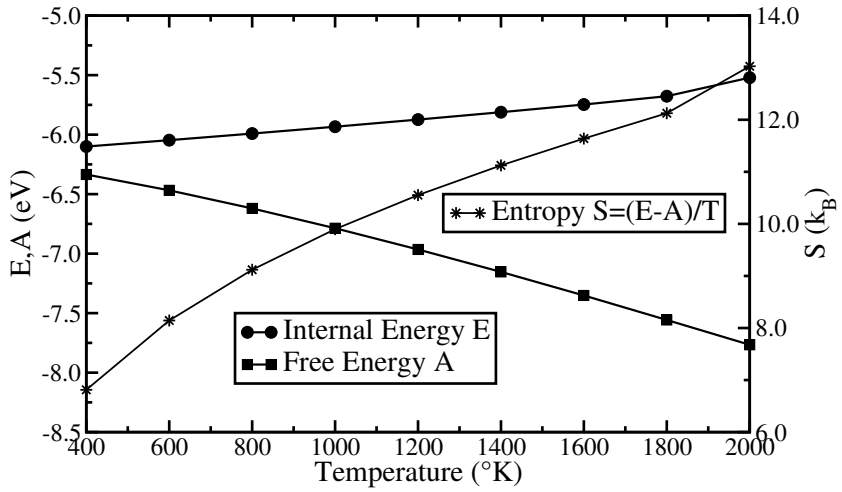

Fig. 6.49: *The* internal energy E, free energy A *and* entropy S *per atom for thorium as a function of temperature* T *between* 400K *and* 2000K *is shown.*

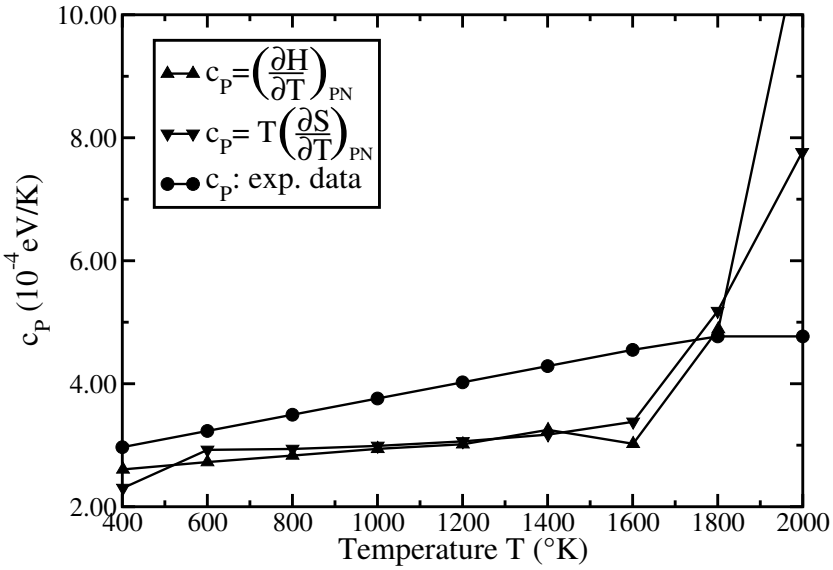

Fig. 6.50: $c_P(T)$ *for thorium is shown for temperatures between* 400K *and* 2000K *as derived from Eqs. (6.66).*

in which the interactions of the atom associated with a certain lattice site are turned off thus reducing the number of atoms in the system by one. Performing such (pT) transformations, the Gibbs free energy difference

$$\Delta G^{OD} = G(N-1, p, T, 1) - G(N, p, T, 0) \tag{6.89}$$

between the respective thermodynamic states can be readily determined using a proper sequence of overlapping distributions. Note that ΔG^{OD} can be identified as the chemical potential $\mu(p, T)$. The relation between the formation enthalpy g^{vf} and ΔG^{OD} can be seen realizing that definition (6.86) is established in the thermodynamic limit of large N. Thus, we may also write the definition as

$$g^{vf} = G(N-1, p, T, n=1) - G(N-1, p, T, n=0)\,. \tag{6.90}$$

Combining Eqs. (6.86),(6.89), and (6.90) it is easily seen that

$$g^{vf} = \Delta G^{OD} + g_0 \tag{6.91}$$

where

$$g_0 := G(N, p, T, 0) - G(N-1, p, T, 0) \tag{6.92}$$

represents the Gibbs free energy of an atom in bulk material, as already determined for tungsten in the preceding section. For ODM we have to use a proper scaling procedure of the functions defining the interatomic interaction. For the vacancy formation, we switch off the W-W interaction for one atom in the simulation cell keeping the remaining interactions unaffected. We use the scaling procedure as already described in Eq. 6.61 for the *lattice formation enthalpy*. The result, the *vacancy formation enthalpy* as a function of temperature, is given in Fig. 6.51. Remarkable here is the fact, that there is a drop in free enthalpy of almost one eV in the temperature range considered from 400K to 2000K.

6.10.3 (*Relaxed*) Th-Impurity Formation Enthalpy

Keeping Eq. (4.19) in mind, the following relation for the *Th-impurity formation enthalpy* can be established:

$$g^{if} := \Delta G^{OD}_{if} := G(N \cdot W, 1 \cdot Th) - G((N+1) \cdot W, 0 \cdot Th)\,. \tag{6.93}$$

$\Delta G^{OD}_{if} := G(N \cdot W, 1 \cdot Th) - G((N+1) \cdot W, 0 \cdot Th)$ can be calculated with the ODM procedure transforming one W-atom of a pure tungsten bulk into a Th-atom at constant pressure and temperature. As we want to use the

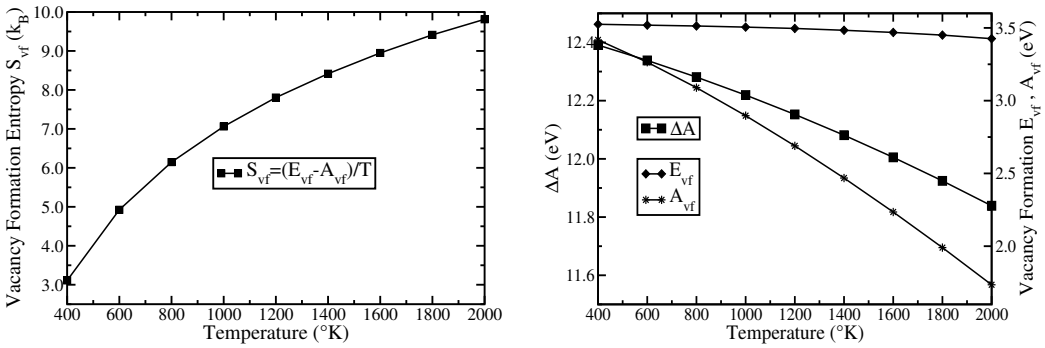

Fig. 6.51: *Left: The vacancy formation entropy for tungsten as a function of temperature is shown. Right: The free energy of vacancy formation in an otherwise undisturbed tungsten lattice.*

overlapping distribution method for calculating G_{if}^{OD}, we utilize the following scaling of the potentials, analogous to the calculations of the vacancy formation enthalpy, with the difference, that the interaction of one atom with the surrounding bulk atoms is gradually shifted from W-Th to W-W:

$$\begin{aligned} \phi_\alpha(r) &:= \alpha \cdot \phi_{ThTh}(r) + (1-\alpha) \cdot \phi_{WW}(r) \\ \rho_\alpha(r) &:= \alpha \cdot \rho_{Th}(r) + (1-\alpha) \cdot \rho_{W}(r) \\ F_\alpha(\rho) &:= \alpha \cdot F_{Th}(\rho) + (1-\alpha) \cdot F_{W}(\rho) \end{aligned} \tag{6.94}$$

and $\alpha \in [0,1]$. The results of the calculations, visualized in Fig. 6.52, are derived from a series of MD-simulations during which the initial situation (1023 tungsten atoms and one thorium atom) is gradually switched to the final situation (1024 tungsten atoms).

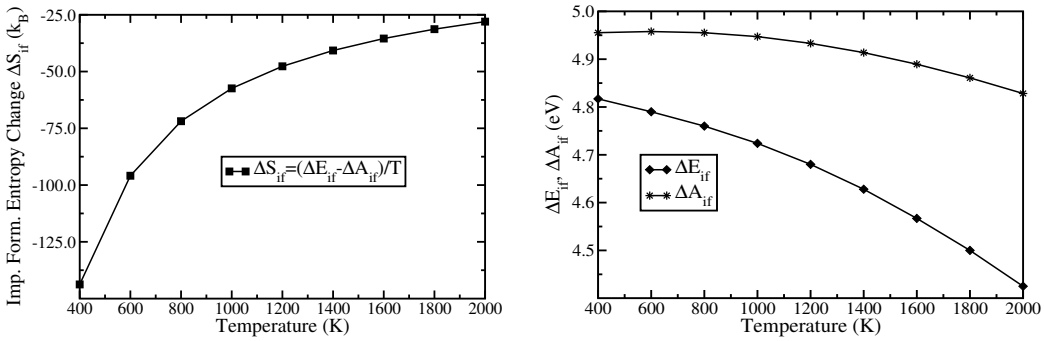

Fig. 6.52: *Left: The impurity formation entropy change* $\Delta S_{if} = (\Delta E_{if} - \Delta A_{if})/T$ *as a function of temperature. Right: The Gibbs free energy change and the internal energy change of impurity formation as derived from a MD-simulation of 1023 tungsten atoms and one thorium atom gradually switched into a tungsten atom.*

Chapter 7

Summary and Outlook

The use of the transition metal tungsten in lamp applications, both incandescent as well as discharge lamps, is demanded by the specific requirements of modern lamps. Tungsten has the highest melting point (approx. 3680K) among all metals in the periodic table of elements. Furthermore, its equilibrium vapor pressure is by far the lowest at a given temperature. Thoria, ThO_2, as an additive (approx. 1 weight-%) before the sintering stage, results in a high temperature creep resistant material, which maintains its shape under moderate mechanical stresses applied through e.g. gravitational forces always present on coils and electrodes. For electrodes, the use of *thoria*-doped tungsten offers another benefit: Thorium covered tungsten surfaces show a drastically reduced *electronic work function* ($\sim$ 4.5eV for "clean" tungsten surfaces down to $\sim$ 2.6eV for a monolayer of thorium on tungsten surfaces). This results in a huge reduction of electronic tip temperatures and, therefore, in dramatically reduced tungsten vapor pressures. Unfortunately, thorium sublimates already at relatively low temperatures ($\sim$ 2000K), so that the high tip temperature of a typical operating electrode ($\sim$ 2900K) would result in an immediately "cleaned" tungsten surface associated with an increase in tip temperature, unless one manages to maintain a constant flow of thorium atoms towards the surface. In case of thoriated tungsten, this has to be accomplished with suitably adjusted diffusional fluxes of thorium in tungsten. This flux responds very sensitively on the local microstructure, as grain boundaries as well as dislocation cores offer "short circuit paths" for thorium atoms. Diffusional jumps through tungsten single crystals is comparably unlikely, as thorium atoms cannot occupy regular lattice sites in tungsten due to the size mismatch of thorium and tungsten atoms.

In this work, we address some open issues for thoriated tungsten in order to gain some more in-depth insights into this material system with the aim to improve the knowledge about operating modes and, therefore, in the

long term, to be able to design the material according to the needs in lamp industry. As we are mainly interested in static as well as dynamic material properties which have their common origin in the atomistic behavior of tungsten and thorium atoms, the method of choice is the *molecular dynamics scheme*. For this, we have to describe the interatomic interactions between thorium and tungsten atoms by proper means. As there is no alloying system known between thorium and tungsten, we have to gather data from purely *ab-initio* grounds. This was accomplished with the meanwhile well-known $WIEN97$ package, version $WIEN97.8$, release $4/99$ [BSL99], a *full potential augmented planewave* code, to get (hypothetical, i.e. not occurring in nature) "alloy" data of W-Th condensed in a $B2$ and $L1_2$ structure. These data include, among others, the elastic properties of these kind of "alloys", which were used to fit an, theoretically justified, interatomic interaction scheme, i.e. the *embedded atom model (EAM)*. The EAM is perfectly adapted for transition metals, as the peculiarities of the d- or f-electrons in the chemistry of these metals, grounded on the quite small *second moment* of the *local density of states (LDOS)* (see also the closely related *Finnis-Sinclair* approach and the reasoning thereof), are described very well. It turned out to be essential for the successful description of the interatomic interaction of tungsten and thorium atoms to use a most flexible parametric scheme. Within the EAM, the following partition of the total (*cohesion*) energy of an (static) interacting N-atomic assembly is used, Eq. (5.58):

$$E_{coh} = \frac{1}{2} \sum_{\substack{i,j \\ (j \neq i)}}^{N} \phi_{t_i t_j}(R_{ij}) + \sum_{i}^{N} F_{t_i}(\bar{\rho}_i) \,,$$

where $\phi_{t_i t_j}(R_{ij})$, describes a pair interaction between atom i and j of *type* t_i and t_j, R_{ij} denotes the distance of particles i and j, $\bar{\rho}_i$ the "electronic density" via

$$\bar{\rho}_i = \sum_{j(\neq i)} \rho_{t_j}(R_{ij}) \,,$$

which mimics the superposition of the atomic electronic densities and, therefore, is assumed to be also of pairlike nature. The aforementioned flexibility of this scheme comes with the *embedding function* $F_{t_i}(\bar{\rho}_i)$, which contributes an additional portion of energy. Whereas $\bar{\rho}_i$ and $\phi_{t_i t_j}(R_{ij})$ are fixed within a suitably chosen parametric ansatz, $F_{t_i}(\bar{\rho}_i)$ is completely free beforehand. The embedding energy $F_{t_i}(\bar{\rho}_i)$ is determined through the assumption, that both, pure as well as alloy systems should follow the *universal binding energy function*, Eqs. (5.64) and (5.65), [RSGF84]. The embedding function $F_{t_i}(\bar{\rho}_i)$ thus determined for tungsten and for thorium, is a highly nonlinear function of

the "electronic density" and, once again, shows, that transition metals cannot be adequately described by purely pairwise interactions, which would necessarily enforce the embedding function to be linear. For the tungsten-thorium system, the embedding functions F_W and F_{Th}, the electronic density functions ρ_W and ρ_{Th} and the pair interaction functions ϕ_{WW}, ϕ_{ThTh} and ϕ_{WTh} are determined by fitting against the *ab-initio* data and the *universal binding energy function* using a multidimensional minimization scheme, the very robust *downhill simplex method* [NM65]. The result of the fitting process is shown in Fig. 5.3 and Fig. 5.4 and a summary of the parameters fixing the potentials are given in Tab. 5.4.

In principle, classical molecular dynamics simulations could now be performed as the *configurational forces* are completely determined and the dynamics is driven by *Newton's equation of motion* which has to be integrated to get the trajectories accordingly. In this thesis, however, we are often interested in properties influenced by pressure as well as temperature applied to the model system. Trajectories of which would be best described within a *NPT ensemble*, i.e. an ensemble where particle number N, pressure P and temperature T would be kept constant. Without any coupling to an external heat bath or volume reservoir, trajectories derived from the integration of Newton's equation of motion would describe a system with energy, volume and particle number conserved, i.e. a *NVE ensemble*. For the NPT ensemble, we used a generalization of the *variable cell* method, based on ideas of H. C. Andersen [And80] and, M. Parrinello and A. Rahman [PR80], in combination with the *Langevin piston*, introduced among others by Feller *et. al.* [FZPB95] and Kolb *et. al.* [KD99], which result in a set of *Langevin equations*, i.e. stochastic differential equations including a properly chosen "noise" term. The equations of motion (EOM) which are integrated in this thesis are given by, Eqs. (5.26) and (5.28):

$$\begin{aligned} \dot{r}_{i\alpha} &= v_{i\alpha} \\ m_i \dot{v}_{i\alpha} &= f_{i\alpha} + m_i \frac{\dot{V}_\alpha}{L_\alpha} r_{i\alpha} - m_i \gamma_0 v_{i\alpha} + m_i \sqrt{2D_i}\, \Gamma(t) \end{aligned}$$

and

$$\begin{aligned} \dot{L}_\alpha &= V_\alpha \\ W_\alpha \dot{V}_\alpha &= \frac{\Omega}{L_\alpha} \left(\Pi_{\alpha\alpha} - P \right) - W_\alpha \gamma_B V_\alpha + W_\alpha \sqrt{2D_\alpha}\, \Gamma(t) \,. \end{aligned}$$

where $r_{i\alpha}$, L_α is α-component of the position of the i-th particle and box dimension, necessary for establishing the volume reservoir. Here, we also

introduced a stochastic force $\Gamma(t)$ which with its *first* and *second moment* is characterized as *Gaussian White Noise*:

$$\langle \Gamma(t) \rangle = 0\,,$$
$$\langle \Gamma(t)\Gamma(t') \rangle = \delta(t-t')\,,$$

where $\langle \ldots \rangle$ denotes, as usual, averaging over the corresponding *random variables*. γ_0 and γ_B are "friction coefficients" which have to be chosen carefully for the particles as well as for the box dimensions. The "diffusion constants" D_i and D_α are determined by applying the *Fluctuation-Dissipation Theorem* (DFT) in a special form:

$$D_\alpha := \frac{k_B T}{W_\alpha}\gamma_B \qquad , \qquad D_i := \frac{k_B T}{m_i}\gamma_0\,.$$

for the box parameters (with "box mass" W_α) and the particle positions (mass m_i), respectively. The EOM as formulated above, are of *markovian* nature and, therefore, can be integrated "from time step to time step". With these "trajectories" (the quotation marks are necessary here, as the generated sequence of particle positions is not differentiable anymore, which is in clear contrast to actual particle motion), thus determined, one is able to average properties within a NPT ensemble. Unfortunately, Gear's predictor corrector scheme of sixth order, while very successful in integrating deterministic equations of motion of second order, cannot be used for stochastic differential equations. Instead, a new integration scheme is derived for our purposes, closely resembling the well-known *Velocity Verlet Algorithm*, Eqs. (5.30) and (5.32), for details see Appendix E. As an direct check of the interatomic interaction derived for the pure systems, we calculated the phonon dispersion for, both, tungsten and thorium through diagonalization of the dynamical matrix, see Eqs. (6.7, 6.9). The main features of the experimentally available dispersions are perfectly reproduced, see Fig. 6.1, a quite nice proof of the reliability of the EAM potentials generated.

The potentials were further used to calculate the *excess volumes* of point defects, i.e. for vacancies and th-impurities in tungsten, grain boundary structures and energies, where we first explored a variety of *CSL* boundaries, here both differences as well as similarities with simulations by different authors and different systems could be found. We then concentrated more on a special model system for an archetype boundary: the $\Sigma 5(310)[001]$ *symmetrical tilt boundary*, for which we investigated the energy variations and the "atomic" volumes, as generated by a *Voronoi tessellation* of the atomic coordinates of the simulation cell to some more detail. Additionally, we took a look at various *stacking fault energies* and linked the results to the question

whether screw dislocations in tungsten can split into partials from purely energetical reasons. To go ahead, we took an in-depth sight into dislocation theory, starting with the edge and screw dislocations, addressing the point whether dislocations of mixed type, i.e. a dislocation which has both, screw as well as edge components, are "more likely to be stable" in tungsten as hinted at in a different work for iron, see [Old86].

Moreover, we were interested in *free enthalpy differences*, quantities, which are generally hard to get evaluated within conventional MD simulations. The most obvious choice, the *thermodynamic integration*, is not always practical due to its inherent insufficiency, so that in general the errors in the calculated free enthalpy differences are huge enough to produce meaningless results. Here, we made use of the *Overlapping Distribution Method* (ODM) [Ben76], an efficient, albeit computationally demanding, method to calculate directly free enthalpy differences, with which we addressed the question of lattice formation, vacancy formation and impurity formation at various temperatures.

The question about diffusion of Th in tungsten could not be fully addressed apart from some energetic considerations, as "hopping" events of thorium atoms in tungsten are supposed to be very rare. As system trajectories are necessarily finite in time and comparably short, a fact which cannot be circumvented even with nowadays computers, the conventional approach is unlikely to produce reasonable results due to the poor statistics to be expected. For future work, therfore, one should improve this situation in implementing more efficient approaches, e.g. those commonly referred to as *Hyperdynamics* as described in [Vot97]. Also, it would be highly beneficial to be able to determine diffusional paths beforehand, in order to construct *biased potentials*, a necessary ingredient for most of the accelerated dynamics schemes. One of which is the nowadays well established *nudged elastic band* method or an adaptive variant of which [MAB$^+$02] to find transition states and minimum energy paths efficiently.

Appendix A

Murnaghan's equation of state

As a method of choice to calculate the bulk modulus of a solid, one should fit a set of energy-volume pairs (E_i, V_i) to a sensible chosen equation of state. A simple fit to a parabola:

$$E(V) - E(V_0) = \frac{B}{2V_0}(V - V_0)^2 \tag{A.1}$$

with

$$V_0 := V(p = 0) \tag{A.2}$$

the equilibrium volume at zero hydrostatic pressure p, would be perfectly correct, if Hooke's Law, which postulates a linear relationship between stress and strain, for the interatomic interactions were strictly valid. Unfortunately this simple assumption is only well justified for infinitesimal strains. For physical strains being not infinitesimal at all, this simple equation is not appropriate anymore.

In this section we derive an equation of state, which takes care of the fact, that the bulk modulus in the most simple case depends linearly on the hydrostatic pressure. The basic idea traces back to F. D. Murnaghan [Mur44], hence the name *Murnaghan's equation of state*.

As starting point serves a linear ansatz of the (isothermal) bulk modulus $B(p)$ as a function of the hydrostatic pressure p:

$$B(p) := B_0 + B' \cdot p \tag{A.3}$$

with

$$B' := \left.\frac{dB}{dp}\right|_{p=0} \tag{A.4}$$

The definition of the (isothermal) bulk modulus [AM76]

$$B(p) := -V_0 \left(\frac{\partial p}{\partial V}\right)_T \Bigg|_{V=V_0} \tag{A.5}$$

inserted and integrated gives

$$\ln\Big(\frac{V_0}{V}\Big) = \ln\Big(1 + \frac{B'}{B_0}p\Big)^{1/B_0} . \tag{A.6}$$

Therefore Murnaghan's equation of state for this model system results in:

$$p(V) = \frac{B_0}{B'}\left[\left(\frac{V_0}{V}\right)^{B'} - 1\right] , \tag{A.7}$$

for $T \to 0K$. To derive the internal energy E as a function of volume V one hast to note a standard result from statistical mechanics:

$$\left(\frac{\partial E}{\partial V}\right)_T = T\left(\frac{\partial S}{\partial V}\right)_T - p \tag{A.8}$$

and a consequence of the $3rd$ law of thermodynamics [Rei65] in the formulation of *Nernst* [Päs75, Ner24]:

$$\lim_{T\to 0K}\left(\frac{\partial S}{\partial V}\right)_T = S_0 \tag{A.9}$$

S_0 being a constant independent of all parameters of the system [Rei65]. Consequently to get the desired relationship one has to integrate:

$$\left(\frac{\partial E}{\partial V}\right)_T = -\frac{B_0}{B'}\left[\left(\frac{V_0}{V}\right)^{B'} - 1\right] \tag{A.10}$$

or

$$E(V) - E(V_0) = -\frac{B_0}{B'}\int_{V_0}^{V}\left[\left(\frac{V_0}{V'}\right)^{B'} - 1\right] dV' . \tag{A.11}$$

This results in an equation which when fitted on a set of pairs (V_i, E_i) determines the bulk modulus B_0 and its pressure derivative B' as well:

$$E(V) - E(V_0) = \frac{B_0 V}{B'}\left(1 + \frac{1}{B'-1}\left(\frac{V_0}{V}\right)^{B'}\right) - \frac{B_0 V_0}{B'-1} \tag{A.12}$$

Appendix B

Random Variables and Stochastic Processes

B.1 Random Variables

Following the treatment of Gillespie [Gil96], we introduce stochastic processes and look at the properties of the type of process, the *Gaussian Process*, which we implemented and use throughout this work. For this we tried to keep the rigid mathematics at an absolute minimum, for a much more thorough treatment see, e.g. [Pap65, KP92, Gar83, Wax54].

Let us start with a summary of the well-known properties of *random variables*. We call X a random variable with *density function* W, if $W(x)\,dx$ is the probability that a sampling of the random variable X gives a value between x and $x + dx$. The *average* or *mean value* of an arbitrary function of the random variable X, $\langle g(X)\rangle$, is defined as

$$\langle g(X)\rangle := \int_{-\infty}^{\infty} g(x)W(x)\,dx. \tag{B.1}$$

If we consider r random variables $\nu_1, \ldots, \nu_r$, where the last $r-1$ variables are assumed to take the fixed values $\nu_2 = x_2, \ldots, \nu_r = x_r$, the *conditional probability*, $P(x_1|x_2, \ldots, x_r)$, is defined as the probability that $\nu_1 = x_1$, given the fact that $\nu_2 = x_2, \ldots, \nu_r = x_r$. As above, the probability of finding the values of the random variables ν_i between x_i and $x_i + dx_i$ (with $i = 1, \ldots, r$) is $W_r(x_1, \ldots, x_r)\,dx_1 \ldots dx_r$. This can be rephrased as the probability of finding ν_1 between x_1 and $x_1 + dx_1$ given that the other variables have the sharp values $\nu_i = x_i$ for $(i = 2, \ldots, r)$,

$$P(x_1|x_2, \ldots, x_r)\,dx_1, \tag{B.2}$$

times the probability of finding the other variables between $x_i + dx_i$,

$$W_{r-1}(x_2, \ldots, x_r)\, dx_2 \ldots\, dx_r, \tag{B.3}$$

from which we get

$$W_r(x_1, \ldots, x_r) = P(x_1|x_2, \ldots, x_r) W_{r-1}(x_2, \ldots, x_r) \tag{B.4}$$

As we will see later, the function P is mainly used in connection with stochastic processes, where $x_i = x_i(t)$ (more about this in the next section). This is the reason for $P(x_1|x_2, \ldots, x_r)$ also being known as the *transition probability*.

The type of random variable which draws our attention is the so called *Gaussian* (or *normal*) random variable, $X = N(\mu, \sigma^2)$, with the density function

$$W(x) := \frac{1}{\sqrt{2\pi\sigma^2}}\, e^{-\frac{(x-\mu)^2}{2\sigma^2}}, \tag{B.5}$$

where μ is the mean and σ^2 the variance. Gaussian random variables have several important properties. For every two numbers α and $\beta \in \mathbf{R}$, one has

$$\alpha + \beta N(\mu, \sigma^2) = N(\alpha + \beta\mu, \beta^2\sigma^2). \tag{B.6}$$

For two statistically independent random variables $N(\mu_1, \sigma_1^2)$ and $N(\mu_2, \sigma_2^2)$ we get

$$N(\mu_1, \sigma_1^2) + N(\mu_2, \sigma_2^2) = N(\mu_1 + \mu_2, \sigma_1^2 + \sigma_2^2). \tag{B.7}$$

An important type of Gaussian random variable is the so called *unit Gaussian*, $G(t) = N(0, 1)$. The unit Gaussian is temporally uncorrekated and since it has unit variance, we have

$$\langle G(t) \rangle = 1. \tag{B.8}$$

B.2 Stochastic Processes

A *stochastic process* Y is a random variable, of which the density function depends on a real parameter, commonly referred to as *time*, such that $Y(t_1)$ and $Y(t_2)$ generally denote two different random variables. A very important type of a stochastic process is the *continuous Markov process*. These are defined as processes, for which (a) the variable Y at time $t + dt$ depends solely on t, dt and $Y(t)$, i. e. , the variable is 'memoryless', (b) the increment $\Xi(dt; y, t) := Y(t + dt) - Y(t)$, given that $Y(t) = y$, depends 'smoothly' on dt, t and y and (c) Y is 'continuous', meaning that $\Xi(dt; y, t) \to 0$ as $dt \to 0$

for each choice of y and t. Due to the lack of memory of the Markov process, it is seen that the transition probability obeys

$$P(x_n, t_n | x_{n-1}, t_{n-1}; \ldots; x_1, t_1) = P(x_n, t_n | x_{n-1}, t_{n-1}), \quad t_n > \ldots > t_1. \tag{B.9}$$

With the definitions above, it is possible to show (see e. g. the appendix in Gillespie [Gil96]) that for a ontinuous Markov process the increment $\Xi(dt; y, t)$ has the following analytical form

$$\Xi(dt; y, t) = h(y, t)\, dt + g(y, t)G(t)\sqrt{dt}. \tag{B.10}$$

h and g are two arbitrary functions of y and t, and $G(t) = N(0, 1)$ is the previously introduced unit Gaussian random variable. The reason for the somewhat strange square root increment is that when one wants to add independent random variables one has to add variances rather than standard deviations. If we insert the definition of $\Xi(dt; y, t)$ into Eq. (B.10) we arrive at a *Langevin equation*

$$Y(t + dt) = Y(t) + h(Y(t), t)\, dt + g(Y(t), t)G(t)\sqrt{dt}. \tag{B.11}$$

The increments are separated in two terms: a deterministic one incremented by dt, and a stochastic one incremented by $\sqrt{dt}$. One could be tempted to argue that since $\sqrt{dt}$ is much larger than dt one could drop the deterministic term. But since the stochastic term is equally likely positive or negative, the deterministic term will still contribute to the mean value. A rearrangement of the Langevin equation

$$\frac{Y(t + dt) - Y(t)}{dt} = h(Y(t), t) + \frac{g(Y(t), t)G(t)}{\sqrt{dt}}\,, \tag{B.12}$$

shows that although Y is continuous, it is not differentiable since the limit $dt \to 0$ does not exist in the conventional sense. This is due to the 'non-equation' nature of the Langevin equation. If we continue, despite our formal problems, we have due to the rules of Gaussian processes

$$\frac{G(t)}{\sqrt{dt}} = (dt)^{-1/2} N(0, 1) = N(0, \frac{1}{dt})\,. \tag{B.13}$$

The relation above finally leads to the definition of the *Gaussian white noise* process g_w:

$$g_w(t) := \lim_{dt \to 0} N(0, \frac{1}{dt})\,. \tag{B.14}$$

We are now in the position to perform the limit $dt \to 0$ in Eq. (B.12) yielding the *white noise form Langevin equation*

$$\dot{Y}(t) = h(Y(t), t) + g(Y(t), t)g_w(t)\,. \tag{B.15}$$

This version of the Langevin equation is the most widely used in the literature. The Gaussian white noise has the properties

$$\langle g_w(t) \rangle = 0, \tag{B.16}$$

$$\langle g_w(t) g_w(t') \rangle = \delta(t - t') \,. \tag{B.17}$$

Appendix C

Box-Mueller Method for generating Normal (Gaussian) Deviates

The generation of *normal* (or *Gaussian*) distributed random numbers on a computer can be very efficiently accomplished with two uniform deviates x_1 and x_2 (chosen from the range $[0, 1]$). The random numbers y_1 and y_2 defined through the mapping of x_1 and x_2 to

$$\begin{aligned} y_1 &:= \sqrt{-2 \ln x_1} \cos(2\pi x_2) \\ y_1 &:= \sqrt{-2 \ln x_1} \sin(2\pi x_2) \end{aligned} \tag{C.1}$$

can be shown to generate Gaussian distributed numbers. To prove this, one has to apply the transformation formula for probability distributions (see e. g. [vK92]):

$$P_{\{Y_1,Y_2\}}(y_1, y_2) = \int \delta(y_1(x_1, x_2) - y_1)\delta(y_2(x_1, x_2) - y_2) \cdot P_{\{X_1,X_2\}}(x_1, x_2)\, dx_1\, dx_2 \tag{C.2}$$

which for invertible mappings reduces to:

$$P_{\{Y_1,Y_2\}}(y_1, y_2) = P_{\{X_1,X_2\}}(x_1, x_2) \left| \frac{\partial(X_1, X_2)}{\partial(Y_1, Y_2)} \right| \tag{C.3}$$

where $\left|\frac{\partial(X_1,X_2)}{\partial(Y_1,Y_2)}\right|$ is the absolute value of the Jacobi determinant of the mapping. For the transformation above the Jacobian is readily evaluated to

$$\left| \frac{\partial(X_1, X_2)}{\partial(Y_1, Y_2)} \right| = \left[\frac{1}{\sqrt{2\pi}} e^{-\frac{Y_1^2}{2}} \right] \left[\frac{1}{\sqrt{2\pi}} e^{-\frac{Y_2^2}{2}} \right] . \tag{C.4}$$

The Jacobian (C.4) factorizes, so that Y_1 and Y_2 are independent random variables and distributed according to the Gaussian distribution:

$$P_{\{Y_1\}}(y_1) = \frac{1}{\sqrt{2\pi}} e^{-\frac{y_1^2}{2}} \,. \tag{C.5}$$

Instead of picking uniform deviates x_1 and x_2 the Box-Mueller method starts with a sample point within a unit circle around the origin. The sum of the squares of the corresponding abscissa v_1 and ordinate v_2, $R^2 := v_1^2 + v_2^2$, is a uniform deviate, which can be inserted for x_1 in Eqs. (C.1). This is easily seen by recognizing that (v_1, v_2) is uniformly deviated within the unit circle $K(0,1)$, which implies, that the corresponding probability density $P(v_1, v_2)$ is given by

$$P(v_1, v_2) = \begin{cases} \frac{1}{\pi} & \text{if } (v_1, v_2) \in K(0,1)\,, \\ 0 & \text{else} \end{cases} \tag{C.6}$$

and simply applying the transformation formula (C.2) once more:

$$P(R^2) = \int \delta(v_1^2 + v_2^2 - R^2) P(v_1, v_2)\, dv_1\, dv_2 \quad \text{with } R \leq 1. \tag{C.7}$$

Introducing polar coordinates (r, ϕ) and the proper integral transformation formula, $dv_1\, dv_2 = r dr\, d\phi$, we arrive at

$$P(R^2) = \frac{1}{\pi} \int_0^{2\pi} \int_0^1 \delta(r^2 - R^2)\, r\, dr\, d\phi \,. \tag{C.8}$$

Performing the integrations, bearing in mind, that $\delta(r^2 - R^2) = \frac{1}{2R}(\delta(r - R) + \delta(r + R))$, which due to the integration limits reduces to $\delta(r^2 - R^2) = \frac{1}{2R}(\delta(r - R))$, we finally get the result:

$$P(R^2) = \begin{cases} 1 & \text{if } R^2 \in [0,1], \\ 0 & \text{else.} \end{cases} \tag{C.9}$$

This shows as claimed that R^2 is a uniform deviate.

It is easy to see that the random variable $Y := cos(2\pi X)$ with X uniformly distributed in $[0;1]$ is deviated as:

$$P(Y) = \begin{cases} \frac{1}{\pi} \frac{1}{\sqrt{1-Y^2}} & \text{when } Y \in [-1;1] \\ 0 & \text{else}\,. \end{cases} \tag{C.10}$$

In order to use $z := v_1/\sqrt{R^2}$ as $\cos(2\pi x_2)$ in (C.1), one has to ensure, that $P(Y) \equiv P(Z)$. To calculate $P(Z)$, one has to solve the following integral:

$$P(z) = \int \delta(z - \frac{v_1}{\sqrt{R^2}}) P(v_1, v_2)\, dv_1\, dv_2 \tag{C.11}$$

with $P(v_1, v_2)$ given by Eq. (C.6). Eq. (C.11) is easily solved using polar coordinates:

$$P(z) = \frac{1}{\pi} \int_0^1 \int_{-\pi}^{\pi} \delta(z - \cos(\phi))\, r dr\, d\phi\,. \tag{C.12}$$

Within $-\pi \leq \phi \leq \pi$ the following relation is valid:

$$\delta(z - \cos(\phi)) = \frac{1}{\sqrt{1 - z^2}} \left(\delta(\phi - \arccos(z)) + \delta(\phi + \arccos(z))\right)\,. \tag{C.13}$$

Performing the integrations, we finally arrive at

$$P(z) = \begin{cases} \frac{1}{\pi} \frac{1}{\sqrt{1-z^2}} & \text{when } z \in [-1; 1] \\ 0 & \text{else}\,. \end{cases} \tag{C.14}$$

which is indeed identical to Eq. (C.10).

Now, we are in the position to formulate the *Box-Mueller Method* to generate Gaussian distributed numbers:

1. choose a point (v_1, v_2) uniformly distributed within a unit circle
2. use $v_1^2 + v_2^2$ as x_1, $v_1/\sqrt{R^2}$ as $\cos(2\pi x_2)$, $v_2/\sqrt{R^2}$ as $\sin(2\pi x_2)$ and in Eq. (C.1)

The advantage of *Box-Mueller's Method* compared to using Eq. (C.1) directly, is that the time consuming process of evaluating the trigonometric functions is avoided. Fig. C.1 shows a sample of 10^6 points and the points rearranged in a histogram together with the corresponding Gaussian distribution function (C.5).

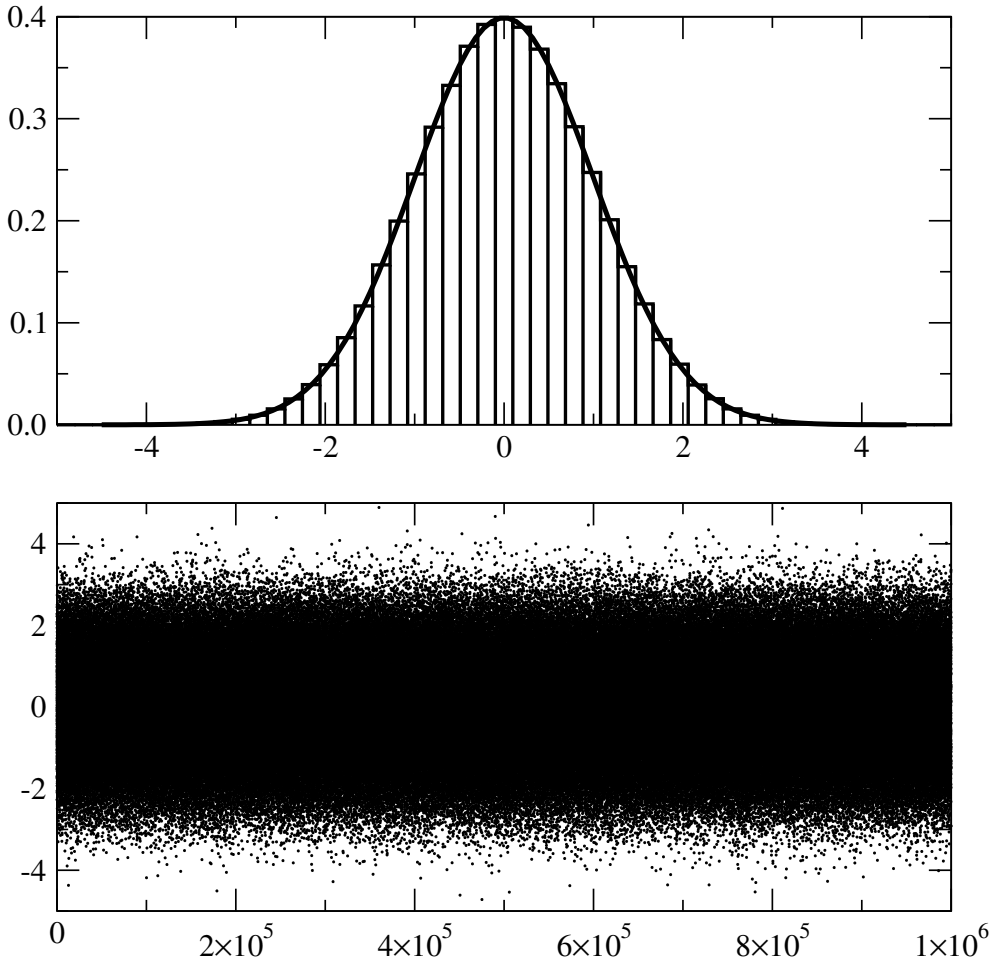

Fig. C.1: *A sample of* 10^6 *points (below) generated with Box-Mueller's method and (on top) the resulting histogram together with the Gaussian distribution (Eq. C.5)*

Appendix D

Langevin Dynamics

Due to the overwhelming importance of the *Langevin equation* in generating the NPT ensemble, a simple derivation of it shall now be presented. A formal way of deriving *Langevin Dynamics* is the projection operator formalism of Zwanzig [Zwa60, Zwa61] and Mori [Mor65b, Mor65a]. In this approach the phase space is devided into two parts, which are called *interesting* and *uninteresting* (sometimes also called *slow* and *fast*) degrees of freedom (DOF). For the approach to be useful, the uninteresting DOF should be rapidly varying with respect to the interesting DOF. Mori introduced two projection operators, which project the whole phase space into the sets of interesting and uninteresting DOF, respectively. These projection operators are used to project the full equations of motion into the set of interesting DOF. The result is a differential equation with three force terms: a mean force between the interesting DOF, a dissipative or frictional force exerted by the uninteresting DOF onto the interesting coordinates and a rest term which consists of forces which are neither correlated with the positions nor with the velocities. The frictional and uncorrelated force have the same memory functions, the shape of which is given by the projection operator formalism. When the uncorrelated force is approximated by a random force the interesting DOF are independent of the uninteresting DOF, so the number of DOF can be reduced.

So, generally speaking a Langevin dynamics system arises from a classical system by removing degrees of freedom. The degrees of freedom exerts conservative and frictional forces on the rest of the system. All other forces are assumed to add up to a random force. To elucidate the origin of the force terms as introduced above, another derivation is useful and shall be sketched now.

In deriving the *nonlinear generalized Langevin equations* for our extended system Lagrangian, Eq. (5.17), we follow closely the very nice articles of

R. Zwanzig [Zwa73] and P. Hänggi [Hän97].

As starting point serves the classical Lagrangian

$$\begin{aligned} L := & \sum_{\substack{i=1\ldots N \\ \alpha=1\ldots 3}} \frac{m_i}{2}(\dot{r}_{i\alpha} - \frac{\dot{L}_\alpha}{L_\alpha} r_{i\alpha})^2 - V(\{r_{i\alpha}\}) + \sum_{\alpha=1\ldots 3} \frac{W_\alpha}{2}\dot{L}_\alpha^2 - P \prod_{\alpha=1\ldots 3} L_\alpha \\ & + \sum_{\substack{i=1\ldots N \\ \alpha=1\ldots 3}} \sum_j \frac{\lambda_j^{i\alpha}}{2}(\dot{q}_j^{i\alpha})^2 - \frac{\lambda_j^{i\alpha}(\omega_j^{i\alpha})^2}{2}\left(q_j^{i\alpha} - \frac{c_j^{i\alpha}}{\lambda_j^{i\alpha}(\omega_j^{i\alpha})^2} r_{i\alpha}\right)^2 \\ & + \sum_{\alpha=1\ldots 3} \sum_l \frac{\Lambda_l^\alpha}{2}(\dot{Q}_l^\alpha)^2 - \frac{\Lambda_l^\alpha(\Omega_l^\alpha)^2}{2}\left(Q_l^\alpha - \frac{C_l^\alpha}{\Lambda_l^\alpha(\Omega_l^\alpha)^2} L_\alpha\right)^2 \quad , \end{aligned} \tag{D.1}$$

i.e. the extended system Lagrangian for orthorhombic cells, Eq. (5.17), where each DOF $(\{r_{i\alpha}\}, \{L_\alpha\})$ is linearly coupled to a bath of harmonic oscillators. With $\{q_j^{i\alpha}\}$, $\{\dot{q}_j^{i\alpha}\}$, $\{\lambda_j^{i\alpha}\}$ and $\{\omega_j^{i\alpha}\}$ we denote the bath coordinates, velocities, masses and frequencies, respectively, of the oscillators coupling to $r_{i\alpha}$. Accordingly, coordinates, velocities, masses and frequencies of the oscillators coupling to the box dimensions L_α are $\{Q_l^\alpha\}$, $\{\dot{Q}_l^\alpha\}$, $\{\Lambda_l^\alpha\}$ and $\{\Omega_l^\alpha\}$.

The *Euler-Lagrange equations of motion* generated from this Lagrangian are

$$m_i \ddot{r}_{i\alpha} = f_{i\alpha} + m_i \frac{\ddot{L}_\alpha}{L_\alpha} r_{i\alpha} + \sum_j c_j^{i\alpha}\left(q_j^{i\alpha} - \frac{c_j^{i\alpha}}{\lambda_j^{i\alpha}(\omega_j^{i\alpha})^2} r_{i\alpha}\right), \tag{D.2}$$

$$W_\alpha \ddot{L}_\alpha = \frac{\Omega}{L_\alpha}(\Pi_{\alpha\alpha} - P) + \sum_l C_l^\alpha\left(Q_l^\alpha - \frac{C_l^\alpha}{\Lambda_l^\alpha(\Omega_l^\alpha)^2} L_\alpha\right), \tag{D.3}$$

with

$$\Pi_{\alpha\alpha} = \frac{1}{\Omega}\sum_i \left(m_i(\dot{r}_{i\alpha} - \frac{\dot{L}_\alpha}{L_\alpha} r_{i\alpha})^2 + f_{i\alpha} r_{i\alpha}\right), \tag{D.4}$$

and for the bath degrees of freedom, respectively,

$$\lambda_j^{i\alpha}\ddot{q}_j^{i\alpha} + \lambda_j^{i\alpha}(\omega_j^{i\alpha})^2 q_j^{i\alpha} = c_j^{i\alpha} r_{i\alpha}, \tag{D.5}$$

and

$$\Lambda_l^\alpha \ddot{Q}_l^\alpha + \Lambda_l^\alpha(\Omega_l^\alpha)^2 Q_l^\alpha = C_l^\alpha L_\alpha. \tag{D.6}$$

The inhomogeneous equations of motion for the bath oscillators, Eq. (D.5) and (D.6), can easily be solved with standard solution methods for ordinary

differential equations, e.g. via *Variation of Parameters* or integral transfomation methods like *Laplace transforms*. An elegant way to deal with these inhomogeneous equations is the *Greens function approach*. The corresponding Greens functions are [MW70, Kuy90, Hän97]

$$G_j^{i\alpha}(t-t') := \frac{\sin(\omega_j^{i\alpha}(t-t'))}{\omega_j^{i\alpha}}\Theta(t-t'), \tag{D.7}$$

for the oscillators corresponding to $q_j^{i\alpha}$, and

$$G_j^{\alpha}(t-t') := \frac{\sin(\Omega_j^{\alpha}(t-t'))}{\Omega_j^{\alpha}}\Theta(t-t') \tag{D.8}$$

for those of Q_j^{α}. Integrating (D.5) and (D.6), we arrive at

$$\begin{aligned} q_j^{i\alpha}(t) &= q_j^{i\alpha}(t_0)\cos(\omega_j^{i\alpha}(t-t_0)) + \frac{\dot{r}_{i\alpha}(t_0)}{\omega_j^{i\alpha}}\sin(\omega_j^{i\alpha}(t-t_0)) \\ &\quad + \frac{c_j^{i\alpha}}{\lambda_j^{i\alpha}\omega_j^{i\alpha}}\int_{t_0}^{t}\sin(\omega_j^{i\alpha}(t-t'))r_{i\alpha}(t')\,dt', \end{aligned} \tag{D.9}$$

and

$$\begin{aligned} Q_l^{\alpha}(t) &= Q_l^{\alpha}(t_0)\cos(\Omega_l^{\alpha}(t-t_0)) + \frac{\dot{L}_{\alpha}(t_0)}{\Omega_l^{\alpha}}\sin(\Omega_l^{\alpha}(t-t_0)) \\ &\quad + \frac{C_l^{\alpha}}{\Lambda_l^{\alpha}\Omega_l^{\alpha}}\int_{t_0}^{t}\sin(\Omega_l^{\alpha}(t-t'))L_{\alpha}(t')\,dt'. \end{aligned} \tag{D.10}$$

Inserting (D.9) and (D.10) into (D.2) and (D.3) gives

$$\begin{aligned} m_i\ddot{r}_{i\alpha} &= f_{i\alpha} + m_i\frac{\ddot{L}_{\alpha}}{L_{\alpha}}r_{i\alpha} - \sum_j \frac{(c_j^{i\alpha})^2}{\lambda_j^{i\alpha}(\omega_j^{i\alpha})^2}r_{i\alpha} \\ &\quad + \sum_j \frac{(c_j^{i\alpha})^2}{\lambda_j^{i\alpha}\omega_j^{i\alpha}}\int_{t_0}^{t}\sin(\omega_j^{i\alpha}(t-t'))r_{i\alpha}(t')\,dt' \\ &\quad + \sum_j c_j^{i\alpha}\left(q_j^{i\alpha}(t_0)\cos(\omega_j^{i\alpha}(t-t_0)) + \frac{\dot{r}_{i\alpha}(t_0)}{\omega_j^{i\alpha}}\sin(\omega_j^{i\alpha}(t-t_0))\right), \end{aligned} \tag{D.11}$$

and

$$W_\alpha \ddot{L}_\alpha = \frac{\Omega}{L_\alpha}\left(\Pi_{\alpha\alpha} - P\right) - \sum_l \frac{(C_l^\alpha)^2}{\Lambda_l^\alpha (\Omega_l^\alpha)^2} L_\alpha + \sum_l \frac{(C_l^\alpha)^2}{\Lambda_l^\alpha \Omega_l^\alpha} \int_{t_0}^{t} \sin(\Omega_l^\alpha (t-t')) L_\alpha(t')\, dt' + \sum_l C_l^\alpha \left(Q_l^\alpha(t_0) \cos(\Omega_l^\alpha (t-t_0)) + \frac{\dot{L}_\alpha(t_0)}{\Omega_l^\alpha} \sin(\Omega_l^\alpha (t-t_0)) \right) \tag{D.12}$$

The last terms in (D.11) and (D.12) will be abbreviated with $F_{i\alpha}(t)$ and $F_\alpha(t)$, respectively. With the second and third terms collected, the equations read

$$m_i \ddot{r}_{i\alpha} = f_{i\alpha} + m_i \frac{\ddot{L}_\alpha}{L_\alpha} r_{i\alpha} + \sum_j \frac{(c_j^{i\alpha})^2}{\lambda_j^{i\alpha} (\omega_j^{i\alpha})^2} \left(\int_{t_0}^{t} r_{i\alpha}(t') \frac{\partial}{\partial t'} \cos(\omega_j^{i\alpha}(t-t'))\, dt' - r_{i\alpha} \right) + F_{i\alpha}(t) \tag{D.13}$$

and

$$W_\alpha \ddot{L}_\alpha = \frac{\Omega}{L_\alpha}\left(\Pi_{\alpha\alpha} - P\right) + \sum_l \frac{(C_l^\alpha)^2}{\Lambda_l^\alpha (\Omega_l^\alpha)^2} \left(\int_{t_0}^{t} L_\alpha(t') \frac{\partial}{\partial t'} \cos(\Omega_l^\alpha (t-t'))\, dt' - L_\alpha \right) + F_\alpha(t)\,. \tag{D.14}$$

It is convenient to carry the partial derivatives in the integrals to the system variables applying a partial integration:

$$m_i \ddot{r}_{i\alpha} = f_{i\alpha} + m_i \frac{\ddot{L}_\alpha}{L_\alpha} r_{i\alpha} - \sum_j \frac{(c_j^{i\alpha})^2}{\lambda_j^{i\alpha} (\omega_j^{i\alpha})^2} \left(\int_{t_0}^{t} \dot{r}_{i\alpha}(t') \cos(\omega_j^{i\alpha}(t-t'))\, dt' + r_{i\alpha}(t_0) \cos(\omega_j^{i\alpha}(t-t_0)) \right) + F_{i\alpha}(t) \tag{D.15}$$

and

$$W_\alpha \ddot{L}_\alpha = \frac{\Omega}{L_\alpha}\left(\Pi_{\alpha\alpha} - P\right) - \sum_l \frac{(C_l^\alpha)^2}{\Lambda_l^\alpha (\Omega_l^\alpha)^2} \left(\int_{t_0}^{t} \dot{L}_\alpha(t') \cos(\Omega_l^\alpha (t-t'))\, dt' + L_\alpha \cos(\Omega_l^\alpha (t-t_0)) \right) + F_\alpha(t)\,. \tag{D.16}$$

This is essentially the final result. The motion of the system variables $(r_{i\alpha}, L_\alpha)$ is expressed in terms of its own history and the bath variables enter only through their initial values. To put these equations in a more concise form, one defines a *noise term* (despite the fact, that the primary equations (D.2) and (D.3) are totally deterministic):

$$\begin{aligned}\Gamma_{i\alpha}(t) &:= F_{i\alpha}(t) - r_{i\alpha}(t_0)\sum_j \frac{(c_j^{i\alpha})^2}{\lambda_j^{i\alpha}(\omega_j^{i\alpha})^2}\cos(\omega_j^{i\alpha}(t-t_0)) \\ &= \sum_j c_j^{i\alpha}\left(\left(q_j^{i\alpha}(t_0) - r_{i\alpha}(t_0)\frac{c_j^{i\alpha}}{\lambda_j^{i\alpha}(\omega_j^{i\alpha})^2}\right)\cos(\omega_j^{i\alpha}(t-t_0)) \right. \\ &\qquad \left. + \frac{\dot r_{i\alpha}(t_0)}{\omega_j^{i\alpha}}\sin(\omega_j^{i\alpha}(t-t_0))\right),\end{aligned} \tag{D.17}$$

and the noise term for the box dimensions reads:

$$\begin{aligned}\Gamma_{\alpha}(t) &:= F_{\alpha}(t) - L_\alpha(t_0)\sum_l \frac{(C_l^{\alpha})^2}{\Lambda_l^{\alpha}(\Omega_l^{\alpha})^2}\cos(\Omega_l^{\alpha}(t-t_0)) \\ &= \sum_l C_l^{\alpha}\left(\left(Q_l^{\alpha}(t_0) - L_\alpha(t_0)\frac{C_l^{\alpha}}{\Lambda_l^{\alpha}(\Omega_l^{\alpha})^2}\right)\cos(\Omega_l^{\alpha}(t-t_0)) \right. \\ &\qquad \left. + \frac{\dot L_\alpha(t_0)}{\Omega_l^{\alpha}}\sin(\Omega_l^{\alpha}(t-t_0))\right).\end{aligned} \tag{D.18}$$

The statistical properties of the noise are determined via the statistical properties of the bath variables. If we assume that the distribution of the bath variables under the condition that the system variables are held constant, is *Gaussian* (the bath variables are harmonic oscillators, so that the Gaussian distribution in this case is identical to the canonical distribution), than the first and the second moments of the noise terms are given through

$$\langle\Gamma_{i\alpha}(t)\rangle = 0, \tag{D.19}$$

$$\langle\Gamma_{i\alpha}(t)\Gamma_{j\beta}(t')\rangle = \delta_{ij}\delta_{\alpha\beta}\delta(t-t') \tag{D.20}$$

and, similar,

$$\langle\Gamma_{\alpha}(t)\rangle = 0, \tag{D.21}$$

$$\langle\Gamma_{\alpha}(t)\Gamma_{\beta}(t')\rangle = \delta_{\alpha\beta}\delta(t-t'). \tag{D.22}$$

Finally, defining the *memory friction kernel*

$$\gamma_{i\alpha}(t-t') := \frac{1}{m_i}\sum_j \frac{(c_j^{i\alpha})^2}{\lambda_j^{i\alpha}(\omega_j^{i\alpha})^2}\cos(\omega_j^{i\alpha}(t-t')) \tag{D.23}$$

and

$$\gamma_{\alpha}(t-t') := \frac{1}{W_\alpha}\sum_l \frac{(C_l^{\alpha})^2}{\Lambda_l^{\alpha}(\Omega_l^{\alpha})^2}\cos(\Omega_l^{\alpha}(t-t')) \tag{D.24}$$

Armed with these annotations, the *generalized Langevin equations* (GLE) for the system under consideration read

$$m_i\ddot{r}_{i\alpha} = f_{i\alpha} + m_i\frac{\ddot{L}_\alpha}{L_\alpha}r_{i\alpha} - m_i\int_{t_0}^{t}\dot{r}_{i\alpha}(t')\gamma_{i\alpha}(t-t')\,dt' + \Gamma_{i\alpha}(t) \tag{D.25}$$

and

$$W_\alpha\ddot{L}_\alpha = \frac{\Omega}{L_\alpha}(\Pi_{\alpha\alpha} - P) - W_\alpha\int_{t_0}^{t}\dot{L}_\alpha(t')\gamma_\alpha(t-t'))\,dt' + \Gamma_\alpha(t). \tag{D.26}$$

These are the equations, which we will make use of extensively within our molecular dynamics considerations and, in this sense, form one of the corner pillars of the present thesis.

Appendix E

An Integration Scheme for Langevin Systems

In this Appendix an efficient integration scheme for stochastic differential equations will be developed. The for *stiff* problems usually very effective *Predictor Corrector Scheme* of six'th order [Gea66, Gea71] can not be used due to the influence of noise. In the following, we first introduce some basic notations and concepts, especially the *Standard Scalar Wiener process* and its connection to *Fokker-Planck Equations* and *Langevin Dynamics*, and second, a better alternative to Gear's scheme to integrate stochastic differential equations will be developed, which closely resembles the *Velocity Verlet Scheme*, of which is known, that it preserves the symplectic structure of phase space. Of course, this cannot be true for the scheme to be developed, but the very nice property of energy conservation up to relatively high time steps should be conserved.

E.1 Fokker-Planck Equation and Langevin Dynamics

For the following we define the *Standard Scalar Wiener process* $W(t)$ over $[0,T]$ as a random variable that depends continuously on $t \in [0,T]$ and satisfies the following three conditions:

1. $W(0) = 0$ (with probability 1)
2. For $0 \leq s < t \leq T$:

$$(W(t) - W(s)) \sim \sqrt{t-s} \cdot G(0,1)\,, \tag{E.1}$$

where $G(0,1)$ denotes the Gaussian distribution with zero mean and unit variance.

3. For $0 \leq s < t < u < v \leq T$:

$$\langle (W(t) - W(s)) \cdot (W(v) - W(u)) \rangle = 0\,. \tag{E.2}$$

In some sense, $\Delta W(t) := (W(t+\Delta t) - W(t))$ can be considered as the integral of the previously defined *Gaussian White Noise* $\Gamma(t)$. For this, we note that $\Gamma(t)$ is defined as a Gaussian distributed random variable. The integral of this is therefore a Gaussian random variable, too. In order to show the equivalence of the likewise Gaussian distributed $\Delta W(t) := (W(t+\Delta t) - W(t))$ and $\int_t^{t+\Delta t} \Gamma(t')\,dt'$, it is only necessary for both random variables to have equal first and second moments.

The first moments for the random variables are zero:

$$\langle \Delta W(t) \rangle := \langle (W(t+\Delta) - W(t)) \rangle = 0 \tag{E.3}$$

and

$$\left\langle \int_t^{t+\Delta t} \Gamma(t')\,dt' \right\rangle = \int_t^{t+\Delta t} \langle \Gamma(t') \rangle \; dt' = 0\,. \tag{E.4}$$

Furthermore, the variances are given as:

$$\left\langle (\Delta W(t))^2 \right\rangle := \left\langle (W(t+\Delta) - W(t))^2 \right\rangle = \Delta t \tag{E.5}$$

and

$$\begin{aligned} \left\langle \left(\int_t^{t+\Delta t} \Gamma(t')\,dt' \right)^2 \right\rangle &= \left\langle \left(\int_t^{t+\Delta t} \int_t^{t+\Delta t} \Gamma(t')\Gamma(t'')\,dt'\,dt'' \right) \right\rangle \\ &= \int_t^{t+\Delta t} \int_t^{t+\Delta t} \langle \Gamma(t')\Gamma(t'') \rangle \; dt'\,dt'' \\ &= \int_t^{t+\Delta t} \int_t^{t+\Delta t} \delta(t'-t'')\,dt'\,dt'' = \Delta t\,, \end{aligned} \tag{E.6}$$

so that the proclaimed correspondence seems to be obvious.

Consider now the rather general form of a *stochastic differential equation* in *Ito's* more formal notation (as indicated by the considerations above and which is preferred by mathematicians, anyway):

$$dX(t) = A(X,t)dt + B\,dW(t)\,, \tag{E.7}$$

where $A(X,t)$ denotes the (deterministic) *drift* and B the (constant) *diffusion* term. The constant diffusion classifies the stochastic term as *additive noise*.

The more general *multiplicative noise* (non-constant diffusion, i.e. $B(X,t)$) involves much more sophisticated mathematics and is treated elsewhere. In particular the definition of an integral of (E.7) shows some ambiguity (*Ito-Stratonovich dilemma*) using multiplicative noise, which can be avoided with additive noise.

The *Fokker-Planck Equation* (FPE) is defined as the equation of motion for the conditional probability density $P(xt|x_0t_0)$ of a system being detected at x at time t assumed that it was at x_0 at t_0. There are numerous ways to derive the probabilistic FPE. One may directly obtain the FPE by utilizing *Kramers-Moyal-Expansion* for $P(xt|x_0t_0)$ [Ris89]. Another, more direct method, which immediately shows the correspondence between Langevin and Fokker-Planck equation starts from the following simple relationship for the conditional probability density $P(xt|x_0t_0)$:

$$P(xt|x_0t_0) := \langle \delta(X(t) - x) \rangle \ . \tag{E.8}$$

The partial derivative of (E.8) with respect to time t can be calculated as follows:

$$\begin{aligned}
\frac{\partial}{\partial t} P(xt|x_0t_0) &= \frac{\partial}{\partial t} \langle \delta(X(t) - x) \rangle \\
&= \lim_{\Delta t \to 0} \frac{1}{\Delta t} \left(\langle \delta(X(t + \Delta t) - x) \rangle - \langle \delta(X(t) - x) \rangle \right) \\
&= \lim_{\Delta t \to 0} \frac{1}{\Delta t} \Bigg\langle \sum_i \Delta X_i \frac{\partial}{\partial X_i} \delta(X(t) - x) \\
&\quad + \frac{1}{2} \sum_{ij} \Delta X_i \Delta X_j \frac{\partial^2}{\partial X_i \partial X_j} \delta(X(t) - x) + o(\Delta t) \Bigg\rangle \\
&= \lim_{\Delta t \to 0} \frac{1}{\Delta t} \Bigg\langle - \sum_i \Delta X_i \frac{\partial}{\partial x_i} \delta(X(t) - x) \\
&\quad + \frac{1}{2} \sum_{ij} \Delta X_i \Delta X_j \frac{\partial^2}{\partial x_i \partial x_j} \delta(X(t) - x) + o(\Delta t) \Bigg\rangle
\end{aligned} \tag{E.9}$$

where we introduced a (formal) expansion of $\delta(X(t) - x)$. The expansion up to second order is necessary due to the fact that $dW(t)^2 = dt$. Inserting (E.7) yields:

$$\begin{aligned}
\frac{\partial}{\partial t} P(xt|x_0t_0) &= - \sum_i \frac{\partial}{\partial x_i} \big\langle A_i(X) \delta(X(t) - x) \big\rangle \\
&\quad + \frac{1}{2} \sum_{ij} \frac{\partial^2}{\partial x_i \partial x_j} \Big\langle \sum_l B_{li}(X) B_{lj}(X) \delta(X(t) - x) \Big\rangle \, .
\end{aligned} \tag{E.10}$$

Finally,

$$\frac{\partial}{\partial t}P(xt|x_0t_0) = \left(-\sum_i \frac{\partial}{\partial x_i}A_i(x) + \sum_{ij}\frac{\partial^2}{\partial x_i \partial x_j}D_{ij}(x)\right)P(xt|x_0t_0) \quad \text{(E.11)}$$

where we defined

$$D_{ij}(x) := \frac{1}{2}\sum_l B_{il}(x)B_{jl}(x)\,. \quad \text{(E.12)}$$

Eq. (E.11) is the *Fokker-Planck Equation*, which represents the equation of motion for the conditional probability density $P(xt|x_0t_0)$, we were looking for.

One should note that our derivation above corresponds to the *Ito Interpretation* of Eq. (E.7). However, in this thesis, we only treat additive noise, so there is no ambiguity (c. f. *Ito-Stratonovich dilemma*) in interpreting Eq. (E.7).

E.2 Stochastic Differential Equations and Gear's Predictor-Corrector Algorithm

In order to explore the usability of Gear's predictor-corrector integration scheme for stochastic dynamics, we further specialize to the following Langevin equation for a one dimensional particle of mass m:

$$m\ddot{x} + m\gamma\dot{x} = m\cdot f(x) + \sqrt{2D}\cdot m\cdot\Gamma(t)\,, \quad \text{(E.13)}$$

where the stochastic force $\Gamma(t)$ is characterized as *Gaussian White Noise*:

$$\langle\Gamma(t)\rangle = 0\,, \quad \text{(E.14)}$$

$$\langle\Gamma(t)\Gamma(t')\rangle = \delta(t-t')\,, \quad \text{(E.15)}$$

γ is the friction coefficient and $f(x)$ is a force to be specified further. Eq. (E.13) is Non-Markovian. The Markovian character can be reestablished via an introduction of additional stochastic variables [Ris89]. In our case for the additional variable we choose the particle velocity v:

$$dx = v\,dt\,, \quad \text{(E.16)}$$

$$dv = (f(x) - \gamma v)\,dt + \sqrt{2D}\cdot dW(t) \quad \text{(E.17)}$$

and $dW(t) := \Gamma(t)\,dt$. The drift vector and the diffusion matrix can be identified with:

$$A = \begin{bmatrix} v \\ f(x) - \gamma v \end{bmatrix},\ B = \begin{bmatrix} 0 & 0 \\ 0 & \sqrt{2D} \end{bmatrix},\ \text{and } D = \begin{bmatrix} 0 & 0 \\ 0 & D \end{bmatrix}, \tag{E.18}$$

respectively. The Klein-Kramers equation derived from the generalized Langevin equation is given by:

$$\frac{\partial}{\partial t}P(xvt|x_0v_0t_0) = \left(-\frac{\partial}{\partial x}v - \frac{\partial}{\partial v}(f(x) - \gamma v) + \frac{\partial^2}{\partial v^2}D\right)P(xvt|x_0v_0t_0) \tag{E.19}$$

A relation between the friction coefficient γ and the diffusion coefficient D can be established using a simplified version of the *Fluctuation-Dissipation Theorem*:

$$D = \frac{k_BT}{m}\gamma\,, \tag{E.20}$$

where m is the mass of the particle. Eq. (E.20) is most easily seen, using the well known fact, that the stationary probability distribution P_{st}, i.e. $\frac{\partial}{\partial t}P_{st} = 0$, is a Boltzmann one:

$$P_{st}(x,v) \sim e^{-\frac{\frac{1}{2}mv^2 + \phi(x)}{k_BT}}\,, \tag{E.21}$$

where the force per mass $f(x)$ is related to the potential energy $\phi(x)$ in the usual way: $f(x) = -\frac{1}{m}\frac{d\phi(x)}{dx}$. Applying the Fokker-Planck operator on (E.21):

$$0 = \left(-\frac{\partial}{\partial x}v - \frac{\partial}{\partial v}(f(x) - \gamma v) + \frac{\partial^2}{\partial v^2}D\right)P_{st}(x,v) \tag{E.22}$$

shows that stationarity can only be obtained, if Eq. (E.20) is valid.

For at most harmonic force fields (i.e. $f(x) := -\omega_0^2 x$) Eq. (E.19) can be solved exactly, where for convenience $t_0 = 0$:

$$\begin{aligned} P(xvt|x_0v_00) = \frac{1}{2\pi\sqrt{\|\sigma\|}}\exp\Bigg[&-\frac{1}{2}\sigma_{xx}^{-1}(t)\cdot(x - x(t))^2 \\ &-\sigma_{xv}^{-1}(t)\cdot(x - x(t))(v - v(t)) - \frac{1}{2}\sigma_{vv}^{-1}(t)\cdot(v - v(t))^2\Bigg] \end{aligned} \tag{E.23}$$

with

$$x(t) := \frac{\lambda_1 e^{-\lambda_2 t} - \lambda_2 e^{-\lambda_1 t}}{\lambda_1 - \lambda_2}x_0 + \frac{e^{-\lambda_2 t} - e^{-\lambda_1 t}}{\lambda_1 - \lambda_2}v_0 \tag{E.24}$$

and

$$v(t) := \omega_0^2 \frac{e^{-\lambda_1 t} - e^{-\lambda_2 t}}{\lambda_1 - \lambda_2} x_0 + \frac{\lambda_1 e^{-\lambda_1 t} - \lambda_2 e^{-\lambda_2 t}}{\lambda_1 - \lambda_2} v_0 \,. \tag{E.25}$$

For $\lambda_{1/2}$ we get:

$$\lambda_1 := \frac{\gamma + \sqrt{\gamma^2 - 4\,\omega_0^2}}{2}\,, \quad \lambda_2 := \frac{\gamma - \sqrt{\gamma^2 - 4\,\omega_0^2}}{2}\,. \tag{E.26}$$

The components of the symmetric matrix σ are:

$$\begin{aligned}
\sigma_{xx}(t) &:= \frac{\gamma k_B T}{(\lambda_1 - \lambda_2)^2 m}\Big[\frac{\lambda_1 + \lambda_2}{\lambda_1 \lambda_2} + \frac{4}{\lambda_1 + \lambda_2}\big(e^{-(\lambda_1+\lambda_2)t} - 1\big) \\
&\qquad\qquad - \frac{1}{\lambda_1} e^{-2\lambda_1 t} - \frac{1}{\lambda_2} e^{-2\lambda_2 t}\Big] \\
\sigma_{xv}(t) &:= \frac{\gamma k_B T}{(\lambda_1 - \lambda_2)^2 m}\big(e^{-\lambda_1 t} - e^{-\lambda_2 t}\big)^2 \\
\sigma_{vv}(t) &:= \frac{\gamma k_B T}{(\lambda_1 - \lambda_2)^2 m}\Big[\lambda_1 + \lambda_2 + \frac{4\lambda_1\lambda_2}{\lambda_1 + \lambda_2}\big(e^{-(\lambda_1+\lambda_2)t} - 1\big) \\
&\qquad\qquad - \lambda_1 e^{-2\lambda_1 t} - \lambda_2 e^{-2\lambda_2 t}\Big]
\end{aligned} \tag{E.27}$$

The determinant and the (likewise symmetric and positive definite) inverse of σ are

$$\|\sigma\| = \sigma_{xx}\sigma_{vv} - (\sigma_{xv})^2 \tag{E.28}$$

and

$$\begin{aligned}
(\sigma^{-1})_{xx} &= \frac{\sigma_{vv}}{\|\sigma\|} \\
(\sigma^{-1})_{xv} &= -\frac{\sigma_{xv}}{\|\sigma\|} \\
(\sigma^{-1})_{vv} &= \frac{\sigma_{xx}}{\|\sigma\|}\,,
\end{aligned} \tag{E.29}$$

respectively.

For the following, the particle and bath properties will be fixed to that of a typical tungsten atom in otherwise tungsten bulk at temperature $T = 2000K$. For this, we start from the (deterministic) damped harmonic oscillator:

$$\ddot{x} = -\gamma \dot{x} - \omega_0^2 x\,. \tag{E.30}$$

Obviously, for small γ the damping can practically be neglected. On the other hand, for $\gamma \approx \omega_0$, the damping force and the harmonic force are of

the same order of magnitude (for a harmonic oscillator, we can estimate the velocity via $\dot{x} \approx \omega_0 x$). The exact calculation yields

$$\gamma_c = 2\omega_0 \tag{E.31}$$

for the *aperiodic limit* (see also Eq. (E.26)). This value quantifies the qualitative distinction between "weak" and "strong" damping, denoting the boundary between oscillatory behaviour ($\gamma < \gamma_c$) and pure relaxational dynamics ($\gamma > \gamma_c$). Only in the weak damping case $\gamma \ll \gamma_c$, the fastest time scale (which governs the time step) is given by ω_0, while for $\gamma \gg \gamma_c$ the damping term dominates, requiring a smaller time step. For this reason γ values beyond γ_c are in general clearly undesirable. Even worse, for $\gamma \gg \gamma_c$ the relaxation also contains a very slow component, whose characteristic time is, for large γ given by $\frac{\gamma}{\omega_0^2}$. Therefore, $\gamma = \gamma_c$ seems to be the optimum choice for fast equilibration.

As we are interested in tungsten atom dynamics in tungsten bulk, we fix ω_0 to the (approximately) highest phonon frequency available. Tungsten's *Debye temperature* is given as $\Theta_D = 400K$. Accordingly, ω_0 will be fixed by the following relationship:

$$\hbar\omega_0 = k_B\Theta_D \tag{E.32}$$

The mass of a tungsten atom equals $m = 183.85\text{u} = 183.85 \cdot 1.6605 \cdot 10^{-27}\text{kg}$.

In close resemblance to the corresponding treatment within MD, the time step Δt is chosen as $\Delta t = \frac{1}{50}\frac{2\pi}{\omega_0}$. For the following, we will apply the results

m(kg)	ω_0(s^{-1})	γ(s^{-1})	T(K)	D(m^2/s^3)	Δt(s)
$3.05 \cdot 10^{-25}$	$5.24 \cdot 10^{13}$	$10.48 \cdot 10^{13}$	2000	$90.53 \cdot 10^3$	$2.40 \cdot 10^{-15}$

Table E.1: *Parameters for the particle dynamics*

above to the case of non vanishing harmonic force field (ω_0 as specified in the aperiodic limit, c.f. Tab. E.1) and to free Brownian motion ($\omega_o \to 0$).

For all simulations, the particle will start at the origin in space with thermal velocity $v_0 := \sqrt{\frac{k_B T}{m}}$. Unfortunately, Gear's sixth order predictor-corrector scheme is by far less stable than the simple explicit Euler's method, which is essentially of first order.

From principal considerations (equivalence of *multi-value* and *multi-step* methods) it is clear, that this high order of Gear's integration scheme "wipes out" the strong "oscillations" of the random force. In essence, this means, that we have to look for a better method for integrating the particle trajectories.

It comes as no surprise that this new scheme could be of at most second order, so that stability should be improved.

For developing the new integrator we consider the following one-dimensional stochastic differential equation of second order:

$$\ddot{x} + \gamma\dot{x} + \omega_0^2 x = \sqrt{2D}\,\Gamma(t) \tag{E.33}$$

with initial conditions $x(0) = x_0$, $\dot{x}(0) = v_0$. This equation can be solved exactly [Cha43]:

$$x(t) = \frac{\sqrt{2D}}{\mu_1 - \mu_2}\left[e^{\mu_1 t}\int_0^t e^{-\mu_1 t'}\Gamma(t')\,dt' - e^{\mu_2 t}\int_0^t e^{-\mu_2 t'}\Gamma(t')\,dt'\right] + a_{10}e^{\mu_1 t} + a_{20}e^{\mu_2 t} \tag{E.34}$$

with

$$\mu_{1/2} = -\frac{1}{2}(\gamma \pm \sqrt{\gamma^2 - 4\omega_0^2}) \quad \text{and} \quad a_{10/20} = \mp\frac{x_0\mu_{2/1} - v_0}{\mu_1 - \mu_2}\,. \tag{E.35}$$

Within the same notation the velocity is given as:

$$\dot{x}(t) = \frac{\sqrt{2D}}{\mu_1 - \mu_2}\left[\mu_1 e^{\mu_1 t}\int_0^t e^{-\mu_1 t'}\Gamma(t')\,dt' - \mu_2 e^{\mu_2 t}\int_0^t e^{-\mu_2 t'}\Gamma(t')\,dt'\right] + a_{10}\mu_1 e^{\mu_1 t} + a_{20}\mu_2 e^{\mu_2 t} \tag{E.36}$$

It comes as no surprise that the corresponding probability distribution $P(xvt|x_0v_00)$ is identical to the previous result, Eq. (E.23).

A useful numerical integration scheme for (E.13) is most easily derived starting with the corresponding set of coupled first order ordinary differential equations:

$$\dot{x}(t) = v(t) \tag{E.37}$$

$$\dot{v}(t) + \gamma v(t) = f(t) + \sqrt{2D}\Gamma(t) \tag{E.38}$$

where $f(t) := f(x(t))$. Together with the *integrating factor* for the left hand term of the velocity part of (E.37), $\frac{d}{dt}\big(v(t)e^{\gamma t}\big) = e^{\gamma t}(\dot{v}(t) + \gamma v(t))$, we get:

$$\frac{d}{dt}\big(v(t)e^{\gamma t}\big) = e^{\gamma t}f(t) + \sqrt{2D}e^{\gamma t}\Gamma(t) \tag{E.39}$$

Integrating (E.39) over a small time intervall δt gives:

$$v(t+\delta t) = e^{-\gamma\delta t}v(t) + \int_t^{t+\delta t} e^{-\gamma(t+\delta t-t')}f(t')\,dt' + \delta v \tag{E.40}$$

where we introduced the notation:

$$\delta v := \sqrt{2D} \int_t^{t+\delta t} e^{-\gamma(t+\delta t-t')} \Gamma(t')\, dt' \,. \tag{E.41}$$

Up to now the integral Eq. (E.40) is exact. To get the desired numerical scheme, we have to perform explicitly the integral over the force $f(t)$. Of course, this cannot be done in general. We arrive at different schemes when we use suitable truncated Taylor series of $f(t)$. A first order scheme resembling *Euler's method* results when we assume, that $f(t)$ is approximately constant over the time intervall $[t, t+\delta t]$, whereas a second order predictor-corrector scheme, closely related to the *Velocity-Verlet* scheme for non-stochastic equations of motion, is derived when we let $f(t)$ vary linearly in time over the time step δt.

For the first order scheme ($f(t') \approx f(t)$), we use:

$$\int_t^{t+\delta t} e^{-\gamma(t+\delta t-t')} f(t')\, dt' \approx \frac{f(t)}{\gamma}\big(1 - e^{-\gamma\delta t}\big) \tag{E.42}$$

and get:

$$v(t+\delta t) = e^{-\gamma\delta t} v(t) + \frac{f(t)}{\gamma}\big(1 - e^{-\gamma\delta t}\big) + \delta v \,. \tag{E.43}$$

From this the updated position is determined by:

$$x(t+\delta t) = x(t) + \int_t^{t+\delta t} v(t')\, dt' = x(t) + \int_0^{\delta t} v(t+s)\, ds \tag{E.44}$$

$$= x(t) + c_1 v(t)\delta t + c_2 f(t)\delta t^2 + \delta x \,, \tag{E.45}$$

where we defined:

$$c_0 \equiv c_0(\delta t) := e^{-\gamma\delta t} \tag{E.46}$$

$$c_1 \equiv c_1(\delta t) := \frac{1}{\delta t}\int_0^{\delta t} c_0(s)\, ds = \frac{1 - c_0}{\gamma\delta t} \tag{E.47}$$

$$c_2 \equiv c_2(\delta t) := \frac{1}{\delta t^2}\int_0^{\delta t} s \cdot c_1(s)\, ds = \frac{1 - c_1}{\gamma\delta t} \tag{E.48}$$

and

$$\delta x := \sqrt{2D} \int_t^{t+\delta t} \left(\int_t^{t''} e^{-\gamma(t''-t')} \Gamma(t')\, dt' \right) dt'' \tag{E.49}$$

$$= \frac{\sqrt{2D}}{\gamma} \int_t^{t+\delta t} (1 - e^{-\gamma(t+\delta t-t')}) \Gamma(t')\, dt' \,, \tag{E.50}$$

where the second line is the result of an integration by parts.

The two random processes $(\delta x, \delta v)$ are not independent because they are the result of the integration involving the same stochastic process $\Gamma(t)$. The statistical properties of $(\delta x, \delta v)$, i.e. the joint probability density $P(\delta x, \delta v, t)$, can be derived among others using *Markoff's Method* [Cha43], or, more straightforward, a Fourier Transformation Method. For this we introduce the following notation:

$$\psi(t') := \frac{\sqrt{2D}}{\gamma}(1 - e^{-\gamma(t+\delta t-t')}) \ , \ \phi(t') := \sqrt{2D}\, e^{-\gamma(t+\delta t-t')} \, . \tag{E.51}$$

$\delta x, \delta v$ therefore is given as:

$$\delta x = \int_t^{t+\delta t} \psi(t')\Gamma(t')\, dt' \ , \ \delta v = \int_t^{t+\delta t} \phi(t')\Gamma(t')\, dt' \, . \tag{E.52}$$

For the moment, we approximate the integrals above with the corresponding *Riemann-Stieltjes Sum*:

$$\delta x = \sum_k \psi(t_k)\Delta W_k \ , \ \delta v = \sum_k \phi(t_k)\Delta W_k \tag{E.53}$$

with

$$\Delta W_k := \int_{t_k}^{t_{k+1}} \Gamma(t')\, dt' \tag{E.54}$$

for a suitable chosen subdivision of the time intervall $[t, t + \delta t]$. and the statistical properties of ΔW_k as previously defined. The joint probability $P(\delta x, \delta v)$ is derived from:

$$\begin{aligned} P(\delta x, \delta v) = \int \delta(\delta x - \sum_k \psi(t_k)\Delta W_k) \\ \cdot \delta(\delta v - \sum_k \phi(t_k)\Delta W_k) \prod_k p(\Delta W_k)\, d\Delta W_k \, , \end{aligned} \tag{E.55}$$

where

$$p(\Delta W_k) = \frac{1}{\sqrt{2\pi\delta' t}} e^{-\frac{\Delta W_k^2}{2\delta' t}} \tag{E.56}$$

and $\delta(\ldots)$ denotes *Dirac's delta function*. To proceed, we use the Fourier representation of the Dirac Delta function:

$$\delta(x - x') = \frac{1}{2\pi} \int_{-\infty}^{\infty} e^{ik(x-x')}\, dk \tag{E.57}$$

Inserting in Eq. (E.55) and rearranging integrations yields:

$$P(\delta x, \delta v) = \frac{1}{4\pi} \int_{-\infty}^{\infty} e^{i(k_x \delta x + k_v \delta v)} A(k_x, k_v)\, dk_x\, dk_v \tag{E.58}$$

with:

$$\begin{aligned} A(k_x, k_v) &= \prod_m \int e^{-i\Delta W_m (k_x \psi_m + k_v \phi_m)} p(\Delta W_m)\, d\Delta W_m \\ &= \prod_m e^{-\frac{(k_x \psi_m + k_v \phi_m)^2}{2}} = e^{-\frac{\sum_m (k_x \psi_m + k_v \phi_m)^2}{2}} \end{aligned} \tag{E.59}$$

Now we can perform the remaining integrations and get:

$$P(\delta x, \delta v) = \frac{1}{2\pi\sqrt{|det(\mathbf{C})|}} e^{-\frac{(\delta x, \delta v)\mathbf{C}^{-1}\binom{\delta x}{\delta v}}{2}}, \tag{E.60}$$

the bivariate Gaussian distribution with *covariance matrix* $\mathbf{C}$:

$$\mathbf{C} := \begin{bmatrix} \int_t^{t+\delta t} \psi^2(t')\, dt' & \int_t^{t+\delta t} \psi(t')\phi(t')\, dt' \\ \int_t^{t+\delta t} \psi(t')\phi(t')\, dt' & \int_t^{t+\delta t} \phi^2(t')\, dt' \end{bmatrix} \tag{E.61}$$

its inverse:

$$\mathbf{C}^{-1} = \frac{1}{det(\mathbf{C})} \begin{bmatrix} \int_t^{t+\delta t} \phi^2(t')\, dt' & -\int_t^{t+\delta t} \psi(t')\phi(t')\, dt' \\ -\int_t^{t+\delta t} \psi(t')\phi(t')\, dt' & \int_t^{t+\delta t} \psi^2(t')\, dt' \end{bmatrix} \tag{E.62}$$

and its determinant:

$$det(\mathbf{C}) = \int_t^{t+\delta t} \psi^2(t')\, dt' \cdot \int_t^{t+\delta t} \phi^2(t')\, dt' - \left(\int_t^{t+\delta t} \psi(t')\phi(t')\, dt' \right)^2, \tag{E.63}$$

where we replaced the *Riemann-Stieltjes Sums* with the corresponding integrals. Finally, inserting Eqs. (E.51) and integrate the expressions gives:

$$\mathbf{C} := D \begin{bmatrix} \frac{2\gamma\delta t - 3 + 4e^{-\gamma\delta t} - e^{-2\gamma\delta t}}{\gamma^3} & \frac{1 - 2e^{-\gamma\delta t} + e^{-2\gamma\delta t}}{\gamma^2} \\ \frac{1 - 2e^{-\gamma\delta t} + e^{-2\gamma\delta t}}{\gamma^2} & \frac{1 - e^{-2\gamma\delta t}}{\gamma} \end{bmatrix}. \tag{E.64}$$

A frequently used and convenient short hand notation for the probability distribution (E.60) is given as:

$$\begin{bmatrix} \delta x \\ \delta v \end{bmatrix} \sim N(\mathbf{0}, \mathbf{C}). \tag{E.65}$$

Numerically, samples drawn from this distribution can be easily arranged using two *independent* Gaussian distributed random variables (say, e.g. (X_1, X_2) with $\mathbf{X} \sim N(\mathbf{0}, \mathbf{1})$), and utilizing the fact, that the joint probability of two random variables generated via a linear transformation of independent random variables (e. g. $\mathbf{Y} = \mathbf{M} \cdot \mathbf{X}$) is a multivariate Gaussian distribution:

$$\mathbf{Y} \sim N(\mathbf{0}, \mathbf{M} \cdot \mathbf{M^T}) \,. \tag{E.66}$$

For the second order scheme ($f(t') \approx f(t) + (t' - t)\dot{f}(t)$) we use the following relation:

$$\int_t^{t+\delta t} e^{-\gamma(t+\delta t-t')}(f(t)+(t'-t)\dot{f}(t)\, dt' = f(t+\delta t)c_2\delta t + f(t)(c_1-c_2)\delta t \tag{E.67}$$

The updated velocity therefore is given as:

$$v(t+\delta t) = c_0 v(t) + c_2 f(t+\delta t)\delta t + (c_1 - c_2) f(t)\delta t + \delta v \,, \tag{E.68}$$

and the positions as:

$$x(t+\delta t) = x(t) + c_1 v(t)\delta t + c_2 f(t)\delta t^2 + \delta x \,. \tag{E.69}$$

This second order scheme closely resembles the *Velocity Verlet* method, which formally can be identified with a second order predictor-corrector scheme in Gear's notation. The *predictor step* can be identified with:

$$\begin{bmatrix} \tilde{x}^P(t+\delta t) \\ \tilde{v}^P(t+\delta t) \\ \tilde{a}^P(t+\delta t) \end{bmatrix} = \begin{bmatrix} 1 & c_1 & 2c_2 \\ 0 & c_0 & 2c_1 \\ 0 & 0 & 1 \end{bmatrix} \cdot \begin{bmatrix} \tilde{x}(t) \\ \tilde{v}(t) \\ \tilde{a}(t) \end{bmatrix} + \begin{bmatrix} \delta x \\ \delta v \cdot \delta t \\ 0 \end{bmatrix} \tag{E.70}$$

and the *corrector step* results in:

$$\begin{bmatrix} \tilde{x}^C(t+\delta t) \\ \tilde{v}^C(t+\delta t) \\ \tilde{a}^C(t+\delta t) \end{bmatrix} = \begin{bmatrix} \tilde{x}^P(t+\delta t) \\ \tilde{v}^P(t+\delta t) \\ \tilde{a}^P(t+\delta t) \end{bmatrix} + \begin{bmatrix} 0 \\ 2c_2 \\ 1 \end{bmatrix} \cdot (\tilde{a}^C(t+\delta t) - \tilde{a}^P(t+\delta t)) \,, \tag{E.71}$$

where $\tilde{a}^C(t+\delta t) := \frac{\delta t^2}{2} f(t+\delta t) \equiv \frac{\delta t^2}{2} f(x^P(t+\delta t))$ and $\tilde{x}(t) := x(t)$, $\tilde{v}(t) := \delta t \cdot v(t)$ and $\tilde{a}(t) := \frac{\delta t^2}{2} \cdot a(t)$.

Together with formulating an integration scheme suitable for Langevin's dynamics, one should also address the for practical needs of utmost important question of discretization errors of the scheme [MS96].

Bibliography

[AC65a] S. I. Altmann and A. P. Cracknell. Lattice harmonics i. cubic groups. *Rev. Mod. Phys.*, 37:19, 1965.

[AC65b] S. I. Altmann and A. P. Cracknell. Lattice harmonics i. hexagonal close-packed lattice. *Rev. Mod. Phys.*, 37:33, 1965.

[AF90] J. Adams and S. M. Foiles. Development of an embedded-atom potential for a bcc metal: Vanadium. *Phys. Rev.* **B**, 41:3316, 1990.

[AKK65] R. L. Andelin, J. D. Knight, and M. Kahn. Diffusion of tungsten and rhenium tracers in tungsten. *Trans. Met. Soc. AIME*, 233:19, 1965.

[AM76] N. W. Ashcroft and N. D. Mermin. *Solid State Physics*. Holt, Rinehart and Winston, 1976.

[And73] O. K. Andersen. Simple approach to the band-structure problem. *Solid State Commun.*, 13:133, 1973.

[And75] O. K. Andersen. Linear methods in band theory. *Phys. Rev.* **B**, 12:3060, 1975.

[And80] H. C. Andersen. Molecular dynamics simulations at constant pressure and/or temperature. *J. Chem. Phys.*, 72:2384, 1980.

[AT87] M. P. Allen and D. J. Tildesley. *Computer Simulation of Liquids*. Oxford University Press, 1987.

[AW57] B. J. Alder and T. E. Wainright. Phase transition of a hard sphere system. *J. Chem. Phys.*, 27:1208, 1957.

[AW59] B. J. Alder and T. E. Wainright. Studies in molecular dynamics. i. general method. *J. Chem. Phys.*, 31:459, 1959.

[Bas87] M. I. Baskes. Application of the embedded-atom method to covalent materials: A semiempirical potential for silicon. *Phys. Rev. Lett.*, 59:2666, 1987.

[BD89] D. L. Beveridge and F. M. DiCapua. Free energy via molecular simulation: Applications to chemical and biomolecular systems. *Ann. Rev. Biophys. Biophys. Chem.*, 18:431, 1989.

[BE89] A. Baranyai and D. J. Evans. Direct entropy calculation from computer simulation of liquids. *Phys. Rev.* **A**, 40:3817, 1989.

[BE90] A. Baranyai and D. J. Evans. Three-particle contribution to the configurational entropy of simple fluids. *Phys. Rev.* **A**, 42:849, 1990.

[Bec88] A. D. Becke. Density-functional exchange-energy approximation with correct asymptotic behavior. *Phys. Rev.* **A**, 38:3098, 1988.

[Ben76] C. H. Bennett. Efficient estimation of free energy differences from monte carlo data. *J. of Comp. Phys.*, page 245, 1976.

[BJ03] J. K. Baria and A. R. Jani. Lattice mechanical properties of some fcc f-shell metals. *Pramana - J. Phys.*, 60:1235, 2003.

[BJA94] P. E. Bloechl, O. Jepsen, and O. K. Andersen. Improved tetrahedron method for brillouin-zone integration. *Phys. Rev.* **B**, 49:16223, 1994.

[BK54] M. Born and H. Kun. *Dynamical Theory of Crystal Lattices*. Oxford University Press, 1954.

[BO27] M. Born and R. Oppenheimer. Zur quantentheorie der molekeln. *Ann. d. Phys.*, 84:457, 1927.

[Boe83] H. Boettger. *Principles of the Theory of Lattice Dynamics*. Akademie-Verlag Berlin, 1983.

[BPvG$^+$84] H. J. C. Berendsen, J. P. M. Postma, W. F. van Gunsteren, A. DiNola, and J. R. Haak. Molecular dynamics with coupling to an external bath. *J. Chem. Phys.*, 81:3684, 1984.

[BSL99] P. Blaha, K. Schwarz, and J. Luitz. *WIEN97, A Full Potential Linearized Augmented Plane Wave Package for Calculating Crystal Properties*. Vienna University of Technology, 1999.

[BSS81] E. V. Borisov, A. D. Senchokov, and V. I. Shlykov. Diffusion of tungsten in tungsten, mo and nb. *Izv. Akad. Nauk SSSR, Neorg. Mater.*, 17:277, 1981.

[BSST90] P. Blaha, K. Schwarz, P. Sorantin, and S. B. Trickey. Full-potential, linearized augmented plane wave programs for crystalline systems. *Comp. Phys. Comm.*, 59:399, 1990.

[Cah62] J. W. Cahn. The impurity-drag effect in grain boundary motion. *Acta Met.*, 10:789, 1962.

[Cah70] R. W. Cahn. *Physical Metallurgy*, chapter 13, page 787. North-Holland, Amsterdam, 1970.

[Car90] A. E. Carlson. Beyond pair potentials in elemental transition metals and semiconductors. *Solid State Phys.*, 43:1, 1990.

[Cha43] S. Chandrasekhar. Stochastic problems in physics and astronomy. *Rev. Mod. Phys.*, 15:1, 1943.

[Cha87] D. Chandler. *Introduction to Modern Statistical Mechanics*. Oxford University Press, 1987.

[CL68] F. Cyrot-Lackmann. Sur le calcul de la cohesion et de la tension superficielle des metaux de transition par une methode de liaisons fortes. *J. Phys. Chem. Solids*, 29:1235, 1968.

[Cra49] B. H. Crawford. The scotopic visibility function. *Proceedings of the Physical Society*, B 62:321–334, 1949.

[CSV89] S. P. Chen, D. J. Srolovitz, and A. F. Voter. Computer simulation on surfaces and (001) symmetric tilt grain boundaries in ni, al, and ni_3al. *J. Mat. Res.*, 4:62, 1989.

[Daw89] M. S. Daw. Model of metallic cohesion: The embedded-atom method. *Phys. Rev.* **B**, 39:7441, 1989.

[DB84] M. S. Daw and M. I. Baskes. Embedded atom method: Derivation and application to impurities, surfaces, and other defects in metals. *Phys. Rev.* **B**, 29:6443, 1984.

[DH85] M. S. Daw and R. D. Hatcher. Application of the embedded atom method to phonons in transition metals. *Solid State Comm.*, 56:697, 1985.

[Dir29] P. A. M. Dirac. Quantum mechanics of many-electron system. *Proc. Roy. Soc. London* **A**, 123:714, 1929.

[EK76] N. Elyashar and D. D. Koelling. Effect of nonmuffin-tin terms on the electronic structure of transition metals: Niobium. *Phys. Rev.* **B**, page 5362, 1976.

[Esc96] H. Eschrig. *The Fundamentals of Density Funtional Theory.* B. G. Teubner, 1996.

[ETP86] F. Ercolessi, E. Tosatti, and M. Parrinello. Au (100) surface reconstruction. *Phys. Rev. Lett.*, 57:719, 1986.

[FBD86] S. M. Foiles, M. I. Baskes, and M. S. Daw. Emebedded-atom-method functions for the fcc metals cu, ag, ni, pd, pt, and their alloys. *Phys. Rev.* **B**, 33:7983, 1986.

[FBEF93] W. Frank, U. Breier, C. Elsässer, and M. Fähnle. Properties of monovacancies and self-interstitials in bcc li: An *ab initio* pseudopotential study. *Phys. Rev.* **B**, 48:7676, 1993.

[Fey39] R. P. Feynman. Forces in molecules. *Phys. Rev.*, 56:340, 1939.

[FGRV88] R. F. Fox, I. R. Gatland, R. Roy, and G. Vemuri. Fast, accurate algorithm for numerical simulation of exponentially correlated colored noise. *Phys. Rev.* **A**, 38:5938, 1988.

[FKSY94] R. Fukuda, T. Kotani, Y. Suzuki, and S. Yokojima. Density functional theory through legendre transformation. *Prog. Theor. Phys.*, 92:833, 1994.

[Foi85] S. M. Foiles. Application of the embedded-atom method to liquid transition metals. *Phys. Rev.* **B**, 32:3409, 1985.

[Fra88] F. C. Frank. Orientation mapping. *Met. Trans.*, 19A:403, 1988.

[Fre85] D. Frenkel. *Molecular Dynamics Simulation of Statistical Mechanical Systems*, page 151. North-Holland, Amsterdam, 1985.

[FS84] M. W. Finnis and J. E. Sinclair. A simple empirical n-body potential for transition metals. *Phil. Mag. A*, 50:45, 1984.

[FS86] M. W. Finnis and J. E. Sinclair. Erratum: A simple empirical n-body potential for transition metals. *Phil. Mag. A*, 53:161, 1986.

[FYW33] G. R. Fonda, A. H. Young, and A. Walker. The diffusion of thorium in tungsten. *Physics*, 4:1, 1933.

[FZPB95] S. E. Feller, Y. Zhang, R. W. Pastor, and B. R. Brooks. Constant pressure molecular dynamics simulation: The langevin piston method. *J. Chem. Phys.*, 103:4613, 1995.

[Gar83] C. W. Gardiner. *Handbook of Stochastic Methods*. Springer, Berlin, 1983.

[Gea66] C. W. Gear. The numerical integration of ordinary differential equations of various orders. *Report ANL 7126, Argonne National Laboratory*, 1966.

[Gea71] C. W. Gear. *Numerical initial value problems in ordinary differential equations*. Prentice-Hall, Englewood Cliffs, NJ, 1971.

[Gil96] D. T. Gillespie. The mathematics of brownian motion and johnson noise. *Am. J. Phys.*, 64:225, 1996.

[GM78] P. E. Gill and W. Murray. Algorithms for the solution of the nonlinear least-squares problem. *SIAM J. Numer. Anal.*, 15:977, 1978.

[GMB57] M. Gell-Mann and K. A. Brueckner. Correlation energy of an electron gas at high density. *Phys. Rev.*, 106:364, 1957.

[Gri76] H. Grimmer. Coincidence-site lattices. *Acta Cryst.*, A32:783, 1976.

[GT23] K. S. Gibson and E. P. T. Tyndall. Visibility of radiant energy. *Scientific Papers of the Bureau of Standards*, 19:131–191, 1923.

[HA58] M. Hansen and K. Anderko. *Constitution of Binary Alloys*. McGraw-Hill Book Company, Inc., 1958.

[Haa78] P. Haasen. *Physical Metallurgy*, chapter 11, page 258. Cambridge University Press, 1978.

[Hah96] T. Hahn, editor. *International Tables for Crystallography*, volume A. Kluwer Academic, 4 edition, 1996.

[Hän97] P. Hänggi. *Stochastic Dynamics*, volume 484 of *Lecture Notes in Physics*, chapter Generalized Langevin Equations: A Useful Tool for the Perplexed Modeller of Nonequilibrium Fluctuations? Springer, 1997.

[Har66] W. A. Harrison. *Pseudopotentials in the Theory of Metals*. Benjamin, New York and Amsterdam, 1966.

[Har80] W. A. Harrison. *Electronic Structure and the Properties of Solids*. Dover Publications, Inc., New York, 1980.

[HEB31] H. Hartmann, F. Ebert, and O. Bretschneider. Electrolysis in fused phosphates. i. electrolytic preparation of α- and β-tungsten. *Z. anorg. Chem.*, 198:116, 1931.

[HK64] P. Hohenberg and W. Kohn. Inhomogeneous electron gas. *Phys. Rev.*, 136:B864, 1964.

[HL82] J. P. Hirth and J. Lothe. *Theory of dislocations*. John Wiley & Sons, Inc., 1982.

[Hoo85] W. G. Hoover. Canonical dynamics: Equilibrium phase-space distributions. *Phys. Rev.* **A**, 31:1695, 1985.

[HVC88] R. J. Harrison, A. F. Voter, and S. P. Chen. *Atomistic Simulation of Materials: Beyond Pair Potentials*, chapter Embedded Atom Potential for BCC Iron, page 219. Plenum Press, New York and London, 1988.

[JAEW95] B. Johansson, R. Ahuja, O. Eriksson, and J. M. Wills. Anomalous fcc crystal structure of thorium metal. *Phys. Rev. Lett.*, 75:280, 1995.

[JNP87] K. W. Jacobsen, J. K. Nørskov, and M. J. Puska. Interatomic interaction in the effective-medium theory. *Phys. Rev.* **B**, 35:7423, 1987.

[Joh78] B. Johansson. Energy difference between trivalent and tetravalent metallic cerium and other f-elements. stability study of various lanthanide- and actinide-halides and -oxides. *J. Phys. Chem. Solids*, 39:467, 1978.

[Joh88] R. A. Johnson. Analytic nearest-neighbour model for fcc metals. *Phys. Rev.* **B**, 37:3924, 1988.

[Joh89] R. A. Johnson. Alloy models with the embedded-atom method. *Phys. Rev.* **B**, 39:12554, 1989.

[JR75] B. Johansson and A. Rosengren. Generalised phase diagram for the rare-earth elements: calculations and correlations of bulk properties. *Phys. Rev.* **B**, 11:2836, 1975.

[KA75] D. D. Koelling and G. A. Arbman. Use of energy derivative of the radial solution in an augmented plane wave method: application to copper. *J. Phys. F: Metal Phys.*, 5:2041, 1975.

[KD99] A. Kolb and B. Duenweg. Optimized constant pressure stochastic dynamics. *J. Chem. Phys.*, 111:4453, 1999.

[KG02] J. Kohanoff and N. Gidopoulos. *Density Functional Theory: basics, new trends and applications*. 2002.

[KH77] D. D. Koelling and B. N. Harmon. A technique for relativistic spin-polarised calculations. *J. Phys. C: Solid State Phys.*, 10:3107, 1977.

[KJBP84] S. M. Kim, J. A. Jackman, W. J. L. Buyers, and D. T. Peterson. Vacancy formation energy by positron annihilation. *J. Phys. F: Met. Phys.*, 14:2323, 1984.

[Knu69] D. E. Knuth. *The Art of Computer Programming*, volume 2. Addison-Wesley, 1969.

[Koh99] W. Kohn. Nobel lecture: Electronic structure of matter—wave functions and density functionals. *Rev. Mod. Phys.*, 71:1253, 1999.

[KP92] P. E. Kloeden and E. Platen. *Numerical Solution of Stochastic Differential Equations*. Springer, Berlin, 1992.

[KPN95] T. Korhonen, M. J. Puska, and R. M. Nieminen. Vacancy-formation energies for fcc and bcc transition metals. *Phys. Rev.* **B**, 51:9526, 1995.

[KS65] W. Kohn and L. J. Sham. Self-consistent equations including exchange and correlation effects. *Phys. Rev.*, 140:A1133, 1965.

[KS77] K. Kurki-Suonio. Symmetry and its implications. *Isreal J. Chem.*, 16:115, 1977.

[Kuy90] F. Kuypers. *Klassische Mechanik*. VCH, 1990.

[Lan34] I. Langmuir. Thoriated tungsten filaments. *J. Franklin Inst.*, 217:543, 1934.

[LB76] A. Larose and B. N. Brockhouse. Lattice vibrations in tungsten at 22 Â?c studied by neutron scattering. *Can. J. Phys.*, 54:1819, 1976.

[LD57] K. Lücke and K. Detert. A quantitative theory of grain-boundary motion and recrystallization in metals in the presence of impurities. *Acta Met.*, 5:628, 1957.

[Ley98] J. Leyendecker. *β-Wolfram*. Hieronymus, 1998.

[Lie83] E. H. Lieb. Density functionals for coulomb systems. *Int. J. Quant. Chem.*, 24:243, 1983.

[LM81] D. C. Langreth and M. J. Mehl. Easily implementable non-local exchange-correlation energy functional. *Phys. Rev. Lett.*, 47:446, 1981.

[LS71] K. Lücke and H. P. Stüwe. On the theory of impurity controlled grain boundary motion. *Acta Met.*, 19:1087, 1971.

[LS99] E. Lassner and W. D. Schubert. *Tungsten: Properties, Chemistry, Technology of the Element, Alloys, and Chemical Compounds*. Springer Verlag, 1999.

[LT72] G. Lehmann and M. Taut. On the numerical calculation of the density of states and related properties. *phys. stat. sol. (b)*, 54:469, 1972.

[LTM02] J. E. Lynn, W. J. Trela, and K. Meggers. Neutron doppler broadening studies of tantalum and tungsten metal. *Nucl. Inst. Meth. Phys. Res. B*, 192:318, 2002.

[MAB+02] P. Maragakis, S. A. Andreev, Y. Brumer, D. R. Reichman, and E. Kaxiras. Adaptive nudged elastic band approach for transition state calculation. *J. Chem. Phys.*, 117:4651, 2002.

[Mar63] D. W. Marquardt. An algorithm for least squares estimation of nonlinear parameters. *J. Soc. Ind. Appl. Math.*, 11:431, 1963.

[Mar67] P. M. Marcus. Variational methods in the computation of enegy bands. *Int. J. Quant. Chem. Symp.*, 1:567, 1967.

[Mer65] N. D. Mermin. Thermal properties of the inhomogeneous electron gas. *Phys. Rev.*, 137:A1441, 1965.

[Mes61] A. Messiah. *Quantum Mechanics*. Amsterdam, North-Holland, 1961.

[MF98] Y. Mishin and D. Farkas. Atomistic simulation of [001] symmetrical tilt grain boundaries in nial. *Phil. Mag. A*, 78:29, 1998.

[MH86] L. F. Mattheiss and D. R. Hamann. Linear augmented-plane-wave calculation of the structural properties of bulk cr, mo, and w. *Phys. Rev.* **B**, 33:823, 1986.

[MHSN57] T. Millner, A. J. Hegedues, K. Sasvari, and J. Neugebauer. über die bildungsbedingungen und eigenschaften des β-wolframs. *Z. anorg. allg. Chem.*, 289:288, 1957.

[MJLMK90] Th. B. Massalski, H. Baker J. L. Murray, L. H. Bennett, and L. Kacprzak, editors. *Binary Alloy Phase Diagrams*. ASM International, 1990.

[Mor65a] H. Mori. A continued fraction representation of the time correlation functions. *Prog. theor. Phys.*, 34:399, 1965.

[Mor65b] H. Mori. Transport, collective motion and brownian motion. *Prog. theor. Phys.*, 33:423, 1965.

[Mor92] J. A. Moriarty. Ultrahigh structural phase transitions in cr, mo and w. *Phys. Rev.* **B**, 45:2004, 1992.

[MP76] H. J. Monkhorst and J. D. Pack. Special points for brillouin-zone integration. *Phys. Rev.* **B**, 13:5188, 1976.

[MP96] M. J. Mehl and D. A. Papaconstantopoulos. Applications of a tight-binding total-energy method for transition and noble metals: Elastic constants, vacancies, and surfaces of monatomic metals. *Phys. Rev.* **B**, 54:4519, 1996.

[MS96] B. Mishra and T. Schlick. The notion of error in langevin dynamics. i. linear analysis. *J. Chem. Phys.*, 105:299, 1996.

[Mün69] A. Münster. *Statistical Thermodynamics*. Springer/Academic Press, 1969.

[Mur44] F. D. Murnaghan. The compressibility of media under extreme pressures. *Proc. N. A. S.*, 30:244, 1944.

[MV79] A. H. MacDonald and S. H. Vosko. A relativistic density functional formalism. *J. Phys. C: Solid State Phys.*, 12:2977, 1979.

[MW70] J. Mathews and R. L. Walker. *Mathematical Methods of Physics*. Addison-Wesley, 1970.

[Ner24] W. Nernst. *Die theoretischen und experimentellen Grundlagen des neuen Wärmesatzes*. Knapp, 1924.

[NK83] S. Nosé and M. L. Klein. Constant pressure molecular dynamics for molecular systems. *Molecular Physics*, 50:1055, 1983.

[NM65] J. A. Nelder and R. Mead. A simplex method for function minimization. *Computer Journal*, 7:308, 1965.

[Nos84] S. Nosé. A molecular dynamics method for simulations in the canonical ensemble. *Molecular Physics*, 52:255, 1984.

[Old86] M. A. Oldfield. *Theoretische Bestimmung der Kernstruktur der* 71°*-Versetzung in* α*-Eisen*. Dissertation, Göttingen, 1986.

[OP79] G. L. Oliver and J. P. Perdew. Spin-density gradient expansion for the kinetic energy. *Phys. Rev.* **A**, 20:397, 1979.

[Pap65] A. Papoulis. *Probability, Random Variables, and Stochastic Processes*. McGraw-Hill, New York, 1965.

[Päs75] M. Päsler. *Phänomenologische Thermodynamik*. Walter De Gruyter, 1975.

[PBE96] J. P. Perdew, K. Burke, and M. Ernzerhof. Generalized gradient approximation made simple. *Phys. Rev. Lett.*, 77(18):3865, 1996.

[Per86] J. P. Perdew. Density-functional approximation for the correlation energy of the inhomogeneous electron gas. *Phys. Rev.* **B**, 33:8822, 1986.

[Phi01] R. Phillips. *Crystals, Defects and Microstructures*. Cambridge University Press, 2001.

[Pla01] M. Planck. On the law of distribution of energy in the normal spectrum. *Ann. d. Physik*, 4:553, 1901.

[PM77] J. D. Pack and H. J. Monkhorst. Special points for brillouin-zone integration – a reply. *Phys. Rev.* **B**, 16:1748, 1977.

[PR80] M. Parrinello and A. Rahman. Crystal structure and pair potentials: A molecular-dynamics study. *Phys. Rev. Lett.*, 45:1196, 1980.

[PR81] M. Parrinello and A. Rahman. Polymorphic transitions in single crystals: A new molecular dynamics method. *J. Appl. Phys.*, 52:7182, 1981.

[PSD88] D. G. Pettifor, A. J. Skinner, and R. A. Davies. *Atomistic Simulation of Materials: Beyond Pair Potentials*, chapter The Tight Binding Bond Model. Plenum Press, New York and London, 1988.

[PW86] J. P. Perdew and Y. Wang. Accurate and simple density functional for the electronic exchange energy: generalized gradient approximation. *Phys. Rev.* **B**, 33:8800, 1986.

[PW92] J. P. Perdew and Y. Wang. Accurate and simple analytic representation of the electron-gas correlation energy. *Phys. Rev.* **B**, 45:13244, 1992.

[Rei65] F. Reif. *Fundamentals of Statistical and Thermal Physics.* McGraw-Hill Inc., 1965.

[Rei01] P. Reimann. A uniqueness-theorem for "linear" thermal baths. *Chem. Phys.*, 268:337, 2001.

[REJ75] A. Rosengren, I. Ebbsjö, and B. Johansson. Calculation of the phonon spectrum in thorium. *Phys. Rev.* **B**, 12:1337, 1975.

[RGL89] V. Rosato, M. Guillopé, and B. Legrand. Thermodynamic and structural properties of f.c.c. transition metals using a simple tight-binding model. *Phil. Mag. A*, 59:321, 1989.

[RGS92] R. S. Rao, B. K. Godwal, and S. K. Sikka. Thorium: A $5f$-band metal at ultrahigh pressures. *Phys. Rev.* **B**, 46:5780, 1992.

[Ris89] H. Risken. *The Fokker-Planck Equation.* Springer Verlag Berlin Heidelberg, 1989.

[RS50] W. T. Read and W. Shockley. Dislocation models of crystal grain boundaries. *Phys. Rev.*, 78:275, 1950.

[RSGF84] J. H. Rose, J. R. Smith, F. Guinea, and J. Ferrante. Universal features of the equation of state of metals. *Phys. Rev.* **B**, 29:2963, 1984.

[RSP73] R. A. Reese, S. K. Sinha, and D. T. Peterson. Phonon spectrum of thorium. *Phys. Rev.* **B**, 8:1332, 1973.

[SAEJ94] P. Soederlind, R. Ahuja, O. Eriksson, and B. Johansson. Theoretical predictions of structural phase transitions in cr, mo and w. *Phys. Rev.* **B**, 49:9365, 1994.

[SB95] A. P. Sutton and R. W. Balluffi. *Interfaces in Crystalline Materials*. Oxford Science Publishing, 1995.

[Sch26] E. Schrödinger. Quantizierung als eigenwertproblem (erste mitteilung) / quantization as a problem of proper values. part i. *Ann. Phys.*, 79:361, 1926.

[Sch87] H. E. Schäfer. Investigation of thermal equilibrium vacancies in metals by positron annihilation. *phys. stat. sol. (a)*, 102:47, 1987.

[Sch90] F. Schwabl. *Quantenmechanik*. Springer, 1990.

[Sch99] U. Scherz. *Quantenmechanik*. B. G. Teubner, 1999.

[SCPS75] J. F. Smith, O. N. Carlson, D. T. Peterson, and T. E. Scott. *Thorium: Preparation and Properties*. Iowa State University Press, 1975.

[Sin91] D. Singh. Ground-state properties of lanthanum: Treatment of extended-core states. *Phys. Rev.* **B**, 43:6388, 1991.

[Sin94] D. Singh. *Plane waves, pseudopotentials and the LAPW method*. Kluwer Academic, 1994.

[SJ80] H. L. Skriver and J. P. Jan. Electronic states in thorium under pressure. *Phys. Rev.* **B**, 21:1489, 1980.

[SK91] D. Singh and H. Krakauer. H-point phonon in molybdenum: superlinearized augmented-plane-wave calculations. *Phys. Rev.* **B**, 43:1441, 1991.

[Sla37] J. C. Slater. Wave functions in a periodic potential. *Phys. Rev.*, 51(846), 1937.

[SR55] H. A. Saller and F. A. Rough. *Compilation of U.S. and U.K. Uranium and Thorium Constitutional Diagrams*. U.S. Atomic Energy Comm., 1955.

[SS78] T. Schneider and E. Stoll. Molecular dynamics study of a three-dimensional one-component model for distortive phase transitions. *Phys. Rev.* **B**, 17:1302, 1978.

[STY91] T. Suzuki, S. Takeuchi, and H. Yoshinaga. *Dislocation Dynamics and Plasticity*, chapter 6, page 77. Springer, Berlin, 1991.

[Suz68] H. Suzuki. *Dislocation Dynamics*, page 679. McGraw-Hill, New York, 1968.

[SWdG98] A. Satta, F. Willaime, and S. de Gironcoli. Vacancy self-diffusion paramters in tungsten: Finite electron-temperature lda calculations. *Phys. Rev.* **B**, 57:11184, 1998.

[TB85] D. Tomanék and K. H. Bennemann. Electronic model for energies, relaxations and reconstruction trends at metal surfaces. *Surf. Sci.*, 163:503, 1985.

[TKT75] TKTD. *Thermophysical Properties of Matter*. Plenum Press, New York, 1975.

[Tur51] D. Turnbull. Theory of grain boundary migration rates. *J. Met.*, 3:661, 1951.

[VA91] Y. K. Vohra and J. Akella. $5f$ bonding in thorium metal at extreme compressions: Phase transitions to 300 gpa. *Phys. Rev. Lett.*, 67:3563, 1991.

[VC87] A. F. Voter and S. P. Chen. Accurate interatomic potentials for ni, al and ni_3al. *Mat. Res. Soc. Symp. Proc.*, 82:175, 1987.

[Vit68] V. Vitek. Intrinsic stacking faults in body-centred cubic crystals. *Phil. Mag.*, 18:773, 1968.

[vK92] N. G. van Kampen. *Stochastic Processes in Physics and Chemistry*. North-Holland, 1992.

[Vot94] A. F. Voter. *Intermetallic Compounds*, volume I, chapter The Embedded-Atom Method, page 77. John Wiley & Sons Ltd., 1994.

[Vot97] A. F. Voter. Hyperdynamics: Accelerated molecular dynamics of infrequent events. *Phys. Rev. Lett.*, 78:3908, 1997.

[VPB70] V. Vitek, R. C. Perrin, and D. K. Bowen. The core structure of 1/2(111) screw dislocations in b.c.c. crystals. *Phil. Mag.*, 21:1049, 1970.

[VWN80] S. H. Vosko, L. Wilk, and M. Nusair. Accurate spin-dependent electron liquid correlation energies for local spin density calculations: a critical analysis. *Can. J. Phys.*, 58:1200, 1980.

[Wal45] G. Wald. Human vision and the spectrum. *Science*, 101:653–658, 1945.

[Wax54] N. Wax, editor. *Selected Papers on Noise and Stochastic Processes*. Dover, New York, 1954.

[WC84] G. K. White and S. J. Collocott. Heat capacity of reference materials: Cu and w. *J. Phys. Chem. Ref. Data*, 13:1251, 1984.

[Wol89] D. Wolf. A read-shockley model for high-angle grain boundaries. *Scr. Met.*, 23:1713, 1989.

[Wol90a] D. Wolf. Correlation between structure, energy, and ideal cleavage fracture for symmetrical grain boundaries in fcc metals. *J. Mater. Res.*, 5:1708, 1990.

[Wol90b] D. Wolf. Structure-energy correlation for grain boundaries in f.c.c. metalsâĂŤiv. asymmetrical twist (general) boundaries. *Acta Metall. Mater.*, 38:791, 1990.

[WR90] M. Watanabe and W. P. Reinhardt. Direct dynamical calculation of entropy and free energy by adiabatic switching. *Phys. Rev. Lett.*, 65:3301, 1990.

[WWF82] M. Weinert, E. Wimmer, and A. J. Freeman. Total-energy all-electron density functional method for bulk solids and surfaces. *Phys. Rev.* **B**, 26:4571, 1982.

[Zur91] W. H. Zurek. Decoherence and the transition from quantum to classical. *Physics Today*, page 36, 1991.

[Zwa60] R. Zwanzig. Ensemble method in the theory of irreversability. *J. Chem. Phys.*, 33:1338, 1960.

[Zwa61] R. Zwanzig. Memory effects in irreversible thermodynamics. *Phys. Rev.*, 124:983, 1961.

[Zwa73] R. Zwanzig. Nonlinear generalized langevin equations. *J. Stat. Phys.*, 9:215, 1973.

Danksagung

Mein herzlichster Dank gilt Herrn Prof. Dr. Ferdinand Haider, der die Arbeit angenommen, diese über die Jahre mit nicht nachlassendem Interesse begleitet und richtungsweisend geprägt hat.

Daneben möchte ich Herrn Priv.-Doz. Dr. Karl-Heinz Höck für die freundliche Übernahme des Zweitgutachtens danken, daß er mir über all die Jahre "die Stange gehalten", und, insbesondere in der Schlussphase, die notwendige Impulse gegeben hat, die den dann zügigen Abschluß der Arbeit ermöglichten.

Zudem bedanke ich mich herzlichst bei Prof. Dr. Georges Martin, der, ohne zu zögern, sich bereit erklärte, in der Kürze der Zeit, ein Drittgutachten zu verfassen.

Weiterhin gebührt größter Dank allen Verwandten, Freunden und Kollegen, hier insbesondere Herrn Dr. Jürgen Almanstötter und seiner Frau Brigitte, die im Laufe der Jahre durch ihr stetes Interesse am Fortgang der Arbeit ("Wann ist's denn jetzt soweit?") den Druck, diese "geordnet" zu beenden, aufrecht erhalten haben.

Darüberhinaus möchte ich die Gelegenheit nutzen, um mich bei meinem persönlichen Umfeld, an vorderster Stelle bei meiner Lebensgefährtin Erika und ihrer Tochter Daniela, und meinem Bruder Werner, die unter den "Begleiterscheinungen" des mächtigen Arbeitspensums zu leiden hatten, zu entschuldigen. Hiermit danke ich ihnen für ihre schier unendliche Geduld mit mir herzlichst.

Die Themenstellung ist Alltagsproblemen bei der Lichterzeugung entlehnt. Für die dadurch gegebenen Denkanstöße und für die Unterstützung, insbesondere in der Anfangsphase der Arbeit, danke ich daher der Fa. OSRAM.

Last but not least, danke ich selbstverständlich meinen Eltern, ohne deren Zutun ich wohl kaum die Möglichkeit bekommen hätte, mich "in der Physik zu versuchen".

Beruflicher Werdegang

Name:	Bernd Eberhard
Geburtsdatum:	23. April 1966
Geburtsort:	Augsburg
Familienstand:	ledig

seit 2000	angestellter wissenschaftlicher Mitarbeiter der Forschung und Entwicklung für Vorerzeugnisse der Fa. OSRAM in Schwabmünchen
1999-2000	freiberuflicher wissenschaftlicher Mitarbeiter der Forschung und Entwicklung für Lichtquellen der Fa. OSRAM in München
1996-1999	freiberuflicher wissenschaftlicher Mitarbeiter der Forschung und Entwicklung für Vorerzeugnisse der Fa. OSRAM in Schwabmünchen
1989-1996	Studium der Physik, Universität Augsburg
1986–1989	Bayernkolleg Augsburg, Allgemeine Hochschulreife
1983–1986	Ausbildung bei der Bayer. Bereitschaftspolizei für den mittlerern Polizeivollzugsdienst